Masafu, Christopher Kusimba (2024) *Flood dynamics derived from video remote sensing.* PhD thesis.

Flood dynamics derived from video remote sensing

Christopher Kusimba Masafu

Submitted in fulfilment of the requirements for the Degree of
Doctor of Philosophy

School of Geographical and Earth Sciences
College of Science and Engineering
University of Glasgow

September 2023

I dedicate this thesis to my beloved parents.

For my father, the late Captain Francis Milimo Masafu, and my loving mother,

Emeldah Nakhumicha Masafu

Abstract

Flooding is by far the most pervasive natural hazard, with the human impacts of floods expected to worsen in the coming decades due to climate change. Hydraulic models are a key tool for understanding flood dynamics and play a pivotal role in unravelling the processes that occur during a flood event, including inundation flow patterns and velocities. In the realm of river basin dynamics, video remote sensing is emerging as a transformative tool that can offer insights into flow dynamics and thus, together with other remotely sensed data, has the potential to be deployed to estimate discharge. Moreover, the integration of video remote sensing data with hydraulic models offers a pivotal opportunity to enhance the predictive capacity of these models.

Hydraulic models are traditionally built with accurate terrain, flow and bathymetric data and are often calibrated and validated using observed data to obtain meaningful and actionable model predictions. Data for accurately calibrating and validating hydraulic models are not always available, leaving the assessment of the predictive capabilities of some models deployed in flood risk management in question. Recent advances in remote sensing have heralded the availability of vast video datasets of high resolution. The parallel evolution of computing capabilities, coupled with advancements in artificial intelligence are enabling the processing of data at unprecedented scales and complexities, allowing us to glean meaningful insights into datasets that can be integrated with hydraulic models. The aims of the research presented in this thesis were twofold. The first aim was to evaluate and explore the potential applications of video from air- and space-borne platforms to comprehensively calibrate and validate two-dimensional hydraulic models. The second aim was to estimate river discharge using satellite video combined with high resolution topographic data. In the first of three empirical chapters, non-intrusive image velocimetry techniques were employed to estimate river surface velocities in a rural catchment. For the first time, a 2D hydraulic model was fully calibrated and validated using velocities derived from Unpiloted Aerial Vehicle (UAV) image velocimetry approaches. This highlighted the value of these data in mitigating the limitations associated with traditional data sources used in parameterizing two-dimensional hydraulic models. This finding inspired the subsequent chapter where river surface velocities, derived using Large Scale Particle Image Velocimetry (LSPIV), and flood extents, derived using deep neural network-based segmentation, were extracted from satellite video and used to rigorously assess the skill of a two-dimensional hydraulic model. Harnessing the ability of deep neural networks to learn complex features and deliver accurate and contextually informed flood segmentation, the potential value of satellite video for validating two-dimensional hydraulic model simulations is exhibited. In the final empirical chapter, the convergence of satellite video imagery and high-resolution topographical data bridges the gap between visual observations and quantitative measurements by enabling the direct extraction of velocities from video imagery, which is used to estimate river discharge. Overall, this thesis demonstrates the significant potential of emerging video-based remote sensing datasets and offers approaches for integrating these data into hydraulic modelling and discharge estimation practice. The incorporation of LSPIV techniques into flood modelling workflows signifies a methodological progression, especially in areas lacking robust data collection infrastructure. Satellite video remote sensing heralds a major step forward in our ability to observe river dynamics in real time, with potentially significant implications in the domain of flood modelling science.

Acknowledgements

Firstly, I would like to extend my sincere gratitude to my supervisor Professor Richard Williams who has guided and constantly supported me throughout my PhD. I offer my sincere appreciation for the learning opportunities provided to me through your kind support. I am indebted to Richard for his invaluable contributions that have elevated the quality and rigor of this research. Thanks to Dr Martin Hurst, his meticulous attention to detail and invaluable feedback have significantly enriched the methodological approaches employed in this work. I acknowledge the University of Glasgow's Lord Kelvin Adam Smith (LKAS) scholarship for generously funding my research, without whose award this thesis would never have been written. Thanks to the academic, technical and support staff at the School of Geographical and Earth Sciences who also supported my work.

I would also like to thank Professor Mark Trigg (University of Leeds) who has been an incomparable mentor, teacher, friend, and a major contributor to my academic success as a postgraduate student. Mark's patient mentorship over the years has not only refined the scholarly aspects of this thesis but has also contributed to my personal and professional growth.

I thank the good friends who have walked with me through this journey and from whom I learnt immensely. Special thanks to Khaled Alghafli, Anthony Kadoma, Fuad Warsame, Haritha Venu, Laura Ebeler, Najma Issa, Hazel Kristoffersen, Pammie Tolentino and Stellah Abei Ekitela, you enriched my time in Glasgow immeasurably. And to my good brother David Echuman Koriang', with whom I have walked since our days at Starehe Boys' Centre and School, you have been a constant source of laughs, advice, and reflection on all things life, thank you.

Finally, and most importantly – I thank Pascalyne Wangechi Koine, my sister and mother for their constant support, prayers, and encouragement.

Author's Declaration

I declare that, except where explicit reference is made to the contribution of others, this thesis is the result of my original work and has not been submitted for any other degree at the University of Glasgow or any other institution.

Chapters 4, 5 and 6 in this thesis follow the 'Alternative Format Thesis' guidelines derived from the University Code of Practice. The rationale for submitting an alternative format thesis was that the work conducted in each chapter was deemed to be a significant contribution to the existing literature that warranted timely publication in academic journals. Each chapter has been published. Much of the texts, figures, and tables presented in Chapters 4, 5 and 6 are identical to the published versions. Supplementary materials from those papers (e.g., supplementary figures/texts/tables) have been moved into the body of these chapters to provide easier readability of the thesis.

The work in Chapter 4 of this thesis has appeared in publication as follows:
Masafu, C., Williams, R., Shi, X., Yuan, Q., Trigg, M. (2022). Unpiloted Aerial Vehicle (UAV) image velocimetry for validation of two-dimensional hydraulic model simulations.
Journal of Hydrology, 612, 128217
https://doi.org/10.1016/j.jhydrol.2022.128217

The work in Chapter 5 of this thesis has appeared in publication as follows:
Masafu, C., & Williams, R. (2024). Satellite video remote sensing for flood model validation.
Water Resources Research,
https://doi.org/10.1029/2023WR034545

The work in Chapter 6 of this thesis has appeared in publication as follows:
Masafu, C., Williams, R., & Hurst, M. D. (2023). Satellite video remote sensing for estimation of river discharge.
Geophysical Research Letters, 50, e2023GL105839.
https://doi.org/10.1029/2023GL105839

I confirm that Chapter 4 was jointly authored with Richard Williams, Xiaogang Shi, Qiangqiang Yuan and Mark Trigg, and I contributed 90% of this work.

I confirm that Chapter 5 was jointly authored with Richard Williams, and I contributed 95% of this work.

I confirm that Chapter 6 was jointly authored with Richard Williams and Martin D Hurst, and I contributed 95% of this work.

Christopher Kusimba Masafu

September 2023, Glasgow

Data availability

Data used in Chapter 4 can be accessed via doi:

http://dx.doi.org/10.5525/gla.researchdata.1325

Data used in Chapter 5 can be accessed via doi:

http://dx.doi.org/10.5525/gla.researchdata.1537

Data used in Chapter 6 can be accessed via doi:

http://dx.doi.org/10.5525/gla.researchdata.1538

Abbreviations

aDcp	Acoustic Doppler Current Profiler
AI	Artificial Intelligence
CNN	Convolutional Neural Network
DEM	Digital Elevation Model
GAN	Generative Adversarial Network
GIS	Geographical Information System
GNSS	Global Navigation Satellite System
GPS	Geographical Positioning System
HEC-RAS	Hydrologic Engineering Centre River Analysis System
InSAR	Interferometric Synthetic Aperture Radar
LiDAR	Light Detection and Ranging
LSPIV	Large Scale Particle Image Velocimetry
LSTM	Long Short-Term Memory
MAE	Mean Absolute Error
MCMC	Markov Chain Monte Carlo
MERIT	Multi Error Removed Improved Terrain Dem
ML	Machine Learning
NASA	National Aeronautics and Space Administration
NDWI	Normalised Difference Water Index
PIV	Particle Image Velocimetry
PTV	Particle Tracking Velocimetry
Q	Discharge
R^2	Coefficient of Determination
ReLU	Rectified Linear Units
RF	Random Forest
RMSE	Root Mean Square Error
SRTM	Shuttle Radar Topography Mission
SVM	Support Vector Machine
TMPA	TRMM Multi-Satellite Precipitation Analysis
TRMM	Tropical Rainfall Measuring Mission
TTA	Test-Time Augmentation
UAV	Unpiloted Aerial Vehicle
UK	United Kingdom

USGS	U.S. Geological Survey
WSE	Water Surface Elevation

List of Figures

List of Tables

Table of Contents

Chapter 1 - Introduction

1.1 Background and rationale

Floods are the most frequent of all natural disasters with over 1.81 billion people, or 19% of the global population, exposed to significant risk during 1% Annual Exceedance Probability (AEP) flood events (Rentschler and Salhab, 2020). Acute flooding episodes are becoming increasingly frequent, primarily due to climate and land use change, disrupting livelihoods and reversing progress towards eradicating extreme poverty (Alfieri *et al*., 2015; Alifu *et al*., 2022; Swain *et al*., 2020; Tabari, 2020). Exposure to flood risk in light of current and projected flood impacts lends urgency to the development and implementation of flood risk management strategies to ameliorate the socio-economic impacts of floods. Managing risks associated with flood events requires accurate flood risk maps which support identification of areas with the highest probabilities of suffering significant flood damage. Flood risk maps are key decision-making tools used to characterize floods, including their expected velocities and depths. Given the complexity and dynamic nature of hydrological systems, numerical hydraulic models, which are used to create flood hazard maps (amongst other products which can inform the design of dams and levees, stormwater management systems, coastal defence systems), are an invaluable means to simulate flooding to varying degrees of complexity, aiding flood risk management (Pender and Faulkner, 2011).

Hydraulic models have proven to be indispensable tools for assessing and delineating flood risk and flood hazard from coastal, pluvial, groundwater, dam break, estuarine, and fluvial sources (Grimaldi *et al*., 2019). Flood hazard maps will typically be derived from hydraulic model simulations showing areas of potential flooding while flood risk maps depict the potential negative impacts on the hazard, including social, economic and environmental (Auliagisni *et al*., 2022).The fluid mechanics of floodplain inundation can be characterized in either one, two or three dimensions. One- and two-dimensional hydraulic models are based on the Saint-Venant equations, also known as shallow water equations. During in-channel flow, a river can be regarded as a 1D vector and flow can be adequately described using 1D Saint-Venant equations. During flood events when flow overtops river banks, floodplain flow is considered a predominantly 2D shallow water process and is expressed using either the full 2D Saint-Venant equations or the diffusion wave based derivations of these equations (Bates *et al*., 2005; Bates and De Roo, 2000; Hunter *et al*., 2008). Although floods are principally a shallow-water phenomenon, 3D processes dominate the floodplain-channel interface. These are most accurately represented using 3D Navier-Stokes equations. However Bates (2022) and Wing (2019) note that the 3D recirculations that exist at the floodplain-channel interface are of very small scale and provide little meaningful information over the large spatial scales within which floodplain inundation occurs and can thus be assumed to be trivial. Further, the complexity of these negligible 3D processes does not necessitate predictions from hydraulic models when simulating large scale flood flows (e.g. Fewtrell, 2008). As a consequence, the proliferation of remotely sensed datasets including terrain and bathymetric data, model boundary condition data as well as airborne/spaceborne observations of flood events which are used to calibrate/validate hydraulic model predictions, full 2D and hybrid 1D-2D model codes remain the most widely adopted models for floodplain hazard mapping (Horritt and Bates, 2002; Hunter *et al.*, 2008; Peña and Nardi, 2018; Pinos and Timbe, 2019).

Hydraulic models, by their very nature, are an approximation of reality and their predictions suffer from varied limitations and uncertainty, chiefly model structural uncertainty, uncertainty of input data, the transient nature of the physical characteristics of flooded areas, and the sparsity and uncertainty of observations used for calibration and validation of model predictions (Bates, 2004; Di Baldassarre and Uhlenbrook, 2012). To improve hydraulic model prediction accuracy of the spatiotemporal patterns of flood dynamics, a rigorous assessment of the sources of prediction uncertainty is essential. However, it would be computationally prohibitive to evaluate all sources of uncertainty in hydraulic model predictions given that there will always be residual error in model representations of the real world (Beven *et al.*, 2015). Indeed, a pragmatic approach to assessing the skill of hydraulic models would entail targeting and constraining established sources of uncertainty while balancing computational burden and the need for timely communication of model predictions.

Spatially distributed calibration and validation data are critical for improving the predictive capability of hydraulic models. The proliferation of remotely sensed datasets for assessment of hydraulic model simulations has proven pivotal in understanding flood dynamics (Domeneghetti *et al.*, 2019). The global availability of optical, radar and microwave instruments has enhanced our ability to monitor floods from space at increasingly high spatial and temporal resolutions. Integrating remotely sensed data with flood models via model calibration or validation, and data assimilation techniques, has been demonstrated to provide significant value in operational flood monitoring and management (e.g., Giustarini *et al.*, 2015; Nguyen *et al.*, 2022; Schumann *et al.*, 2009). Although field-based gauging stations remain invaluable in constraining flood model predictions, their decline globally has necessitated the uptake of remote sensing observations (McCabe *et al.*, 2017a). Thanks to funding constraints and inadequate institutional frameworks (amongst other reasons), there has been a marked decline in the density of discharge gauges globally, including a 90% reduction in the number of stations reporting discharge to the WMO Global Runoff Data Centre (GRDC) between 1996 – 2001, as well as a 79% and 51% decline in station network density in Russia and North America between 1986 to 1999 (Group *et al.*, 2001; Haile *et al.*, 2022; Mishra and Coulibaly, 2009; Shiklomanov *et al.*, 2002). Indeed in some cases, the calibration and validation of hydraulic model predictions can only be accomplished using a combination of field data and remotely sensed data (Domeneghetti *et al.*, 2014; Matgen *et al.*, 2010; Montanari *et al.*, 2009).

The calibration of hydraulic models is traditionally accomplished by varying a friction parameter (Manning's roughness coefficient, *n*) assigned to the main channel and floodplain, based on empirically derived tables (e.g., Attari and Hosseini, 2019; Chow, 1959) over multiple model runs until model results closely match observed benchmark data. Benchmark data to guide hydraulic model calibration efforts generally includes: river gauge water levels measured at stream gauging stations (Horritt *et al.*, 2010; Kumar *et al.*, 2017), surveyed post-flood event water marks and wrack lines (Grimaldi *et al.*, 2016a; Parkes *et al.*, 2013), airborne or satellite images of flood extent (Di Baldassarre *et al.*, 2009; A. Tarpanelli *et al.*, 2013) and less commonly, directly observed surface velocities from acoustic doppler current profilers (aDcps), radar gauges or Unpiloted Aerial Vehicles (UAVs) (Barker *et al.*, 2018; Masafu *et al.*, 2022). The calibration of hydraulic models therefore calls for multiple model simulation runs relying on suitable benchmark data in order to attain optimal model parametrization.

Validation of hydraulic model predictions, which entails comparing a single model run to benchmark data independent from the calibration data set, is a prerequisite for the successful derivation of fit for purpose flood hazard maps. Barker *et al.*, (2018) and Bates, (2022) contend that hydraulic models are in need of further rigorous and comprehensive validation, as high-performance computing resources and a deluge of remotely sensed data transform flood science from a data-poor to a data-rich field. Hydraulic model outputs typically include spatial patterns of flood extents, velocity magnitudes and water surface elevations from which other hydraulic variables can be computed including Froude number, shear stress, Courant number etc. Validation of the predictive skill of hydraulic models has been based on comparisons of how well flood extent maps match observed extents, typically drawn from airborne photography or satellite sensors (e.g., Bernhofen *et al.*, 2018; Wing *et al.*, 2017). Less commonly, other studies have relied on quantitative comparisons of velocity magnitude and direction, collected using current/electromagnetic meters and acoustic doppler current profilers (aDcp), for model validation (e.g., Jowett and Duncan, 2012; Williams *et al*., 2013).

Observation and monitoring of surface water dynamics has benefitted enormously from the rapid advancement of remote sensing technologies. A wide variety of platforms supplying spatially distributed observations of flood extents, water stages and more recently, velocities, offers the prospects of systematically evaluating the predictive skill of hydraulic models. An ever-growing number of remote sensing platforms, including satellite constellations, airborne sensors on aircraft and helicopters, as well as unpiloted aerial vehicles (also referred to as unpiloted aerial systems, or drones) are supplying fine scale spatial and temporal resolution data at unprecedented volume. This data deluge has led to the big data phenomenon and the evolution of data science which is offering novel techniques to efficiently process and analyse all this data. Advances such as artificial intelligence techniques (AI) offer the ability to automatically extract useful hydrometeorological information from multisource (e.g., microwave, optical), multitemporal and multiresolution remotely sensed data (Ghamisi *et al*., 2018). Furthermore, the opportunities offered by data analytics are enabling the ingestion of new sources of data, such as video remote sensing, into hydraulic modelling in more informative ways as compared to traditional data-assimilation techniques. Remote sensing-derived digital elevation models (including LiDAR – light detection and ranging; SfM – Structure from Motion photogrammetry), land cover, channel morphology, inundation extents and velocities are providing powerful support for the development, calibration, and validation of hydraulic models.

Whilst high resolution still imagery can provide exceptionally clear and valuable insights into flood extents and propagation, the advent of high-definition video sensors on board UAV and satellite platforms are providing temporal insights previously unattainable by traditional remote sensing techniques. The ubiquity of consumer grade UAVs alongside analogous advances in digital photogrammetry, computer vision techniques for image segmentation and non-contact methods of flow estimation have increased our ability to monitor river parameters rapidly and at reasonable costs (Eltner *et al*., 2021, 2019). UAV video data has been demonstrated to monitor and assess surface flow velocities (e.g., Koutalakis *et al*., 2019; Liu *et al*., 2021) and derive flood extents (e.g., Girisha *et al*., 2019) permitting contactless measurements of floodplain phenomena even for difficult-to-access locations.

Space-based optical satellite video sensors are another emerging frontier for dynamic earth observation, with the launch of high temporal resolution satellite-based video sensors, it is now possible to leverage on these platforms to estimate discharge directly from space, as well monitor flood dynamics, thanks to the feature-rich temporal dimensions offered by video. Although plagued by the limitations of cloud cover and low spatial resolution, advances in computer vision techniques, such as deep learning-based cloud removal techniques (e.g., Ma *et al.*, 2023; Meraner *et al.*, 2020) as well as video super-resolution (e.g., Liu *et al.*, 2022; Xiao *et al.*, 2021), the ultra-high temporal resolution offered by satellite video presents important avenues to advance flood hydrology.

Artificial Intelligence (AI) and Machine Learning (ML) techniques are radically transforming the possibilities for handling and processing the exploding volume and variety of earth observation imagery from satellites, aerial, and ground sensors. The substantial quantities of remote sensing data generated from multi-source, multi-scale sensors have heralded the ‘Big Data’ era for remote sensing, defined as a collection of datasets whose volume, variety, complexity and rate of production exceeds state-of-the-art/traditional data processing capacity and require new forms of processing to enable optimal interpretation (Chen and Zhang, 2014; Ma *et al.*, 2015). Applications of AI and ML algorithms in remote sensing are enabling implementation of complex tasks such as super-resolution, denoising, scene classification, object detection, semantic segmentation by leveraging on high-performance computing and computer vision algorithms which are helping to glean meaningful information from spatial big data. Further, deep neural networks, which are multivariate, non-parametric AI algorithms inspired by biological neural networks, are finding applications in flood hazard mapping and complementing outputs from traditional physics-based models of flood hazard (e.g. Gebrehiwot *et al.*, 2019; Hashemi-Beni and Gebrehiwot, 2021; Satarzadeh *et al.*, 2022).

1.2 Research aim

The emergence of airborne and space-borne optical video sensors is offering fine spatial and temporal resolution data with the feasibility to enhance our understanding of flood dynamics including flow velocities, inundation extents and water levels.

The principal aim of this thesis is to leverage advances in remote sensing technology, particularly UAVs and satellite platforms, to enhance the predictive capabilities of hydraulic models. It strives to bridge the gap between real-world observations and computational simulations by utilizing video data from these platforms to validate hydraulic model predictions. Additionally, the thesis explores the innovative concept of estimating discharge using satellite video data, potentially opening new avenues for non-intrusive hydrological assessments.

To achieve this aim, a set of specific objectives (O) and research questions (RQ) were to:

O1. Assess whether hydraulic model predictions can be accurately assessed using video data.

RQ1a Can UAV-based video be used to comprehensively calibrate and validate hydraulic model predictions at the reach scale?

RQ1b Can satellite-video based image velocimetry and deep-learning-based image segmentation be used to validate hydraulic model predictions at the reach scale?

O2 Evaluate the application of satellite-based video in estimating river discharge from space.

RQ2a Can image velocimetry techniques provide plausible riverine velocity estimates from space?

RQ2b How well do discharge estimates based on satellite-video compare with ground observations and hydraulic model predictions?

These aims and objectives are addressed within three empirical chapters that are published in peer-reviewed journals.

1.3 Thesis structure

This thesis is divided into 8 chapters structured sequentially to address each research question (Section 1.2). An overview of each of the chapters is provided below.

Chapter 2 provides a comprehensive evaluation of hydraulic modelling tools and their present data requirements, alongside highlighting the essential contribution of remote sensing in developing flood models.

In Chapter 3, an overview of the methods used in the thesis is provided, with specific methodologies detailed in subsequent empirical chapters. The chapter begins with an overview of the study sites, followed by a description of the hydraulic model. Image processing techniques, specifically image-based velocimetry and Structure-from-Motion photogrammetry are described, followed by a discussion on artificial intelligence techniques for image segmentation.

In Chapter 4, non-intrusive techniques for measuring river velocities are explored, in support of RQ1a. The feasibility of image velocimetry in providing credible data for calibration and validation of 2D hydraulic models predictions is investigated within the first study catchment, Swindale Beck, United Kingdom.

This chapter is adapted from:

Masafu, C., Williams, R., Shi, X., Yuan, Q., Trigg, M., (2022). Unpiloted Aerial Vehicle (UAV) image velocimetry for validation of two-dimensional hydraulic model simulations. *Journal of Hydrology*, 612, 128217. https://doi.org/10.1016/j.jhydrol.2022.128217

Chapter 5 focuses on validating 2D hydraulic model predictions using satellite video-derived flood extents and velocities within the Darling River, Australia to address RQ1b and RQ2a.

This chapter is adapted from:

Masafu, C., & Williams, R. (2024). Satellite video remote sensing for flood model validation. *Water Resources Research,* https://doi.org/10.1029/2023WR034545

Chapter 6 showcases the potential of estimating river discharge using a combination of satellite-derived video imagery, non-contact velocity estimation techniques, and high-resolution topography within the Darling River, Australia, addressing RQ2a and RQ2b.

This chapter is adapted from:

Masafu, C., Williams, R., & Hurst, M. D. (2023). Satellite video remote sensing for estimation of river discharge. *Geophysical Research Letters*, 50, e2023GL105839. https://doi.org/10.1029/2023GL105839

Chapter 7 comprises a synthesis of the thesis, reiterating how each research question has been addressed to fulfil the overarching thesis aim. This chapter discusses the limitations of the research, contribution of the research to the scientific community and identifies avenues for potential future research directions.

Chapter 8 concludes the thesis with a summary of the main findings.

Chapter 2 - Modelling floods

2.1 Introduction

In Chapter 1, the importance of obtaining reliable spatially distributed flood model predictions was broadly outlined, noting that improved scientific understanding of floodplain processes simulated by hydraulic models will help ameliorate the negative impacts of ever-increasing flood events. The proliferation of newly available remote sensing datasets, computing power and the accelerated rise of innovative analytical techniques is opening up new opportunities to meet increasing demands for accurate predictions of phenomena associated with floods, including flow velocities, inundation extents and water surface elevations. The need for integrating these new data and methods into existing flood modelling processes is apparent and will help progress both the accuracy and near-real time characterization of flood velocity, depths, and extents, aiding in decision making especially in data poor regions. Chapter 2 will provide a detailed appraisal of hydraulic modelling tools and their current data needs as well as the integral role of remote sensing in the development of spatially accurate flood hazard maps. This chapter will further refine the research objectives and explicitly outline existing knowledge gaps that will be addressed in subsequent chapters.

2.2 Hydraulic modelling

2.2.1 Introduction

The modelling of floodplain processes relies on extensive data on channel and floodplain geometry, time series of bulk flow rates which serve as model boundary conditions, spatially distributed roughness coefficients as well as data for model calibration and validation. The extent to which these data are available to adequately represent the complex flow interactions occurring at both reach and catchment scales has been the subject of several studies (e.g., Di Baldassarre and Uhlenbrook, 2012; Yan *et al.*, 2015). A key driver for advances in hydraulic modelling has been the proliferation of remotely sensed data from air- and space-borne platforms. The two-dimensional representation of remotely sensed data has enabled the efficient parametrization of hydraulic models which generally tend to represent hydrodynamics of the river-floodplain continuum in two dimensions. Despite the prevalence of complex three-dimensional processes within the channel zone, the utilization of 3D models has remained modest. This is due to evidence suggesting that the heightened intricacy of 3D models doesn't result in significant benefits when contrasted with predictions based on 2D model methods (Bates, 2022; Kesler, 2023). Indeed, the computational costs of simulating 3D inundation dynamics at reach or catchment scale would be prohibitive and as a result, most studies to date have relied on 1D and 2D representations of in-channel and floodplain flows.

Although the principals of flood routing using 2D hydraulic models are well understood, an issue of relative importance when simulating complex channel-floodplain flows is the availability of appropriate data for process representation. Indeed, the data requirements for hydraulic modelling can broadly be categorized as; (i) input data required to parametrize the model, and (ii) data required to evaluate the predictions of hydraulic flood models. In this context, a review of data required by numerical models for flood inundation modelling is provided.

2.2.2 Topographical data

Topographical representation of the physical-land surface over which hydraulic model simulations occur can be characterized via numerical representations of the bare-earth surface known as Digital Elevation Models (DEMs). DEMs have traditionally been generated through classical ground surveys and digitization of topographic maps, both time-consuming and expensive exercises which cannot always be accomplished in remote locations. The generation of terrain elevation at large-scale has been driven by advances in remote sensing techniques including the use of airborne and spaceborne Interferometric Synthetic Aperture Radar (InSAR), airborne/satellite photogrammetry and Light Detection and Ranging (LiDAR). The accuracy of hydraulic model simulations relies strongly on the quality of topographical data since overland flow is driven by gravity. While most platforms acquire terrain data as Digital Surface Models (DSMs) that capture ground objects including vegetation, building and other artifacts that could obstruct flow paths, flood inundation modelling requires the use of 'bare earth' topography referenced to a vertical datum. Filtering of objects from DSMs is therefore required for flood modelling applications (however in detailed modelling studies these objects are essential and could also be represented using appropriate manning roughness values).

On the global scale, DEMs have been created using satellite InSAR and disseminated freely via open access portals. Due to its ease of accessibility, resolution and vertical accuracy, the most popular of global DEMs for flood inundation mapping remains the Shuttle Radar Topography Mission (SRTM) which was first released in February 2003 and covers around 80% of the earth's land surface between 60°N and 56°S (Hawker *et al.*, 2018). Originally distributed at a resolution of 3-arc seconds (~90m), SRTM was re-released at 1 arc-second (~30m) in 2015 with a vertical accuracy of 16 m absolute error at 90% confidence worldwide (Mukul *et al.*, 2017). Other global scale 1-arc-second DEM products include the ASTER-Global Digital Elevation Model 2 (ASTER GDEM 2) (Tachikawa *et al.*, 2011), the global advance land observing satellite (ALOS) world 3D-30m (AW3D30) DEM (Tadono *et al.*, 2015), TanDEM-X DEM (Krieger *et al.*, 2007) and MERIT (Multi-Error-Removed Improved-Terrain) DEM (Yamazaki *et al.*, 2019, 2017). A key limitation when using global DEMs for flood modelling is their low spatial resolution and significant vertical error which can often be larger than the amplitude of most flood waves (Archer *et al.*, 2018; Wilson *et al.*, 2007). Asides for the fact that most global DEMs, such as the popular SRTM-DEM, are dated and not regularly updated to account for geomorphological changes in topography, such as during extreme events including floods and landslides, global spatial resolution of these products is limited making them unsuitable for local scale applications of flood modelling. The requirement for local-scale flood models is essential for validating larger scale models amongst other uses. Thus accurate, high resolution DEMs are very important for modelling inherently local scale processes which cannot be captured using global DEMs.

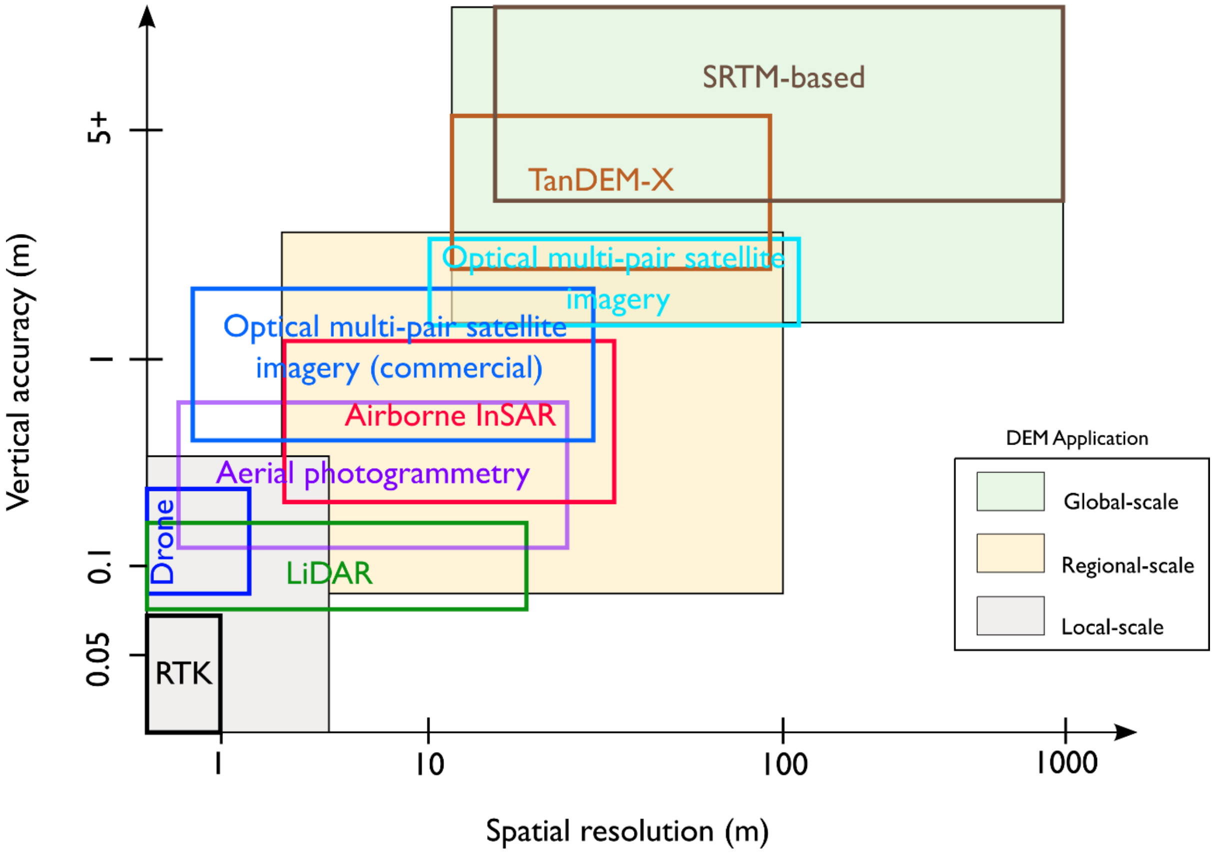

Figure 2.1 DEM data sources, spatial resolution, and vertical accuracies for different scales. From Schumann and Bates (2018).

Technological advancements have led to the production of high-precision digital surface models, with the two most notable technologies being high resolution laser altimetry data, LiDAR (light detection and ranging), and more recently, UAV based Structure-from-motion (SfM) photogrammetry (Figure 2.1). Although the elevation accuracies and precision achieved by LiDAR digital terrain models was a crucial step from coarse resolution global DEMs in flood inundation modelling, the availability of national-scale high-quality LiDAR data is still largely limited to a few countries due to high acquisition costs. UAV-based SfM photogrammetry has emerged as cost-effective means of acquiring high-resolution and high-accuracy elevation information thanks to the falling costs of lightweight consumer-grade UAVs/drones alongside increasingly affordable photogrammetric processing software (Coveney and Roberts, 2017; Niethammer *et al.*, 2012). The positional accuracy and quality of DTMs based on SfM photogrammetry has been demonstrated to attain accuracies comparable to LiDAR even without the use of ground control points (Schumann *et al.*, 2019; Stott *et al.*, 2020), further demonstrating the capability for rapidly producing DEMs on the centimetre to kilometre scale. The ability of computer vision algorithms deployed by SfM processing chains has enabled the generation of DEM surfaces with vertical accuracies of up to < 20 cm at spatial resolutions ranging from 0.5 – 5 m (Carrivick and Smith, 2019). SfM DEMs can also provide data on surface roughness, a key hydraulic model parameter which will further enable detailed local-scale hydraulic modelling.

2.2.3 Channel bathymetry data

The accurate representation of riverbed topography, often referred to as channel bathymetry, is vital for accurate description of channel discharge capacity when modelling river systems. Often, topographic data in the form of DEMs lacks embedded accurate channel geometric data which can lead to erroneous hydraulic conveyance affecting simulated flood dynamics including water depths, velocities, time to peak and inundation extents. Detailed channel bathymetry data are not available in most rivers and remain sparse or outdated even in highly resourced countries where high resolution DEMs, such as those obtained using LiDAR sensors, lack detailed channel bathymetry due to the inability of LiDAR systems to penetrate water columns. At present, channel bathymetry cannot be reliably obtained using remote sensing techniques and remains a key challenge for hydraulic modelers when simulating in-channel conveyance.

Channel bathymetry data are traditionally collected via bathymetric surveys using total stations and RTK-GNSS (Real Time Kinematic – Global Navigation Satellite System) where cross-sectional measurements are taken at regular intervals. Other techniques include the use of Sound Navigation and Ranging (SONAR) techniques on-board piloted or un-piloted vessels and quite popularly, the use of acoustic Doppler current profilers (aDcps) mounted on boats. Whilst these well-established methods generate highly accurate data, they remain expensive, time-consuming, and impractical in large multichannel rivers.

Remote sensing techniques for estimating channel depth have been proposed in order to overcome the afore mentioned limitations of in-situ surveys and have been described as being either direct or indirect methods (Bandini *et al*., 2023). Indirect retrievals of channel depths using satellite estimates of water surface elevation has been demonstrated via satellite altimetry (e.g., Durand *et al*., 2014; Jiang *et al*., 2019; Ma *et al*., 2020). Meanwhile, techniques that observe inundated channel topography and attempt to reconstruct channel cross-sections fully include bathymetric LiDAR, through-water photogrammetry based on SfM algorithms combined with RTK-GNSS and spectral methods relying on multispectral and RGB imagery for 3D reconstruction of submerged river sections (Alvarez *et al*., 2017; Dietrich, 2017; Eltner *et al*., 2021; Kasvi *et al*., 2019). Woodget *et al*. (2015) demonstrated the capabilities of UAV-SfM DEMs to retrieve submerged channel bathymetry deploying simple refraction correction techniques to improve their accuracy at the mesoscale (channel lengths between ~10 m to a couple hundred meters). Despite their promise, these techniques remain limited to shallow rivers with low turbidity limiting their application to a narrow range of river systems.

2.2.4 Discharge characterization

Discharge data are a key hydraulic model boundary condition and can be obtained either from observations of flow, or where such in-situ data are lacking, via approximations using hydrological models. Although observations of flow are the most accurate data source for parametrizing hydraulic models, they are not error-free. Water levels obtained from rating curves, which relate river stage (water level) measured at a gauging station to discharge, are subject to uncertainties especially during flood events when extrapolation has to be done beyond the gauge maxima. McMillan *et al*. (2012) report discharge measurement errors of up to ±40% during flood flows and estimate typical errors of ± 10-20% for medium or high (in-bank) flows. Di Baldassarre and Uhlenbrook (2012) further report additional sources of uncertainty for river flow data emanating from errors in individual stage and discharge measurements used to construct rating curves as well as errors introduced by unsteady flow conditions during flood events. The evolution of new technologies, such as aDcps has also offered an opportunity to collect velocity and cross-section area data, hence discharge, with mean relative errors of -3 to 5 % as compared to current meters and -7 to 5% as compared to rating curves (Mueller, 2003; Mueller *et al.*, 2013). Large Scale Particle Image Velocimetry (LSPIV) based discharges have also been found to generally be in good agreement (±10%) with concurrent aDcp measurements and deviating < 20% from rating curve observations in field studies including those by Dramais *et al.* (2011), Le Coz *et al.* (2010) and Lewis *et al.* (2018).

Hydrological models have been used to estimate river flows by utilizing remote sensing inputs, such as evapotranspiration, land cover, topography and runoff, supplementing river discharge measurements such as in Bravo *et al.* (2012) who coupled a hydrological and hydraulic model in the Upper Paraguay River Basin. Although coupled hydrological-hydraulic modelling approaches have been applied in flood prediction studies, such as in ungauged catchments (e.g., Hasan *et al.*, 2019; Komi *et al.*, 2017), cascading uncertainties from parameterization and inputs used to drive hydrological models can significantly degrade hydraulic model predictions. Remotely sensed datasets have been favoured in driving hydrological models as they are often easier to obtain, can cover extensive geographic regions and are generally temporally consistent (Xu *et al.*, 2014). However, most of these key datasets, have been shown to be highly uncertain, such as precipitation derived from PERSIANN-CCS (Precipitation Estimation from Remotely Sensed Information using Artificial Neural Network–Cloud Classification System) product (Moazami *et al.*, 2014; Moradkhani *et al.*, 2006) and the Tropical Rainfall Measuring Mission (TRMM) (AghaKouchak *et al.*, 2009; Rauniyar *et al.*, 2017). The poor correlation between remotely sensed and in-situ datasets used to drive hydrological models, as well as the tendency of remotely sensed datasets to underestimate extremes (Bharti *et al.*, 2016; Lo Conti *et al.*, 2014; Palharini *et al.*, 2020) remains a challenge for accurate predictions of spatio-temporal patterns of flooding based off coupled hydrological-hydraulic models.

2.2.5 Model calibration and validation

Calibration of hydraulic models is commonly attained by varying channel and floodplain friction coefficients based on empirically derived Manning's *n* values (Chow, 1959). Bates *et al.* (2014) indicated roughness values as being a key source of uncertainty in flood inundation modelling. Indeed, all model calibrations are subject to uncertainty as it is impossible to specify with complete accuracy the initial and boundary conditions appropriate for model simulations. Beven (2006) and Beven and Freer (2001) provided an extensive analysis on the uncertainty of model calibration efforts, in particular the fact that multiple calibrated parameter sets can yield acceptable simulations (i.e., equifinality) therefore resulting model predictions will always bear some uncertainty. The calibration of hydraulic models using methods that acknowledge residual parametric uncertainty have been proposed by Beven and Binley, (2014) who introduced the Generalized Likelihood Uncertainty Estimation Technique (GLUE). GLUE utilizes Monte Carlo sampling to estimate model predictive uncertainty and has been deployed to estimate spatially distributed uncertainty by Aronica *et al.* (2002), Jung and Merwade (2012), Liu *et al.* (2020) and Mason *et al.* (2009). Model calibration often uses a varied number of quantitative metrics to compare model simulation to benchmarks which commonly include the Nash-Sutcliffe efficiency (NSE), coefficient of determination (R^2), percent bias (PBIAS) and a central tendency of absolute errors e.g., mean absolute error (MAE), root mean square error (RMSE) and mean square error (MSE). Traditionally, field data such as discharge values, time-series of gauged water levels and debris marks of peak water level have been shown to provide acceptable information that sufficiently helps constrain hydraulic models (e.g., Domeneghetti *et al.*, 2014; Reynolds *et al.*, 2020). The use of binary metrics for comparison of modelled versus observed flood extent data has also been used to maximize model performance through calibration in various studies (e.g., Bernhofen *et al.*, 2018; Hoch and Trigg, 2019; Wing *et al.*, 2017). Contingency tables that report the number of pixels predicted correctly or incorrectly as wet or dry are used to compute model performance measures including the ubiquitous Critical Success Index (CSI), false alarm ratio, bias and hit rate.

The proliferation of spatially detailed remote sensing datasets, such as SfM DEMs, satellite video flood inundation imagery and non-contact image velocimetry are enabling the rigorous validation of hydraulic models (Barker *et al.*, 2018; Masafu *et al.*, 2022). Bates (2022) asserted the vital significance of comprehensive hydraulic model validation using fine scale resolution data (such as LiDAR terrain data), arguing the proper benchmarking of flood models remains a key challenge for flood modelers. Further, the use of high resolution datasets for rigorous validation of hydraulic models has been shown to have a greater impact on improving model skill as opposed to advancing model physics (Fewtrell *et al.*, 2011; Smith *et al.*, 2012). The surge of comprehensive sets of remotely sensed data, particularly in data scarce areas, against a limited set of model validation studies that explore this wealth of information indicate a clear need for advancements in benchmarking of hydraulic models. Although there is an acknowledged lack of scientific consensus on the quantitative standards and criteria for evaluation of hydraulic models (Grimaldi *et al.*, 2019; Pasternack, 2011), the requirement for testing model results for precision and accuracy remains paramount.

2.3 Remote sensing of floods

2.3.1 Introduction

The landscapes over which flood flows propagate are typically vast and complex with varied topography, making remotely sensed data useful for monitoring floods at such wide scales. A key issue with gathering observation data using ground stations is the fact that ground monitoring stations are on a persistent and pervasive decline globally, adversely impacting meaningful flood flow analysis (Walker *et al.*, 2016; World Bank, 2019). The lack of institutional capacity to maintain gauging stations coupled with reductions in budgets for field maintenance are problems not unique to developing nations but indeed are significant issues in developed countries as well (Fekete and Vörösmarty, 2007; Grimes *et al*., 2022; Houghton-Carr *et al*., 2006). Further, observation gauges are typically installed in remote settings and quite far apart, which leads to sparse monitoring of flood dynamics in both space and time (Schumann *et al*., 2015). Remote sensing of floods can therefore complement ground-based observations, providing crucial data including DEMs, land cover data, river velocities which can be utilized to support detailed hydraulic modelling.

Whilst remote sensing observations are of immense value, the data provided are generally snapshot observations, meaning a high temporal resolution is missing which is a crucial element in understanding the evolution of flood events. A new generation of optical video sensors are however enabling the acquisition of high temporal resolution data that shall enable detailed studies of flood dynamics.

Detailed reviews of efforts to integrate remotely sensed data with hydraulic models were presented by Bates *et al*. (2014a) and Schumann *et al*. (2009). Asides from providing direct observations of flood events, remotely sensed data can be integrated with hydraulic models via calibration of model parameters, through validation of model predictions and data assimilation for real time updating of flood forecasts (Barthélémy *et al*., 2018; Oubanas *et al*., 2018). In addressing the considerable contributions of detailed and accurate data for parametrizing hydraulic models, Bates (2012) underlined the importance of accurate and new data sources in understating flood plain inundation as opposed to efforts directed towards developing new numerical solutions and small increments in model physics. The growing availability of fine-scale remotely sensed data will vastly improve the predictive ability of hydraulic models and will play a greater role in addressing the principal uncertainties associated with field-scale applications of flood models.

2.3.2 Optical remote sensing

Optical imaging sensors function by collecting incident electromagnetic radiation, spanning the visible (optical) range of the electromagnetic spectrum, which is then converted to visible imagery. Acquisition of information about floods is typically achieved via airborne or satellite platforms and depends upon weather conditions (primarily the absence of clouds), vegetation canopy cover (which might obstruct floods) as well as water quality parameters (such as turbidity) (Schumann, 2017). Optical techniques are an uncomplicated way of acquiring and processing flood imagery, with images depicting water bodies being easier to interpret, however the logistical set-up of dedicated flights comes at a steep price. UAV based sensors are now serving to alleviate these concerns, however, they suffer from low spatial extents as compared to satellite-based sensors. Optical satellite imagery offers varying spatial resolutions of data and are generally multi-mission, though the low temporal resolution (revisit period) of these platforms means the acquisition of useful satellite imagery of a flood might occur by chance depending on the satellite's revisit orbit (Table 2.1). Optical remote-sensing systems can be classified according to the number of spectral bands used in the imaging process. First, panchromatic imaging systems acquire images with only one spectral band that combines red, green, and blue bands and usually displayed as a grey scale image. Second, multispectral imaging systems obtain images composed of multiple spectral bands which can be displayed in combinations know as composites. Appropriate band combinations require knowledge on spectral, reflectance signatures. Third, hyperspectral imaging systems capture and process multiple, typically a hundred or more, spectral bands for better discrimination of objects in imagery (Teodoro, 2016).

Table 2.1 Selected optical, multispectral satellites operating at coarse, medium, and high resolutions.

Sensor group	Satellite sensor	Spectral bands	Spatial resolution (m)	Temporal resolution (day)	Data availability
Coarse resolution sensors	MODIS	36	250-1000	0.5	1999--
	Suomi NPP VIIRS	22	375-750	0.5	2012--
	MERIS	15	300	3	2002-2012
	Sentinel-3 OLCI	21	300	2	2016--
Medium resolution sensors	Landsat	4-11	15-80	16	1972--
	SPOT 1-7	4-5	1.5-20	26	1986--
	ASTER	14	15-90	16	1999--
	Sentinel-2 MSI	13	10-60	5	2015--
	Planetscope	4-8	3	1	2015--
	GaoFen-1	4	2-8	4	2013--
High resolution sensors	IKONOS	5	1-4	1.5-3	1999--
	Quickbird	5	0.61-2.24	2.7	2001--
	WorldView	4-17	0.31-2.40	1-4	2007--
	RapidEye	5	5	1-5.5	2008--
	ZY-3	4	2.1-5.8	5	2012--
	GF-1/GF-2	5	1-16	4-5	2013--
	Pléiades Neo	6	0.3 – 1.2	0.5	2021--
	Skysat	4	0.5 - 1	0.3-0.08	2013--
	KOMPSAT-3A	4	0.5-2.2	0.9-2.7	2015--
	Jilin-1	3-4	0.3-1.2	0.16	2015--

The retrieval of flood information from optical imagery often relies on the fact that water has a lower reflectance as compared to other landcover types, enabling the extraction of binary maps consisting of flooded and dry pixels. A well-established technique for generating these binary maps is the use of water indices used to extract flood inundation extents, including the popular Normalized Different Water Index (NDWI) (McFeeters, 1996), modified NDWI (Xu, 2006), the automated water extraction index (AWEI) (Feyisa *et al.*, 2014) and the water index (WI) (Fisher *et al.*, 2016).

Machine learning (ML), a branch of artificial intelligence that relies on vast amounts of data (known as training data) in order to accurately identify patterns and make predictions without being explicitly programmed to do so, are enabling accurate and automated extraction of water bodies from remotely sensed images (e.g. Elkhrachy, 2022; Munawar *et al.*, 2022).

With an ever-increasing flood of data from diverse sources, machine learning techniques hold the promise of reliably detecting water bodies with higher accuracy than the well-established water indices discussed earlier. Machine learning algorithms used in pixel-based analysis of remote sensing images can broadly be classed into three categories namely: (i) supervised learning; (ii) unsupervised learning; and (iii) reinforcement learning. In supervised learning the machine learning models are trained on given inputs and their corresponding labels/expected outputs. Unsupervised learning entails training ML algorithms only on input without their labels. In reinforcement learning, ML models learn to perform tasks through repeated trial and error, learning the optimal behaviour in a dynamic environment to obtain maximum reward. Data is not used as input as in supervised and unsupervised ML. Deep learning, a subset of ML that utilizes artificial neural networks, is a disruptive computer vision technology that considerably outperforms ML. Convolutional Neural Networks (CNNs), a prominent class of deep learning algorithms, has attained expert-level accuracy in classifying pixels and assigning them semantic labels (semantic segmentation). Pixel-level segmentation of flood extents from satellite and UAV imagery have successfully been conducted in previous studies (e.g. Gebrehiwot *et al.*, 2019; Hashemi-Beni and Gebrehiwot, 2021; Pally and Samadi, 2022) offering the potential for automated real-time segmentation of flood imagery.

2.3.3 Microwave remote sensing

A complementary approach to optical remote sensing for flood hazard mapping is microwave remote sensing, which encompasses both active and passive sensors. The systematic application of optical sensors for monitoring flood events is limited by clouds, fog and vegetation which can obscure flooded surfaces. Optical sensors can only acquire images during the day, further limiting the atmospheric window over which flood imagery can be gathered. Given these limitations, microwave remote sensing, which relies on electromagnetic radiation with wavelengths between 1 mm to 1 m (commonly referred to as microwaves) offers the ability to penetrate cloud cover, haze, possible ash or powder coverages and heavy rainfall that typically accompanies floods, since longer wavelengths are unaffected by atmospheric scattering which impacts shorter optical wavelengths. The application of microwave imaging is also particularly useful in flood detection within small to medium sized catchments where the combination of cloudy weather and the rapid recession of flood events cannot be captured by optical instruments (Schumann and Moller, 2015).

The most commonly used microwave imaging sensor is the Synthetic Aperture Radar (SAR), an active sensor that transmits signal and receives backscatter of surface features, capable of providing high-resolution microwave images of rivers smaller than 1 km in width. Amongst the more popular SAR missions used for flood hazard mapping are imagery acquired from Sentinel-1A and its twin Sentinel 1-B satellite, thanks to the convenient trade-off between their spatial resolution (5 m) and frequency of acquisition (12 days) (e.g. Carreño Conde and De Mata Muñoz, 2019; Perrou *et al*., 2018; Uddin *et al*., 2019). Other spaceborne SAR missions that are relevant to flood mapping applications at high spatial resolution (i.e., 3 – 30 m) are detailed in Table 2.2.

Table 2.2 Selected satellite missions featuring a microwave, Synthetic Aperture Radar (SAR) sensor capable of flood mapping[1]**.**

Spaceborne sensor[2]	Sensor Frequency (Band, λ)	Polarization[3]	Spatial resolution (m)	Orbit repeat cycle (days)[4]
RADARSAT-1	5.3 Ghz (C, 5.6 cm)	HH	8-100	24
RADARSAT-2	5.3 Ghz (C, 5.6 cm)	HH, HV, VV, VH	3-100	24
TerraSAR-X & TanDEM-X	9.6 Ghz (X, 3.1 cm)	HH, HV, VV, VH	1-16	11
Cosmo-SkyMed	9.6 Ghz (X, 3.1 cm)	HH, HV, VV, VH	15-100	16
Sentinel-1A	5.4 Ghz (C, 5.4 cm)	H or V – H and/or V	5-40	12
SAOCOM-1	1.3 GHz (L, 23.5 cm)	H and/or V – H and/or V	10-100	16
ALOS-2/PALSAR	1.3 GHz (L, 22.9 cm)	HH, HV, VV, VH	3-100	14
ENVISAT	5.3 GHz (C, 5.6 cm)	HH, HV, VV, VH	12.5-1000	35
RISAT-1	5.4 GHz (C, 5.6 cm)	H and/or V – H and/or V Compact Pol	1-50	25

[1] References used to compile table information include: The European Space Agency (ESA) SAR Missions (https://earth.esa.int/eogateway/activities/edap/sar-missions) and The National Aeronautics and Space Administration (NASA) Earth Data (https://www.earthdata.nasa.gov/learn/backgrounders/what-is-sar)

[2] Full text for sensor acronyms in the table:

RADARSAT: Radar Satellite
Cosmo-Skymed: Constellation of Small Satellites for Mediterranean basin Observation
SAOCOM-1: Satelite de Observation y Communicacion
ALOS-2/PALSAR: Advanced Land Observing Satellite 2/ Phased Array L-band SAR
ENVISAT: Environmental Satellite

RISAT-1: Radar Imaging Satellite 1

[3] Polarization: VV, vertically sent and vertically received; HH, horizontally sent and horizontally received; VH, vertically sent and horizontally received; HV, horizontally sent and vertically received.

[4] Repeat imaging capability at highest spatial resolution. timely acquisition can be programmed (tasked) for all satellites in case of emergency (usually, 24 – 48 h advance notice is required)

Whilst microwave systems permit collection of imagery in any weather as well as during the night, the inaccuracies in classification of flooded areas (i.e., flooded areas mapped as dry and vice versa) are noteworthy (Clement *et al*., 2018; Scotti *et al*., 2020). Further, passive microwave remote sensing for flood mapping is limited to very large catchments (with areas greater than ~10^3 km^2) given the large angular beams of these systems, which result in spatial resolutions as large as 20 – 100 km, making the interpretation of such imagery challenging (Rees, 2013). Although efforts to blend optical imagery with SAR imagery, leveraging on SAR's capabilities for all-weather mapping, have been attempted (e.g. Kulkarni and Rege, 2020; Tong *et al*., 2018), challenges in such image fusion abound including computational complexity, differences in sensor geometry and resolution as well as inconsistencies in temporal image registration. Whilst the application of SAR-based flood mapping continues to grow thanks to current and planned high resolution sensor missions, such as the NASA-ISRO Synthetic Aperture Radar (NISAR) mission due for launch in 2024, the requirement for high temporal-spatial resolution imagery to support flood modelling in small to medium sized catchments remains pressing as underscored in recent studies by Bauer-Marschallinger *et al*. (2022), Dasgupta *et al*. (2020) and Shen *et al*. (2019).

2.3.4 Emergent remote sensing platforms and technologies

Advances in near-earth flood inundation observations are being strengthened by new imaging technologies capable of providing fine scale datasets at resolutions unmatched by current satellite missions. CubeSats, a class of miniature nano-satellites satellites (10 cm x 10 cm x 10 cm, weighing roughly 1 Kg) (Davoli *et al*., 2019), and drones/UAVs equipped with miniaturized high resolution multispectral and RGB (Red-Green-Blue bands) camera systems can observe the natural environment at much finer spatial and temporal scales (Table 2.3) than possible with current satellite multi-sensor satellite platforms.

CubeSats, which cost roughly 1/100th to 1/1000th of large space-agency missions such as Landsat or Sentinel, have dramatically cut the multi-billion costs associated with launching of twin sensor systems, such as with Sentinel-1A and 1B. CubeSat constellations, such as Planet Lab's (https://www.planet.com/our-constellations/) 'Doves' which are launched in large batches referred to as 'flocks' are capable of acquiring near-daily high resolution data (3 -5 m ground sampling distance) at a fraction of the costs which would be associated with tasking commercial satellites. Large constellations of CubeSats, which are launched using reusable rockets, can overcome obstructions such as cloud cover as they can exploit their frequent revisit time to deliver high-resolution clear-sky imaging. The use of imagery collected using CubeSats and automatic segmentation using AI for flood mapping has been demonstrated by Mateo-Garcia *et al*. (2021) who reported acceptable performance when comparing water detection using a CNN and the spectral index NDWI. In their assessment of the capabilities of CubeSats and other such miniaturized satellites for earth observation Aragon *et al*. (2021) and Selva and Krejci (2012) note the limitations of cross-sensor inconsistencies when acting as a constellation as well as inadequate radiometric quality as compared to large mission satellites such as Landsat and Sentinel whose sensors undergo rigorous calibration. As CubeSats platforms are predominantly equipped with visible to near-infrared sensors, the temporally rich data from these platforms will complement rather than supplant the high resolution imagery currently acquired by conventional large satellite missions (McCabe *et al*., 2017a).

Table 2.3 Comparison between Satellite and UAV platforms

	Satellite	**UAV**
Spatial resolution/GSD	1-1000 m	mm-cm
Spatial accuracy	1-3 m	mm-cm
Flying height	>160 km	m – km (< 1 km)
Surface coverage	High (>10 km)	Low (0.1 km)
Observation footprint	Global	Local
Revisit period	Day(s)	Minutes
Data acquisition costs	Very high	Moderate-low

Unpiloted Aerial Vehicles (UAVs) also referred to as unmanned aerial systems, unpiloted aerial systems or drones have considerable complementarity with satellite data and can be leveraged, in conjunction with hydraulic models, to understand flood dynamics. UAV remote sensing has been enabled by developments in computer vision and sensor miniaturization, offering decisive advantages in field scale flood monitoring such as; (i) the ability to collect, on-demand, ultra spatial resolution (centimetre to millimetre) scale data at reasonable costs; (ii) the ability to carry multiple sensors (optical, thermal, multi- and hyperspectral) and (iii) ability to be less-affected by clouds as opposed to optical satellites which are susceptible to low-cloud cover. Amongst the key breakthroughs of UAVs in supporting flood hazard mapping are the evolution of machine-learning algorithms for generating Structure-from-Motion (SfM) high-resolution DEMs which are essential inputs for flood models. UAV-based ultra-high resolution RGB imagery and video for calibration and validation of hydraulic models has been demonstrated in various studies, including (Masafu *et al.*, 2022; Yalcin, 2019). Image processing using deep learning algorithms for analysis of UAV imagery, such as automatic flood segmentation, are enabling accurate and near real-time mapping of floods enabling timely disaster and emergency response. Although the resolution of data supplied by UAVs remains unmatched by satellite sensors, the spatial scale of observations by satellites are way larger. The synergy between the spatial and temporal capabilities of UAV and satellite based-sensors for flood monitoring is still underexploited as a lot of focus has so far been directed at the calibration and validation of satellite products using UAV data (Alvarez-Vanhard *et al.*, 2021; Jiang *et al.*, 2019). UAV-based sensors will continue to play a vital role in filling the observation gap between in-situ and satellite data, serving as a critical data source for hydraulic models.

2.4 Discussion

2.4.1 The role of remote sensing in constraining hydraulic model predictions

Increasingly accurate implementation of hydraulic models will demand leveraging on the non-trivial advances in computational capacity (e.g., graphical and tensor processing units GPU and TPUs), data processing algorithms such as artificial intelligence (AI) networks powered by deep-learning, and the deluge of very high spatio-temporal data from a plethora of satellite and airborne sensors. Remote-sensing derived digital elevation models, as well as observations of flood extent and water levels remain important for informing flood modelling processes. Integrating the new generation of remote sensing data with hydraulic models via calibration, validation and data assimilation will open avenues for the rigorous assessment of the uncertainty associated with model structure, parameters, and inputs, which are fundamental, yet largely unexplored avenues with potential to drive advances in flood modelling. Further, the predicament of balancing computational efficiency with prediction accuracy in operational flood mapping scenarios, can now be addressed via the exponential growth in computing power which will help unravel the complexities of high-resolution remote sensing data from new sensors aboard small satellites and drones. Whilst the need for in situ observations in flood modelling cannot be replaced entirely by remotely sensed data, the problem of a strong inverse relationship between the spatial and temporal resolution of remotely sensed data, which has constrained the ability to rigorously assess hydraulic models, can now begin to be addressed.

Chapter 3 - Overview of methods

3.1 Introduction

Chapters 1 and 2 contextualized the pertinence and value of the thesis' aim, demonstrating opportunities for research through leveraging on newly available remote sensing datasets (e.g., SfM DEMs, UAV and satellite video) and processing techniques (e.g., optical flow velocimetry and artificial intelligence techniques for optical image segmentation) to both parameterize and rigorously assess the performance of hydraulic models. With substantial advances in the availability of fine scale data for flood modelling, it is important to consider the techniques needed to process this data to enable their successful utilization in facilitating and constraining model predictions. In summarizing these advances and their subsequent relevance to progressing numerical modelling of inundation, three key themes emerge linked to; i) optical methods for estimation of river surface velocities; ii) generating floodplain topography from optical imagery, and iii) the role of AI in automated image analysis. This chapter will provide details about the study sites and hydraulic model used to conduct simulations followed by a discussion of the methods used to process optical imagery for the derivation of topography, velocity, and discharge. This chapter will provide a general explanation of the chosen techniques with further discussion and investigation detailed in the subsequent empirical Chapters 4, 5 and 6.

3.2 Study sites

3.2.1 Eden Catchment, United Kingdom

The Eden catchment is located in Cumbria, Northwest England and covers an area of 2288 km^2, draining the uplands of the Pennines and Lake District, to its outlet via the Solway Firth to the Irish Sea. The principal sub-catchments are the Upper and Lower Eden, Eamont, Irthing, Petteril and Cladew, with the major population centres being Carilse, Penrith and Appleby-in-Westmorland (Figure 3.1). The Eden catchment contains two major lakes, Ullswater (884 ha) and Haweswater Reservoir (387 ha), as well as several small tarns and reservoirs which regulate flow in the catchment. The catchment is largely rural with just 1% classified as urban with the main land use being agricultural practice; tourism is growing in importance. The catchment is significant for its cultural and nature conservation with 30% of its area classified as an Area of Outstanding Natural Beauty (AONB) (Environment Agency, 2009).

The Upper Eden is the largest sub-catchment at ~600 km^2 and drains the western slopes of the Pennines with elevations ranging from 788 m above ordnance datum at the High Scald Fell to approximately 93 m at Temple Sowerby gauging station (Mayes *et al.*, 2006). The Lower Eden is characterised by wide floodplains and contains several of the Pennine peaks on the eastern side, such as the Cross Fell (893 m) (Leedal *et al.*, 2013). The Eamont sub-catchment (158 km^2), made up of majority livestock grazing land, experiences the highest rainfall in the catchment (approximately 1700 mm yr^{-1}) and conveys runoff from the central Lake District and comprises 23 water bodies, including the Swindale Beck (Figure 3.1).

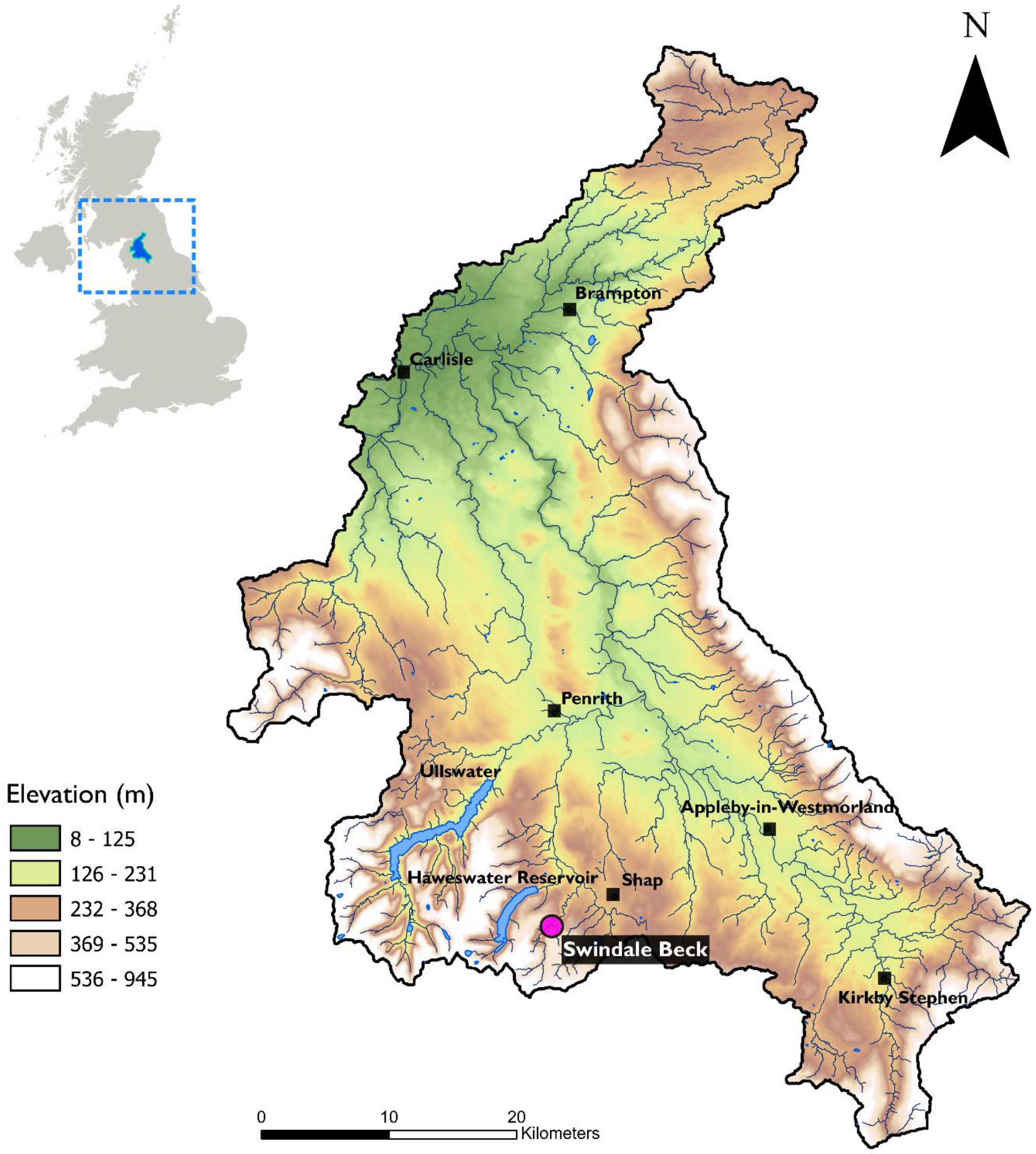

Figure 3.1 Eden Catchment and study location (Swindale Beck).

Rainfall across the catchment is highest in the uplands with Eden Valley being drier due to the rain shadow effect from the Lake District hills to the west. Average annual rainfall is 1183 mm (SAAR 1961 – 1990) with large variations of less than 650 mm in the lowland valleys to more than 2000 mm in the uplands (Mayes *et al.*, 2006). Upstream of Penrith average annual rainfall exceeds 2800 mm as compared to 920 mm across England and Wales. Runoff from the catchment is controlled by topographic and geological differences, with many of the upland tributaries rising on steep hard rock with little soil cover resulting in flashy runoff with high river levels occurring soon after heavy rainfall. In the lowlands limestone and sandstone aquifers benefit are important in maintaining baseflows.

The Eden catchment has been instrumented extensively via the CHASM (Catchment Hydrology and Sustainable Management) project (O'Connell *et al.*, 2007) with a network of over 11 event-recording tipping-bucket rain gauges and a network of stage gauges maintained by the Environment Agency and private entities allowing localized insights into hydrological characteristics of the catchment. Swindale Beck, a stream located within the Eamont sub-catchment, a partnership between a water company (United Utilities) and the Royal Society for the Protection of Birds (RSPB) instituted river restoration efforts in order to allow natural process to help manage flood risk. The stream flows north-east along Swindale and joins the River Lowther near Rosgill and Shap and takes in water from a ~17 km^2 area (Figure 3.1). The Swindale Beck underwent straightening approximately 160 years ago to clear land for grazing, appearing in straightened form in an 1869 Ordnance Survey Map (Dallow, 2020). Removing the beck's natural bends not only accelerated flow downstream of the channel increasing the risk of flooding, this also destroyed in-river wildlife habitats such as gravel bars, pools and riffles. Restoration efforts began in 2016, with the creation of a much-longer sinuous 890 m channel replacing the 750 m of straightened channel, allowing for natural flooding patterns to occur with high event rainfall spilling onto the floodplain meadows. The restored beck allowed for more diverse flora and fauna to thrive whilst reconnecting the stream to its adjacent floodplain. River restoration schemes can produce highly variable impacts on high flow events within catchments, with consequent alterations in flow dynamics caused by changes in channel morphology warranting further empirical and modelling studies to further unravel the interconnections between river engineering and flood risk management (Dixon *et al.*, 2016; Mondal and Patel, 2018).

3.2.2 Murray-Darling River Basin, Australia

The Murray and Darling River systems together form the Murray-Darling Basin (MDB), located in southeast of Australia and covers parts of four states – New South Wales, Victoria, South Australia and Queensland (Figure 3.2). The MDB drains approximately 14% of the Australian continent with a drainage area of over 1 million km^2 with the combined length of the two major rivers the Murray and Darling being ~5500 km (MDBA, 2010). The basin contains more than 20 other rivers and is climatically divided into the northern rivers (Darling system) and the southern rivers (Murray system) (Hart *et al.*, 2021). The Murray River is approximately 2530 km long and rises at an elevation of 2228 m in eastern Australia and drops to an elevation of 150 m, gradually reducing in gradient from 0.29 m km^{-1} to 0.03 m km^{-1}. The Darling system (2740 km long) flows across New South Wales in a southwesterly direction and confluences with the River Murray close to the border of South Australia, Victoria and New South Wales (Stewardson *et al.*, 2021).

The Murray Darling Basin has a long term annual average rainfall of 469 mm of which 94% evaporates or transpires and 4% turns into runoff. The basin experiences a pronounced climate gradient that is also subject to the El Niño -Southern Oscillation climatic variability characterized by long dry spells and large flood events (Heimhuber *et al.*, 2016). The hydrology of the MDB is amongst the most variable in the world with the northern basin experiencing a strong monsoonal influence leading to more summer dominated flow patterns as compared to the southern basin's winter-dominated flow patterns (Stewardson *et al.*, 2021). The MDB basin has a high interannual variation in streamflow, total flow in the basin has varied between 6740 GL (2006) to 117,907 GL (1956) as a result of the prevailing arid and temperate climate of the basin (MDBA, 2010). Although largely arid, the surface water ecosystems of the MDB include over 70,000 lakes and roughly 20,500 km^2 of wetlands (Brooks, 2017).

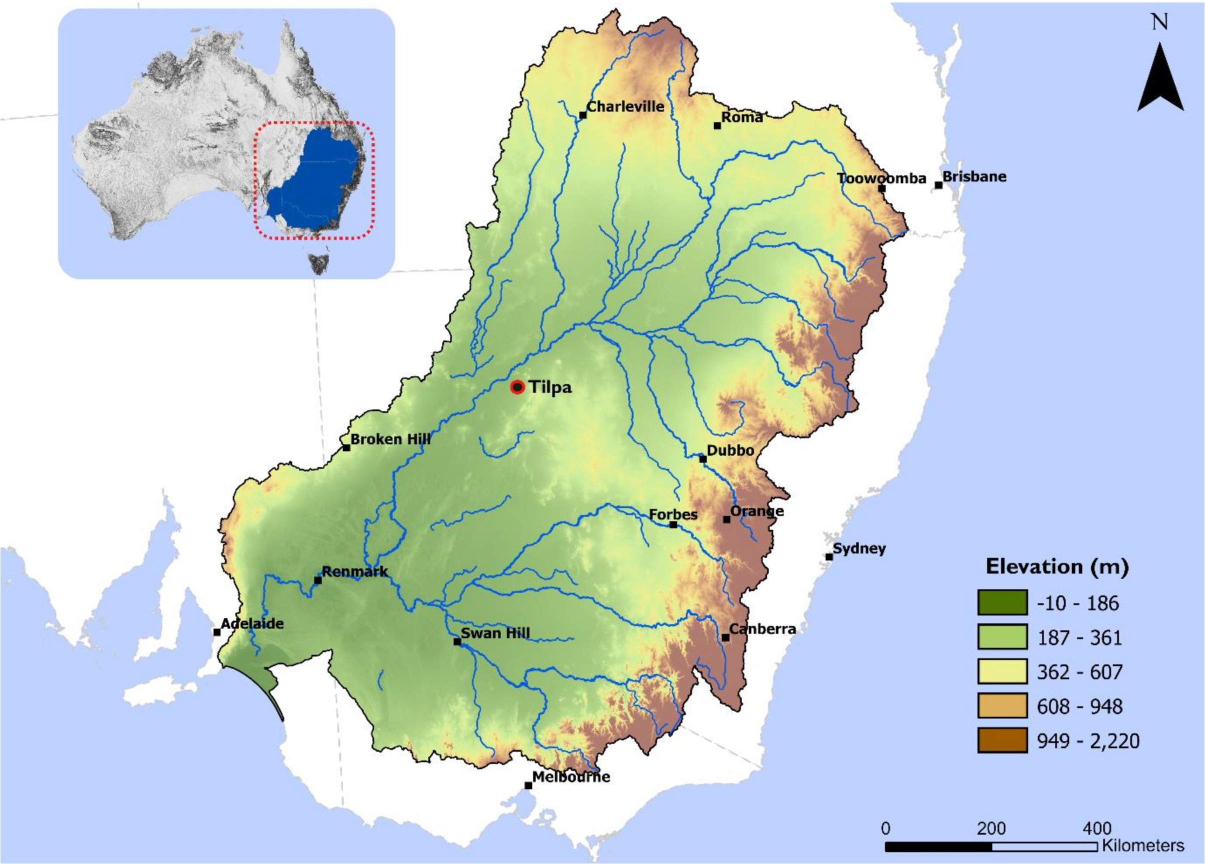

Figure 3.2 The Murray-Darling Basin and study location (Tilpa).

With the exception of Canberra, there are no large cities within the basin, with around 2.2 million people living with the basin and roughly 4 million reliant on its water resources (Authority, 2017). The economic mainstay within the catchment is agriculture with the region producing more than 50% of Australia's irrigated produce over more than 1.5 million ha of land (ABS, 2019). The MDB has been the focus of debates over the consumption of water, with floods being a highly valued resource. Human-induced stress on the basin's water resources as well as severe drought and flood cycles driven by climate change (King *et al*., 2020) illustrate the need for rigorous inclusion of knowledge from new technologies to advance the ability to make accurate decisions in managing the MDB's water resources. Earth observations for monitoring flood events as well as quantifying streamflow will complement existing in-situ networks and supply additional data that will help underpin decisions in the MDB. The capabilities for strategic management of water resources in near-real time leveraging on advances in science and technology will offer even better options for water management in the MDB.

3.3 Hydraulic Model

Two-dimensional hydraulic flood models have been deployed extensively in simulating river hydraulics and floodplain inundation dynamics (e.g. Dottori and Todini, 2013; Hunter *et al.*, 2008; Shen *et al.*, 2015). Whilst a spectrum of model codes and structures exist for numerical modelling of flood plain dynamics, the choice of an appropriate model was driven by the need to balance model complexity, data requirements and the ability to resolve spatial resolution at reasonable computational costs. Additionally, a 2D hydraulic model code that was easily available and has been used in both commercial and research domains would help build upon existing literature and operational flood hazard modelling studies. An important development in 2D hydraulic modeling approaches is the emergence of sub-grid modeling capabilities, an extremely computationally efficient approach allowing coarse grid cells to be implemented over fine topographic details while also helping maintain numerical stability (Shustikova *et al.*, 2019), such capabilities further helped to refine model choice. In a study by Néelz and Pender (2013) benchmarking 14 2D hydraulic model codes based on shallow-water equations, the representation of both floodwater velocities and extents by all modelling codes was performed comparably. Thus, the current version of the Hydrologic Engineering Center-River Analysis System (HEC-RAS) was selected as a representative class of hydraulic model fitting the above criteria with which to explore this thesis' objectives. Indeed, any conclusions reached in this thesis should be obtainable with other hydraulic model codes.

HEC-RAS is an open-source hydraulic model developed by the U.S. Army Corps of Engineers that can perform both one-dimensional steady flow hydraulics and one and two-dimensional unsteady flow river hydraulics. HEC-RAS solves both the bidimensional 2D Saint Venant equations (shallow water equations) and the 2D diffusion wave equations. In this thesis a purely 2D approach was used to characterize modelled flows and details of the 2D solver as summarized in general terms here.

2D shallow water equations take the form of the continuity equation expressed as:

$$\frac{\partial H}{\partial t} + \frac{\partial (hu)}{\partial x} + \frac{\partial (hv)}{\partial y} + q = 0 \tag{3.1}$$

where H is the water surface elevation, t is time, h is the water depth, u and v are the depth averaged velocities in the x- and y-directions, and q is the source term.

Momentum equations for 2D flow are expressed as:

$$\frac{\partial u}{\partial t} + u\frac{\partial u}{\partial x} + v\frac{\partial u}{\partial y} = -g\frac{\partial H}{\partial x} + v_t\left(\frac{\partial^2 u}{\partial x^2} + \frac{\partial^2 u}{\partial y^2}\right) - c_f u + fv \tag{3.2}$$

$$\frac{\partial v}{\partial t} + u\frac{\partial v}{\partial x} + v\frac{\partial v}{\partial y} = -g\frac{\partial H}{\partial y} + v_t\left(\frac{\partial^2 v}{\partial x^2} + \frac{\partial^2 v}{\partial y^2}\right) - c_f v + fu \tag{3.3}$$

where g is gravity, v_t is the eddy viscosity coefficient, c_f is the friction coefficient, and f is the Coriolis parameter.

The friction coefficient, c_f, is determined using Manning's formula formulated as:

$$cf = \frac{n^2 g|u|}{R^{\frac{4}{3}}} \tag{3.4}$$

where n is Manning's n and R is the hydraulic radius.

Before solving fluxes using the equations described, HEC-RAS prepares detailed hydraulic property tables for the 2D computational cells based on the underlying terrain, the so-called "sub-grid high resolution model" (Brunner *et al*., 2020; Casulli, 2009). The sub-grid approach allows for the 2D flow area pre-processor to prepare detailed hydraulic property tables even for larger mesh sizes, allowing the use of larger computational cells results in fewer computations and faster model run times without losing details on the underlying topography.

In this thesis, the use of HEC-RAS's adaptive mesh refinement was utilized, allowing for precise and detailed representation of desired results in targeted locations where additional detail was required. This further enhanced model run stability because refined mesh sizes focused on areas where sudden changes occur, which is typically within river channels or hydraulic structures within the flood plain.

Assigning an appropriate computational time step that worked well with hybrid computational meshes, adaptive time-steps based on the Courant-Freidrichs-Lewy condition were estimated when using both the full momentum Saint Venant equations (3.5) and the diffusive wave equations (3.6) expressed as follows (Brunner *et al*., 2015):

$$C = \frac{V\Delta T}{\Delta X} \leq 1.0\ (with\ a \max[\![C = 3.0)]\!]or\ \Delta T\ \leq \frac{\Delta X}{V}\ (with\ C = 1.0) \tag{3.5}$$

$$C = \frac{V\Delta T}{\Delta X} \leq 2.0\ (with\ a \max[\![C = 5.0)]\!]or\ \Delta T\ \leq \frac{2\Delta X}{V}\ (with\ C = 1.0) \tag{3.6}$$

Where C = Courant number, V = flood wave velocity (m s^{-1}), ΔT = computational time-step (s) and ΔX = average cell size (m).

The basic boundary and initial condition requirements for performing unsteady two-dimensional flow calculations in HEC-RAS consist of external, internal, and global boundary conditions. External boundary conditions are applied to the boundary of 2D flow areas and can either be flow/stage hydrographs, normal depth (calculated using an energy slope and Manning's equation) or a rating curve. Internal and global boundary conditions, including precipitation (application of a time series of rainfall excesses on the entire 2D flow area, e.g. Zeiger and Hubbart, 2021), evapotranspiration and wind were not utilized in this thesis.

3.4 Image processing techniques

3.4.1 Structure from Motion (SfM) photogrammetry

The rapid emergence of UAV-based photogrammetry for high resolution-topographic reconstruction has been aided by technological advancements in UAVs/drones, camera sensor technology and computer vision techniques, primarily Structure from Motion (SfM) algorithms. SfM is a technique for developing 3D models from a series of overlapping 2D imagery. The resolution of 3D point clouds from SfM are typically improved using Multi-View Stereo (MVS) techniques by generation of dense point clouds, thus SfM-MVS (Figure 3.1). UAV-SfM-MVS has several advantages over traditional ground-based photogrammetry techniques, LiDAR, Terrestrial Laser Scanning (TLS) and Airborne Laser Scanning (ALS) which are expensive, highly dependent on weather conditions and relatively challenging to deploy in difficult/remote terrain without risk to operators. UAV-SfM DEMs have been deployed in several riverine environments for reconstruction of flood events (e.g., (Govedarica *et al.*, 2018; Hashemi-Beni *et al.*, 2018; Özcan and Özcan, 2021) and are now a proven alternative to traditional photogrammetry. SfM-MVS produces fully 3D multidimensional data and can be applied at large spatial scales (from 10^{-2} to 10^{6} m^{2} (Carrivick and Smith, 2019; Smith and Vericat, 2015) with accuracies comparable to traditional topographic survey techniques. Examining the advantages of UAV-based DEMs in a small river floodplain, Schumann *et al*. (2019) noted identical performance between SfM and LiDAR based DEMs for characterization of hydraulic predictions. Further, Annis *et al*. (2020) quantified the accuracy of UAV-derived DEMs against a high-resolution LiDAR DEM for small-scale flood hazard mapping and found simulated flow dynamics were significantly better reproduced by a SfM-DEM.

The general steps for SfM photogrammetry are detailed in Figure 3.3. The focus of this section is to provide an overview of the SfM image processing methodology typical to SfM based approaches for DEM production regardless of specific software implementation. Whilst advances in the field of computer vision have led to a plethora of commercial software (e.g., Pix4DMapper, AgiSoft PhotoScan, 123D Catch/ReCap, Autodesk Image Modeler, Photo Modeler, Microsoft Photosynth amongst others) and open-source code (e.g. Bundler, VisualSFM, Python Photogrammetry), the workflow steps described here broadly address the approaches used to produce SfM DEMs and are based on the steps described by Carrivick *et al*. (2016), Eltner *et al*. (2016) and Smith *et al*. (2016).

Given overlapping images acquired at different angles from UAV surveys, the first step in the SfM workflow aims to match the 3D location of matching features. Conventionally, images acquired from UAV flights will have a front overlap of 55 – 60% and a side overlap of 40 - 90%, with high degrees of overlap allowing for the development of detailed 3D point clouds following dense multi-image matching (Jiménez-Jiménez *et al*., 2021).

The initial step in image processing is the identification of features (or ‘keypoints’) in individual overlapped images regardless of perspective or scale. Keypoints allow for the scene geometry to be reconstructed and can be implemented via several techniques including FAST (features from accelerated segment test) (Rosten and Drummond, 2005), BRISK (binary robust invariant scalable keypoints) (Leutenegger *et al*., 2011), ORB (oriented BRIEF) (Rublee *et al*., 2011), SURF (speeded up robust features) (Bay *et al*., 2008), KAZE features (Alcantarilla *et al*., 2012) and most commonly, SIFT (scale-invariant feature transform) (Lowe, 2004). Whilst SIFT has gained popularity in SfM applications, subsequent developments in computer vision algorithms based on deep-learning have emerged including DetNet (Lenc and Vedaldi, 2016), TILDE (Verdie *et al*., 2015), LIFT (Yi *et al*., 2016) and SuperPoint (DeTone *et al*., 2018).

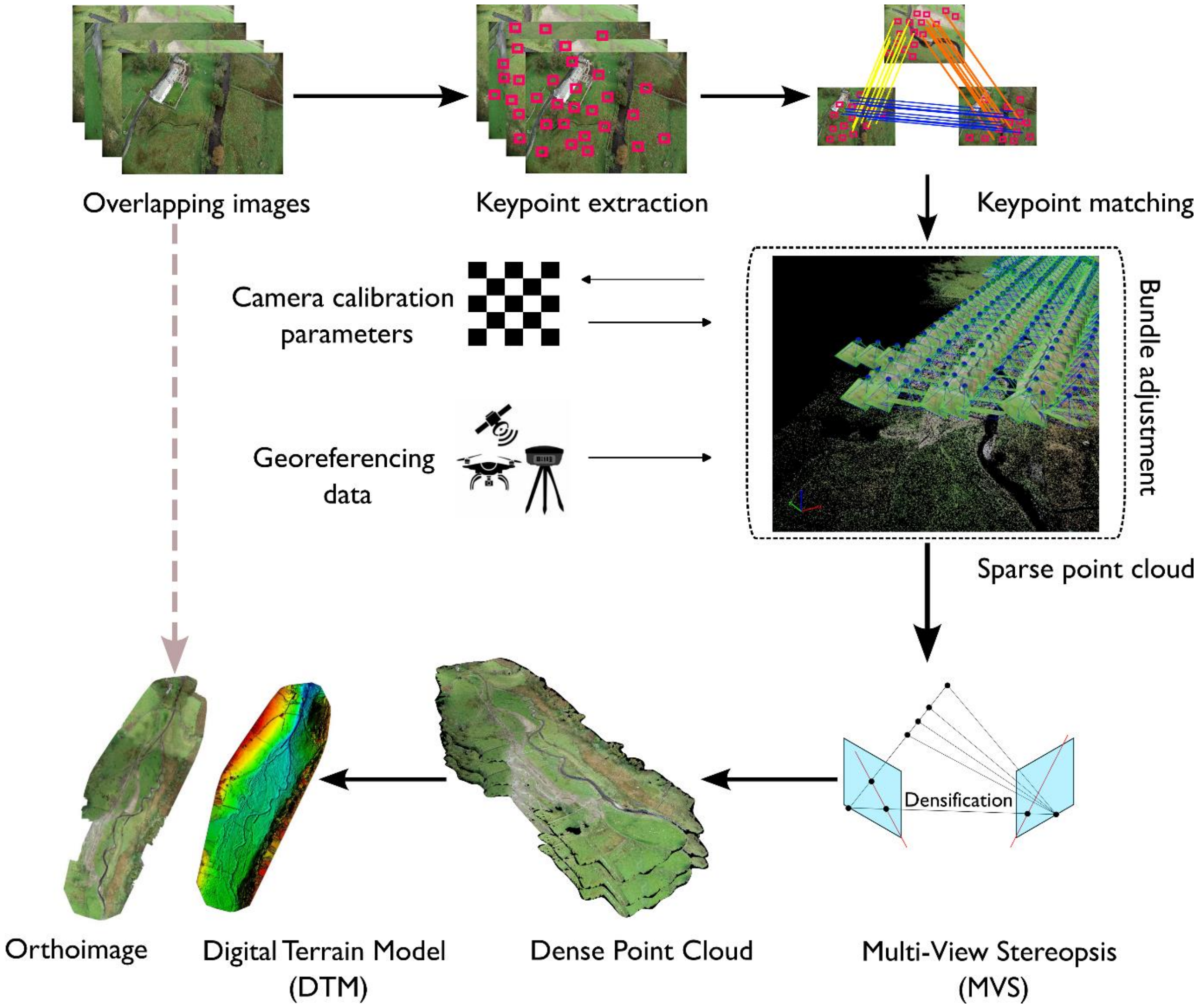

Figure 3.3 SfM photogrammetry workflow.

Keypoint matching requires the identification of corresponding points in multiple images, although not all keypoints will always have matches in partner images. Techniques for discarding of keypoint data without matches are based on the application of thresholds, such as SIFT's use of the ratio of the Euclidean distance of the nearest neighbour with that of the second nearest, termed as the distance ratio with a minimum threshold value of 0.6 – 0.8 (Smith *et al*., 2016). Using this distance ratio criteria, more than 90% of incorrect keypoint matches can be discarded with less than 5% of correct matches being eliminated. Muja and Lowe (2009) developed a *k*-dimensional binary partition tree to address the large high-dimensional space of keypoint descriptors. These binary trees efficiently partition multidimensional data with significant reduction in search times and relies on graphical processing units (GPUs) (Carrivick *et al*., 2016). To ensure only correct keypoint correspondences are applied and incorrect matches are removed, a further step is applied to filter out erroneous keypoints. A fundamental matrix (F-matrix) is computed based on the location of keypoints in multiple images of the same scene. The F-matrix relies on the relationship between matching image keypoints in order to constrain the location precisely known keypoints and is computed using the eight-point algorithm (Longuet-Higgins, 1981). The eight-point algorithm computes a 3D structure from a correlated pair of images when the spatial relationship between them is unknown. The F-matrices are computed over several iterations using the commonly applied random sample consensus (RANSAC) (Fischler and Bolles, 1981) that divides all keypoints into outliers and inliers. A set threshold is defined for determining keypoints considered to be outliers, RANSAC continuously samples different subsets until there is a 95% chance that subset contains only inlier keypoints (Carrivick *et al.*, 2016; Smith *et al.*, 2016).

Utilizing the geometrically consistent feature correspondences from the previous step, SfM relies on bundle adjustment algorithms to simultaneously reconstruct a 3D geometry, different camera poses and the camera's intrinsic calibration parameters. Bundle adjustment produces sparse point clouds and reconstructed camera poses by simultaneously solving for the intrinsic and extrinsic orientation parameters (Javadnejad *et al.*, 2021; Ullman, 1979). Iterative minimization of a defined cost function is conducted by fitting a local quadratic approximation which results in optimal 3D structure and camera parameters (Carrivick *et al.*, 2016; Snavely, 2011; Triggs *et al.*, 2000).

The outputs from the preceding SfM process are the scene geometry and a 3D point cloud with an undefined coordinate system. Georeferencing and scaling of the 3D point cloud requires a minimum of three ground control points (GCPs) with XYZ coordinates. The use of more than three well-distributed GCPs which are clearly visible in images and surveyed using RTK-GNSS or total stations is required for most SfM-MVS software workflows (James *et al.*, 2019; Javernick *et al.*, 2014). Additional optimization to minimize the georeferencing error and the re-projection error as a result of the use of GCP coordinates is available in most software packages where bundle adjustment can be re-run to optimize alignment.

Multi-View Stereo image matching are used to increase the density of the georeferenced sparse point cloud by at least two orders of magnitude (Carrivick *et al.*, 2016). Seitz *et al.*, (2006) provide a taxonomy of MVS algorithms which can be classified into voxel-based methods, surface-evolution based methods, depth-map merging methods and patch-based methods, which are more commonly applied in SfM due to their relative cost effectiveness and simplicity (Lou *et al.*, 2014; Shen, 2013; R. Zhang *et al.*, 2022). Whilst most algorithms in commercial SfM software packages are considered to be 'black box' (Nguyen *et al.*, 2012), the rapid evolution of open-source code is allowing users to identify common underlying concepts in the SfM processing chain.

3.4.2 Large Scale Particle Image Velocimetry (LSPIV)

Non-intrusive techniques for measuring river surface velocities, especially during hazardous flood events, have been aided by the proliferation of high-resolution imaging sensors capable of being deployed on UAVs and satellite platforms, as well as rapid advancements in computational capacities. Whilst the evolution of aDcps was instrumental for advancing hydrometric flow measurements in the field, their application is limited during extreme events such as floods. Image based techniques for estimation of velocity have primarily been based on two techniques; Particle Tracking Velocimetry (PTV), a Lagrangian approach that determines velocity vectors based on individually tracked particles in successive images, and Particle Image Velocimetry (PIV) which relies on cross-correlation to determine the displacement of a group of particles within small analysis regions. Conventional PIV analysis was first applied in controlled laboratory environments (see, Adrian, 1991), however in the mid-1990s Fujita *et al.*, (1998) introduced techniques for field scale application of PIV, and thus the development of the so-called large-scale PIV (LSPIV). Several LSPIV-based algorithms have been proposed and utilized for estimation of riverine velocities, and streamflow, including Surface Structure Image Velocimetry (SSIV - Leitão *et al.*, 2018) and digital particle image velocimetry (Thielicke and Stamhuis, 2014).

Although both PIV and PTV based techniques are relatively inexpensive, relying on consumer-grade cameras and open-source software for image analysis, LSPIV has found wider application in field studies as compared to PTV. Whilst PTV relies on the identification and tracking of highly resolved individual tracers, LSPIV requires a comparatively lower concentration of tracers, usually a group of particles/speckle patterns rather than individual tracers, in order to compute surface velocities. Indeed, a large number of studies on the hydraulic applications of image velocimetry in natural environments, such as during floods when tracers are likely to cluster rather than be evenly distributed across the water surface, have been based on LSPIV (e.g. Al-mamari *et al*., 2019; Dramais *et al*., 2011; Huang *et al*., 2018; Le Boursicaud *et al*., 2016). Tauro *et al*. (2017) further note that in outdoor settings, the large-scale flow behaviour captured by LSPIV allows for analysis of lower resolution image frames, allowing for the investigation and mapping of spatial flow structures in difficult-to-access environments.

The first step in LSPIV workflows is recording images to be used for analysis, this is generally accomplished through optical video sensors mounted on still standing structures, such as bridges, UAVs, and recently satellite-based sensors (Legleiter and Kinzel, 2021a) (Figure 3.4). Recording of images using UAVs and other space-borne sensors is generally done from a nadir perspective rather than obliques angles, which eliminates the requirement for complex image transformations which can negatively influence the accuracy of velocimetry results (Pearce *et al*., 2020a). Analysis of images using LSPIV requires the presence of visible tracers/seeds/particles on the water surface, in sufficiently illuminated settings, in order for the displacement of these tracers to be tracked in a series of images. Since tracers are not always sufficient in natural streams, artificial seeding – the introduction of tracers such as corn ships, eco-foam, or wood shavings, can be conducted to enable tracking of their movement and measure surface velocities. Following image acquisition and extraction of frames for analysis the next key steps in LSPIV generally include image preprocessing, image orthorectification and image processing.

Preprocessing of images before inferring surface velocities will generally be preceded by image stabilization, to account for camera/platform movements due to wind, drift or orbiting (in the case of UAVs and satellite platforms) which can result in erroneous computation of velocities based on the motion of the imaging platform rather than the advection of flow. Following stabilization, images can be pre-processed to increase the contrast between tracers and the water. Manipulation of stabilized images is also conducted to reduce glare and can be accomplished via operations such as contrast stretching, histogram equalization and application of band pass filters.

In order to scale the pre-processed image sequences from a pixel coordinates to real-world coordinates as well as avoid distortion due to perspective effects, geometrical projections can be conducted either via the application of direct scaling functions based on established pixel and metric co-ordinate relationships or full image orthorectification, based on ground control points (GCPs). In this thesis, conventional orthorectification techniques based on GCPs was applied to calibrate images to surveyed coordinates. Explicit 2D transformations are possible when GCPs and the river surface are on a similar plane and requires at least 4 GCPs proximal to the river banks in order to increase the reliability of orthorectification (Jolley *et al*., 2021; Moraitis and Baltas, 2020; Tauro *et al*., 2014). Le Coz *et al*. (2014) recommend having more than 10 GCPs distributed within the field of view of the camera, which increases redundancy of the orthorectification network thus improving the accuracy of velocimetry results.

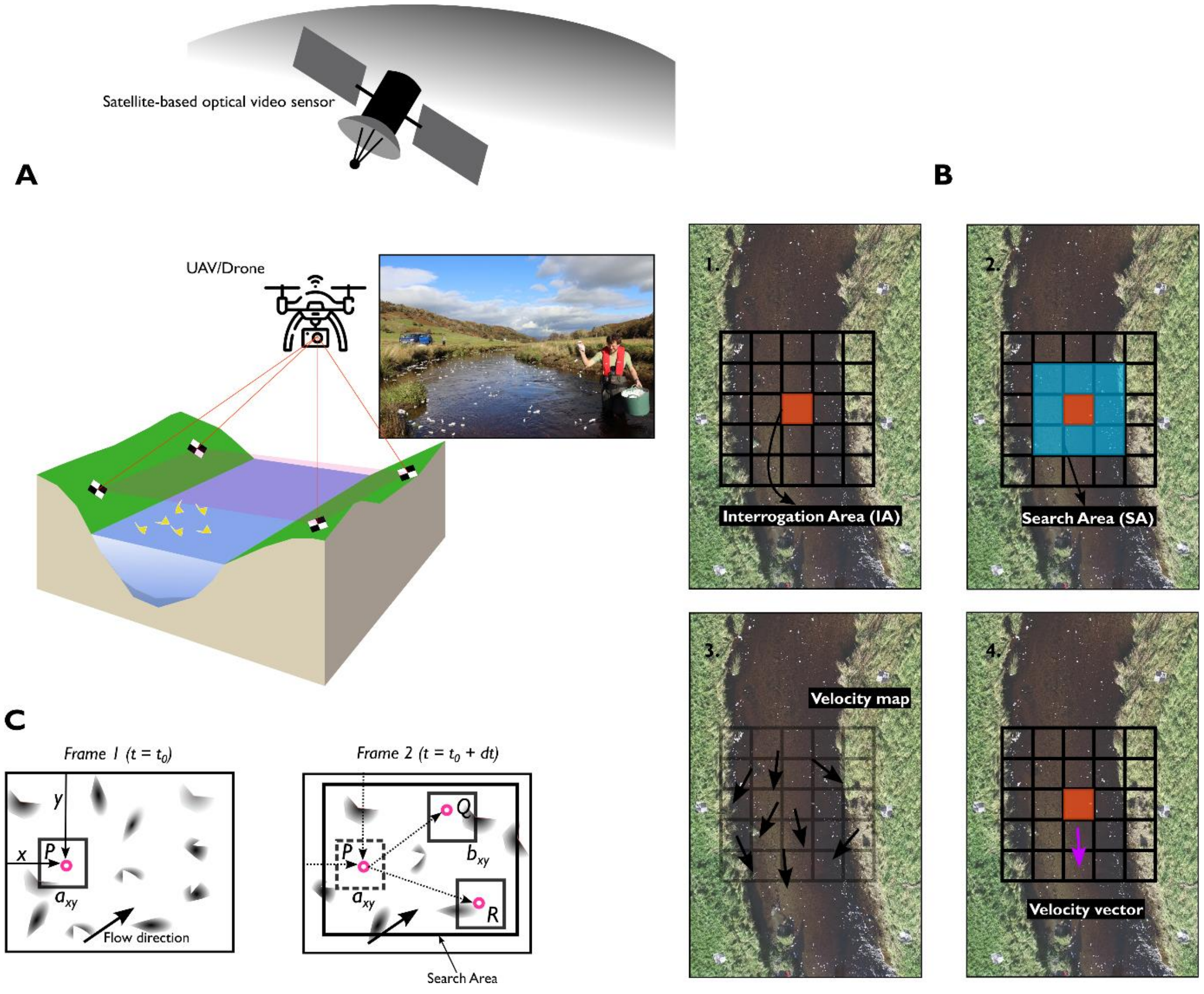

Figure 3.4 Large Scale Particle Image Velocimetry (LSPIV) implementation, (a) UAV/Drone/Satellite based optical sensors capture videos of river surface with tracers; (b) LSPIV velocity vector generation explained in graphics; (c) Conceptualization of the LSPIV image processing algorithm.

In estimating surface velocities, classical two-dimensional cross-correlation is applied between pairs of orthorectified images separated by a given time interval, Δt. Cross-correlation is computed between an interrogation area (IA - Figure 3.4) in an initial frame and IAs located within a search area (SA) in a subsequent frame. A group of particles forming a pattern is used to trace displacement with a pair of particles yielding maximum cross-correlation resulting in a candidate velocity vector. The cross-correlation coefficient, R_{ab}, is expressed as (Fujita *et al.*, 1998; Muste *et al.*, 2008a):

$$R_{ab}=\frac{\sum_{i=1}^{MX}\sum_{j=1}^{MY}\left\{\left(a_{ij}-\bar{a}_{ij}\right)\left(b_{ij}-\bar{b}_{ij}\right)\right\}}{\left\{\sum_{i=1}^{MX}\sum_{j=1}^{MY}\left(a_{ij}-\bar{a}_{ij}\right)^{2}\sum_{i=1}^{MX}\sum_{j=1}^{MY}\left(b_{ij}-\bar{b}_{ij}\right)\right\}^{1/2}} \tag{3.7}$$

Where MX and MY are the sizes of the interrogation areas, and a_{ij} and b_{ij} are the distributions of the gray-level intensities in the two interrogation areas separated by the time interval *dt* (refer to Figure 3.4).

Following generation of velocity vectors postprocessing to remove erroneous velocity vectors can be conducted based on manual removal of vectors, the use of local median filters, imposing correlation thresholds or via flow continuity analysis methods (e.g., Perks, 2020; Thielicke and Stamhuis, 2014; Westerweel and Scarano, 2005). Whilst a certain amount of noise is inevitable in PIV analyses, different algorithms deploy techniques, such as data smoothing (Raffel *et al.*, 1998) in order to improve the accuracy of generated velocity vector maps. In this thesis, all LSPIV workflows are based on the open access PIVLab algorithm (Thielicke and Stamhuis, 2014) which has been utilized in various field scale investigations of riverine velocities (e.g., Cao *et al.*, 2022; Koutalakis *et al.*, 2019; Koutalakis and Zaimes, 2022; McIlvenny *et al.*, 2022).

3.4.3 Deep learning based semantic segmentation.

Deep learning models, a class of artificial neural networks, have emerged as a powerful tool for digital image processing thanks to their ability to learn from vast amounts of unstructured data. An important application of deep neural networks is in the domain of computer vision, with application use-cases including image classification, object detection and segmentation, in increasing order of their complexity. Image segmentation is a commonly used digital image processing technique that aims at grouping similar regions or segments of an image based on the characteristics of the pixels in the image. Image segmentation modes are divided into three categories based on the information extraction task: (i) Semantic segmentation, (ii) Instance segmentation and (iii) Panoptic segmentation. Semantic segmentation, also called pixel-level segmentation, entails the classification of each pixel belonging to the same object class. Instance segmentation models detect and classify each object in an image and classifies pixels on the basis of their ‘instances’ of occurrence rather than classes. This task is analogous to object detection but with the added task of segmenting a detected object’s boundaries. Panoptic segmentation is a combination of semantic and instance segmentation, involving pixel-level labelling as well as identification of each object instance in an image.

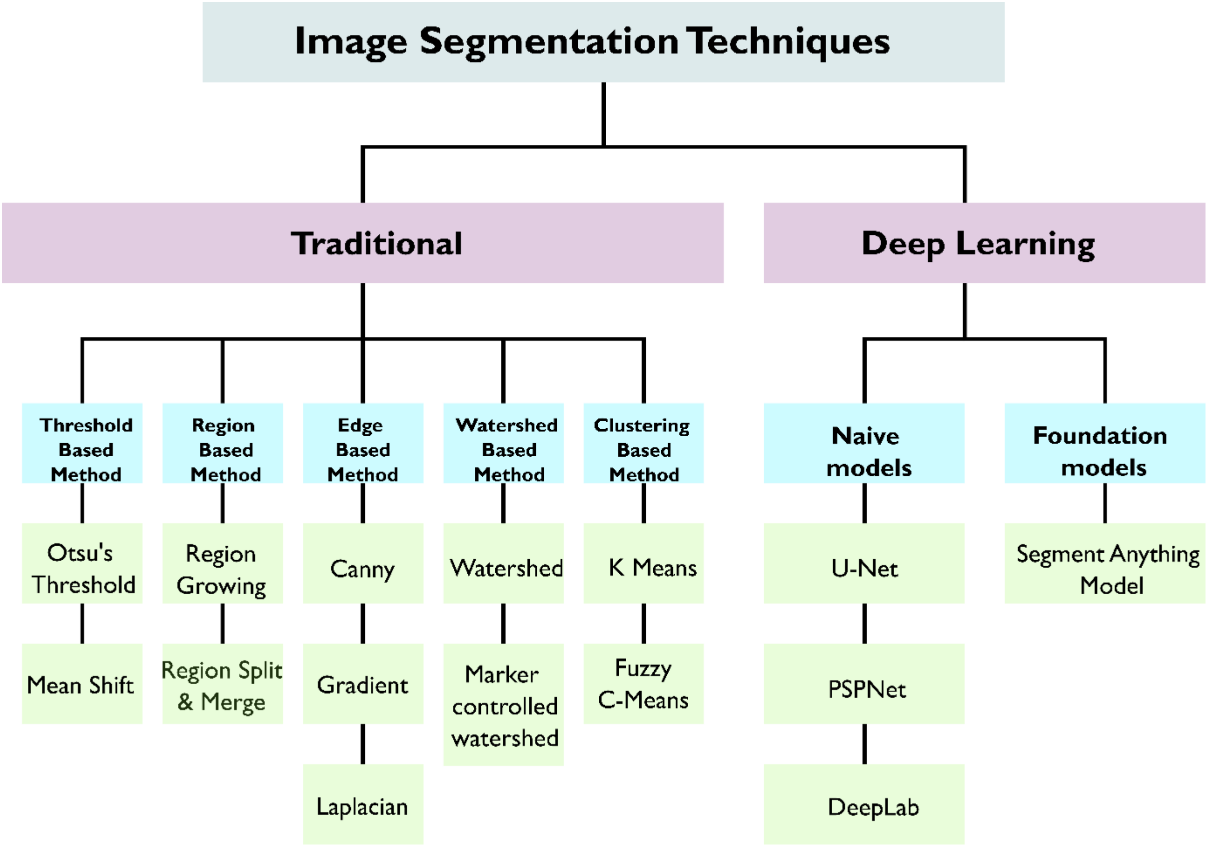

Figure 3.5 Image segmentation techniques.

Image segmentation techniques can generally be described as falling under two categories: (1) traditional techniques and (2) deep learning-based techniques (Figure 3.5). Algorithms based on traditional techniques can broadly be categorized as being either spectrally-based (such as thresholding-based and feature space-clustering algorithms, see, for example, Abd Elaziz *et al*., 2019; Pare *et al*., 2020; Sarkar and Das, 2013; Upadhyay and Chhabra, 2021), spatially-based (such as edge-based, region growing, region merging and splitting, and graph based such as in Bleau and Leon, 2000; Camilus and Govindan, 2012; Padmapriya *et al*., 2012; Preetha *et al*., 2012) or a hybrid of both methods.

Deep learning-based image segmentation relies on training neural networks and can accomplish superior accuracy as compared to traditional segmentation techniques (Minaee *et al*., 2020). The most prominent deep-learning-based image segmentation models typically use an encoder-decoder architecture e.g., U-Net (Ronneberger *et al*., 2015) (Figure 3.6). Lately, a disruptive new class of models known as foundation models, has emerged. Foundation models are AI models pre-trained on extremely large datasets that can be adapted to a wide range of tasks, including tasks for which they have not previously been trained for. Foundation models for image segmentation are based on the use of convolutional neural networks, including Facebook's Segment Anything Model (SAM) (Kirillov *et al.*, 2023), which is considered to be the first foundation model for image segmentation. Foundation models are still in their infancy have been criticized for their inductive biases and lack of explainability due to the depth of the neural network layers and size of training datasets used (Bommasani *et al.*, 2021).

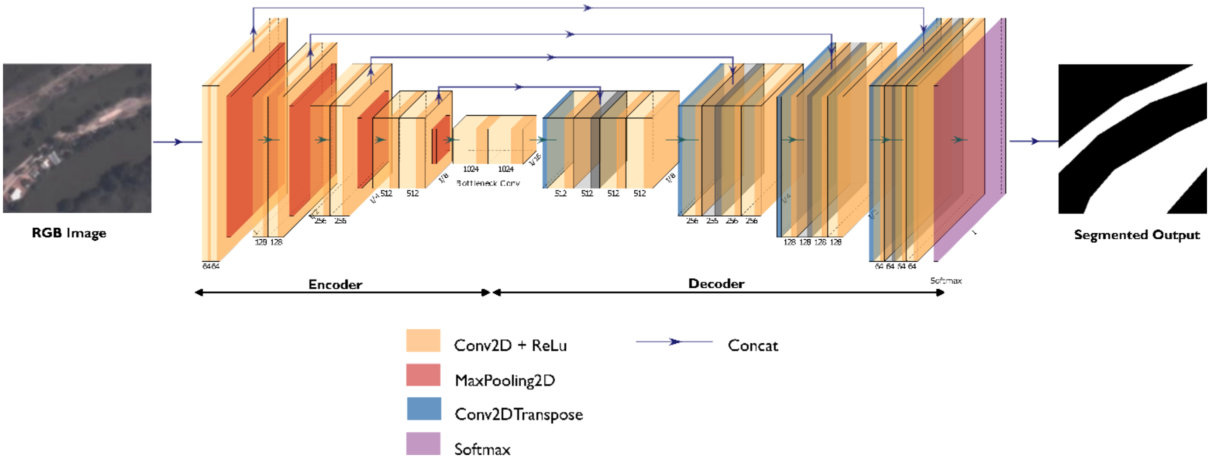

Figure 3.6 U-Net architecture (CNN).

Convolutional Neural Networks (CNNs) are the most successful and widely used architecture in the field of computer vision and have been applied to many tasks including image classification (Lee and Kwon, 2017; Sultana *et al.*, 2018), super resolution (Dong *et al.*, 2014; Tai *et al.*, 2017; Tian *et al.*, 2022) and semantic segmentation (Yurtkulu *et al.*, 2019; C. Zhang *et al.*, 2022). Deep learning-based neural network architectures have outperformed classical machine learning techniques in the semantic segmentation of remotely sensed imagery, including Bayesian networks (BN, Dechesne *et al.*, 2021; Xiong *et al.*, 2020), k-nearest neighbours (k-NN, Garg *et al.*, 2021; Su *et al.*, 2022), Support Vector Machines (SVM, Farag *et al.*, 2005; Moliner *et al.*, 2020; Song and Civco, 2004), Markov random field (MRF, Kato and Zerubia, 2012; Zheng and Wang, 2014), decision trees and Random Forest techniques (DT, RF, Sevak *et al.*, 2017; Smith, 2010) due to their ability to detect the most salient features efficiently and accurately in images without manual feature engineering or preprocessing. CNNs do not require human supervision in identifying important features and are designed to learn spatial hierarchies automatically and adaptively in images, allowing them to generalize well to unseen or new data.

CNN architectures are composed of three layers, convolutional layers, pooling layers and fully connected or dense layers. Convolutional layers are the key building block of the CNNs, they rely on a series of filters to extract important features, such as edges, lines, and textures. These filters, known as feature detectors, consist of a small matrix of weights which are convolved with the input image to produce a feature map. A filter with a defined size will usually be applied to a region within the input image and will shift until the entire image has been covered, producing multiple feature maps which contain a discrete set of learned features. Outputs from the convolutional layer are then passed through a nonlinear activation function (Hao *et al.*, 2020) and passed on to the pooling layer. Pooling layers downsample the feature maps (reduce the spatial size) received from the convolutional layers, decreasing the computational power required to process the data and reducing the risk of overfitting. Two types of pooling are generally applied, and this can either be average or max pooling. Average pooling averages the elements visible in the region of the feature map covered by the filter while max pooling returns the maximum values from the portion of the image covered by the filter. Unlike convolution layers which are used for feature detection, pooling layers are used for feature selection. Outputs from the convolutional and pooling layers are then passed through one or more fully connected layers which make a prediction about the class or label of the input image.

CNNs for semantic segmentation are generally based on encoder-decoder type structures. The encoder is usually a pre-trained classification network (for example VGG (Simonyan and Zisserman, 2015), ResNet (Krizhevsky *et al.*, 2017), GoogLeNet (Szegedy *et al.*, 2015)) and extracts features used for segmentation of the input image using the knowledge acquired from the pre-training through transfer learning. Since outputs from the encoder are usually of low dimensions, the decoder is used to reconstruct a segmentation mask of the same height and width as the input image. In this thesis, a U-Net encoder was used. Although a broad spectrum of deep learning neural networks have been proposed for semantic segmentation of images, amongst the most popular encoder-decoder type architectures that have attained state-of the art performance include U-Net (Ronneberger *et al.*, 2015) (Figure 3.6), PSPNet (Zhao *et al.*, 2017) , DeepLab (Chen *et al.*, 2017). Although deep learning-based analysis of remote sensing imagery is still in its infancy, there is promising evidence for its use in flood hazard mapping studies.

Although CNNs have been the go-to architecture for image segmentation, as images have grown more intricate and varied, CNNs have faced challenges capturing long-range dependencies, contextual nuances, and global interactions within images. Transformers, a type of deep learning architecture, have recently emerged as a competitive alternative to CNNs. The transformer architecture was originally proposed for sequence to sequence learning and natural language processing tasks (Tunstall *et al*., 2022; Wolf *et al*., 2020). Transformer-based language models, such as the Generative Pre-Trained Transformer (GPT), have attained popularity, such as the ChatGPT (Liu *et al*., 2023) AI chatbot, and led to breakthroughs in language understanding, generation, translation, and more, and continue to drive progress in the field of natural language processing. This led to the adaptation of transformers for processing image data. The Vision Transformer (ViT) was proposed by (Dosovitskiy *et al*., 2021). Different from traditional CNNs, ViTs process images as sequences of fixed-size patches, enabling them to capture global context and relationships between pixels at various scales (Khan *et al*., 2022). Their key feature is the self-attention mechanism, which allows ViTs to weigh the importance of different patches in relation to each other, facilitating the understanding of spatial hierarchies and long-range dependencies within images (Han *et al*., 2022). This holistic perception enhances their ability to recognize intricate patterns, objects, and their interactions, leading to accurate and context-aware image analysis. ViTs have demonstrated remarkable performance in tasks like image classification, object detection, and segmentation, offering a promising alternative to traditional CNN-based approaches in the field of computer vision (Karimi *et al*., 2021; Strudel *et al*., 2021; Yang *et al*., 2022).

Although ViTs have attained state-of-the-art performance in many computer vision tasks, they do not necessarily outperform CNNs across the board (Yuan *et al*., 2023). In fact, ViTs and CNNs complement each other in image segmentation by combining their respective strengths. Whilst ViTs leverage self-attention mechanisms to obtain global connects and long-range dependencies across images, CNNs excel at capturing local features through convolutional layers enabling them to identify intricate details that are crucial for accurate segmentation. By integrating CNNs and ViTs, enhanced segmentation accuracy can be attained through a comprehensive understanding of both fine-grained and high-level image characteristics.

3.5 Summary

The methods presented in this chapter will serve as the foundation for the subsequent empirical chapters. The utilization of Structure from Motion (SfM) photogrammetry will be examined for the creation of high-resolution Digital Elevation Models (DEMs) (Chapter 4), which are essential for accurate terrain representation in flood modelling. Additionally, the application of image velocimetry is investigated as a means to estimate river surface velocities from video data (Chapters 4, 5 and 6). The incorporation of deep-learning techniques into image segmentation offers an approach for precise flood pixel identification within complex visual datasets (Chapter 5). These methodologies collectively pave the way for the empirical chapters that follow, where their practical implementation is aimed at advancing the theoretical understanding of hydraulic processes and also practically enhancing the predictive capabilities of hydraulic models.

Chapter 4 - Unpiloted Aerial Vehicle (UAV) image velocimetry for validation of two-dimensional hydraulic model simulations

The following chapter is a reformatted version of a manuscript published in the *Journal of Hydrology* by Christopher Masafu, Richard Williams, Xiaogang Shi, Qiangqiang Yuan and Mark Trigg, which is available at https://doi.org/10.1016/j.jhydrol.2022.128217

Highlights

- A 2D hydraulic model fully calibrated/validated using LSPIV surface velocities.
- Performance of LSPIV on par with aDcp calibrated/validated model.
- Velocity depth-averaging using the Probability Concept significantly constrains model prediction errors.
- LSPIV is justified as an alternative dataset for parametrising 2D hydraulic models.

Abstract

Non-intrusive image-based techniques for measuring surface river velocities have rapidly evolved as a cost-effective and safe means for quantifying flow patterns. Large-scale particle image velocimetry (LSPIV) can provide instantaneous surface velocities over a large spatial footprint rapidly and with little pre-calibration as compared to traditional techniques. Assessment of the spatial distribution of flow velocities in hydraulic models has been comparatively harder to achieve than assessment of depth due to logistical challenges but would be aided using large observational datasets that represent the variability and distribution of flow hydraulics. Additionally, the efficacy of image velocimetry in assessing the accuracy of outputs from 2D hydraulic models has not been addressed. Here, we demonstrate how LSPIV can be used to calibrate and validate 2D model predictions in a gravel bed river reach. LSPIV velocities are depth-averaged using standard velocity coefficients (α) and then using the Probability Concept (PC) - a probabilistic formulation of velocity distributions that accounts for non-standard velocity profiles, typical in field settings. UAV surveys were used to acquire video for LSPIV and imagery for Structure from Motion (SfM) topographic modelling. We use spatially dense acoustic doppler current profiler (aDcp) velocity data for benchmark assessment of the velocity outputs of HEC-RAS 2D model simulations. 2D model prediction error, based on seeded LSPIV velocities, was within range (4.2%) of the aDcp parametrised model, with improvements in modelled versus predicted velocity correlations (up to 7.7%) when using PC to depth average LSPIV velocities. Validation bias reduced significantly (11%) with tighter error distributions when compared to the aDcp based model. Although additional hydraulic measurements are required to parametrise the Probability Concept algorithm, the performance of 2D hydraulic models calibrated/validated with LSPIV velocities is on par with traditional techniques, demonstrating the potential of this non-intrusive, low-cost approach.

4.1 Introduction

Two-dimensional (2D) hydraulic modelling has been widely used to assess flood risk at varying temporal (such as hourly to daily) and spatial scales (including regional to catchment). The assessment of 2D model simulations has previously been achieved by comparing model outputs to observations of water surface elevations, extents, and depths (Bernhofen *et al*., 2018; Cea *et al*., 2014) and, less commonly, velocity (Barker *et al*., 2018; Fischer *et al*., 2015). Previous investigations (e.g., Gard, 2008; Lane *et al*., 1999; Pasternack *et al*., 2006; Williams *et al*., 2013) utilized velocity measurements collected using conventional sensors (acoustic Doppler current profilers; aDcp) to assess 2D model performance. However, the use of velocity observations obtained using traditional measurements to assess 2D models has notable challenges, including safety considerations during high discharge events and limitations on the spatial extent of observations that can be acquired. There remains a pressing need for velocity data that fully samples the range and distribution of channel velocities to validate 2D hydraulic models (Barker *et al*., 2018; Cea *et al*., 2014; Wagner and Mueller, 2001).

The advent of powerful, cost-efficient computing power and precise remote sensing datasets has offered an avenue for new, high quality, fine spatial scales benchmark data, for the validation of flood models (Wing *et al*., 2017). In particular, the use of Unpiloted Aerial Vehicles (UAVs) as a non-contact method to investigate flood extents has eliminated the need to deploy staff in dangerous field conditions (DeBell *et al*., 2016; Eltner *et al*., 2020; McCabe *et al*., 2017; Perks *et al*., 2020; Tokarczyk *et al*., 2015). The fine spatial and temporal resolution of UAV data has also allowed for the mapping of velocity dynamics of flood events at unprecedented scales (Al-mamari *et al*., 2019; Smith *et al*., 2014) leading to improved insights into local catchment processes. Additionally, UAV topographic surveys based on Structure from Motion (SfM) are providing fine scale digital terrain models (DTMs), which are enhancing model parametrisation efforts, such as better descriptions of surface roughness for calibrating Mannings roughness (DeBell *et al*., 2016).

Image velocimetry has generated considerable interest in hydrology, presenting capabilities to derive spatially distributed surface flow velocities at high temporal resolution using UAVs as a camera platform (Koutalakis *et al*., 2019; Pizarro *et al*., 2020b; Tauro *et al*., 2017). Although various image velocimetry algorithms have been applied to monitor river flows (Cao *et al*., 2020; Perks *et al*., 2020), Large-Scale Particle Image Velocimetry (LSPIV) is the most commonly used algorithm and is in many respects considered proven and tested (Jodeau *et al*., 2017). LSPIV, the large-scale implementation of PIV techniques in outdoor environments, is based upon Eulerian principles (Euler, 2008), where the average displacement of cluster particles within an interrogation window is measured. This can be differentiated from Particle Tracking Velocimetry (PTV) methods, which are based on Lagrangian motion (Amelinckx, 1971) that tracks the motion of individual particles over time. Depth-averaged velocities may then be retrieved from LSPIV surface velocities using logarithmic velocity profiles, by fitting power laws to velocity profiles (Welber *et al*., 2016; Wilcock, 1996) or using a velocity coefficient to adjust surface velocities (Le Coz *et al*., 2010).

Whilst a great deal of research has been dedicated to the development and assessment of the performance of various image velocimetry algorithms, such as the impact of seeding densities under low flow conditions (Pearce *et al*., 2020), inter-comparisons of algorithm implementation under diverse hydro-geomorphic settings (Perks *et al*., 2020) and development of workflows to compute and benchmark surface flow velocities (Eltner *et al*., 2019), few studies have systematically assessed the accuracy of LSPIV based surface flow velocities in natural environments. The need for high quality data to validate flood models, coupled with a benchmark evaluation of image velocimetry data in both high and low flows, has significant potential in reducing uncertainty associated with spatially distributed model predictions.

Research evaluating the capability of 2D hydraulic models to accurately reproduce the spatial distribution of water velocity has been limited. Several studies have validated 2D models using aDcp velocity data. For example, Williams *et al*. (2013) demonstrated the capability of spatially dense RTK-GNSS (Real Time Kinematic – Global Navigation Satellite System) positioned Acoustic Doppler Current Profiler (aDcp) data in the calibration and verification of a 2D hydraulic model. Meanwhile, Barker *et al*. (2018) evaluated aDcp and kayak (positioned with RTK-GNSS) particle surface velocity vector methods to validate a 2D model, concluding that surface velocity tracking data outperforms fixed-point data validation for all the statistical validation metrics. In practice, most 2D model assessment efforts that have used velocity data have done so using limited-location samples, usually with selected cross-sections, where 1D current meter time-averaged velocity data or 2D acoustic instrumentation measurements have been collected, leaving room for significant uncertainties and errors. For example, Kasvi *et al*. (2015) used four aDcp cross-sections to validate a 2.1 km long 2D model, Tiffan *et al*. (2001) used two aDcp cross-sections to validate a 33 km long 2D model while Parsapour-Moghaddam and Rennie (2018) used one aDcp cross-section to validate a 0.19 km long 3D model. They all concluded that more field data would have resulted in more robust validation outcomes. When simulating flow dynamics using 2D models, a small number of cross-sections to assess model simulations are insufficient. It is also time-intensive to identify appropriate cross-sections and then gather velocity measurements. Further, classical wading and aDcp methods are not evolving with the scales of model assessment required and they remain remarkably slow field techniques (Pasternack, 2011). In summary, the acquisition of aDcp velocity measurements are limited in: (i) shallow rivers, as observations can only be acquired beyond a vertical blanking distance; (ii) turbulent conditions due to boat instability and bedload transport; and (iii) high velocities due to logistical challenges. With respect to the latter challenge, in some situations remote controlled boats (Flener *et al.*, 2015) and RTK-GNSS positioning can be used to overcome bias in bottom tracking due to bedload transport (Rennie and Church, 2010; Williams *et al.*, 2015) but challenges monitoring high flows still remain prevalent in many situations.

Although the use of non-contact methods to estimate surface velocities in riverine environments has been demonstrated (e.g., Pearce *et al.*, 2020; Pumo *et al.*, 2021; Ran *et al.*, 2016), the majority of studies have relied on a commonly established multiplicative constant known as a velocity-index, typically varying between 0.70 to 0.90, for the computation of depth-averaged velocity (Bechle and Wu, 2014). The use of a constant velocity-index for translation of surface velocities not only fails to account for atypical velocity distributions, such as when maximum velocity occurs below the water surface, but it also assumes that the vertical-velocity distributions in a river channel can be characterized using a logarithmic or power law, which is not always true (Moramarco *et al.*, 2017). An alternative approach for accurately estimating two-dimensional velocity distributions, based on the entropy probability density function of velocity, was proposed by Chiu (1987). Previous studies have demonstrated that the maximum entropy method can be a suitable means to constrain velocity bias towards known parameters, thus serving as a suitable approach to relate surface velocities to depth-averaged velocities (Marini *et al.*, 2011).

The first objective of this paper is to investigate whether spatially continuous surface velocities computed using LSPIV can be used to accurately calibrate and validate 2D hydraulic model simulations in a natural environment. We aim to demonstrate the utility of models fully parametrised using LSPIV, as compared to those calibrated/validated using spatially dense aDcp data. The second objective is to evaluate the utility of the entropy-based surface velocity method Chiu (1987), named Probability Concept (PC), as a mathematical basis for transforming LSPIV-derived surface velocities to depth-averaged velocities, in order to account for velocity distributions that do not conform to logarithmic or power laws within a shallow gravel-bed river. We provide an explicit assessment of the variance between numerical model velocity simulations based on aDcp observations and LSPIV derived estimates. The spatial uncertainties in 2D model simulations based on both aDcp and LSPIV are assessed using standard hydraulic model performance metrics. Advancing prior studies in this research domain (e.g., Barker *et al*., 2018; Pasternack *et al*., 2006), this work presents a hitherto untested application of spatially explicit, high-resolution LSPIV-derived velocities in calibrating and validating a 2D hydraulic model. Calibration and validation terminology used in this paper follows the definitions of Refsgaard and Henriksen (2004).

The following sections describe the study site, outline the methods that are used to generate the model topography and detail the field surveys used to acquire aDcp, LSPIV and electromagnetic flow meter measurements. The next section presents the results from 2D calibration and validation using aDcp, then LSPIV measurements. A discussion follows that examines the hydraulic predictions and assesses the uncertainty and value of both model simulations.

4.2 Study Site

This investigation is undertaken along a restored reach of Swindale Beck, Cumbria, England (Figure 4.1), which is a 13.4 km^2 sub-catchment of the River Eden. Restoration of the study reach was undertaken in 2016 and involved channel re-meandering, with 890 m of a new sinuous channel, positioned along the course of a paleochannel, replacing 750 m of straightened channel (Wildhaweswater, 2020). Post-restoration, the river is considerably more geomorphologically diverse, being characterised by pools, riffles and gravel bars; and is geomorphologically active in response to high flow events. The floodplain is mostly vegetated with species-rich hay meadow, bog, and grassland. Catchment descriptors derived from the UK Flood Estimation Handbook (FEH) (Institute of Hydrology, 1999) were used to estimate the median annual maximum flood (QMED) which is 26.96 m^3 s^{-1}. A telemetry gauging station (United Utilities station 761113) records stage in the river at a weir every 15 minutes from 1997 to present (Hankin *et al*., 2019). The extent of the 2D hydraulic model domain is shown in Figure 4.1; within this extent a set of image velocimetry and aDcp observations were acquired along a reach that is approximately 540 m long.

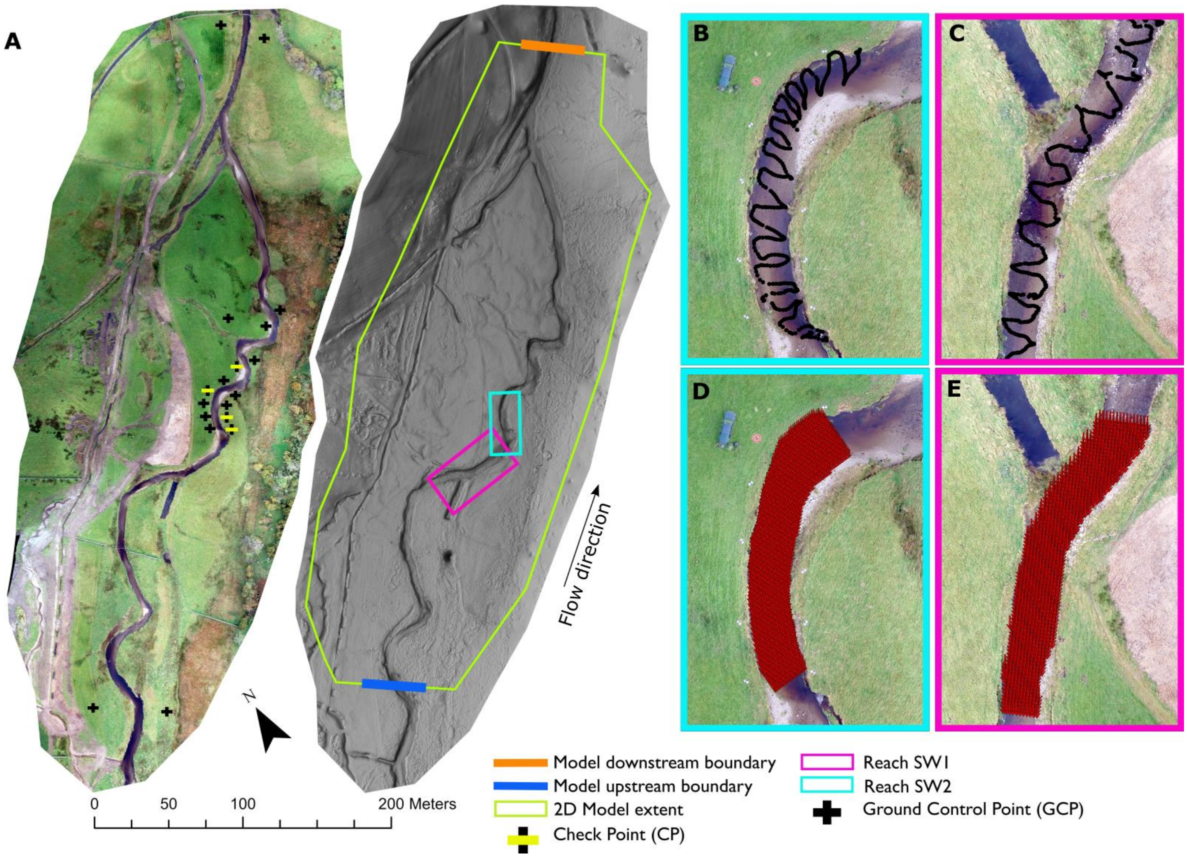

Figure 4.1 (A) Orthomosaic image of the Swindale (351074E 512754N, British National Grid) study reach (left) and hillshaded SfM DEM (right) showing the extent of the 2D model domain and investigated sub-reaches; (B, C) aDcp survey transects (black traces); (D, E) LSPIV surface velocity

4.3 Methodology

The experiments conducted within the study reach are described in the experimental framework (Figure 4.2), which commenced with the acquisition of UAV imagery (still; oblique), used to generate a detailed terrain model using SfM photogrammetry (section 4.3.1.2). UAV video sequences were subsequently acquired on 24 February 2021 over two sub-reaches (hereafter referred to as SW1 and SW2; Figure 4.1).

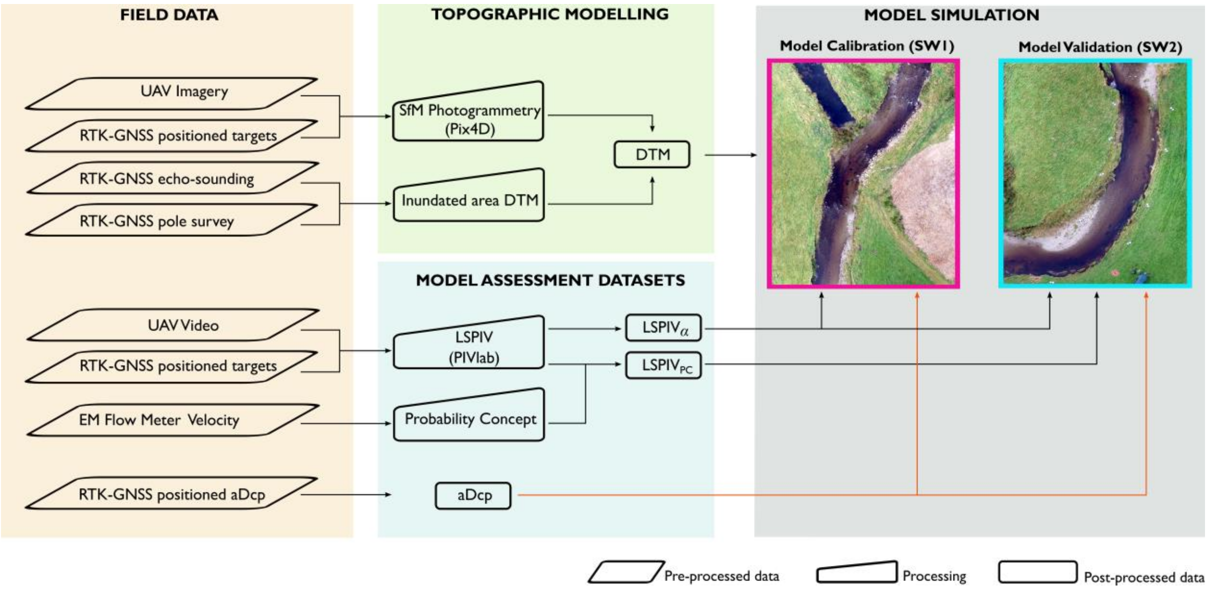

Figure 4.2 Experimental framework.

Conventional water velocity measurements were conducted using an aDcp (section 4.3.2) and a current meter (section 4.3.3). aDcp river velocity measurements were collected during the falling limb of a storm event that occurred on 24 February 2021 and peaked at 20.6 m^3 s^{-1}. The aDcp dataset was processed to derive velocity magnitude vectors which were used to calibrate/validate the 2D hydraulic model. UAV videos were processed using the LSPIV algorithm, PIVlab (Thielicke and Stamhuis, 2014) to generate instantaneous surface velocity vectors (section 4.3.4). A subsequent field campaign to acquire flow meter measurements was conducted on 21 June 2021 during the summer low flow period at an average discharge of 2.5 m^3 s^{-1}. Flow meter measurements provided detailed vertical velocity distribution profiles that were used to parametrise the Probability Concept algorithm (Chiu, 1987) for depth averaging of LSPIV surface velocities (section 4.3.5). Hydraulic modelling was then performed using a 2D model (HEC-RAS 6.0 (Brunner *et al.*, 2020)) following which an assessment of model velocity outputs was conducted using conventional aDcp measurements and LSPIV measurements. The following sub-sections provide further details on these methods.

4.3.1 DTM generation

4.3.1.1 Inundated area: RTK-GNSS and echo-sounding

A field campaign was undertaken using a hybrid approach to map dry and inundated areas of the study reach. A Leica GS10 receiver was positioned over a surveyed base station in GNSS mode. To survey channel bathymetry within the study reach, a combination of wading surveys using a Leica GS10 antenna mounted on a pole, in RTK-GNSS mode, and vertical beam echo sounding observations from a Sontek M9 aDcp with RTK-GNSS positioning from a Leica GS16 RTK-GNSS antenna were deployed. During the wading survey, an operator traversed the river channel collecting bed, bank toe and water edge RTK-GNSS points with approximately 1 m point spacing. The resulting composite (wading-based and aDcp-based) dataset comprised over 13,000 bed level measurements with a mean density of 1.77 points m^{-2}.

A DTM of the river channel was then generated in ArcGIS Pro by interpolating a Triangular Irregular Network (TIN) from the aggregated wading and aDcp-based RTK GNSS datasets. A Delaunay conforming triangulation was used ensuring that breakline segments were densified. Linear interpolation was then used to convert the channel TIN into a 0.2 m DTM.

4.3.1.2 Dry areas: SfM Photogrammetry

SfM with multiview stereo photogrammetry (hereafter together referred to as SfM photogrammetry (Carrivick and Smith, 2019)) was used to generate a DEM of the study area using images acquired by a DJI Phantom 4 RTK UAV. SfM photogrammetry is a technique used to generate a three-dimensional point cloud (i.e., structure) from the motion of a camera across a scene of interest (Escobar Villanueva *et al.*, 2019). DEMs that have been generated using SfM are now widely used to investigate river floodplain environments (e.g., Annis *et al.*, 2020; Javernick *et al.*, 2014; Schumann *et al.*, 2019).

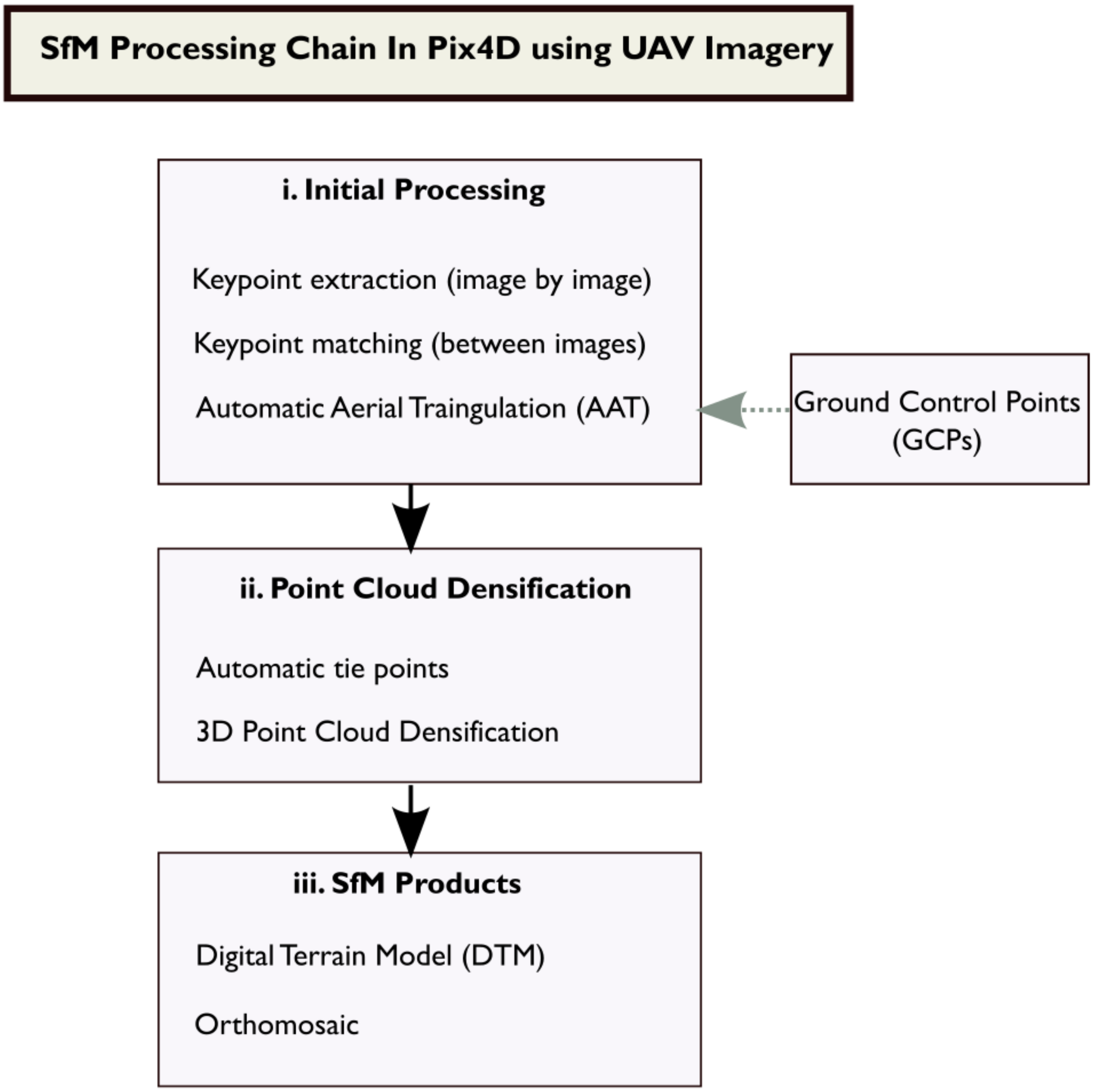

Figure 4.3 Simplified workflow of Pix4D SfM processing steps.

Pix4D software was used for SfM photogrammetry following the method reported in Stott *et al*. (2020), with guidance based on James *et al*., (2019) (Figure 4.3). SfM processing parameters used in this study are summarised in Table 4.1. 944 images from the UAV were automatically geotagged with WGS84 coordinates during acquisition. These were then transformed to the ETRS89 geodetic reference system, used in the UK as the datum for the Ordnance Survey reference system. SfM processing in Pix4D was largely automated and comprised three-stages to generate both Digital Surface Models (DSMs) and bare terrain DEMs. The initial step involved the computation of key points on the images to enable matching. Matched images were then processed using automatic aerial triangulation and bundle block adjustment to create a 3D point cloud of the study area.

Table 4.1 SfM photogrammetry survey and processing specification, based on James *et al.* (2019) guidance.

Setting:	Survey Type	Gravel Bed River Survey
	Location	Swindale Beck, Cumbria, England
	Latitude, Longitude	54.515347°, -2.741841°
	Date (dd/mm/yyyy)	11/15/2020
Equipment:	Camera Manufacturer	DJI
	Camera Model	FC6310R_8.8_5472×3648
	Number of Images	944
	Number of Flights	1, Flying 5 Flight Blocks
	Image size (pixels)	5472 × 3648
	Sensor Size	1” CMOS; Effective pixels: 20 M (13.2 × 8.8 mm)
	Focal Length	8.55 mm; 3658.3 pixels
	Lens Type	FOV (Field of View) 84◦, 8.8 mm
	Sensor Shutter Type	Rolling
	Mechanical Shutter Speed	8-1/2000s
	Electronic Shutter Speed	8-1/8000s
Survey Design:	Flight Height (m)	70
	Ground Sampling Distance	2.276 cm
	Area Covered (km2)	0.304
	Perspective of Images	Oblique (15◦)
	Image Overlap (front)	80%
	Weather	Sun and Cloud, <20 mph Winds, 10 ◦C
Photogrammetric Processing:	Software	Pix4D Mapper Version 4.4.12
	Keypoints Image Scale	1 (original image size)
	Matching Image Pairs	Aerial Grid or Corridor
	Calibration Method	Standard
	Internal Parameters Optimization	All
	External Parameters Optimization	All
	Lens Used	Perspective Lens

Internal Camera Parameters	**Focal Length (mm)**	**Principal Point x (mm)**	**Principal Point y (mm)**	**R1**	**R2**	**R3**	**T1**	**T2**
Initial Values	8.580	6.385	4.304	-0.269	0.112	-0.033	0.000	-0.001
Optimised Values	8.618	6.405	4.253	-0.267	0.112	-0.034	0.000	-0.001
Uncertainty (Sigma)	0.000	0.000	0.000	0.000	0.000	0.000	0.000	0.000

Manual classification of Ground Control Points (GCPs) was then carried out. A matrix of 18 ground control targets, each measuring 0.6 x 0.6 m, were laid out within the study reach on dry land. A Leica GS10 GNSS antenna, mounted on a 2 m pole, was used to observe each of the ground control targets for at least 5 minutes in GNSS static mode. Postprocessing of the raw GNSS observations relative to the base station observations was carried out using proprietary Leica GeoOffice software to establish the true coordinates of the ground control targets. To independently evaluate errors in subsequent processing, 5 targets were used as check points (Figure 4.1a).

The second and third processing steps involved the generation of a DSM using an inverse distance weighting algorithm and generation of a bare earth DTM by classifying a dense point cloud using a proprietary Pix4D machine learning algorithm. The accuracy of the UAV-Derived DEM was acceptable (Table 4.2), with Root Mean Square Errors (RMSE) for CPs being <0.05 m. The fused 0.2 m SfM DTM (Figure 4.1a) served as the final topographic surface for 2D modelling.

Table 4.2 Localisation accuracy per check point and mean errors in the three coordinate directions for the SfM DTM.

Dimension	**Check Points (CP)**		
	X (m)	**Y (m)**	**Z (m)**
Mean Error	-0.009	-0.007	0.001
Root Mean Square (RMS) Error	0.013	0.014	0.048

4.3.2 aDcp Velocity Survey Data

Acoustic survey velocity measurements were acquired using a SonTek M9 RiverSurveyor. The theory of aDcp system operation is discussed in detail by Kostaschuk *et al.* (2005) and Simpson (2001). The M9 RiverSurveyor is equipped with four profiling beams (3.0 and 1.0 MHz) and one 0.5 MHz vertical beam for depth measurement. Due to the shallow nature of the river, all velocity measurements used the 3 MHz transducers. The aDcp was mounted on an SonTek Hydroboard and calibrated as outlined by Williams *et al.* (2013). Accurate positioning of the moving aDcp was provided by a Leica GS16 RTK-GNSS receiver fitted on the trimaran boat. This provided RTK corrections to position depth and velocity observations.

Field aDcp surveys were conducted during a hydrograph recession in winter (February 2021). Average discharge during the survey was 13.1 m^3 s^{-1}. During field measurements, the aDcp was dragged in a zig-zag trajectory by two operators standing on opposite sides of the riverbank. Each survey provided over 1000 sample points at a mean spacing of 1 m between transects (Figure 4.1; B-C), with some minor spacing alterations being made to accommodate riverine features such as riffles and shallow gravel bars.

The aDcp logged approximately 1,124 georeferenced velocity ensembles in the *x* and *y* directions. Post-processing of the raw aDcp outputs focused on the horizontal components (*x* and *y*) of mean velocity. Sontek's proprietary RiverSurveyor Live software was used to export the datasets to MATLAB, where a custom script was written to extract the horizontal velocity vectors. Depth-averaged velocity magnitude was then calculated from the two horizontal velocity vectors, *x* and *y*. Measurements that failed to meet location thresholds (less than 4 GNSS satellite observations or where Horizontal Dilution of Precision (HDOP) was greater than 8) were discarded (Environment Canada, 2004). Points close to the channel edges were also disregarded as the ability of aDcps in measuring shallow-water velocities is limited by side-lobe interference and the instrument's blanking distance (distance below the transducer where velocity cannot be measured) (Mueller *et al.*, 2013).

4.3.3 Flow Meter Measurements

A Valeport Electromagnetic (EM) Flow Meter, widely used for wading measurements, was used to acquire two-dimensional water velocities (Figure 4.4). The EM flow meter has an accuracy of ± 0.5% of readings (plus 5 mm) and a range of -5 m s^{-1} to 5 m s^{-1} with the ability to operate at a minimum depth of 0.05 m. Velocity data were collected at six cross-sections. The vertical velocity profile of each vertical was sampled beginning from the channel bottom to the water surface with a minimum of six (and mean of eight) individual velocities measured. This procedure was repeated from the left to the right bank of each cross-section to confirm the location of the vertical containing the maximum velocity. The vertical containing the maximum velocity at each cross-section, referred to as the *y*-axis (Fulton *et al.*, 2020b), was then used to parametrise a Probability Concept algorithm (Chiu and Hsu, 2006) for depth-averaging of surface velocities in subsequent field experiments.

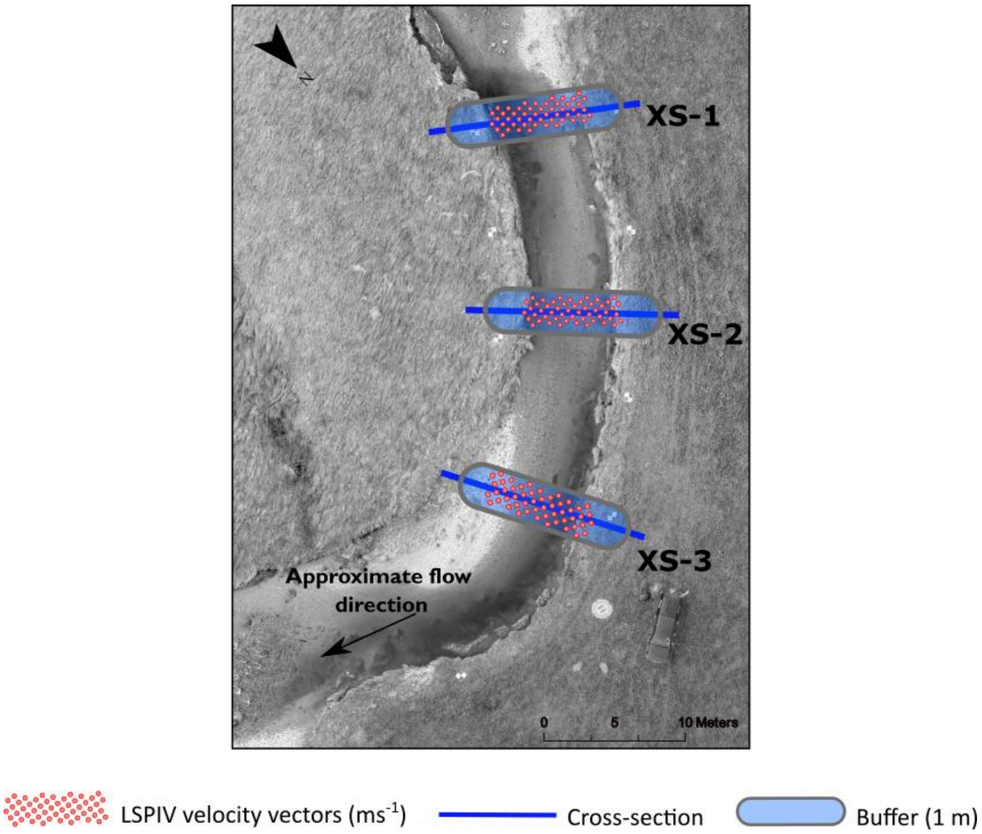

Figure 4.4 Locations of cross-section velocities acquired using a current meter at sub-reach SW2.

4.3.4 Image velocimetry (LSPIV) surface velocities

Hydraulic applications of LSPIV are based on the conventional PIV technique (Adrian, 1991), which was first modified and applied to riverine environments by Fujita *et al*. (1998). The computation of flow velocities in LSPIV is achieved by interrogating consecutive orthorectified images using cross-correlation algorithms (e.g., Dobson *et al*., 2014; Ran *et al*., 2016). Surface velocity is then computed by dividing the displacement of tracer particles by the time interval, Δt. LSPIV analysis yields time-averaged 2D surface velocity surfaces, which can be filtered for errors, commonly based on velocity magnitude thresholds. A comprehensive discussion of the concepts and applications of LSPIV in riverine environments is provided in Muste *et al*. (2008) and Tauro *et al*. (2017).

In this study, video sequences were acquired at select locations (Figure 4.1; D-E) along the study reach using the same DJI Phantom 4 RTK UAV used in acquiring images for SfM photogrammetry. Videos were captured using the UAV's default 1" CMOS, 20 MP camera (8.8 mm focal length) at a native resolution of 4K (3840 x 2160) and a frame rate of 29.97 frames per second (fps) in non-RTK mode. During the field campaign, six videos were shot at a flying height of 30 m above the Swindale Beck, with a ground sampling distance (GSD) of 0.82 cm/pixel. All videos were shot at nadir with the UAV's anti-shake 3-axis gimbal countering vibration effects to deliver stable video scenes.

To ensure the synchronicity of data collection between the two methods (aDcp and UAV videos), given their joint role in evaluating the hydraulic model, timing of the surveys was kept very close. The UAV videos were acquired immediately following aDcp surveys to minimize temporal discrepancies and maintain as close a resemblance of discharge conditions as possible. Specifically, the video acquisition was initiated within 15 minutes of completing the aDcp measurements. This approach was adopted to enhance the accuracy of hydraulic model evaluation by reducing potential variations introduced by temporal differences between data collection methods.

We processed video sub-samples of 5 min 27 sec (SW1) and 4 min 04 sec (SW2) both recorded at 30 m height. From the videos recorded during the field campaigns, a total of 856 consecutive images were extracted at a frame rate of 10 Hz. Table 4.3 summarizes the experimental conditions and frames used in the LSPIV analysis.

Table 4.3 LSPIV parameters adopted for the study.

Reach	Experimental Conditions	fps	Frame window	Number of frames
SW1	Seeded	10	6505 - 8641	214
SW1	Unseeded	10	2381 - 4517	214
SW2	Seeded	10	4513 - 6649	214
SW2	Unseeded	10	1559 - 3659	214

To enhance optical tracking of surface water features, which are central to the determination of surface water velocities (Pizarro *et al.*, 2020b), we continuously introduced biodegradable Ecofoam cornstarch chips at a straight and narrow section of the stream during video recording. The displacement rate of these highly contrasting artificial tracers (also known as 'seeds'), in clear water where the channel bed was largely visible, provided a sufficiently distinct background for surface velocity computations.

4.3.4.1 PIVlab Analysis

The open-source toolbox PIVlab (Thielicke and Stamhuis, 2014), developed in MATLAB (R2021a, MathWorks, Natick, MA, USA), was used to analyse the UAV images. The PIVlab processing workflow consists of three key stages: (1) image pre-processing; (2) image evaluation and (3) post-processing.

Individual frames from the two videos were first extracted (in PIVlab) at the frame windows detailed in Table 4.3. This entailed a visual inspection of the videos to identify sequences with either relatively uniform, dense seeding, or plain river flow. These respective windows were trimmed and extracted for further analysis. Although the UAV flights were conducted during favorable weather conditions, further stabilization of the extracted images was conducted in the Rectification of Image Velocity Results (RIVeR) toolbox (Patalano *et al.*, 2017) to counter residual camera movements. Stabilized images were loaded on to PIVlab for the first stage of analysis; image pre-processing.

The image pre-processing steps were conducted to enhance the appearance of tracers with respect to the background. The PIVlab algorithm applies a Contrast-limited adaptive histogram equalization (CLAHE) filter (set to 20 pixels) to enhance contrast in images. We further utilized the high pass filter to supress low frequency background information from the images, which helped emphasize particle tracers in the images.

PIVlab features two different cross-correlation algorithms for image evaluation, D-CC (single pass Direct Cross-Correlation) and FFT window deformation (Fast Fourier Transform correlation with multiple passes and deforming windows). Both techniques are based on cross correlation of small sub-images (interrogation areas, IAs) of image pairs. To estimate the correlation between image frames this study utilized FFT window deformation due to; 1) its computational efficiency (as compared to DCC), and 2) increased accuracy due to the ability to run several passes of FFT correlation on the same dataset, yielding high spatial resolution velocity vectors at a high signal-noise-ratios, according to the methodology described in Thielicke and Stamhuis (2014).

To obtain optimal parameters for LSPIV analysis, we conducted sensitivity tests on the sampling rate of image sequences and number of passes of different IA kernels in PIVlab. PIV analysis for all scenarios was conducted using four passes with progressively reducing IA window sizes (Table 4.4). Initial IA sizes were chosen based on criteria suggested by Pumo *et al.* (2021) considering values that were not lower than 50% of the minimum image dimensions and higher than twice the maximum presumable frame-frame displacement. Sensitivity analysis was carried out on the video acquired over reach SW1 at a single cross-section (Figure 4.5).

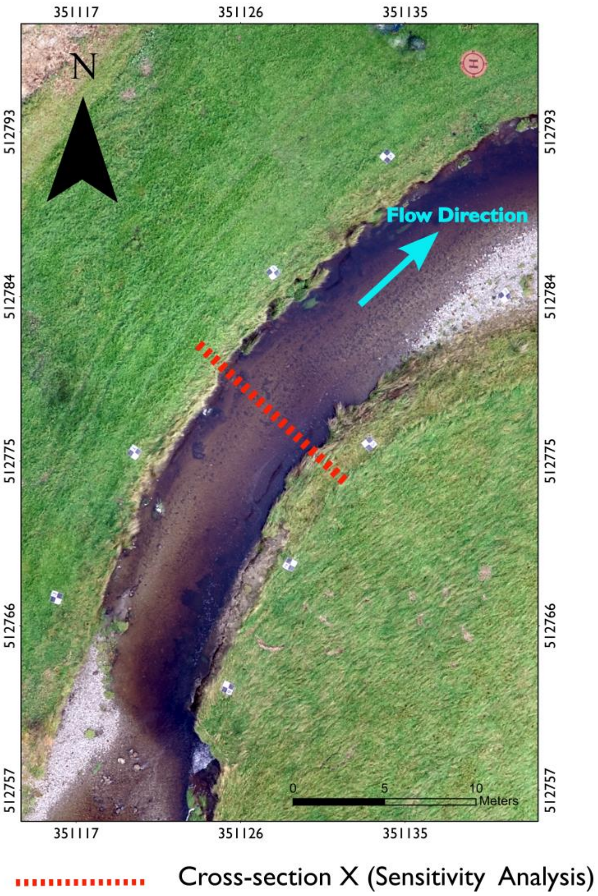

Figure 4.5 Location of transect across which sensitivity analysis was conducted at sub-reach SW1.

We follow the method reported in (Pearce *et al*., 2020b) to conduct our sensitivity analysis. Three configurations were processed with varying sampling rates: 2, 5, 10, 15 fps, providing 12 different configurations for each scenario (seeded/unseeded), therefore a total of 24 different runs were conducted (Table 4.5). Velocity outputs from these runs were gridded at 0.2 x 0.2 m yielding 33 cells, the average cell velocities were then computed. This cell size was sufficient to capture cross-sectional changes in velocities. Median values for each cell were then computed across all 12 configurations for each scenario (seeded/unseeded). A score was then computed for each configuration for each cell based on the absolute deviation between the configuration specific velocity and the median cell velocity. These scores were added up along the cross-section, providing a total score for each configuration; the lower the score, the less variance that is associated among the configurations.

Table 4.4 Sensitivity analyses of key parameters in PIVlab, all measurements in pixels. IA = Interrogation Area (px), SA = Search Area (px).

	Configuration 1	Configuration 2	Configuration 3
SA (px)	128	256	512
IA (px)	64	128	256

Results of the sensitivity analyses showed that LSPIV computations using PIVlab are very sensitive to parametrization dependant on both the (video) frame sampling rate and the IA and SA sizes. Calculated sensitivity scores are summarized in Table 4.5. The sensitivity scores are overall lower for sampling rate at 10 fps with an average score of 0.57. Thus, the configuration with the lowest variance from the mean was a sampling rate of 10 fps with SA = 256 and IA = 128, which was used to compute LSPIV surface velocity measurements.

Table 4.5 Sensitivity scores for PIVlab at cross-section X (C1 = Configuration 1, C2 = Configuration 2, C3 = Configuration 3 – See Table 4.4). Light colours represent lowest sensitivity scores increasing as the colour gradient darkens. The configuration with the lowest sensitivity score is reported in bold text.

2 fps			5 fps			10 fps			15 fps		
C1	C2	C3	C1	C2	C3	C1	C2	C3	C1	C2	C3
0.193	0.155	0.494	0.488	0.631	0.307	0.403	**0.139**	1.168	2.129	1.116	1.267

The width of the IAs for subsequent passes was obtained by halving the width relative to the previous pass. PIV analysis was performed with a first pass IA of 256 x 256 px, a second pass of 128 x 128 px, then 64 x 64 px, followed by 32 x 32 px all with 50% overlap. The use of smaller IAs resulted in higher resolution vector maps, however this also increased noise and the number of erroneous correlations.

Derivatives from PIVlab are referenced to an image coordinate system whose origin is typically the top-left of the 2D plane. Calibration of the analysed images was performed to convert the analysed vector units from pixels per frame to m s^{-1} with reference to control points (GCPs) positioned using the same survey techniques used to observe the position of GCPs for SfM photogrammetry. To georeference the velocity vectors, we specified the offsets of our known co-ordinate system in PIVlab, this shifted the image coordinates and mapped them into a projected coordinate reference system (OSGB 1936/British National Grid) that was consistent with the DTM.

Post-processing of the vector fields involved a data validation process in PIVlab where erroneous vectors (outliers) were filtered using thresholds which were semi-automatically derived by comparing each velocity vector with a lower and upper threshold (primary velocities, u: -0.4 to 0.31 m s^{-1}; secondary velocities, v: -0.36 to 0.35 m s^{-1}). Following tests varying the standard deviation and local median filters (key determinants in the vector validation process) we arrived at values of 8 and 3 respectively for removal of outliers. Finally, residual noise in the vectors was removed by applying a data smoothing technique based on a penalized least squares method (Garcia, 2010).

4.3.5 LSPIV Depth-Averaged Velocities

4.3.5.1 Surface Velocity Index

To convert the LSPIV surface velocity results to depth averaged velocities, a surface velocity index/coefficient (also referred to as alpha, α, in several studies (e.g., Fulton *et al*., 2020(a); Hauet *et al*., 2018; Moramarco *et al*., 2017) was computed using a nonlinear Generalized Reduced Gradient optimization algorithm (Solver). We utilized velocities from the aDcp calibrated model (at the calibration sub reach SW1) to arrive at an appropriate theoretical depth-averaging constant. Several objective functions were used to optimize Solver in order to derive a α value, in this case; (i) a value of regression slope between the LSPIV surface velocities and (aDcp) model depth-averaged velocities that yielded a value as close to unity (1) as possible; (ii) the mean velocity difference between LSPIV and (aDcp) model velocities (a difference of ~0 m s^{-1}); and (iii) a mean error of ~0%. The optimization algorithm referred to the gradient of each objective function as the input values changed and when the partial derivatives equalled zero, an optimum solution of the surface velocity index/coefficient was derived.

4.3.5.2 Probability Concept (PC)

Whilst field velocity measurements from the aDcp and the 2D model are depth averaged, LSPIV measurements represent surface flow velocities. A conventional method for transforming surface velocity, u_{surf}, to depth-averaged velocity, u_{vert} involves the use of a constant, known as a surface velocity-index (α) (e.g., Creutin *et al*., 2003; Le Coz *et al*., 2010; Legleiter and Kinzel, 2021; Tauro *et al*., 2017). The use of α to translate surface velocities to depth-averaged velocities is a simple yet convenient method that assumes that the vertical velocity profile is monotonous and can be characterized by a logarithmic distribution or power law (Hauet *et al*., 2018; Huang, 2018). The variability of published α values (0.70 to 0.90) at any given cross-section with stage and variations in channel geometry makes it difficult to select an appropriate value and is thus unreliable for conversion of surface velocities to mean velocities (Fulton *et al*., 2020b). Moreover, the use of a constant α coefficient fails to account for the dip-phenomenon (Moramarco *et al*., 2017), where the maximum velocity, u_{max}, occurs below the water surface due to the presence of secondary currents, resulting in $\alpha > 1$ (Fulton and Ostrowski, 2008; Fulton *et al*., 2020a). Dramais *et al*. (2011) and Welber *et al*. (2016) established that the principal source of error in LSPIV discharge estimates is the use of a singular α coefficient since cross-section specific values from field measurements differed significantly. This justified the acquisition of several cross-section velocity profiles in order to derive α values using the Probability Concept.

The Probability Concept, developed by Chiu (1987), is based on Shannon's Information Entropy and can be used to characterize non-standard velocity distributions where u_{max}, occurs below the water surface. The probabilistic approach provides a numerical basis for the transformation of surface velocities to depth-averaged velocities and provides a least biased two-dimensional velocity distribution that is constrained by known parameters (Marini *et al*., 2011). Velocity and depth data are collected to establish a y-axis, which is a vertical in the stream cross-section that contains the maximum surface velocity (Fulton *et al*., 2020a). Chiu and Hsu (2006) established that the location of the y-axis rarely coincides with the thalweg, is static, and insensitive to variations in flow, stage, velocity, or channel geometry.

Surface velocities measured using LSPIV were transformed to depth-averaged velocities using the PC that is based on Chiu's original velocity distribution equation (Chiu and Chiou, 1986), which maximizes entropy $f(u)$ in order to find the best velocity distribution fit. Equations (4.2) to (4.5) summarize the Chiu equations used, where the probabilistic velocity distribution at any point in the cross-section (y-axis) is represented by Equation (4.1):

$$u = \frac{u_{max}}{M}\, ln\, [1 + (e^{M} - 1)\, F(u)] \tag{4.1}$$

where u = velocity as a function of depth at the y-axis; u_{max} = maximum velocity at the y-axis; M = dimensionless probability parameter that describes velocity distribution; and $F(u) = \int_0^u f(u)du$ which is the cumulative distribution function, or the probability of a randomly sampled point velocity less than or equal to u. At cross-sections where u_{max} falls below the water surface, velocity distribution at the *y*-axis can be characterized by Equation (2):

$$u = \frac{u_{max}}{M}\, ln\, \left[1 + (e^M - 1)\, \frac{y}{D-h} exp\left(1 - \frac{y}{D-h}\right)\right] \tag{4.2}$$

where *D* = total distance from the channel bottom to the water surface at the *y*-axis, y = incremental distance from the channel bottom to the water surface, h = vertical distance from the water surface to u_{max}. An orthogonal coordinate system is used to translate the velocity distribution from probability space to physical space and is used to describe the variables h, D and y in Equation *(*2*)*. Where u_{max} occurs at the water surface, the velocity distribution at the *y*-axis is defined by Equation (3):

$$u = \frac{u_{max}}{M}\, ln\, \left[1 + (e^M - 1)\, \frac{y}{D} exp\left(1 - \frac{y}{D}\right)\right] \tag{4.3}$$

The probability distribution *f(u), M* and *h/D* are all constant at a channel cross-section where u_{max} occurs below the water surface, LSPIV-derived surface velocities are used to estimate u_{max} assuming *u* is equal to *uD*, which is the velocity as which *y* equals *D* (Chiu and Hsu, 2006) and is represented by Equation (4):

$$u_{max} = uD\ \times M \times \left\{ ln \left[1 + (e^M - 1) \frac{1}{1 - \frac{h}{D}} exp\left(1 - \frac{1}{1 - \frac{h}{D}}\right)\right]\right\}^{-1} \tag{4.4}$$

The parameter *φ*, which is a function of M, was then derived following (Fulton *et al.*, 2020b), using point velocities measured along the *y*-axis from the channel bed to the water surface. Current meter vertical velocity and depth measurements were used to compute u_{max}, *M*(*φ*), and *h/D* using a non-linear least-squares estimator in R v4.1.0 (R Core Team, 2013). The Gauss-Newton nonlinear least-squares method was used to solve for *φ,* which is a surrogate for u_{mean}/u_{max}.

4.3.6 2D Hydraulic Modelling

The open-source Hydrologic Engineering Centre - River Analysis System (HEC-RAS version 6.0), developed by the US Army Corps of Engineers, was used to simulate depth-averaged flow conditions. Two-dimensional unsteady state flow was solved using the full momentum (Saint-Venant) equations. Despite the intensive computational demand, application of the Saint-Venant equations allowed for a detailed and accurate representation of velocity distributions (Pilotti *et al.*, 2020) in the relatively flat mixed-flow river regime that characterizes Swindale Beck. HEC-RAS has previously been used to study channel hydraulics in a wide variety of studies (e.g., Afshari *et al.*, 2018; Shustikova *et al.*, 2019; Yalcin, 2020); further details on the numerical scheme are available in Brunner (2002, 2018).

4.3.6.1 Model configuration and calibration

A heterogenous 2D computational mesh of the Swindale Beck reach was generated, using a cell size of 5 x 5 m. HEC-RAS implements a sub-grid bathymetry approach that allows for implementation of a coarse grid on fine topographic surfaces, which saves on model computation time. To simulate fine-scale flow velocity commensurate to the resolution of measurements from the aDcp and image velocimetry, the spatial resolution of the computational reach was refined to 0.5 x 0.5 m between the channel banks by enforcing a break-line running along the thalweg.

A discharge hydrograph from the United Utilities gauging station was used as the inflow boundary condition, with flow scaled (by a factor of 0.9) to the catchment size, since the actual gauging station was located 650 m downstream from the upstream boundary. An energy slope gradient, equivalent to the normal depth, was estimated by computing the bed slope along the terrain profile. The energy slope value was used as the outflow boundary condition, situated downstream of the computational mesh. To avoid errors arising from downstream backwater effects and upstream velocity distributions, the boundaries were located appropriately downstream from the domain of interest.

The 2D model was calibrated at sub-reach SW1 for both the aDcp model (hereinafter referred to as model M_{aDcp}) and the LSPIV model (hereinafter referred to as model M_{LSPIV}) by adjusting a spatially discretized manning's roughness coefficient *n* and eddy viscosity coefficients until model simulations closely matched observed (aDcp and LSPIV) velocities (Figure 4.6). Model simulations were calibrated by varying a spatially discretized Manning's roughness coefficient, *n*, whilst keeping the *n* of the overbank zones constant at 0.035. We further calibrated the models using the eddy viscosity terms by turning on HEC-RAS's turbulence mixing coefficients. Since eddy viscosity in HEC-RAS's numerical scheme is computed as the sum of the Longitudinal Mixing Coefficient D_L, the Transverse Mixing Coefficient D_T and the dimensionless Smagorinsky Coefficient C_s, these mixing parameters were calibrated to the spatially distributed aDcp (model M_{aDcp}) and LSPIV velocities (model M_{LSPIV}). The conservative turbulence model formulation, which ensures little to no momentum loss, was utilized., Variable-time step control using the Courant-Friedrichs-Lewy condition was used to ensure model stability and better model velocity distributions.

4.3.6.2 Calibration/Validation Performance Assessment

LSPIV and aDcp observed velocities were compared to the model simulation runs, with the aDcp calibrated model (model M_{aDcp}) serving as an initial benchmark of minimum validation performance indicators. Whilst there are no set standards for 2D model performance assessment, Pasternack (2011) proposed a rigorous suite of metrics, which can be used to assess 2D model validation performance. Complemented with some of the hydrological validation metrics presented by Moriasi *et al*. (2007) and Biondi *et al*. (2012), most of the uncertainty in 2D shallow-water models can be quantified. Thus the assessment metrics used were: (i) regression analysis evaluating the slope of the regression line between observed versus predicted velocities, the y-intercept, regression slope standard error, regression intercept standard error and the coefficient of determination, R^2 ; (ii) hydrological performance metrics; Nash-Sutcliffe efficiency (NSE), percent bias (PBIAS) and ratio of the root mean square error to the standard deviation of observations (RSR); (iii) error statistics; Mean Absolute Error (MAE), Root Mean Square Error (RMSE), Standard Deviation of Error (SDE) and the Mean Absolute Percentage Error (MAPE).

4.4 Results

The results are presented as follows: First, we report the 2D model calibration results at sub-reach SW1 using a subset of aDcp data, which formed the benchmark for field velocity observations (model M_{aDcp}) (section 4.4.1). Results of a separate model similarly calibrated at SW1 using LSPIV surface velocity data (model M_{LSPIV}) are then presented (section 4.4.1). This is followed by results from the validation model M_{aDcp} using aDcp data at sub-reach SW2 (section 4.4.2.1). Results of the validation performance of model M_{LSPIV} using LSPIV surface velocities, depth-averaged using a spatially constant theoretical coefficient (referred to as $LSPIV_{\alpha}$) are then presented (section 4.4.2.2). Further detailed results of the validation of model M_{LSPIV} velocity simulations are reported, based on a sub-set of LSPIV surface velocities within a 1 m distance of three field cross-sections, all depth-averaged using the Probability Concept (hereinafter referred to as $\mathrm{LSPIV_{PC}}$) (section 4.4.2.3).

4.4.1 2D Model Calibration

A sensitivity analysis of the appropriate bed roughness, based on previous modelling studies using HEC-RAS (e.g., Shustikova *et al.*,2019), set starting *n* values in the range of 0.025 to 0.033 and was adjusted by 0.002 increments to a final value of 0.030 (model $\mathrm{M_{aDcp}}$) and 0.032 (model $\mathrm{M_{LSPIV}}$). Eddy viscosity is computed as the sum of the longitudinal (D_L), transverse (D_T) and Smagorinsky coefficients (dimensionless, C_s) in the HEC-RAS numerical modelling scheme. Figure 4.6 shows the calibrated model velocity predictions for sub-reach SW1 using the aDcp and LSPIV datasets. Simultaneously adjusting the turbulence mixing and dispersion parameters yielded final values of $D_L = 1$, $D_T = 0.3$ and $C_s = 0.05$ for model $\mathrm{M_{aDcp}}$ and; $D_L = 1.4$, $D_T = 0.26$ and $C_s = 0.03$ for model $\mathrm{M_{LSPIV}}$ with both parameterisations yielding the lowest errors in the distribution of modelled velocities. In scenarios characterized by non-turbulent flow, such as during normal discharge rather than flood events, the influence of turbulence mixing coefficients on calibration outcomes remained modest. This observation aligns with the nature of non-turbulent flow conditions. The Mannings n roughness coefficients exhibited a more substantial impact on the calibration process as opposed to the turbulence mixing and dispersion parameters. The limited effect of turbulence mixing coefficients could be attributed to the absence of turbulent flow, emphasizing the heightened significance of Mannings n modifications in characterizing hydraulic behaviour during regular discharge conditions which were observed during this survey. Computational grid sizes were discretized for the channel and floodplain, with a refined grid size of 0.5 m in-channel and 5 m for the rest of the floodplain yielding optimum model performance.

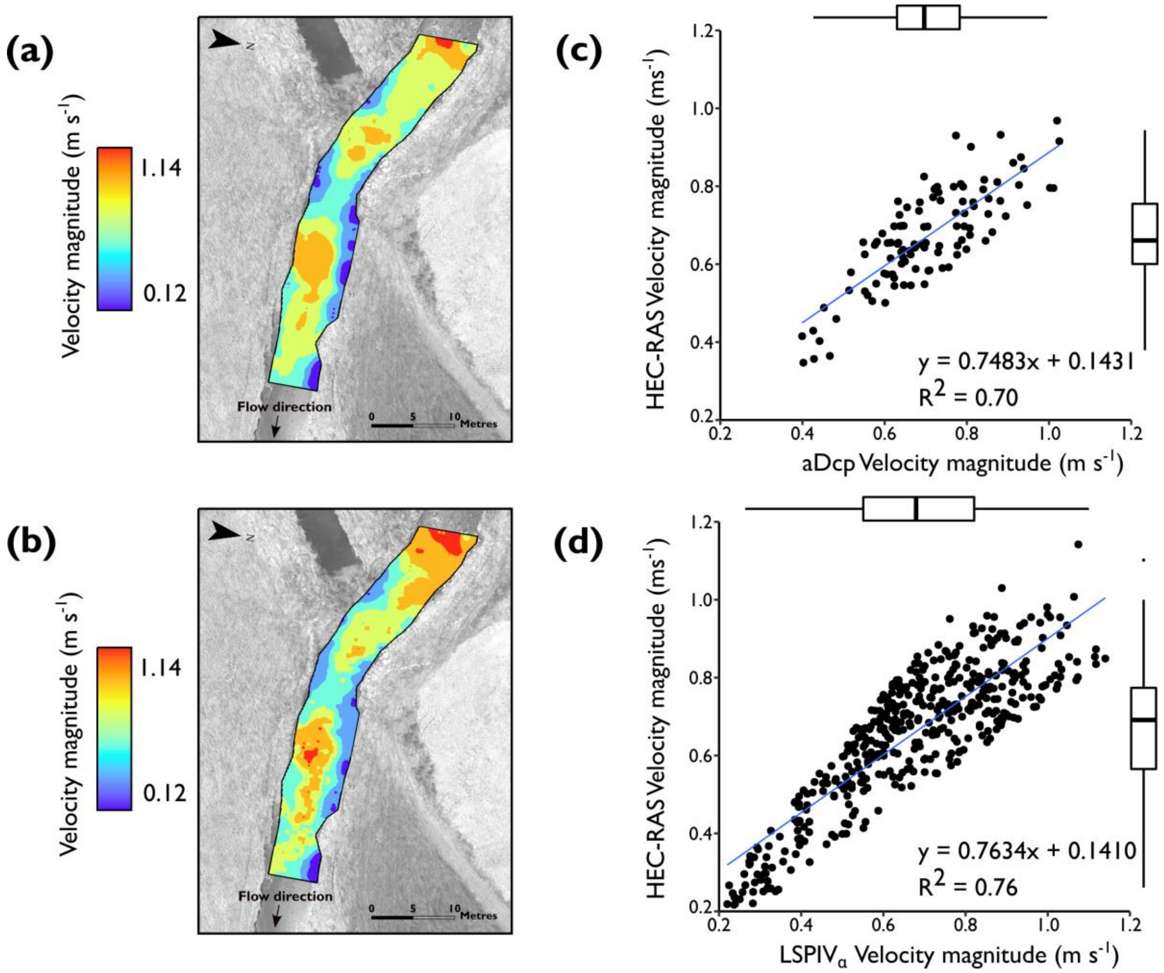

Figure 4.6 Calibration results of 2D model simulations at sub-reach SW1. Model MaDcp (a) and model MLSPIV (b) velocity predictions. Scatter plots of aDcp (c) and LSPIV$_\alpha$ (d) velocity observations versus model predictions. (In the box plots, the boundary of the box closest to zero indicates the 25th percentile, the black line within the box marks the median, and the boundary of the box farthest from zero indicates the 75th percentile. Points above or below the plots indicate outliers outside the 10th and 90th percentiles).

Table 4.6 shows the error analysis results from the calibrated models. Higher precision of all benchmarks was observed when the river's flow was seeded versus when left unseeded. These results are corroborated by other studies, such Pearce *et al*. (2020), Dal Sasso *et al*. (2021) and Liu *et al*. (2021) who showed that the LSPIV algorithm performs better when tracers (which are important for mapping flow fields between image frames), whether natural or artificial, are abundant on the water surface. Because of the drastic drop in most assessment benchmarks when using the unseeded flow scenario to calibrate the 2D hydraulic model (most notably bias (13.2%), and R^2 (37.5%)) we used only the seeded runs for model calibration. The uncertainty associated with insufficient seeding is discussed (section 4.5.2.1).

Table 4.6 2D model calibration/validation metrics for Models M_{aDcp} and M_{LSPIV}

	Model M_{aDcp}		Model M_{LSPIV}		
	Calibration (aDcp)	Validation (aDcp)	Seeded Calibration ($LSPIV_\alpha$)	Unseeded Calibration ($LSPIV_\alpha$)	Seeded Validation ($LSPIV_\alpha$)
R^2	0.70	0.70	0.76	0.52	0.75
NSE	0.65	0.67	0.75	0.23	0.76
PBIAS	-4.76%	0.13%	-2.48%	10.71%	0.02%
MAE, m s^{-1}	0.07	0.06	0.09	0.13	0.09
RSR	0.59	0.58	0.49	0.87	0.50
Trendline Slope	0.74	0.85	0.76	0.82	0.75
Regression Slope Standard Error	0.0463	0.0401	0.0204	0.0395	0.0199
Regression Intercept Standard Error	0.0332	0.0189	0.0143	0.0208	0.0137
n	112	196	445	410	461

Note. R^2 = coefficient of determination; NSE = Nash-Sutcliffe efficiency; PBIAS = percent bias; RMSE = root mean square error; MAE = Mean absolute error, SD = standard deviation; RSR = ratio of the root mean square error to the standard deviation of observed data; *n* = number of observations

4.4.2 2D Model Validation

4.4.2.1 aDcp Model Validation

aDcp data were used to validate the 2D model at sub-reach SW2 (Figure 4.7) and set a benchmark for comparison with model M_{LSPIV} which was fully calibrated and validated using LSPIV velocity fields. Results from the aDcp model validation are detailed in Table 4.6, with a final R^2 of 0.70 and slope of 0.85. Similar studies (e.g., Gard., 2008; Lane *et al.*, 1999; Pasternack *et al.*, 2006) have reported R^2 of predicted versus modelled velocity values ranging from 0.4 to 0.99 with slopes between 0.6 and 1. The results from this study were in the upper range of published results. The hydrological performance indicator NSE yielded an acceptable value at 0.67 with a PBIAS of 0.13%. This shows the 2D model tended towards an overestimation bias, with high velocity values being underpredicted whilst low values were overpredicted, similar to the findings of Barker *et al.* (2018).

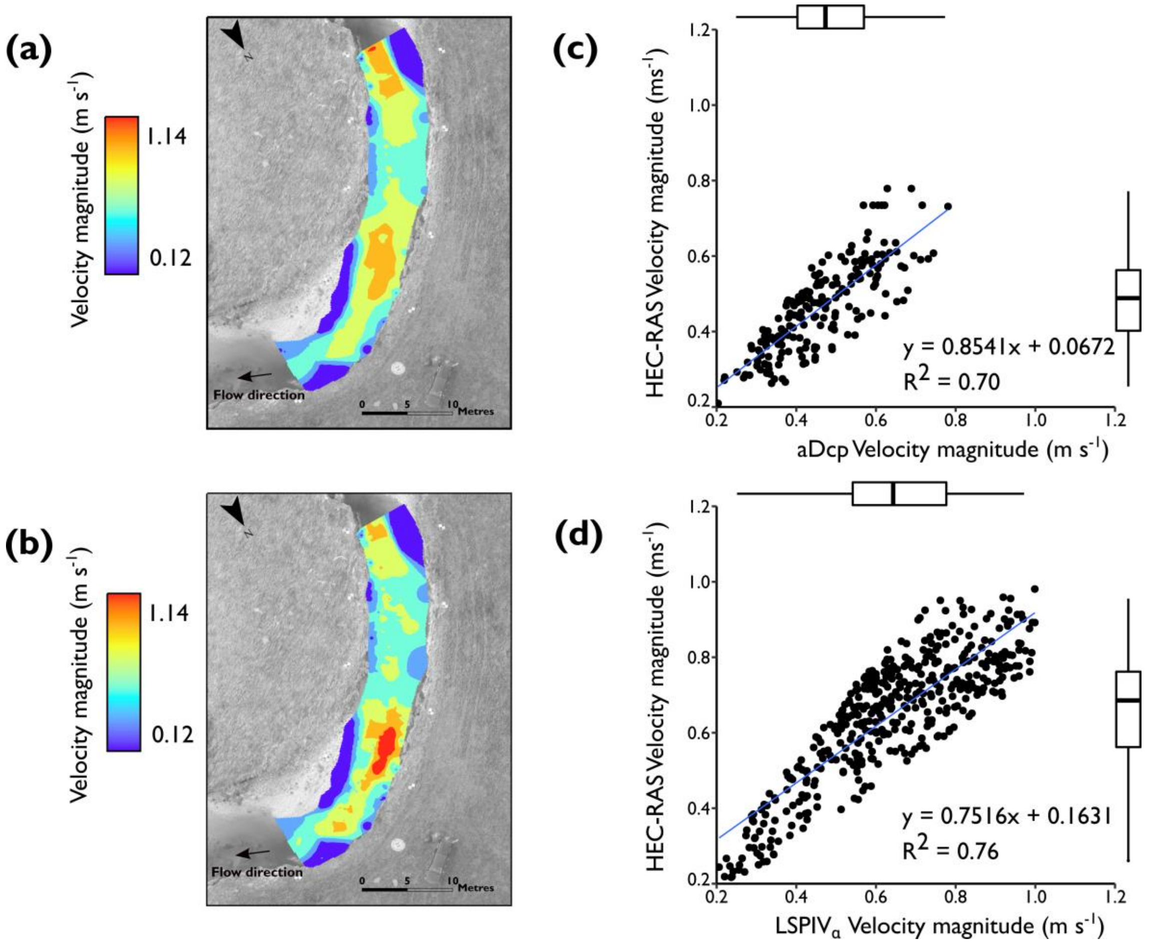

Figure 4.7 Validation results of 2D model simulations at sub-reach SW2. Model M_{aDcp} (a) and model M_{LSPIV} (b) velocity predictions. Scatter plots of aDcp (c) and LSPIV$_{\alpha}$ (d) velocity observations versus model predictions.

4.4.2.2 LSPIV$_{\alpha}$ Model Validation

Model M_{LSPIV} (calibrated using LSPIV data) was validated against all the performance metrics used to evaluate the validation performance of model M_{aDcp}. A surface velocity index (α) of 0.89 (derived using the method described in section 4.3.5.1) was used to depth average the LSPIV velocities at SW2, further optimising the validation results. Referencing the standard error of the regression slope, Model M_{LSPIV} had a validation error magnitudes half that of Model M_{aDcp}. A PBIAS value of 0.02% indicated a slight model overestimation bias, which is consistent with the findings of Liu *et al*. (2021) and can also be attributed to the use of a singular coefficient (α) to transform surface velocities to depth-averaged velocities.

Overall, there was a strong correlation between modelled velocities and LSPIV$_{\alpha}$ velocities with a R^2 value of 0.75 and slope of 0.75. These high correlation values can be attributed to not only the quality of the model, but also the abundance of LSPIV observations which enabled the full statistical structure of the correlation to be revealed, as opposed to having fewer validation points which would tend to be biased to low or intermediate velocities.

4.4.2.3 LSPIV$_{PC}$ Model Validation

Different from the initial validation of the model M$_{LSPIV}$, which relied on a theoretical constant (α) to translate LSPIV surface velocities to depth averaged velocities, a probability-based cross-sectional validation of the model was carried out using the Probability Concept to further understand LSPIV's performance (referred to as LSPIV$_{PC}$) in 2D model validation. Three cross-sections (Figure 4.4) were collected at sub-reach SW2 using an EM flow meter and vertical velocity profiles sampled at these locations were used to compute φ, following which LSPIV velocity vectors within a 1 m range of the respective cross-sections were extracted for further model validation.

Values of φ, which is constant at any cross-section and used to transform u_{max} to u_{mean}, ranged from 0.539 to 0.571, which is consistent with previously published work (Chiu and Hsu, 2006; Fulton *et al.*, 2020b, 2018; Moramarco *et al.*, 2017) where values ranging from 0.522 to >1 have been reported. Table 4.7 shows the velocity distributions at the *y-axis* for each cross-section of interest, which was established through repeat current-meter wading measurements.

Table 4.7 Probability-Concept-derived metrics and velocities measured using a Valeport electromagnetic current meter at three cross-sections along the Swindale Beck (*M* = dimensionless parameter characterizing velocity distribution; φ = a function of *M* equal to the ratio of the mean velocity to the maximum velocity; u_s = surface velocity in m s^{-1}; u_{max} = maximum velocity; *y-axis* = vertical depth in a cross-section that contains the maximum velocity in metres, m).

Cross-section	Probability-Concept Metrics				
	M (dim)	φ (dim)	U_s (m s^{-1})	u_{max} (m s^{-1})	Water depth at *y*-axis (m)
XS-1	0.325	0.571	0.493	0.493	0.14
XS-2	1.169	0.595	0.053	0.053	0.29
XS-3	0.478	0.539	0.041	0.041	0.35

Goodness-of-fit statistics (Table 4.8) showed the model was validated with correlations outperforming the LSPIV$_{\alpha}$ validation results for all but one cross-section (XS-1), which was located slightly downstream of a riffle bend making it susceptible to well documented turbulence-closure uncertainties at such points (Barker *et al.*, 2018). R^2 correlation values ranged from 0.73 – 0.81 (Figure 4.8a), despite the reduction in data points used to evaluate 2D model performance, indicating that φ represented an appropriate velocity distribution unique to each profile. PBIAS values revealed a bias in which higher velocity values were underestimated by LSPIV$_{PC}$ and lower values overestimated, similar to the findings of Pasternack *et al*. (2006), indicating the 2D model less accurately reproduced the highest and lowest flows in the channel.

Table 4.8 Velocity magnitude validation metrics comparing LSPIV$_{PC}$ velocities versus HEC-RAS (modelled) velocities.

Cross-section	**LSPIV$_{PC}$ Validation Metrics**					
	R^2	**NSE**	**PBIAS**	**Trendline Slope**	**RS. Standard Error**	**RI. Standard Error**
XS-1	0.73	0.67	6.42%	0.91	0.1471	0.0423
XS-2	0.81	0.81	0.91%	0.73	0.0843	0.0310
XS-3	0.78	0.68	3.74%	1.04	0.0656	0.0206

Velocity magnitude correlations between modelled and observed (LSPIV$_{PC}$) velocities closely tied to 1:1 linearity with regression slopes ranging from 0.73 – 1.04 (Table 4.8) following conditioning of the regression slope at each section using φ, these results are well within peer-reviewed studies of 2D model validation (Barker *et al*., 2018; Pasternack *et al*., 2006). Comprehensive scatterplot analysis when validating a 2D model using velocity magnitude should also include results of zero intercept values, which were suggested by Pasternack *et al*. (2006) to be < 5% of maximum velocity. All regression zero intercept values were well below this threshold.

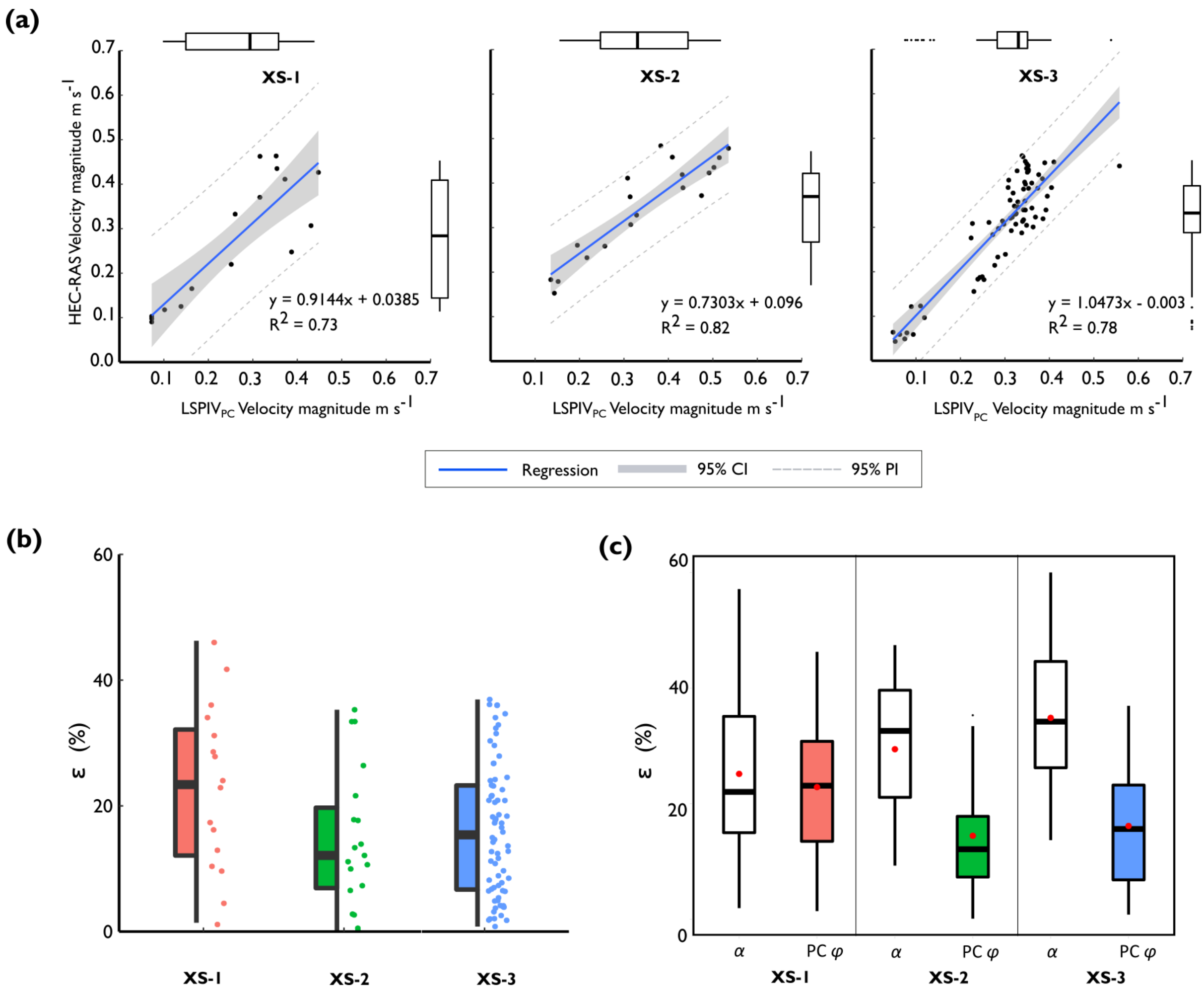

Figure 4.8 Scatter plots of LSPIV_{PC} vs HEC-RAS velocity magnitudes with linear regression fits, 95% confidence (CI) and prediction (PI) intervals; (b) Variation in absolute LSPIV_{PC} velocity error (ε) as compared to modelled velocities across the six cross-sections. Individual velocity error observations are represented by the coloured dots. Horizontal line in the boxplot indicates the median, box shows the interquartile range (IQR), and the whiskers are 1.5*IQR; (c) Absolute percentage errors (*ε*) in estimating depth-averaged velocity using the standard velocity index (α, white) and the Probability Concept approach (PC, *φ*) at cross-sections XS1 – 3 (red dot indicates mean error).

Mean absolute LSPIV_{PC} velocity magnitude error (as compared to calibrated model results) across all cross-sections was less than the 15-30% benchmark suggested by Pasternack, (2011), with the highest value being 24.35%, while the highest median error was 24.01% (Figure 4.8b). The negative mean velocity differences, following depth averaging using *φ* at each cross-section, can all be explained by the fact that most velocity values were quite low (<0.5 m s^{-1}) yet the model typically overpredicted low velocities. Percent rank analysis of all deviations revealed that 98% of the velocity values had error less than 50%, with outliers falling within a maximum error bin of 75%. Further, mean errors from using LSPIV_{PC}

velocities for model validation reduced by 7.7% as compared to depth averaging using a single constant (α) (Figure 4.8c).

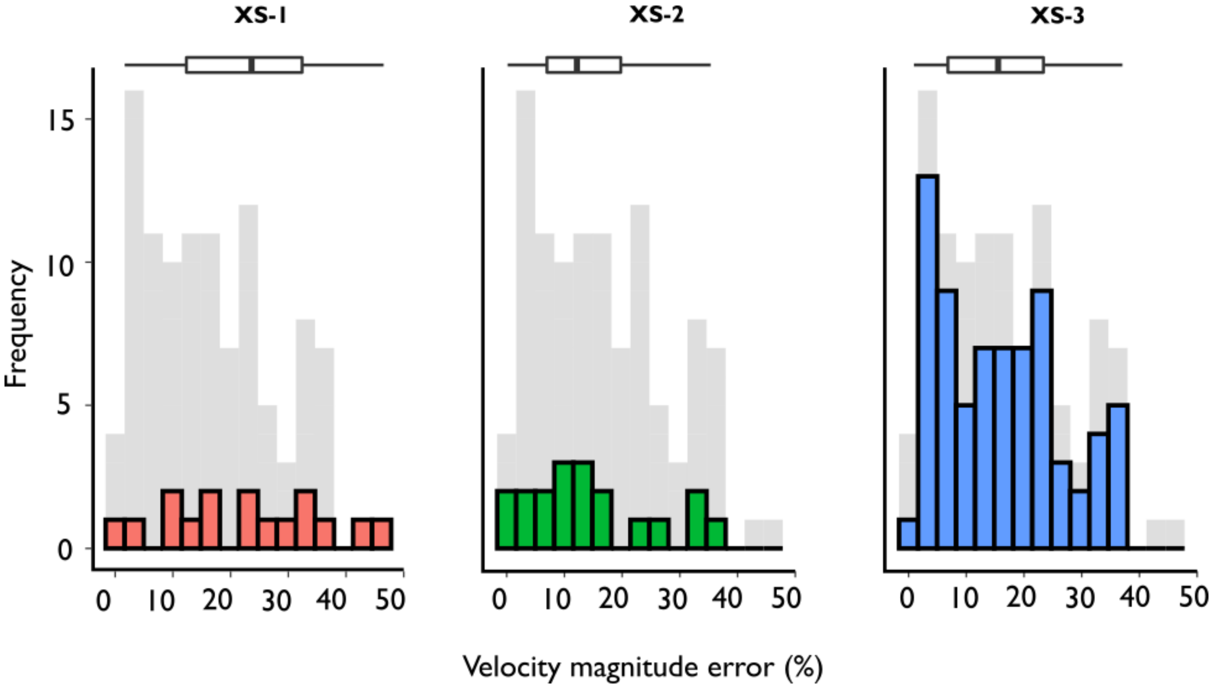

Figure 4.9 Velocity magnitude error histograms for all LSPIV$_{PC}$ cross-sections (relative to model M$_{LSPIV}$ predictions) with overall error in the background (grey).

The histogram analysis of error distributions (Figure 4.9) revealed that 98.2% of the data from LSPIV$_{PC}$ cross sectional validation had an error of 50% or less. The mean absolute velocity error across all sections was 16.86% with error peaks observed at XS-3 where 94.4% of the data had errors of 35% or less.

4.5 Discussion

4.5.1 Advanced sampling of spatial velocity distributions

The calibration and validation of a 2D model using both conventional aDcp and LSPIV velocities was demonstrated, with the performance of the model fully calibrated/validated using LSPIV data being on par with results reported in peer-reviewed literature (Table 4.6, 4.8). With both approaches yielding valid performance, discussion focuses on the additional novelties introduced by using LSPIV surface velocity datasets combined with the Probability Concept (PC) for derivation of a velocity depth-averaging index (φ).

Although field measurements of velocity using aDcps can be achieved for depths >80 m (e.g., Sontek's M9), the impracticality of deploying them in very fast and deep waters precludes their ability to sample very high velocity events. Further, aDcps cannot be operated in very shallow rivers due to the instrument's blanking distance. In contrast, the capability of LSPIV to sample a boarder range of velocities allowed for the collection of previously unattainable velocity data. Statistical analyses of the results revealed the first key novelty of this study, which was the remarkable improvement in model validation performance when using (seeded) LSPIV to parametrise a 2D model instead of aDcp data. Plotting $\mathrm{LSPIV_{PC}}$ velocities against model results yielded coefficient of determination values (R^2) of between 0.73 and 0.81, which was up to 10% better when compared to the model fully parametrised using aDcp data ($\mathrm{M_{aDcp}}$), and among the highest values reported in peer-reviewed literature for direct velocity magnitude validation of 2D models (e.g., Barker *et al.*, 2018; Fischer *et al.*, 2015; Gard, 2008). A statistical explanation offers insight into this high performance; with the ability of LSPIV to sample and obtain a wide range and distribution of velocities (as compared to the aDcp), a better characterization of the spatial patterns of velocity was available for analysis. In addition, the number of LSPIV observations, which was several orders of magnitude higher than that of the aDcp at both sub-reaches, helped reveal the full statistical structure of the correlations as opposed to having fewer observations which would tend to be biased to either low or intermediate velocities. As suggested by Pasternack (2011), an appropriate benchmark for determining whether a model has been validated, based on velocity simulations, should be centred on the magnitude of measurements observed as the greater the number of observations, the better the spread of velocity distributions and the resultant R^2 correlations.

Departing from the well-established method of using selected cross-sections to validate 2D models, we successfully validated model performance across a wider range of velocities spanning varying morphological structures, which are typically left out in velocity validation studies. The LSPIV surface velocity measurements were generally in very good agreement with the model simulations which can partly be attributed to the rather shallow depth and high gradient of the gravel bed channel. Given these hydraulic settings, the accuracy of LSPIV velocities tended to be higher than the aDcp's, which depends on extrapolation of the top and bottom subsections of the channel to compute velocities. Similar to an earlier study by Baird *et al.* (2021), the 2D model overpredicted high velocities and underpredicted low velocities in both modelling scenarios, underlining the added benefit of LSPIV that sampled a significantly wider range of velocity bins for a robust analysis of the 2D model's performance. The spatially dense coverage of LSPIV not only captured the diversity and transitions of low-flow velocity fields but presented the possibility for mapping surface velocities in high flow, steep channel sections where bankfull flow conditions could typically have ruled out model validation using aDcp observations due to physical inaccessibility (e.g. Abu-Aly *et al.*, 2014; Sawyer *et al.*, 2010).

4.5.2 Uncertainty

4.5.2.1 Uncertainty of LSPIV surface velocity measurements

The accuracy of image velocimetry techniques in field conditions is heavily influenced by the ability to identify and track surface features, which are central in the computation of surface velocity (Dal Sasso *et al.*, 2021b; Pizarro *et al.*, 2020a; Tauro *et al.*, 2017). Recent studies by Pizarro *et al.*, 2020b) introduced a tracer seeding metric known as the seeding distribution index (SDI) in an attempt to identify the optimal spatial distribution of tracers. However, the errors computed using all the image frames from their study were not different from the optimal window suggested by the SDI. Therefore, the experimental settings adopted in this study focused on the overall performance of natural/unseeded velocity estimates versus seeded estimates in assessing spatial velocity outputs from the 2D model.

Field experiments using artificial seed tracers had better model calibration performance across all assessment metrics when compared to unseeded scenarios (Table 4.6). The coefficient of determination (R^2) dropped by 37.5% when the flow was left unseeded. This reduction in collinearity between simulated (model) and observed (LSPIV) data for the unseeded scenarios was unsurprising as the magnitude and spatial distribution of the *u* and *v* components of velocity magnitude tended to dramatically decline. The NSE results further underlined the strong influence of seeding on the reliability of LSPIV results, with differences of up to 50% in the residual variance in velocity compared to the measured variance. These results are consistent with the findings of Pearce *et al.* (2020) who observed a high sensitivity of LSPIV to seeding density when assessing aDcp velocities. Although the reliability of LSPIV results diminishes dramatically under unseeded conditions, Naves *et al.* (2021) demonstrated that the presence of bubbles caused by raindrops could positively influence cross-correlation algorithms. This implies future scope for the application of these methods during flooding events, which are typically accompanied by heavy rainstorms.

4.5.2.2 Variability in velocity coefficient, α

The accurate derivation of a velocity coefficient, α, which represents the ratio of surface velocity to depth-averaged velocity remains a key source of uncertainty in the use of non-contact methods to compute mean channel velocities (Dal Sasso *et al.*, 2021a). Dramais *et al.* (2011) identified the variability of α as the dominant source of error when using LSPIV to compute velocity estimates, recommending the derivation of site-specific α values. To the best of our knowledge, previously published studies have generally utilised the standard value of α (0.85), assuming a logarithmic vertical velocity distribution (e.g., Le Coz *et al.*, 2010, Lewis *et al.*, 2018), or derivation of a power-law exponent (e.g., Johnson and Cowen,

2017) when translating surface velocities to depth-averaged velocities. The variability of φ in gravel bed rivers has been reported to be larger (Lee and Julien, 2006) further suggesting the requirement for locally calibrated α values. Moreover, α values derived assuming a monotonous velocity distribution fail to account for the 'dip phenomenon', where maximum flow velocity, u_{max} occurs below the water surface resulting in $\alpha > 1$.

Using Chiu's PC (Chiu, 1987), which is based on Shannon's Information Entropy (Shannon, 1948), we successfully computed α at three cross-sections within the study sub-reaches. The entropy method showed marked variability in α across XS1-3 (Table 4.7), with analysis showing that our results were on the lower end of published values (0.539 – 0.658). Whilst the use of cross section specific α in depth averaging LSPIV values had no impact the coefficient of determination (R^2) tests, there was a notable trend in the improvement of other validation metrics such as the best-fit trendline slope (i.e., slope tending towards 1) and the values of regression slope standard error and regression intercept standard error all improving substantially.

Results from our study propose that the use of default values of α is insufficient in gravel bed rivers, likely due to the influence of bed roughness, as suggested by Hauet *et al.* (2018). We suggest that probabilistically derived values of α yield better estimates of depth-averaged LSPIV velocity with the ability to account for the dip-phenomenon. As highlighted in Table 4.7, where surface velocities align with maximum velocities, the utilization of φ continued to demonstrate superior performance. This is attributed to φ's inherent flexibility in accommodating variations in vertical velocity profiles and spatial distributions, even in scenarios where the surface velocities mirror the maximum velocities. The effectiveness of φ in these instances stems from its capacity to capture subtle variations in velocity profiles throughout the water column. Unlike the α coefficient, which relies on a simplified approach, φ, informed by a probability concept, provides a more nuanced and accurate representation of depth-averaged velocities. This adaptability allows φ to address the intricacies of real-world velocity distributions, showcasing its utility beyond scenarios where surface velocities diverge from maximum velocities. This observation underscores the broader applicability of φ in enhancing the accuracy of depth-averaging techniques, offering valuable insights into the spatial and vertical variations of velocities within natural environments.

Overall, we find that the use of locally derived α using Chiu's (Chiu, 1987) probability function more accurately constrains velocity bias at all cross-sections (Table 4.8) with average errors of 27.73% (Probability Concept, φ) and 18.90% (α) indicating a 37.9% improvement in velocity predictions. These findings are expected and corroborated by other studies such as Moramarco *et al*. (2017). The median error did not exceed 24% and 34% for the Probability Concept and velocity index methods respectively with the 95th percentile of errors at every cross-section being lower when assuming a non-logarithmic velocity distribution. Our field experiments show that using alternative velocity distribution approaches provides better fits of depth-averaged velocity profiles than reliance on theoretical *a priori* indices commonly used in several studies. Further research is necessary to ascertain the variability of φ with different discharges as well as its dependence on cross-sectional distancing.

4.6 Conclusion

This investigation has shown that a 2D hydraulic model can be accurately calibrated and validated using image velocimetry data, yielding results comparable to traditional aDcp approaches. Further, we established that the uncertainty commonly associated with depth-averaging surface flows in standard LSPIV workflows can be significantly reduced using numerical methods, based on the channel's hydraulic parameters (φ, y-axis, u_{max}) rather than relying on the often-used constants or indices based on an assumption of logarithmic velocity distributions in channels. The use of probabilistically derived φ for surface velocity averaging resulted in error reductions of up to 7.7% when validating a hydraulic model; however, the Probability Concept approach does require in-channel cross-section measurements to obtain y-axis (profile with maximum velocity) data. To the authors' knowledge, the joint deployment of LSPIV with the Probability Concept for estimation of depth-averaged channel velocities in assessing simulated flows in a natural gravel bed river has not been demonstrated previously. This study allowed two other significant conclusions to be reached. First, whilst image velocimetry and aDcp yielded comparable model performance, the greater size of the LSPIV dataset, which spanned a wider range of flows and depths, allowed for the full statistical structure of field measurements to be revealed. However, the limitations of LSPIV-derived surface velocity fields were clear in conditions where there is sparse seeding on water surfaces or in poorly illuminated conditions. Whilst this assessment is not a direct comparison between LSPIV and aDcp observations, it demonstrates the capabilities of LSPIV in deriving meaningful data that can be used to calibrate and validate 2D models. Second, and more broadly, the use of high-quality datasets to validate model performance is key for the reduction in uncertainty in model predictions. The overall reduction in error distributions and low bias during model validation demonstrates that LSPIV, coupled with the Probability Concept, is a fit for purpose tool in evaluating reach-scale hydraulic model predictions.

Chapter 5 - Satellite video remote sensing for flood model validation

The following chapter is a reformatted version of a manuscript published in *Water Resources Research* by Christopher Masafu & Richard Williams, available at: https://doi.org/10.1029/2023WR034545

Key Points

- Satellite video derived flood extents and velocities successfully validate 2D hydraulic model predictions.
- Test-time augmentation during deep learning inference improved flood extent delineation and enhanced 2D model validation metrics.
- Incorporating characterization of discharge uncertainty into hydraulic model predictions resulted in more accurate model validation.

Abstract

Satellite-based optical video sensors are poised as the next frontier in remote sensing. Satellite video offers the unique advantage of capturing the transient dynamics of floods with the potential to supply hitherto unavailable data for the assessment of hydraulic models. A prerequisite for the successful application of hydraulic models is their proper calibration and validation. In this investigation, we validate 2D flood model predictions using satellite video-derived flood extents and velocities. Hydraulic simulations of a flood event with a 5-year return period (discharge of 722 m^3 s^{-1}) were conducted using HEC-RAS 2D in the Darling River at Tilpa, Australia. To extract flood extents from satellite video of the studied flood event, we use a hybrid transformer-encoder convolutional neural network (CNN)-decoder deep neural network. We evaluate the influence of test-time augmentation (TTA) – the application of transformations on test satellite video image ensembles, during deep neural network inference. We employ Large Scale Particle Image Velocimetry (LSPIV) for non-contact-based river surface velocity estimation from sequential satellite video frames. When validating hydraulic model simulations using deep neural network segmented flood extents, critical success index peaked at 94% and on average improved by 9.5% when TTA was implemented. We show that TTA offers significant value in deep neural network-based image segmentation, compensating for aleatoric uncertainties. The correlations between model predictions and LSPIV velocities were reasonable and averaged 0.78. Overall, our investigation demonstrates the potential of optical space-based video sensors for validating flood models and studying flood dynamics.

5.1 Introduction

Satellite video presents a significant advance in remote sensing. This novel technology enables the acquisition of high-definition video from space (Xiao *et al.*, 2018), offering the potential for novel hydrological applications and providing unique insights into flood dynamics, flow pattern, and disaster management and recovery. As more of the world's population faces exposure to floods (Rentschler and Salhab, 2020; Tellman *et al.*, 2021) there is an ongoing need to assess how fine-scale earth observation data, such as satellite video, can be used to improve the calibration and validation of two-dimensional flood inundation models. There are, however, inherent tradeoffs between the challenge of acquiring stable video from a non-geostationary platform in sun-synchronous orbit, the duration and pixel size of satellite videos, and the integration and ingestion of satellite video derived data products into existing hydrological modelling frameworks (Ghamisi *et al.*, 2018; McCabe *et al.*, 2017b; Shu *et al.*, 2021). To harness the value of these big data, deep learning, a facet of artificial intelligence (AI), offers potential to handle the volumes of data associated with satellite video and to automatically learn and extract flood extent patterns in this data, opening up a plethora of opportunities to progress research in water sciences (Shen, 2018; Sit *et al.*, 2020; Z. Sun *et al.*, 2022). Although traditional machine learning techniques have been widely used to delineate flood extents in traditional satellite imagery (Qi *et al.*, 2020; Su *et al.*, 2020), satellite video scenes present unique challenges in the form of limited annotated data and complexity of both spatial and temporal information, which calls for advanced architectures suited for understanding the complex spatial and temporal relationships present in dynamic video scenes. Further developments in optical flow monitoring techniques, a facet of computer vision, are enabling the analysis of the motion of objects within a sequence of images or video frames. Specifically, non-intrusive optical flow-based techniques for estimation of velocities in rivers have been demonstrated as viable tool for acquiring spatially distributed flow velocity information in natural environments (Pearce *et al.*, 2020a; Perks *et al.*, 2019). Estimating surface river velocities from satellite-based video is a promising domain for flood science, although issues around the low temporal resolution of satellite video, image pre-processing and satellite platform drift demand further investigation.

Two dimensional hydraulic models are an integral tool for understanding flood dynamics. Outputs from these models are actively used for flood risk management (Tsakiris, 2014), infrastructure design (Shrestha *et al.*, 2022), disaster preparedness (Nkwunonwo *et al.*, 2020) as well as in modeling the future of flooding under different climate change scenarios

(Mishra *et al*., 2018), thus aiding in the design of long-term adaptation strategies. Inundation modeling using hydraulic models serves as the principal tool for understanding the intensity of riverine flood hazards. Despite their extensive applicability, two dimensional hydraulic models have rarely undergone rigorous validation against observed data to assess the skill of their predictions (Pasternack, 2011; Wing *et al*., 2021). In general, 2D modelling studies often use minimal data to assess model accuracy, meaning that models typically target the most basic performance benchmarks, and in many cases, models have simply not been validated (Molinari *et al*., 2019). Indeed, many regions around the world lack comprehensive and high-quality data of commensurate coverage that can be used to validate these models (Rollason *et al*., 2018). A handful of studies that exemplify the validation of 2D models include those by Bernhofen *et al*. (2018), Eilander *et al*. (2023) and Wing *et al*. (2017). These studies utilized satellite-derived flood extents to validate global flood models, which offer a macro-level understanding of flood risk and do not capture the fine-scale intricacies of local flood dynamics. Even fewer studies report the validation of two-dimensional hydraulic model simulations using velocities, such as Barker *et al*. (2018), Fischer *et al*. (2015) and Williams *et al*. (2013) who relied upon traditional point-velocity measurements for assessing model skill. In fact, whilst some two-dimensional models might accurately replicate flood extents, substantial deviations of simulated velocity might be observed when compared to field observations (Li *et al*., 2022). Further, there is wide recognition that both two-dimensional models and observations come with their own set of uncertainties such as those linked to extreme discharge measurements, terrain data accuracy and observation field data errors which can introduce discrepancies when validating models (Grimaldi *et al*., 2016a; Schumann, 2017). A systematic investigation of the role of alternative spatially distributed datasets for validating 2D flood models is pertinent.

Remote sensing for flood inundation studies relies on two categories of sensors for monitoring surface water dynamics - microwave and optical sensors (Dasgupta *et al*., 2018; Grimaldi *et al*., 2020). Flood water pixel identification from optical satellite imagery has conventionally largely relied on spectral water indices (e.g. the Normalized Difference Water Index (NDWI) (McFeeters, 1996) and the modified NDWI (Xu, 2006)) as well as supervised and unsupervised classification. These techniques have been known to misclassify (overestimate) water bodies (Khalid *et al*., 2021). Machine learning methods, such as Support Vector Machine (SVM) classifiers and Random Forest (RF) algorithms have also been adopted in several floodplain mapping studies (e.g. Mobley *et al*., 2021, Nandi *et al*., 2017) and have been shown to be complex and slow, thus ineffective for real-time flood hazard mapping (Lee *et al*., 2017). Big data analytics and computer vision techniques (specifically, deep learning) are now paving the way for automated delineation of flood extents with high accuracy (J. Wang *et al*., 2022). Deep convolutional neural networks (CNNs) have revolutionized binary and multi-class image classification and are especially relevant in time-sensitive applications such as flood inundation mapping (Shastry *et al*., 2023). CNNs overcome several key limitations of traditional machine learning in image classification tasks; they are highly scalable and can process large amounts of complex data with little human intervention. CNNs can also leverage on transfer learning; the use of networks pre-trained on extremely large datasets, then fine-tuned for new tasks, enhancing model generalization, and avoiding overfitting (Tan *et al*., 2018). Convolutional neural networks (CNNs) have benefited greatly from the rapid development of large labeled datasets, such as ImageNet, which offer high-quality training images at an unprecedented scale (1.3 million training images, 50,000 validation images and 100,000 test images spanning 1000 classes), allowing generic features learned to be used in complex classifications of presumably disparate datasets (Huh *et al*., 2016; Ridnik *et al*., 2021; Yamashita *et al*., 2018).

Semantic image segmentation using CNN-based networks entails pixel-level identification, classification, and labelling. Applications of deep learning networks for semantic segmentation of floods in remote sensing images have mostly been demonstrated on fully convolutional networks (FCNs) and to a lesser extent, encoder-decoder architectures. Hashemi-Beni and Gebrehiwot (2021) utilized FCN-8s to generate binary classification maps of flood inundated areas. Gebrehiwot *et al.* (2019) applied a CNN-based network (FCN-16s) to extract flooded regions from UAV imagery. Basnyat *et al.* (2021) utilized a modified version of the U-Net architecture for binary segmentation tasks on their flood detection system while Girisha *et al.* (2019) successfully utilized both FCN-32s and U-Net for semantic segmentation of UAV videos within an urban zone.

Transformers, a class of neural network architecture originally built to solve sequence to sequence problems in natural language processing (e.g., the transformer based-chatbot ChatGPT (Generative Pre-trained Transformer) (Liu *et al*., 2023)), have now been adapted as a complement to CNNs for semantic segmentation of remotely sensed imagery attaining state-of-the-art performance (see, for example, Gu *et al*., 2022; Xu *et al*., 2021; Zhang *et al*., 2022). Transformers, unlike CNNs, rely on "self-attention" mechanisms which allows them to extract and use information from arbitrarily large contexts of the input data (e.g., pixels in an image) simultaneously. It enables the network to capture long-range dependencies and consider global context, making it well-suited for understanding complex patterns and relationships within the data. CNNs on the other hand can only exploit local information correctly due to their small convolutional kernel sizes. However, it's worth noting that due to the quadratic complexity of self-attention, Transformers can be computationally more expensive, especially for large images, and do not generalize well when trained on insufficient amounts of data, as compared to CNNs. Consequently, hybrid architectures that combine the strengths of transformers and CNNs to achieve a balance between global context modeling and computational efficiency for semantic segmentation tasks have been proposed (e.g., A. He *et al*., 2023; Q. He *et al*., 2023; Zhou *et al*., 2023). Although the adoption of these architectures is still evolving, their robustness in understanding complex scenes which exhibit large variations within the same class and subtle differences between different classes, such as in video remote sensing, is yet to be explored.

Traditional methods for measurement of instantaneous water flow velocity, including impellor-type current meters, electromagnetic flow meters, acoustic Doppler velocimeters and acoustic Doppler current profilers (aDcp) remain limited during flood conditions due to logistical challenges such as inaccessibility of flooded areas, flow turbulence as well as limitations in instrument measurement ranges. Image velocimetry, a non-contact method used to measure fluid flow velocities by analyzing images of flow patterns, such as those from video, has gained traction as a method of collecting river velocity data (e.g., Dal Sasso *et al*., 2021; Pearce *et al*., 2020). Large Scale Particle Image Velocimetry (LSPIV) is a frequently adopted technique for water-surface velocity analysis and relies on tracking the motion of appropriate artificial or natural 'seeding' particles, such as bubbles or debris, between successive images in a time series. LSPIV based on Unpiloted Aerial Vehicle (UAV) video has been demonstrated in several studies (e.g., C. Chen *et al*., 2021; Lewis *et al*., 2018; W.-C. Liu *et al*., 2021). Legleiter and Kinzel (2021) successfully derived surface river flow velocities from satellite video to within 8.65% of independent radar gage based measurements, building upon the work of Kääb *et al*. (2019) who utilized near-simultaneous satellite still images (acquired with a nominal time lapse of ~90 seconds between each other) to estimate river surface velocities in the Yukon River, Alaska. Depending on the video acquisition frame rate, video sequences of between 8 – 30 seconds are sufficient for image velocimetry over large spatial extents in rapid fashion (Legleiter and Kinzel, 2020; Pearce *et al*., 2020a; Strelnikova *et al*., 2023). The next step in the domain of satellite video-based image velocimetry is the deployment of these velocity estimates in an operationally useful manner – the validation of hydraulic model predictions.

The aim of this investigation is to present the first attempt at validating flood model simulations using satellite video observations. The principal contributions of this work are threefold. First, we leverage on the temporal richness of satellite video to fine-tune a hybrid CNN-Transformer network for semantic segmentation of flood extents. Specifically, we evaluate the accuracy of six variants of a transformer encoder – CNN decoder architecture in segmenting our test video image. Second, we utilize optical flow techniques to analyze the motion of naturally occurring features between consecutive video frames to estimate the velocity of flow in our study reach. Finally, we utilize these flood extents and velocities to validate 2D flood model outputs, explicitly accounting for uncertainty in our 2D modelling. As non-intrusive optical flow measurement and deep-learning based techniques for delineation of flood pixels in near-real time evolve, and further constellations are established, satellite video presents a potential opportunity to exploit a temporally rich data source, capable of providing data to comprehensively validate flood model predictions. Though limited to cloud-free acquisitions, the unmatched temporal resolution of satellite video can compensate for the limitation of optical atmospheric imaging windows.

5.2 Data and methodology

5.2.1 Overview

The investigation consisted of four stages (Figure 5.1). In stage 1, Jilin-1 satellite video-based flood extents are derived using a state-of-the-art deep-learning network. We adopt a hybrid architecture consisting of a transformer-based encoder and a CNN-based decoder, this allows us to integrate the strengths of both transformers and CNNs. Whilst CNNs excel at local feature extraction, transformers are stronger at capturing global context and long-range dependencies. This hybrid approach for semantic segmentation allows us to benefit from the strengths of each architecture. Specifically, we adopt SegFormer (Xie *et al.*, 2021) as the encoder, a lightweight yet efficient and powerful model that has attained state-of-the-art semantic segmentation performance on popular benchmarks like the Cityscapes dataset and ADE20K (Cordts *et al.*, 2015; Zhou *et al.*, 2017). We utilize a U-Net decoder which allows the model to leverage multi-level information, reconstruct spatial details, and efficiently integrate low-level and high-level features to generate accurate and fine-grained segmentation masks. We evaluate the segmentation capabilities of six different variants of the SegFormer encoder, from SegFormer B0 to B5 and narrow down on one model series. We train the selected deep learning model, relying on transfer learning and Test-Time Augmentation (TTA) for improved flooded class prediction accuracy. TTA involves the creation of augmented copies of a test dataset, following which the deep-learning network returns ensemble predictions of class labels which are averaged to produce segmentation maps.

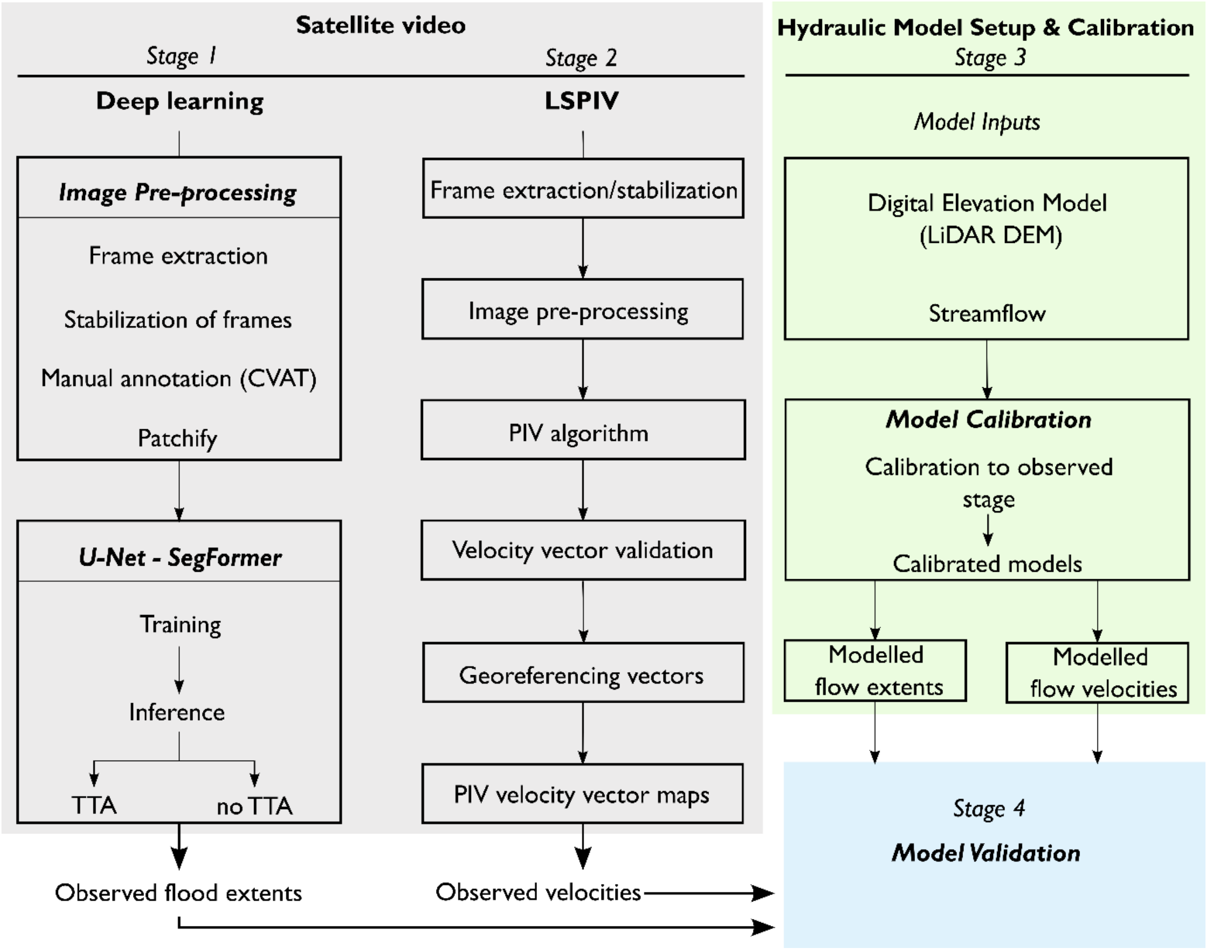

Figure 5.1 Experimental framework.

(*Note.* CVAT = Computer Vision Annotation Tool; LiDAR = Light Detection and Ranging)

In Stage 2, we utilize LSPIV to compute river surface velocity vectors over two cloud-free subsets of our video (Figure 5.2). Stage 3 involves simulation of a recent flood event using a hydraulic model (Hydrologic Engineering Centre - River Analysis System (HEC-RAS) version 6.0) driven by uncertain discharge estimates derived from Bayesian analysis of stage-discharge relations (see section 2.3.2). This HEC-RAS 2D model is calibrated using stage height from the gauge at Tilpa (Figure 5.2). Stage 4 validates the HEC-RAS 2D model predictions using both the deep-learning segmented images from Stage 1, and the velocity vectors estimated in Stage 2.

5.2.2 Study Area

The study area covers a 6.5-km-long section of the middle Darling River at Tilpa floodplain, located in north-western New South Wales (NSW), which is part of the Murray-Darling River basin in south-eastern Australia (Figure 5.2). A gauging station at Tilpa (Station number 425900) records water course discharge every 15 min from 1995 to present, for an upstream catchment area of 502,500 km^2. Extreme multi-day rainfall, caused by a series of deep low-pressure systems, resulted in intense storms and major flooding in eastern New South Wales from 22 February to 9 March 2022. Between 19 January and 11 February 2022, the Darling River at Tilpa was above major flood level (11.5 m), with the flood wave peaking at 12.3 m on 31 January 2022 (Bureau of Meteorology, 2022). The town of Tilpa experienced extensive floodplain inundation.

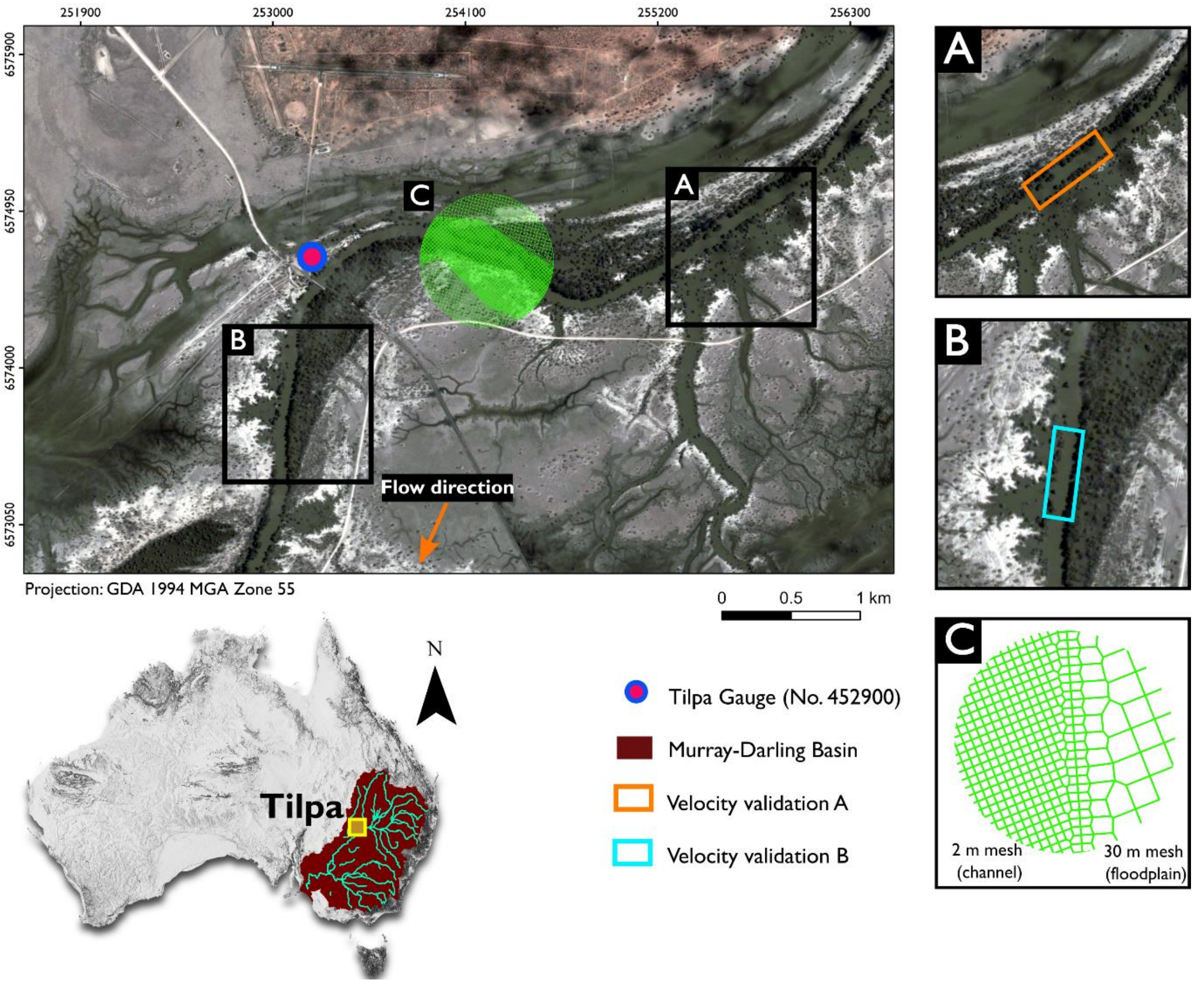

Figure 5.2 The Darling River at Tilpa study area, located in the Murray-Darling basin (shaded inset), New South Wales, Australia, with a basemap of Jilin-1 satellite video acquired at 23:12 UTC on 5 February 2022. Panels A and B indicate flood model validation locations. Panel C presents the hybrid mesh used in hydraulic modelling.

The Darling River at Tilpa has a river style (Brierley *et al*., 2002) that is meandering, is planform controlled and features discontinuous floodplain. Creeks are connected to the Tilpa's main channel and fill with water when the Tilpa's stage is high. This complex floodplain configuration demands high-resolution 2D flood inundation modelling. We calibrated our HEC-RAS 2D model using stage height observations from the gauging station at Tilpa (Figure 5.2) and validated our model simulations at two locations (A and B, Figure 5.2), geographical extents that adequately represent the complexity of the floodplain and enabled us to capture fine scale flood hydraulics at a resolution sufficient to comprehensively assess inundation dynamics. Additionally, using these two locations, rather than the whole study area, overcomes the potential problem of jagged prediction patches, which are artifacts associated with the reconstruction of large sized deep learning-based prediction mosaics. This is a limitation when making flood pixel predictions using neural networks which generally results in data loss around the border of large image patches (Heller *et al*., 2018; Yuan *et al*., 2021).

5.2.3 Data

5.2.3.1 Satellite Video

Satellite video (Table 5.1) was acquired on 5 February 2022 at 23:12 UTC by Jilin-1 GF-03, which is part of the Jilin-1 constellation operated and developed by Chang Guang Satellite Technology Company. The video has a spatial resolution of 1.22 m and was acquired at 5 frames per second for a duration of 28 seconds, yielding 140 frames, with each frame measuring 12000 x 5000 pixels.

Table 5.1 Jilin-1 GF03C02 Satellite sensor specifications and video product information

Attribute	Details
Product components and format	Video file – AVI Individual video frames – TIFF Images
Image mode	Gaze imaging Conventional and multi-target pushbroom imaging/space target imaging
Spectral bands	RGB (Bayer pattern) Red B1: 580-730 nm Green B2: 490-580 nm Blue B3: 430-520 nm
Scene size	14.4 km x 6 km
Orbit	Type: Sun-synchornous Altitude: 535 km
Spatial Resolution (Ground Sampling Distance)	1.2 m
Video duration	28 s

5.2.3.2 Rated Discharge

5.2.3.2.1 Rating Curve Uncertainty Estimation

The influence of rating curve uncertainties on streamflow time series estimates is particularly pronounced in natural river systems, especially during floods, when a rating curve is typically extrapolated beyond the maximum gauging in the rating, resulting in significant systematic errors (Horner *et al.*, 2018). The propagation of errors from flood model forcing data (i.e. streamflow) to eventual model outputs warrants explicit consideration of uncertainties associated with the rating curve. Kiang *et al.* (2018) investigated different techniques for estimation of stage-discharge rating curve uncertainty concluding that the choice of methods is fully dependent upon the constraints of the specific application. Bayesian inference has however been suggested as a robust technique to handle independent gauging errors and provide precise discharge series uncertainty envelopes (Ocio *et al.*, 2017) and was adopted here.

Rating curve uncertainty in this investigation is assessed using the BaRatin (Bayesian Rating Curve) method (J. Le Coz *et al.*, 2014) which combines uncertain gaugings and prior hydraulic knowledge to derive uncertain stage-discharge relations. The BaRatin framework defines stage and discharge measurement uncertainties as Gaussian distributions with a mean of zero and is composed of three main components; i) a measurement error model, consisting of prior estimates of parameters based on preliminary hydraulic analysis of a gauging station,

ii) Posterior rating curves, which are a derived from a simulation consisting of gauging data, and iii) The application of Markov Chain Monte Carlo (MCMC) and Bayesian inference to sample the posterior distribution of the rating curve parameters relying on information contained in observed gaugings. The eventual rating curve equation is based on a matrix of hydraulic controls that relates discharge Q to stage h using power functions:

$$Q(h) = \sum_{r=1}^{N_{segment}} \left(1_{[k_{r-1};\, k_r]}(h) \times \sum_{j=1}^{N_{control}} M(r,j) \times a_j \left(h - b_j\right)^{c_j} \right) \tag{5.1}$$

In the above equation, $M(r,j)$ is the matrix of controls, and the notation $\boldsymbol{1}_I(h)$ denotes a function equal to 1 if h is included in the interval I, and 0 otherwise. Segments in the rating curve ($N_{segment}$) are user defined while segment limits k_r, coefficients a_j and exponents c_j are inferred.

For our flood model simulations, we forced our hydraulic model using streamflow time series (Figure 5.3) based on two scenarios: (a) Q_{obs}, observed discharged drawn directly from the Tilpa gauging station (Q_{obs} was obtained from a stage-discharge rating curve); and (b) $Q_{maxpost}$, discharge computed from measured stage and the *MaxPost* rating curve (a rating curve that maximizes the posterior distribution of a set of parameters inferred from the Bayes theorem (see Kiang *et al*. (2018) for detail). The $Q_{maxpost}$ streamflow timeseries is based on uncertain rating curves (with 95% confidence bounds), computed by Bayesian analysis of prior hydraulic controls and gagings with individual uncertainties.

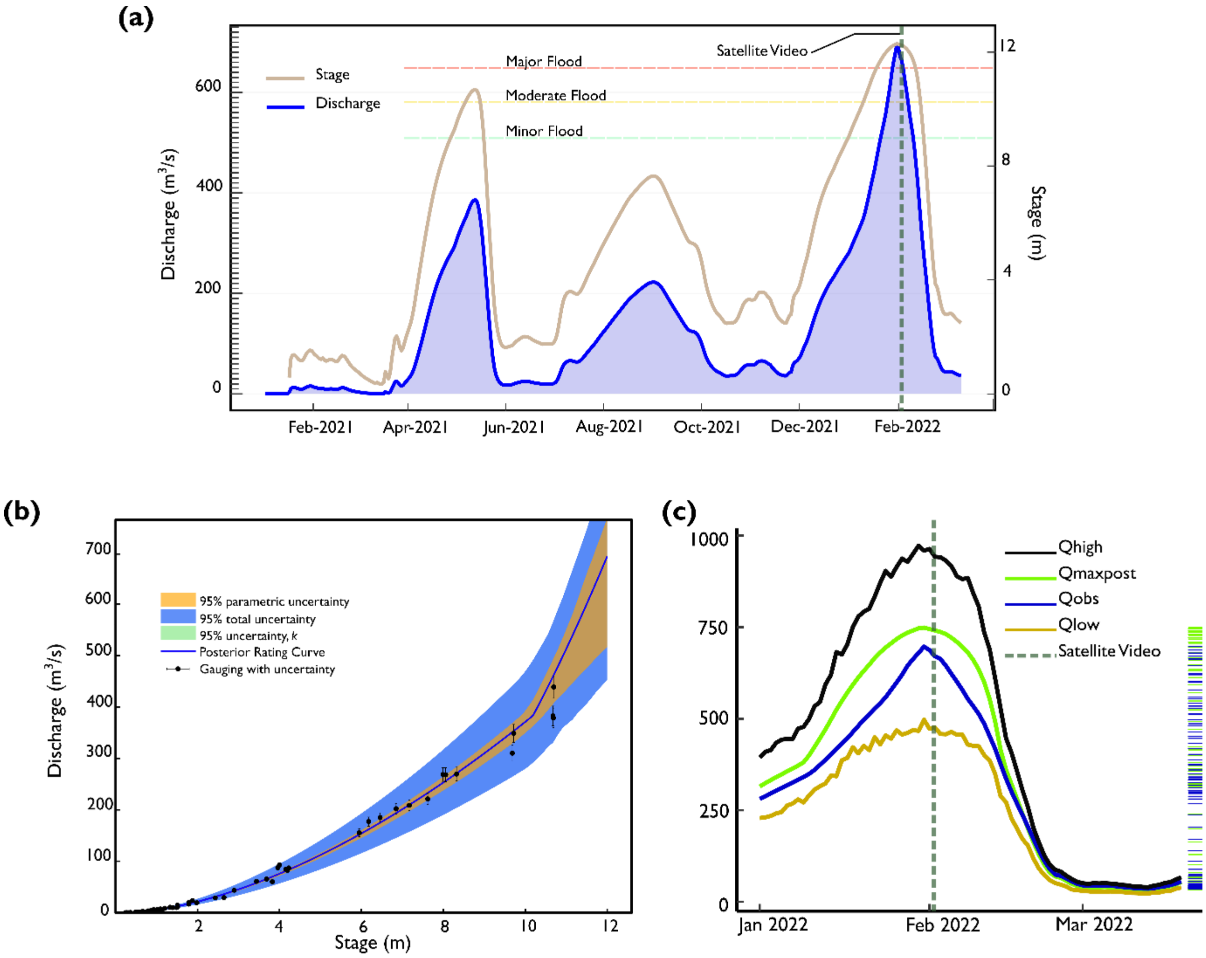

Figure 5.3 (a) Timeseries plot of stage and dsicharge for the Darling River at Tilpa gauging station from Feb 2021-2022. (b) Posterior rating curves and associated uncertainties derived using the BaRatin method. (c) Discharge time series. Q_{obs} is the observed discharge. Q_{high} and Q_{low} are discharges with associated stage (non-systematic and systematic stage measurement errors) and rating curve (parametric errors and structural/remnant errors) uncertainty. $Q_{maxpost}$ is the upper 95% confidence band of a streamflow timeseries based on an uncertainty analysis of the rating curve. The rug plot to the right depicts the distribution of Q_{obs} and $Q_{maxpost}$ discharges.

5.2.4 Deep learning Model

5.2.4.1 Transformer-based encoder

Transformer based models were initially designed for Natural Language Processing tasks and excelled over CNNs and Recurrent Neural Network models (e.g., Long-Short Term Memory that process sequence elements recursively and can only attend to short-term context) thanks to their ‘self-attention mechanism’. In the context of semantic segmentation, the self-attention mechanism helps the model understand the relationships between different spatial locations (pixels) in an image. By using self-attention, Transformers can capture long-range dependencies and understand global context, which is essential for accurate semantic segmentation, where the label of a pixel may depend on distant regions in the image. Although the field of deep learning is evolving rapidly, the most successful transformer architectures adapted for semantic segmentation tasks include Vision Transformer (ViT) (Dosovitskiy *et al*., 2021), Swin Transformer (Z. Liu *et al*., 2021) and SegFormer (Xie *et al*., 2021). Here we leverage on SegFormer, which uses a hierarchical Transformer architecture (called "Mix Transformer") as its encoder and a lightweight decoder for segmentation. SegFormer's encoder leverages tokenization, self-attention, and hierarchical aggregation to efficiently capture important visual information from input images, making it well-suited for semantic segmentation tasks. Here, we fine-tune six variants of SegFormer (B0 – B5) with increasing model sizes offering improved performance at the cost of increased computational requirements.

5.2.4.2 Convolutional Neural Network (CNN)-based decoder

Convolutional neural networks (CNNs) are a widely used architecture in deep learning, initially proposed by Fukushima (1980) and refined by Lecun and Bengio (1995). CNNs, a class of artificial neural networks, are mostly defined as a series of layers, with the initial layers performing feature learning and the final layers performing classification. CNNs consist of three types of layers: a) convolutional layers, which are the first layers to extract features from an input image whose outputs (feature maps) are then passed on to sequential layers; b) pooling layers, which take feature maps as inputs and progressively reduce the spatial size of the feature maps, controlling model overfit; and c) an activation function applied to the outputs of the CNN that enable the model to capture non-linear behavior in the input data (Hosseiny, 2021).

Whilst a plethora of deep-learning CNNs exist, the most prominent architectures that have attained state-of-the art performance in semantic segmentation of remote sensing images are U-Net (Ronneberger *et al*., 2015), Google's DeepLab (Chen *et al*., 2017) and PSPNet (Zhao *et al*., 2017). In a comparative study of semantic segmentation of remote sensing images using the three aforementioned models, Hu *et al*., (2019) reported U-Net achieving the best accuracy. A more recent investigation by Sun *et al*., (2022), who similarly carried out an intercomparison of the three CNN networks, found U-Net outperforming the other three models in the segmentation of remotely sensed images.

Originally developed for biomedical image segmentation, U-Net (and its variants) has gained prominence in diverse fields for its ability to leverage on data augmentation to efficiently learn from a small number of annotated images. U-Net's fairly simple architecture, consisting of a downsampling (encoder) and upsampling (decoder) path allows for precise localization of segmented pixels. The U-Net decoder is a crucial component that contributes to the strength of the U-Net architecture in semantic segmentation tasks. The decoder is responsible for upsampling the low-resolution feature maps from the encoder to the original input image resolution while also fusing multi-level features to create final segmentation maps. Thanks to the U-Net decoder's low memory requirements as well as its ability to be trained end-to-end (meaning both the encoder and decoder are learned jointly during the training process) we deployed a U-Net decoder for our segmentation tasks.

5.2.4.3 Neural Network Training

Training deep neural networks typically requires a vast amount of data, which may not always be available. Here, rather than train our model from scratch, we fine-tuned our encoder to improve its segmentation capabilities on our dataset. Fine tuning entails taking a pre-trained model's encoder (in our case, SegFormer models B0-B6) and further training it on a specific dataset, the objective being to adapt the learned features to perform well on a new task. For instance several studies have utilized pre-trained models, such as VGG16 or ResNets, which have learned to recognize general image features from ImageNet, then fine-tuned the models on much smaller datasets for specific image segmentation tasks (see, for example Hashemi-Beni and Gebrehiwot, 2020; Tong *et al.*, 2020).

We leverage on the temporal richness of video to extract images used for fine-tuning our model. Although our video was acquired at a native frame rate of 5 Hz (resulting in 140 images in sequence), we subsample our video at a much lower frame rate of 1 Hz by retaining only every 10th frame from the original 5 Hz series resulting in a sequence consisting of 28 images. Skipping frames enabled us to decouple temporal information in our images. When frames are skipped, the information captured in one frame is temporally further apart from the information in the skipped frames. As a result, the sequential order of frames is disrupted, and the temporal information becomes less tightly coupled, reducing the strength of autocorrelation. Also, because there was minimal movement or low temporal variation in consecutive satellite video scenes, by skipping frames, we omit redundant or near-duplicate information, which leads to a reduction in autocorrelation since repetitive patterns are less prominent.

To ensure that all our extracted frames were aligned and free from any motion artifacts as a result of the satellite platform's vibrations, we aligned our images in TrakeEM2 (Cardona *et* *al.*, 2012) using the SIFT (Scale-Invariant Feature Transform) algorithm adopting the same workflow as that used by Legleiter and Kinzel (2021) in stabilizing their satellite video frames. In TrakEM2, frame alignment was accomplished using Scale-Invariant Feature Transform (SIFT), a technique used to align multiple images or frames from a video to ensure their spatial coherence and accuracy in subsequent analyses (see, for example, Ma *et al.* (2016)). For each frame, SIFT detects and extracts distinctive key points and matches these points in adjacent frames to identify corresponding features. Based on the matched key points, TrakEM2 estimates the transformation (e.g., translation, rotation, scale) required to align the frames properly and applies the necessary adjustments to align the frames, ensuring that they match spatially and temporally. Stabilized frames were exported to Intel's open-source image annotation tool CVAT (Computer Vision Annotation Tool) and were manually labelled. Labeled masks were then converted to binary format in Python (with background = 0, flood = 1). These annotated masks served as the ground truth for training and validation of our deep neural network.

At the training stage, the full-sized satellite images could not be loaded on to the network due to memory limitations, a common challenge faced when training deep learning models which require extensive memory to store input images, weight parameters and activations as images are channeled through the network. Therefore, the original images were split into patches of 256 x 256 x 3. To artificially diversify and increase the size of our training dataset, we deployed data augmentation. Data augmentation is a technique that reduces generalization errors (model overfitting) by adding a range of deformations and noise to the training data. To implement data augmentation, we used the Albumentations library (Buslaev *et al.*, 2020) in Python, where we applied vertical and horizontal flips, transposition, grid distortions, elastic transforms and random gamma to both the images and corresponding binary masks. A total of 5660, 1698 and 566 image patches (256 x 256 x 3) were used for training, validation and testing the network.

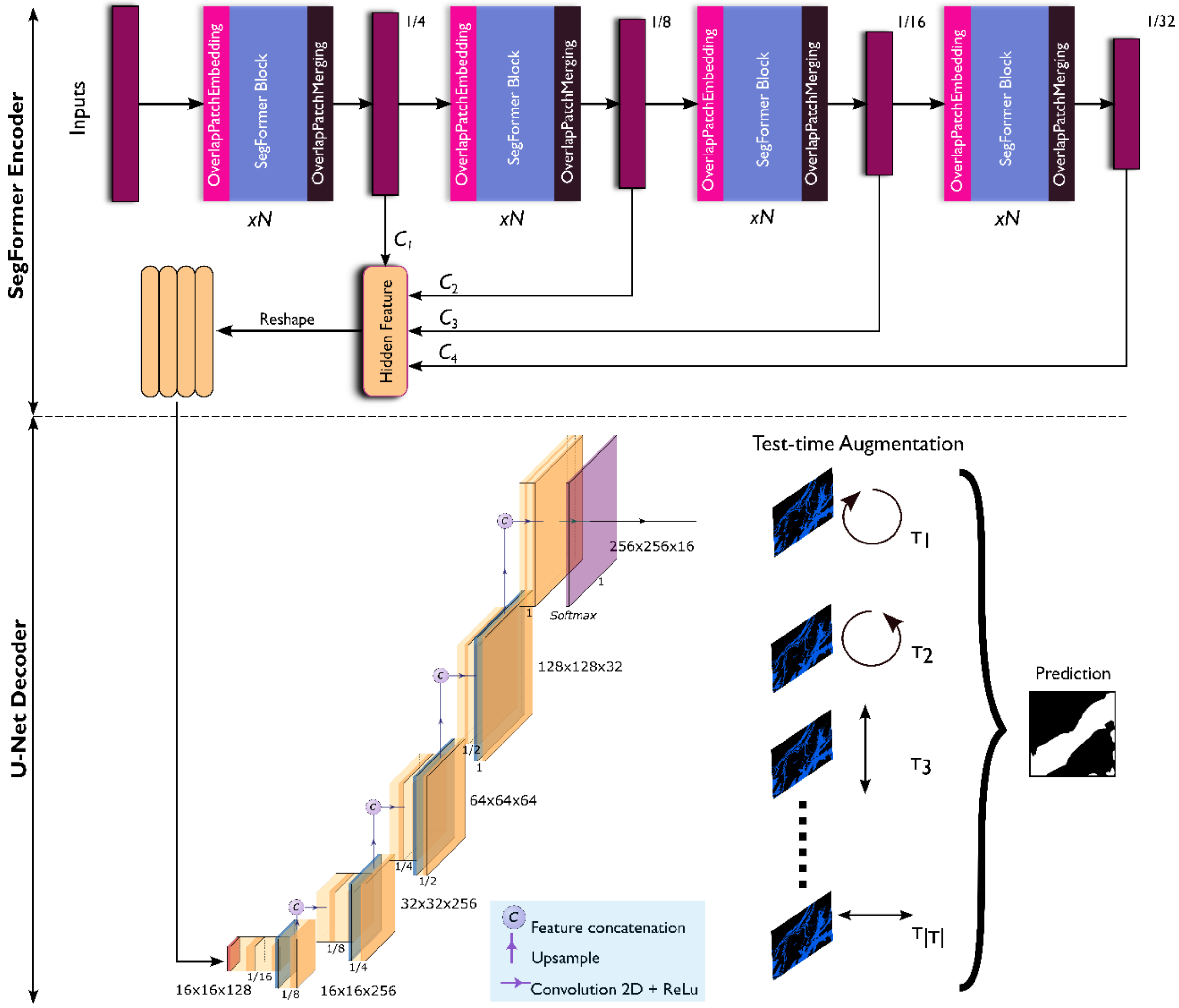

Figure 5.4 End-to-end deep learning network training, validation, and testing pipeline.

To initiate training, pre-trained ResNet-34 SegFormer weights were imported and hyper-parameters set as follows: we used a batch size of 8 and a learning rate of 1 x 10^{-4} with a call back to reduce the learning rate by a factor of 2 x 10^{-4} when the validation metric (Intersection-Over-Union/Jaccard Index) stopped improving. The deep learning model was implemented within the PyTorch deep-learning framework and trained on an NVIDIA GeForce RTX 2070 Super GPU for 150 epochs. The trained network learned to associate images and masks and make an independent prediction on a test image which was independent of the 28 frames used in the original training/validation/testing pipeline.

5.2.4.4 Neural Network Evaluation Metrics

Model segmentation performance was assessed using two metrics, Binary Cross Entropy loss (LBCE) and the Intersection Over Union (IoU; also known as the Jaccard Index). LBCE, compares model predicted probabilities to the ground truth labels (see section 2.3.1), which can either be 0 or 1. It then computes a score that penalizes the probabilities based on the distance from the expected values. L_{BCE} calculates the difference between the actual and precited probability distributions for predicting class 1 (Jadon, 2020). The score is minimized, and a perfect value is zero:

$$L_{BCE} = -\frac{1}{n}\sum_{i=1}^{n}\left(Y_i \cdot log\,\hat{Y}_i + (1 - Y_i) \cdot \log(1 - \hat{Y}_i)\right) \tag{5.2}$$

where Y denotes the ground truth label while $\hat{Y}$ is the precited probability of the classifier.

IoU is a simple ratio that compares how close a pixel is between the training sample and predicted regions (Bebis *et al.*, 2016):

$$IoU = J(A, B) = \frac{|A \cap B|}{|A \cup B|} \tag{5.3}$$

where A and B denote the ground truth and the prediction segmentation maps respectively. IoU ranges between 0 and 1. If the model prediction is perfect, IoU = 1. The lower the IoU, the worse the predicted result.

Since our binary segmentation task involved a dataset with an inherent class imbalance, we utilize L_{BCE} and IOU as our loss functions during model training. Although we report other metrics including recall, precision and the F1 score, we do not use them as loss functions during training as these metrics would strongly bias our results to the class that occupies a large portion of our images (flood imagery has disproportionately few pixels per image being identified as flooded).

Precision, Recall and F1 Score were reported for a threshold of 0.5 on the prediction probabilities. Precision measures the accuracy of the positive predictions made by the model. It is the ratio of the true positive (TP) predictions to the sum of true positives and false positives. Recall measures the ability of the model to correctly identify positive instances. It is the ratio of true positive predictions to the sum of true positives and false negatives (FN). The F1 score is the harmonic mean of precision and recall. It provides a balance between the two metrics and is a single value that summarizes the model's overall performance. These indicators can be expressed as:

$$Precision = \frac{TP}{TP + FP} \tag{5.4}$$

$$Recall = \frac{TP}{TP + FN} \tag{5.5}$$

$$F1\, Score = \frac{2\ x\ Precision\ x\ Recall}{Precision + Recall} \tag{5.6}$$

Where TP, FP, TN, and FN mean true positive, false positive, true negative, and false negative respectively.

5.2.4.5 Test-time Augmentation (TTA)

Although data augmentation has been widely used when training deep learning networks, a less common way of improving semantic segmentation prediction accuracy is Test-Time Augmentation (TTA) (see, for example, Gonzalo-Martín *et al.*, 2021; Liu *et al.*, 2022; Moshkov *et al.*, 2020; Wieland *et al.*, 2023). TTA involves applying augmentation transformations on the test image to create an ensemble of predictions, which are then averaged, to improve prediction results. Assuming x to be our input image and τ a transformation operation, choosing $T = \{\tau_1,\ \tau_2, \dots, \tau_{|\tau|}\}$ as a set of augmentations at model inference time, we can formulate test-time augmentation as:

$$y_{tta} = \frac{1}{|T|} \sum_{i=1}^{|T|} \Theta_{target}\big(\tau_1(x)\big) \tag{5.7}$$

where Θ_{target} is the neural network trained on our target dataset (satellite video frames).

In our application, we supplied the network with a full-sized satellite video scene, which is patched into 256 x 256 x 3 sized patches without overlap. The network then made predictions on multiple transformations of the image patches, creating an ensemble of predictions. The transformations were then reverted, a process known as dis-augmentation, following which predictions were averaged, thresholded then stitched back to the original full-size image using the Patchify library in Python.

Image parsing which assigns semantic class labels, in this case flooded vs non-flooded pixels, for our trained deep learning network returned probability maps, which were thresholded to binarize final pixel classes. Assuming a base (true) segmentation probability map is returned by the network during testing, binary segmentation is done by thresholding as follows (Hong *et al.*, 2021):

$$P = \delta\big(p(y)\big), \tau \tag{5.8}$$

Where $P \in \{0,1\}^{WxH}$ is a predicted segmentation label and $p(y)$is the true probability map of the potential segmentation labels $y \in \{0,1\}^{WxH}$for an image with height H, and width W. δ is the thresholding function with a threshold τ. We set a fixed τ value of 0.5 for our model training and testing.

5.2.4.6 LPSIV Velocity estimation

Whilst a variety of image velocimetry algorithms have been deployed for river surface velocity estimation (see Perks *et al.* (2020) for a summary), we rely on the frequently used PIVLab algorithm (Thielicke and Sonntag, 2021; Thielicke and Stamhuis, 2014) for our LSPIV analysis. Our general LSPIV workflow is depicted in Figure 5.1. For ease of processing, we crop our original video, focusing on the reaches A and B (Figure 5.2). We sub-sample our videos to lower frame rates of 1, 0.5 and 0.25 Hz by retaining only the 5th, 10th, and 20th frames respectively from the original 5 Hz series. By lowering the frame rate, the time interval between consecutive images is increased. Resultantly, tracked features move farther between frames, leading to larger displacements which translate to larger feature sizes in the PIV analysis, making it easier for the PIV algorithm to accurately track the features. We then stabilize all our images in TrakEM2 to counter any residual motion effects from the satellite platform.

We import and process our images in PIVLab. To optimize the quality of our velocimetry results, we pre-process the images by applying *contrast limited adaptive histogram equalization* (CLAHE) (Pizer, 1990; Yadav *et al.*, 2014), which enhances the contrast and improves the visibility of details in an image. We also applied an *intensity high-pass* filter which removed low-frequency background noise and enhanced the visibility of flow features in the images, making it easier for the PIV algorithm to accurately detect and track them (Thielicke and Stamhuis, 2014). A crucial parameter input to the PIVLab algorithm is the interrogation area (IA) usually measured in pixels. Whilst a large interrogation area may improve the accuracy of velocity measurements, it can also lead to a loss of spatial resolution. Conversely, a small IA may provide higher spatial resolution but could also be sensitive to noise or errors in particle tracking. A step-size, which is usually 50% of the IA, determines the spacing of PIV output vectors. Here, we utilized an IA of 128 pixels with reducing sizes over 4 passes (i.e., 128 – 64 – 32 – 8 pixels). For our PIV analysis, we utilized the FFT window deformation (direct Fourier transform correlation with multiple passes and deforming windows) cross-correlation algorithm (for details, see; Astarita, 2008; Thielicke and Sonntag, 2021; Thielicke and Stamhuis, 2014). We postprocessed our computed velocities to remove spurious velocity vectors due to poor particle tracking, image artifacts, or other issues. Our post-processing specifically entailed setting a standard deviation filter which was used to filter out noisy or erroneous velocity vectors from the calculated velocity field based on their standard deviation values (set to PIVLab's default value of 8 in our study). Velocity vectors were georeferenced within PIVlab from an image coordinate system back into a projected coordinate reference system (GDA 1994 MGA Zone 55) and exported to ArcGISPro for analysis.

5.2.5 Flood Model

Two dimensional (2D) flood flow modelling was accomplished using HEC-RAS version 6.0, building on previous flood modelling studies using this code (e.g. Mokhtar *et al*., 2018; Navarro-Hernández *et al*., 2023; Pradhan *et al*., 2022). The model domain was 4.4 x 7.7 km. Topography was defined from a 1 m resolution LiDAR-based bare-earth digital surface model acquired when the river channel was dry (Geoscience Australia, 2022). A heterogenous 2D computational mesh was generated using a cell size of 30 x 30 m within the floodplain and 2 x 2 m between channel banks (Figure 5.2). The HEC-RAS model domain extended from upstream of box A and downstream of box B as shown in Figure 5.2. Model upstream inflow boundary conditions were set using data from the gauge located at Tilpa, with 15-minute interval gauged streamflow being used. We simulated two scenarios with different upstream boundary forcing: model M_{obs}, based on observed discharge data; and model $M_{qmaxpost}$ using uncertain streamflow estimates (see section 2.3.2.1). An energy slope value was used as the outflow boundary condition; the gradient, equivalent to the normal depth, was estimated by computing the bed slope along the terrain profile. Unsteady 2D flow simulations were conducted from 00:00 4 February to 23:59 6 February 2022 using HEC-RAS's diffusive wave equations since the flood wave was not highly dynamic (Brunner *et al*., 2020; Yalcin, 2020).

Model calibration data were available in the form of stage height from the gauge at Tilpa (Figure 5.2). 2D model runs (see section 2.3.2.1) were calibrated by adjusting a spatially discretized (meaning a different *n* value for the channel and floodplain) manning's roughness coefficient *n* over a parameter space between 0.025 – 0.033, with 0.002 increments until model simulations closely matched observed stage height data. Given the large, wide, and gently sloping nature of the river in a relatively flat terrain, spanning a domain of less than 8 km, the likelihood of significant discharge variations between the input boundary and gauging station was deemed minimal. The gradual flow and expansive character of the River Darling reduced the potential for substantial changes in discharge over the short distance considered. Moreover, the use of stage measurements at the calibration location ensured a localized validation, emphasizing the appropriateness of this workflow for the specific hydraulic characteristics of the Darling River at Tilpa. Modelled stage height accuracy was assessed using two commonly used metrics (Moriasi *et al.*, 2007), the percent bias (PBIAS) and root-mean-square error (RMSE).

5.2.5.1 Analysis: Flood model validation using observed extents

We validated models M_{obs} and $M_{qmaxpost}$ against flood masks derived from the observed satellite video frames. HEC-RAS modelled, and satellite video-derived flood extents were converted into binary masks (wet/dry) representing only flood extent, then overlapped, using ArcGISPro software. To preserve the detail of the model output's higher resolution, specifically close to the floodplain where model performance matters most due to the occurrence of complex inundation dynamics, and because comparison of validation performance needed to be done at the same spatial resolution, binary masks derived from the satellite video frames were resampled using the nearest neighbor method to 1 m. During resampling, binary pixel interpolation did not yield new additional values, avoiding false accuracy errors. Since we were resampling a binary raster with only one of two values (0 or 1), each new pixel in the target 1 m resolution raster was assigned the value of the nearest corresponding pixel, meaning extents of the binary raster remained unchanged because no new information was introduced. The extent of overlap between the modelled inundation boundaries and the observed satellite video, were calculated according to the number of pixels that showed model agreement, overprediction and underprediction, as per the states in Table 5.2. Data from these computations were then used to calculate performance scores.

Table 5.2 Confusion matrix of cell descriptors in binary classification of flood masks

	Wet in observed data	**Dry in observed data**
Wet in model simulation	A_1	B_2
Wet in model simulation	C_3	D_4

To analyse model skill in reproducing the observed flood inundation extent, we rely on well-established spatial performance measures which account for the most critical attributes of model simulation precision: model bias (*E*), hit rate (*HR*) - proportion of the observed flood event that was successfully predicted by the model, the false alarm ratio (*F*) and a rigorous composite measure (Critical Success Index, *CSI*) which penalized model overpredictions (Bates *et al.*, 2021; Bernhofen *et al.*, 2018; Wing *et al.*, 2017).

Error bias (*E*) which indicates whether the model is biased towards overprediction or underprediction:

$$Bias = \frac{F_m \cap F_o + F_m}{F_m \cap F_o + F_o} - 1 \tag{5.9}$$

where F_m is the total modelled flood extent. A Bias score of 0 indicates an unbiased model while positive and negative scores indicate a tendency towards overprediction and underprediction respectively.

The hit rate (*HR*) which measures proportion of observed flood that was simulated by the model, ignoring whether the observed flood extents were exceeded. *HR* can range from 1 (entire flood captured) to 0:

$$HR = \frac{F_m \cap F_o}{F_o} \tag{5.10}$$

where F_o is the total observed flood extent. The HR ranges from 1 (entire flood captured) to 0.

The false alarm ratio (*F*), a measure of whether the model has a tendency to overpredict flood extent and can range from 0 (no false alarms) to 1 (all false alarms):

$$FAR = \frac{False\ alarm\ area_{area}}{False\ alarm_{area} + hit_{area}} \tag{5.11}$$

The Critical Success Index (*CSI*) accounts for both overprediction and underprediction and can range from 0 (no match between modelled and observed data) to 1 (perfect match between modelled and observed data). *CSI* ignores areas that are dry in both the modelled and observed data, as these can be aptly predicted by the flood model and so would bias results:

$$CSI = \frac{F_m \cap F_o}{F_m \cup F_o} \tag{5.12}$$

where $F_m \cap F_o$ is the intersection of the modelled and observed flood extent, or number of correct predictions, and $F_m \cup F_o$ is the union of modelled and observed extent. The *CSI* ranges from 1 (best) to 0 (worst).

5.2.5.2 Analysis: Flood model validation using observed velocities

Whereas the HEC-RAS 2D model is developed to estimate depth-averaged water velocities, satellite video-based LSPIV computations yielded surface river velocities. For a like to like comparison, we depth-average our LSPIV velocities. A well-established technique for converting surface velocities into depth averaged velocity is by utilizing published values of depth-averaging constants, also referred to as alpha coefficients, α (Biggs *et al.*, 2021; Creutin *et al.*, 2003). Rantz (1982) proposed α values of between ~0.85 – 0.86 for natural channels. Hauet *et al.* (2018) recommend α values of 0.8 for water depths of less than 2 m and 0.9 for greater water depths with an uncertainty of ±15% at 90% confidence level within natural rivers. Vigoureux *et al.* (2022) suggested α values of between 0.85 – 1.2 for their LSPIV analysis and experimented with values between 0.8 to 1.0 for their depth averaging constants. To quantify the impact of choice of α coefficient on our estimated velocities, we utilize α coefficients of between 0.7 and 1.

We compare HEC-RAS model predictions with LSPIV velocities via linear regression where we fit a linear trend line and use R^2 and slope as indicators of model performance. The coefficient of determination, R^2, value between HEC-RAS 2D model velocities and LSPIV remains unaffected when the LSPIV velocities are adjusted by varied α values. However, other statistical indicators are sensitive to the choice of α coefficient, including the mean velocity difference between model and LSPIV-based velocity (with an optimum difference of 0 m s^{-1}), which we use to evaluate the accuracy of our validation.

5.3 Results

5.3.1 Segmentation accuracy

We evaluated the segmentation performance of six variants of our model based on SegFormer encoders (B0 – B5) of increasing sizes, all pre-trained on ImageNet, to select an architecture that robustly segments flood pixels from a satellite video test image set. We retained the same hyperparameters of learning rate, batch size and number of epochs for all models during the testing phase to attain a fair comparison between the different backbones.

Table 5.3 Segmentation accuracy for increasing sizes of SegFormer encoders (B0- B5) coupled with a U-Net decoder

	L_{BCE}	**IoU**	**F1 Score**	**Recall**	**Precision**
SegFormer-BO/U-Net	0.2522	0.8178	0.8789	0.8826	0.917
SegFormer-B1/U-Net	0.2597	0.8192	0.8848	0.8959	0.9138
SegFormer-B2/U-Net	0.3515	0.7383	0.8171	0.8396	0.8253
SegFormer-B3/U-Net	0.3218	0.8186	0.8791	0.8801	**0.9212**
SegFormer-B4/U-Net	0.3456	0.8196	0.8819	0.8889	0.9161
SegFormer-B5/U-Net	**0.2518**	**0.8276**	**0.8878**	**0.8972**	0.9181

Bold font highlights optimal values.

Quantitative results of model performance are detailed in Table 5.3. Overall, we find segmentation performance of all models to be satisfactory (IoU >0.7). In general the performance of the deep-learning networks was on par with values reported in literature where hybrid CNN/transformer networks have been deployed for semantic segmentation (e.g. T. Wang *et al.*, 2022). Unsurprisingly, we found the SegFormer-B5/U-Net network attained the most accurate scores across all metrics, except for the precision metric where the SegFormer-B3/U-Net network returned a better score of 0.9212. This can be explained by the higher number of parameters which leads to better segmentation accuracy, but at the cost of additional computational demand. Visual test results are presented in Figure 5.5 and further support the quantitative scores from model training and testing.

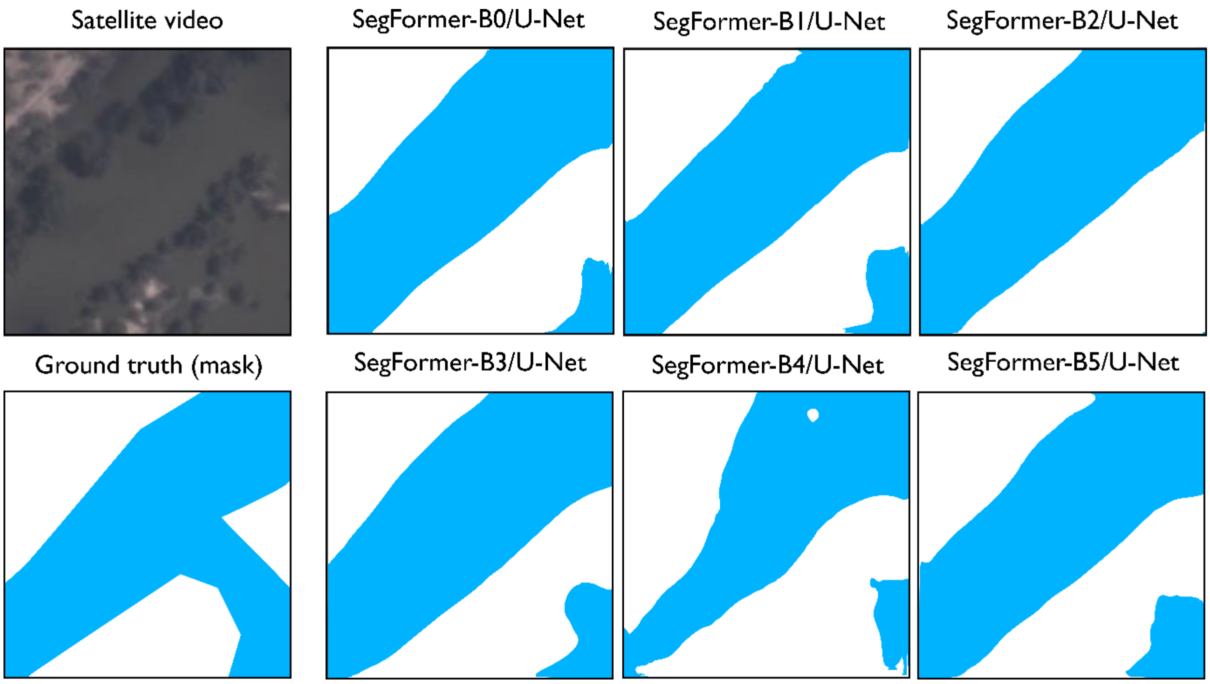

Figure 5.5 Results of the semantic segmentation of a sample satellite video patch using varied combinations of SegFormer encoders coupled with a U-Net decoder. The annotated mask serves as the ground truth with water pixels labelled blue, background pixels labelled white.

5.3.2 Flood model calibration

The 2D hydraulic model was calibrated to observed stage at the Tilpa gauging station by varying Manning's *n* roughness. The calibration focused on the narrow range of high-stage measurements (12.12 – 12.14m) to specifically address the period of peak flood conditions. This targeted approach ensured rigorous evaluation under circumstances of heightened uncertainty (McMillan *et al.*, 2012), crucial for accurately modelling and managing extreme flood events. In our investigation, both models were considered to be adequately calibrated with RMSE (0.46 m, 0.45 m) and PBIAS (0.77, 0.16) for models M_{obs} and $M_{qmaxpost}$ respectively (Table 5.4), comparable to ranges reported in other similar studies (Timbadiya *et al.*, 2011; Zeiger and Hubbart, 2021). Median error (Figure 5.6c) increased marginally for model M_{obs} with both models showing a strong correlation between modelled and observed stages (R^2 of 0.72 and 0.71) for models M_{obs} and $M_{qmaxpost}$ respectively (Figure 5.6).

Table 5.4 2D model calibration metrics for Models M_{obs} and $M_{qmaxpost}$. Model predictions are calibrated against observed stages over a time step of 15 minutes on 5th February 2022 (04:00 – 12:30).

	Model M_{obs}		**Model $M_{qmaxpost}$**	
Manning's *n*	**RMSE, m**	**PBIAS**	**RMSE, m**	**PBIAS**
0.025	1.30	-8.08	0.81	-4.65
0.027	1.11	-6.64	0.53	-0.32
0.029	0.72	-1.94	0.56	2.29
0.031	0.46	0.77	0.45	0.16
0.033	0.51	2.48	0.61	2.20

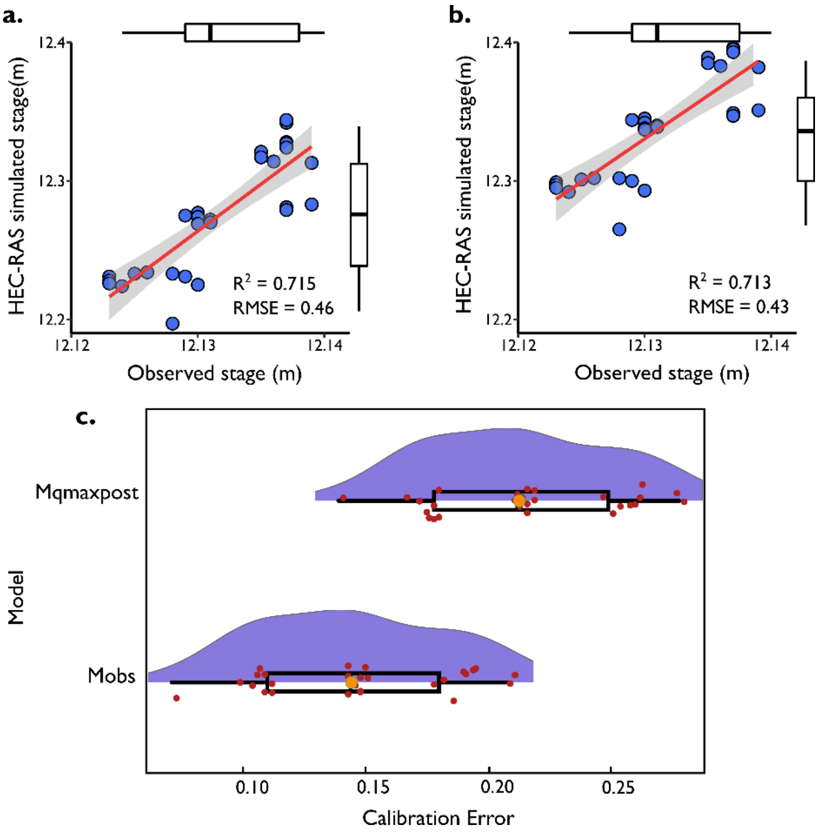

Figure 5.6 HEC-RAS calibration results. Observed water surface elevations are compared against calibrated model M_{obs} (a) and $M_{qmaxpost}$ (b) predictions over a time step of 15 minutes on 5th February 2022 (04:00 – 12:30). Coefficient of determination (R^2) and RMSE represent the results of regression analysis of the data. (c) Raincloud plot, a boxplot with a half-side violin plot, showing the error distributions for both models. In the boxplots, the bold centerline represents the median score, the box encompasses the 2nd and 3rd quartiles, and the top and bottom whiskers respectively represent the largest and smallest values within 1.5 times the interquartile range.

5.3.3 Flood extent validation using deep learning-based flood extents

Results from validation of both models at locations A and B (Figure 5.2) using satellite-video derived flood extents are detailed in Table 5.5. The predictive accuracy of both models was tested by choice of uncertainty associated with model forcing data (streamflow) and the influence of TTA. We report both results in detail in the following sections.

Table 5.5 Validation metrics for models M_{obs} and $M_{qmaxpost}$ against observed satellite video data at validation locations A and B (see Figure 5.2).

Validation Area	Model	Error Bias (*E*)	Critical Success Index (*CSI*)	False Alarm Ratio (*F*)	Hit Rate (*HR*)
A	M_{obs}	1.085	0.910	0.085	0.993
A	M_{obs} TTA	1.050	0.941	0.053	0.994
A	$M_{maxpost}$	1.020	0.873	0.077	0.941
A	$M_{maxpost}$ TTA	0.986	0.896	0.049	0.938
B	M_{obs}	1.072	0.7	0.204	0.853
B	M_{obs} TTA	0.808	0.803	0.003	0.805
B	$M_{maxpost}$	1.152	0.716	0.221	0.898
B	$M_{maxpost}$ TTA	0.868	0.862	0.004	0.865

Note. M_{obs} = Model forced using observed streamflow, = Model forced using uncertain streamflow, TTA = Test-time Augmentation applied to validation images

5.3.3.1 Model comparison scores

We assess the performance of both models at validation locations A then B, followed by a summary of the key findings from both reaches.

At validation location A, the predictive skill of both model M_{obs} and $M_{qmaxpost}$ was nearly similar, with CSIs ranging between 0.873 – 0.91. For both models, CSI declined when the models were validated against lower-quality observations, without implementation of TTA. When the model was forced using uncertain streamflow data, CSI averaged 0.918 as compared to 0.891 when using observed streamflow, a 3% improvement in performance. Average model bias declined marginally (by 3.3%) when forcing our model with uncertain streamflow.

At validation location B, we observed lower values of CSI, ranging between 0.700 – 0.862, representing, on average, a 16% decline in model accuracy. Similar to validation location A, model performance scores improved across the board when TTA was applied. We however observe a consistent drop in model hit rate when TTA is applied at both validation location A and B.

For both models at both validation locations, underestimation of the flood extent is concentrated in the downstream end of the study reach (validation location B) where, on average, the hit rate was 85.5% as compared to 96.7% in validation location A. To contextualize these results, the skill of both models is in line with previous studies (e.g. Ongdas *et al.*, 2020 using Sentinel-1B) who reported *HR* scores of between 59% - 77%. The models forced with uncertain streamflow data yielded superior results for all assessment metrics except for HR which declined whenever we applied TTA. Validation bias overall ranged between 0.808 – 1.152, with our scores being in line with those from other comparable validation studies in literature ranging from -1 – 5 (e.g. Wing *et al.*, 2021, 2017 using a combination of HEC-RAS model outputs and Special Flood Hazard Maps from the United States Geological Service).

5.3.3.2 Test-time Augmentation (TTA) and model performance scores

Figure 5.7 shows an overview of the influence of TTA in the binarization of flood pixels in the observed data. Results differed substantially when TTA was applied during validation of both models M_{obs} and $M_{qmaxpost}$ at both locations. At both reaches, CSI scores ranged from 0.7 to 0.91, and improved to between 0.803 – 0.941 when TTA was implemented. Overall, these CSI results are in line with other flood model validation studies which range from 0.1 to 0.9 (e.g. Mester *et al.*, 2021; Wing *et al.*, 2017).

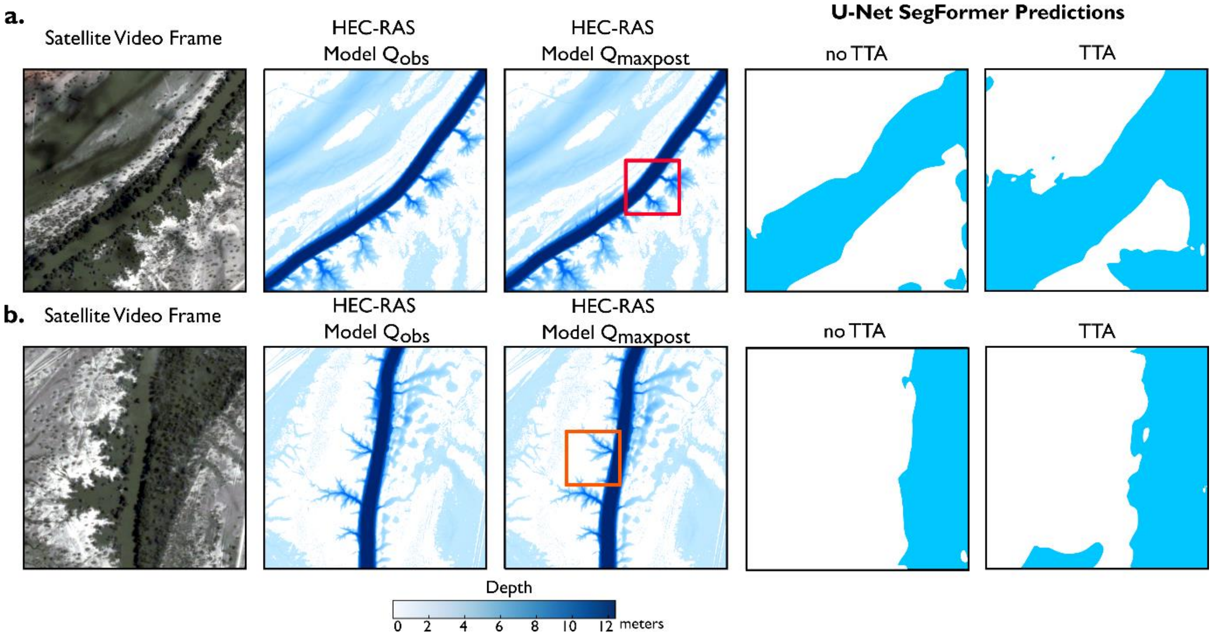

Figure 5.7 Semantic segmentation results at reach A (a) and B (b): The first panel to the top left shows the observed satellite video flood image followed by HEC-RAS model flood outputs (all sampled at the same time stamp) from Models M_{obs}, $M_{maxpost}$ and corresponding binary segmentation maps from zoomed-in insets with no TTA then TTA applied.

HR scores generally followed a negative trend when TTA was implemented as compared to the other performance measures. Since this metric only considers the proportion of wet observed pixels, ignoring whether observed flood extents were exceeded, increasing the flood pixel class had an inverse impact on the flood capture. For both models at both validation locations, average *HR* scores decreased by 0.1% (at location A) and 4.8% (at location B). With TTA implemented, both models Models M_{obs} and $M_{maxpost}$ reached a nearly similar skill level across all metrics, indicating the importance of TTA in our segmentation strategy, which resulted in better agreement between model predicted and observed flood extents.

5.3.4 Flood velocity validation using LSPIV

Figure 5.8 shows the comparison of satellite-derived velocity estimates against 2D model predictions, depth averaged using varying α coefficients (see section 2.6.2) . Gard (2008) provide criterion for assessing whether 2D model predictions are validated or not based on the correlation coefficient between measured and simulated velocities, with a correlation of 0.6 – 0.8 being moderately strong and 0.8 to 1 being very strong. Further, Ballard *et al.* (2010) proposed that an R-value of 0.6 (R^2 =0.36) constitutes a validated 2D model, with Pasternack (2011) recommending R^2 of between 0.4 to 0.8 between observed versus 2D model predicted velocities. Correlations between both model predictions and LSPIV velocities were reasonable and averaged 0.78. Water velocities predicted by both model variants at both reaches were generally within the observed variability of the LSPIV data.

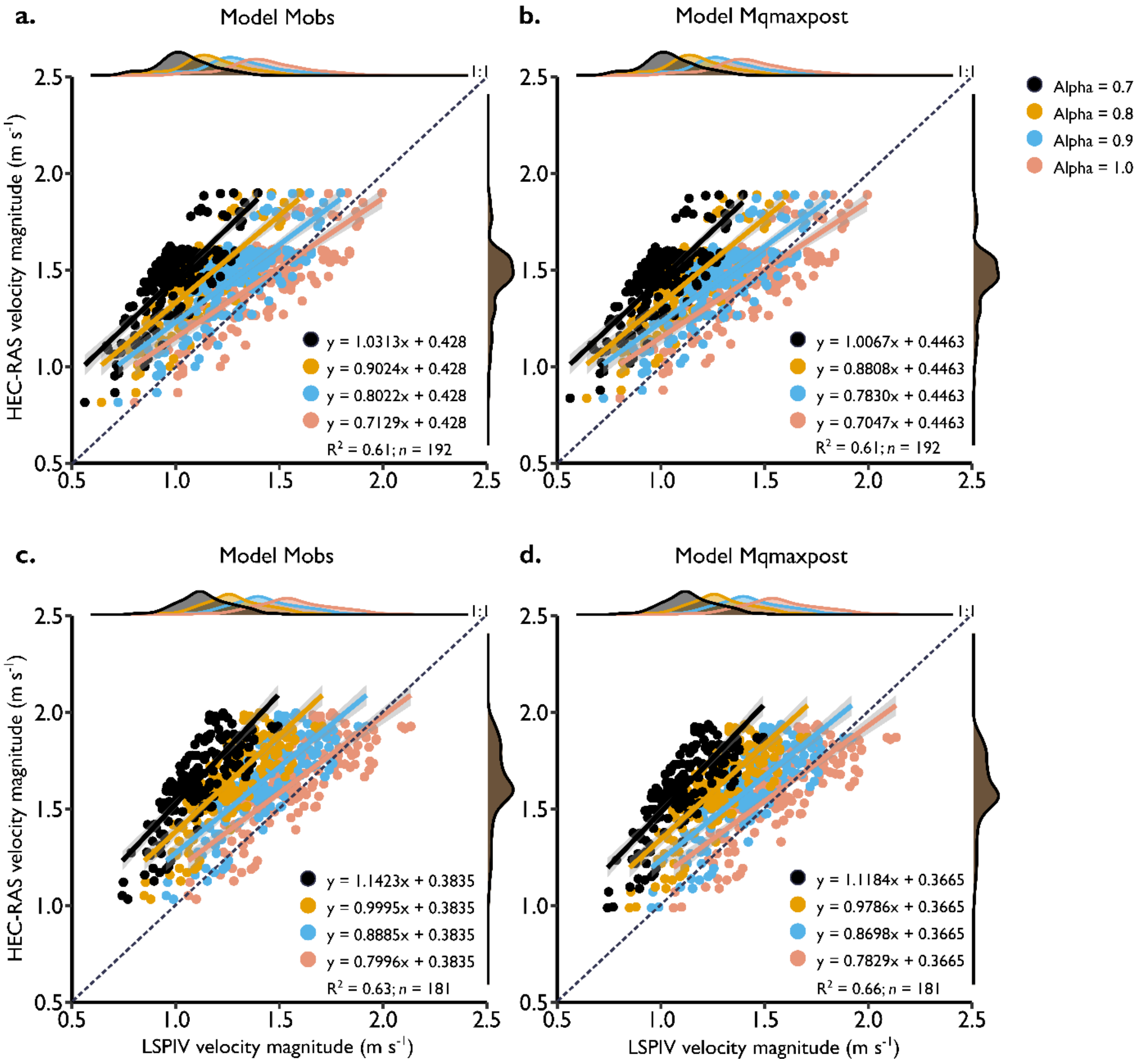

Figure 5.8 Satellite video-based LSPIV velocities versus HEC-RAS 2D model simulations for Models M_{obs} and $M_{maxpost}$ at reach A (a), (b) and reach B (c), (d) respectively.

We find that accounting for discharge uncertainty had minimal influence on velocity validation metrics. A key influence on the accuracy of 2D model velocity predictions, however, was choice of α coefficient. We report consistently low values of mean absolute error as α approaches 1, with an average value of 0.12 m s^{-1}. We partly attribute these results to the use of high-quality topography for our 2D modelling. These results affirm the findings of previous work, such as that by Lane *et al.* (1999) who similarly found that topographic specification has a larger role to play in constraining model velocity predictive ability as compared to inflow data.

5.4 Discussion

5.4.1 Flood extent segmentation using a hybrid Transformer/CNN network.

Satellite video, unlike traditional still imagery, is composed of both static and motional context (temporal information), with static context being the scenes that remain relatively still or unchanged, with minimal or no movement over a period of time and motional context encompassing dynamic elements. Both static and motion-based contexts share a significant correlation, with image semantic segmentation particularly benefiting from the static context (e.g., Hashemi-Beni and Gebrehiwot, 2020; Leach *et al.*, 2022) and the latter in video semantic segmentation (Hu *et al.*, 2020; Li *et al.*, 2018). Although research into means for simultaneously exploiting both the static and motional contexts has been attempted (G. Sun *et al.*, 2022), we did not pursue this line of inquiry for the reasons we outline forthwith.

While video segmentation can be valuable for analyzing dynamic changes during a flood event and for various research purposes, image segmentation provides a focused and practical approach for flood model validation tasks, where the primary goal is to assess model accuracy based on specific flood extents at critical time points. Hydraulic flood model predictions are typically produced as snapshots in time, representing flood extents at specific time points. By using a single image for validation, our validation process aligns naturally with the instantaneous nature of the 2D hydraulic model outputs. Additionally, state-of-the-art deep learning models, such as 3D convolutional networks or spatio-temporal transformers, can be computationally intensive for video semantic segmentation and may require specialized hardware to achieve real-time performance. Moreover, many current deep learning models process video frames independently, leading to limited temporal consistency in segmentation results. We therefore opted to exploit image semantic segmentation.

In evaluating the performance of our hybrid transformer-encoder, CNN-decoder structure, we evaluated segmentation performance with increasing SegFormer encoder depths (i.e., SegFormer B0-B5). The training and inference performance of our six models were largely comparable (Table 3), with the SegFormerB5 encoder yielding the best performance, thanks to it having the greatest number of trainable parameters (81M as compared to 60, 44, 24, 13 and 3M for the models B0 to B4). Although it has been shown that transformers make strong encoders for semantic segmentation tasks (L. Wang *et al.*, 2022), they come with the cost of increased computational requirements. For our decoder, we find the original (vanilla) U-Net architecture still allowed us to obtain acceptable performance. In fact, while several variants of the U-Net architecture have been proposed (e.g., Attention U-Net, Inception U-Net, U-

Net++) to improve segmentation performance, studies have found that the marginal segmentation performance gains of these new architectures may not be worthwhile as they come at significantly increased complexity and computational demand (e.g. Kugelman *et al.*, 2022). Our results demonstrate that a vanilla U-Net decoder, combined with a transformer backbone can still provide comparable and competitive segmentation results. This finding has significance as the operationalization of these segmentation techniques will have greater impact when the complexity of model structures is low and accuracy high, which would encourage adoption in flood mapping studies. We note that although other hybrid structures composed of transformer-based encoder and CNN-based decoder architectures exist (e.g. TransUNet based on the vision transformer (J. Chen *et al.*, 2021) and DC-Swin (L. Wang *et al.*, 2022) based on the Swin transformer (Z. Liu *et al.*, 2021)), it would be unmanageable to test them in this investigation. We speculate that any performance gains would be marginal at best.

Image segmentation performed by deep neural networks exploits two powerful features; (1) the capacity of deep learning architectures to overcome data scarcity by leveraging on previously trained networks and, (2) data augmentation techniques, which are used to increase the diversity and size of the training dataset by applying various transformations to the original images which improves the model's generalization performance by reducing overfitting and capturing more representative features of the underlying data distribution. A recent study by Wieland *et al.* (2023) attributed improvements to their segmentation performance as a result of data augmentation, which helped introduce variations, as would be expected in real-world scenarios, that were otherwise not present in their training dataset. Wieland *et al.* (2023) and Gonçalves *et al.* (2023) also found that adapting pre-trained models (trained on non-remote sensing specific databases such as ImageNet) which are fine-tuned on a custom dataset, like in our case, led to superior model performance as opposed to initializing a model with random weights. Although domain-specific datasets of flood images with labelled masks exist, such as Sen1Floods11 based on Sentinel 1 and 2, (Bonafilia *et al.*, 2020), SEN12-FLOOD based on a set of multimodal SAR and multispectral satellite imagery (Rambour *et al.*, 2020), WorldFloods based on Senitnel-2 images (Mateo-Garcia *et al.*, 2021) and FloodNet (Rahnemoonfar *et al.*, 2021) training a good deep-learning model on data from disparate sensors remains a complex task due to issues including the fact that data from different sensors may have significant domain shifts, meaning that statistical characteristics (e.g., color distribution, resolution, lighting conditions) of the data can vary widely. Deep learning models are sensitive to such variations, and when faced with data from disparate sensors, they may struggle to generalize well to unseen sensor data. Further, data from disparate sensors may have inconsistencies in labeling or annotation standards with ground truth labels not being directly comparable between sensors, leading to challenges in creating a consistent and accurate training dataset.

The uncertainty of inundation data used to validate our models has the potential to introduce observational bias. That said, our bias scores were all positive and small, indicating that satellite video derived flood extents either largely matched or were slightly overestimated by model predictions. Satellite-based observations, both optical and radar, face well documented limitations including cloud cover as well as uncertainties associated with the timing of sensor overpass relative to the advancement of the flood wave. Incorporation of some of these observational uncertainties (such as timing of the sensor overpass) would clearly offset some of the error related to our validation. Previous studies have relied on machine learning models (e.g. Tanim *et al.*, 2022), thresholding techniques (e.g. Tiampo *et al.*, 2022) and histogram-based models (e.g. Singh and Kansal, 2022) to derive flood extents for model validation. Departing from these well-established methods, our trained neural network extracted flood extents from RGB images in a topographically complex natural river floodplain. Our results demonstrate that satellite video RGB imagery, which is essentially a stack of images rich in temporal dynamics rather than a snapshot in time, can attain acceptable accuracies for flood model validation and can be used in place of multispectral/hyperspectral imagery. Further, as satellite video remote sensing is emerging as a key technology in earth observation, there is great scope for advancing the synergy between deep learning algorithms and high spatial/temporal resolution RGB data in operational flood hazard mapping studies.

5.4.2 Effects of TTA on segmentation performance

Although implementing TTA introduced additional computational overhead during inference, since we had to process multiple augmented versions of each test image, the performance gains offered outweighed the computational cost. Similar to the findings of Liu *et al.* (2022) who utilized TTA during semantic segmentation of their remote sensing images, we found that the skill of both our models improved. In general, both models M_{obs} and $M_{qmaxpost}$ were highly sensitive to TTA with significant disparity between model skill at both validation locations reported (Table 5.5). CSI, model bias and *F* scores all improved significantly, while the flood capture/hit rate decreased, indicating an increase in model overprediction as the segmented flood pixel class reduced. The sensitivity of model CSI performance to TTA was heighted more in validation location B where flood extent was less constrained by topography leading to more favourable *F* scores as compared to location A.

It is further manifest from our results that where model performance matters most, in zones of complex channels with localised spill, our *HR*, CSI and *F* scores remained high, demonstrating satisfactory flood extent prediction accuracy by our hydraulic model. Overall, we find that TTA helped our model to generalize better and reduced overfitting to our test image set.

5.4.3 2D Model validation using satellite video derived flood extents.

The performance of our 2D hydrodynamic models in reproducing observed flood extent varied significantly, highlighting a key result – that discharge data uncertainty is a fundamental driver of out-of bank flood processes and plays a crucial role in model evaluation. It is well established in literature that an assessment of the uncertainty of input boundary data is cardinal to any model validation exercise (Grimaldi *et al*., 2016b; Hoch and Trigg, 2019). Streamflow data from stage-discharge relations has been reported to have errors as much as 20% or more during extreme floods (McMillan *et al*., 2012), further underlining the importance of quantifying discharge data uncertainty when deriving inundation maps from hydraulic models (Bales and Wagner, 2009). We observed that the input boundary condition (inflow hydrograph) had a strong effect on the modelled flood extent at both the lower and upper reaches of our study area where flood capture (*HR*) varied by an average of 5% when using uncertain discharge estimates to drive our model, which also explained the variance in other validation scores. Although inundation extent by itself may not be sufficient for the assessment of model skill, and is primarily effective in flat extensive floodplains (Hesselink *et al*., 2003), our results account for uncertainty typically ignored in most inundation modelling studies. At a minimum, we propose that an appropriate application of 2D model simulations for generation of flood inundation maps must account for discharge uncertainty, especially in highly variable terrain, if reliable extent maps are to be expected.

Although most of the differences between the skill of our models could be attributed to streamflow uncertainty, there remains some uncertainty linked to the satellite observation data, likely linked to the timing of image acquisition. Previous research (Horritt, 2006) found that satellite inundation data may have added uncertainty if the overpass does not coincide with the advancement of the flood wave, which was the case in our investigation as the satellite video was acquired during the receding phase of the flood event when the floodplain was gradually dewatering. Nevertheless, an improvement in identifying flooded pixels correctly when using uncertain streamflow estimates shows that our analysis adopted a reasonable compromise with regards to total uncertainties and that the presence of uncertainty in the observed satellite video did not significantly impact our findings. These conclusions further advance the evidence rendered by Grimaldi *et al*., (2016) who similarly singled out the uncertainties of upstream boundary conditions as the prime propagator of error when calibrating and validating hydraulic models. Therefore, evaluating the skill of models remains a challenging task due to the residual uncertainty in validation data coupled with the inconsistencies inherent in evaluation metrics, whose reliability varies depending on flood magnitude.

5.4.4 Limitations in applying satellite video for flood model validation

Our study evidenced the utility of satellite video datasets in assessing reach scale 2D hydraulic model simulations. The likely future proliferation of nanosatellite constellations will lead to more opportunities to acquire satellite video. However, satellite video datasets come with limitations that can affect their applicability and accuracy in analyzing river dynamics. While video datasets capture dynamic changes over the time of recording, their spatial resolution is still limited compared to dedicated high-resolution still imagery. Moreover, limited spectral bands in satellite video means that some information relevant to river dynamics is not available, especially when compared to multispectral still imagery and Synthetic Aperture Radar (SAR) data. Near-infrared (NIR) bands are particularly beneficial in providing crucial information for delineating flood extents. SAR imagery, which operates in the microwave region of the electromagnetic spectrum and can capture data under various atmospheric conditions and at different times (night and day) make it highly reliable during stormy or cloudy conditions when optical sensors are ineffective. Similar to other commercial satellite data, satellite video is not yet open access and requires tasking for image acquisition. Further, the current satellite video imaging catalogue is very limited compared to other publicly available still image satellite data.

Our use of temporally and spatially autocorrelated data from the same event for both training and testing can lead to overestimation of the deep neural network’s performance. This is because the network was not challenged with data that significantly differed from what it had already encountered. This narrow dataset scope limited our neural network’s exposure to diverse flood characteristics like varying water levels, different terrain types, or urban versus rural flood dynamics. In urban settings, complexity increases due to diverse features like buildings, roads, and varied land use. Our hybrid deep neural network fine-tuned with rural catchment data, might not perform as well in urban landscapes without additional training on urban-specific features. To address the potential overestimation of our network's performance due to the use of autocorrelated data, we fine-tuned a deep neural network that had been pre-trained on ImageNet, a large and diverse dataset encompassing a wide range of scenes and objects. This preliminary training provided our model with a foundational understanding of varied features and textures, which is beneficial for initial feature detection in flood scenarios.

Despite this initial step, the use of more diverse and distinct flood scenes for training and testing remains crucial. While the pre-training on ImageNet partially compensated for the lack of diversity in our flood-specific dataset, it cannot entirely substitute for the direct input of varied flood scenes. Future research could focus on incorporating datasets that include multiple flood events from different geographical locations and times. This will significantly improve the ability of deep neural networks to generalize and perform accurately across various real-world flooding scenarios. Additionally, the challenge of determining optimum threshold values in semantic segmentation was amplified by our dataset's limited diversity. Addressing this limitation by testing and optimizing deep neural networks across a variety of flood events would aid in identifying more universally applicable threshold values. The development of more adaptable neural network models, capable of adjusting threshold parameters based on the characteristics of each unique flood event, remains a key area for future improvement. In our study, we acknowledge a limitation inherent to satellite imagery, which may not effectively identify very small flood depths, such as those measuring a few centimeters. It is imperative to highlight that our hydraulic model output deliberately maintains these small flood depths without any filtering. This strategic decision is grounded in the pursuit of a holistic representation of flood extents, aligning with established practices in flood modelling (Bernhofen *et al*., 2018; Wing, 2019; Wing *et al*., 2017). By retaining the entirety of the hydraulic model output, we ensure transparency, objectivity, and a comprehensive assessment of the flooding scenario in our study area.

Nonetheless, our approach is pioneering in its use of satellite video for flood analysis, providing a valuable proof of concept and a baseline for future models that could be trained and validated on more varied datasets.

5.4.5 2D Model validation using satellite video derived velocities.

Although our 2D model predictions performed on par with results from scientific literature (Barker *et al*., 2018; Pasternack, 2011), the uncertainty associated with the choice of a depth-averaging constant remained consistent. Complexities surrounding spatial variations of flow velocities, channel geometry, bed roughness and the transient nature of river flows means that published depth-averaging constants must be used judiciously. Similar to other studies where LSPIV velocities were depth-averaged using α coefficients (e.g., Le Coz *et al*., 2010;

Masafu *et al*., 2022; Vigoureux *et al*., 2022), we find that α value of between 0.9 – 1 to be more realistic. Recognizing that 2D models, like all models, have limitations that impact their accuracy and reliability, we acknowledge that in fact, a more robust means to validate the accuracy of our satellite-based LSPIV velocities would be against aDcp or other observed data such as that collected by current/electromagnetic meters – the gold standard for field-based river velocity measurements. However, here we aim to build upon previous studies that have estimated river surface velocities (Legleiter and Kinzel, 2021a) and further show that an independent satellite-video dataset can attain equally comparable results which can be validated by 2D model simulations.

5.4.6 Satellite video for flood risk science: current status and future perspectives

High resolution full-color earth observation video presents a fundamental paradigm shift away from the conventional periodic snapshots offered by most current satellite platforms with imagery sensors. Although full-motion satellite video offers previously unavailable temporal insights for monitoring flood dynamics, this data will not necessarily replace conventional earth observation missions but rather they will augment current sensors to foster further advances in hydrological process understanding. Moving from single image analysis to processing video streams presents a unique challenge due to the sheer size of satellite video. However, parallel developments in data analytics such as machine and deep-learning techniques are making processing of such big datasets less computationally intensive. Satellite video sensors suffer from the key constraint of cloud cover which impairs their ability to provide quality imagery during potentially critical storms which are typically accompanied by cloudiness. However, as demonstrated here, for large catchments where a period of clear skies follows a storm and the passage of a flood wave has relatively long duration, daylight acquisition satellite video is feasible. Although spatial and temporal-based cloud removal methods in optical satellite imagery have been proposed (e.g. Huang *et al*., 2015; Li *et al*., 2019), their application in satellite video scenes is yet to be explored and changes in cloud obscuration are likely to be minimal during a single video sequence.

Nanosatellite constellations, such as CubeSats, which are highly modular and inexpensive imagers, are rapidly allowing real-time delivery of RGB video with very high-frequency revisits, up to 15 minutes for some constellations (Ivliev *et al*., 2022; Liddle *et al*., 2020; Lomaka *et al*., 2022; Marinan *et al*., 2013). As satellite video becomes increasingly available to commission, new opportunities for applications such as direct estimation of discharge from space are now in the horizon. Legleiter and Kinzel, (2021) used satellite video to estimate flow velocities of the Tanana River directly from space. The production of digital surface elevation models using satellite video and Structure-from-Motion (SfM) photogrammetry type techniques was proposed by d'Angelo *et al*., (2016, 2014). Combining space-derived velocities with quality digital elevation and bathymetry data presents the potential for estimating discharge from flash floods and ungauged catchments where in-situ gauges might be too expensive to install and operate. The UK's Centre for Ecology and Hydrology FluViSat study ("FluViSat - Hydrological Flow Measurements from Satellite Video,", https://www.ceh.ac.uk/our-science/projects/Fluvisat, last access: 16 August 2023) currently underway, is another application that will aim to demonstrate computation of surface velocities and river discharges using satellite video. Nanosatellite constellations, which are any satellite with a mass between 1 – 10 kg including Cubesats and SunSats, are widely believed to the future of low Earth orbit observations. These satellites are cheap to launch and provide high revisit capabilities as compared to other larger satellite missions. Such disruptive earth observation technologies, combined with rapidly advancing big data analytics will transform satellite video applications in flood hydrology.

5.5 Conclusion

Using satellite video-derived flood extents and velocities, we were able to assess the skill of a two-dimensional hydraulic model to predict a flood event. Two sets of simulations were undertaken, with one set focused on simulating the flood event whilst accounting for discharge uncertainty while the other set did not account for discharge uncertainty. Flood extents were derived from satellite video scenes using a hybrid transformer-encoder convolutional neural network (CNN)-decoder deep neural network. Leveraging on the transformer's self-attention mechanism and CNN's effectiveness at local spatial feature detection, we attained robust predictions of flood pixels. Implementation of test-time augmentation while delineating flood extents resulted in further improvements in segmentation performance. Validation of both models using flood extents showed good model performance. Models were also validated using satellite based LSPIV; to the best of our knowledge, this study presents the first attempt of this nature to use satellite derived LSPIV velocities for validating 2D model predictions. Although there remains uncertainty with regards to choice of a depth-averaging constant (α), our linear regression models still showed that model-predicted and LSPIV velocities had a significant statistical relationship. This demonstrates the notable benefits of non-contact-based velocity estimation from space, especially during high flow conditions when the use of traditional river velocity measurement techniques is precluded. Although discrepancies between model and satellite-derived flood extents can be linked to other uncertainties, such as those associated with the satellite data itself, topography, and the model, this study emphasized the importance of accounting for uncertainty in discharge; a dominant yet often neglected source of uncertainty which is especially heightened during flood events. We find that accounting for discharge uncertainty had less impact on metrics associated with velocity-based validation than those associated with inundation extent. This is likely due to the fact that model velocity estimates are subject to greater spatial variability from factors such as hydraulic parameters, roughness coefficients and channel geometry. The wider implication of this study is the demonstration that high resolution satellite video has significant potential as a source of temporally rich data for the validation of velocity and extent predictions. With rapid advances in remote sensing sensor technologies and constellations, satellite video is likely to become more straightforward and cheaper to commission. In many regions of the world, where ground-based hydrological observations are not routine, this will open the door for wide-scale observations of flow velocities and extents in real-time, enabling further progress in the science of flood modelling.

Chapter 6 - Satellite video remote sensing for estimation of river discharge

The following chapter is a reformatted version of a manuscript published in *Geophysical Research Letters* by Christopher Masafu, Richard Williams & Martin D. Hurst available at: https://doi.org/10.1029/2023GL105839

Key Points

- Satellite video acquired along 12.6 km of the River Darling, Australia, at 5 Hz for 28 s during a 1-in-5-year storm event.
- Satellite video-based velocities coupled with high resolution topography estimate riverine discharges to within 15% of *in situ* gauge data.
- Parametrization of non-contact velocimetry and choice of a depth-averaging coefficient (α) influence the accuracy of discharge estimates.

Abstract

We demonstrate that river discharge can be estimated by deriving water surface velocity estimates from satellite-derived video imagery when combined with high-resolution topography of channel geometry. Large Scale Particle Image Velocimetry (LSPIV) was used to map surface velocity from 28 s of 5 Hz satellite video acquired at a 1.2 m nominal ground spacing over the Darling River, Tilpa, Australia, during a 1-in-5-year flood. We stabilized and assessed the uncertainty of the residual motion induced by the satellite platform, enhancing our sub-pixel motion analysis, and quantified the sensitivity of image extraction rates on computed velocities. In the absence of in-situ observations, LSPIV velocity estimates were validated against predictions from a calibrated 2D hydrodynamic model. Despite the confounding influence of selecting a surface velocity depth-averaging coefficient, inference of discharge was within 0.3 – 15% compared with gauging station measurements. These results provide a valuable foundation for refining satellite video LSPIV techniques.

6.1 Introduction

Globally, 29% of the world's population is exposed to flood risk and insecure water supplies, yet knowledge of the river discharges upon which flood and water resource management depends remains inadequate (Rentschler and Salhab, 2020). Global monitoring networks for quantifying river discharge are in decline, gauging remains logistically difficult and there are political influences on data sharing (King *et al.*, 2018; Lins, 2008; Zakharova *et al.*, 2020). However, satellite-based remote sensing approaches to monitoring discharge are helping to alleviate these issues (e.g., Sichangi *et al.* 2016).

Approaches to satellite-based river discharge monitoring typically rely upon statistical and hydraulic approximations to make indirect estimates of river discharge. Widely applied satellite radar altimetry measures water elevations at virtual river cross-sections (Revel et al., 2023; Angelica Tarpanelli et al., 2013; Zakharova et al., 2020) and near-simultaneous optical imagery can be used to infer water surface flow velocity from space (Kääb *et al.*, 2019). Other satellite approaches have relied on remote sensing of discharge (RSQ) algorithms, which retrieve hydraulic variables from remotely sensed data and then relate these quantities to river discharge (Q) (e.g., Gleason and Durand, 2020; Riggs *et al.*, 2022). These techniques are limited by relatively coarse spatial resolution and the requirement for near-simultaneous satellite swath overlaps, constraining global coverage.

High resolution commercial satellite video sensors can record the dynamics of river flow and floods. Optical flow measurement algorithms can estimate velocity by tracking the movement of visible features between frames (e.g., Eltner *et al.*, 2019; Perks *et al.*, 2020). Currently, optical satellite video acquired by low earth orbiting sensors offer spatial resolutions (pixel sizes) ranging from 0.9 – 1.2 m at frame rates up to 30 Hz [e.g. SkySat (Bhushan *et al.*, 2021) and Jilin-1 (European Space Agency, 2022) constellations]. Inference of flow velocities using satellite video has previously been demonstrated by Legleiter and Kinzel (2021), who used 17 frames of cloud-free satellite video acquired by Planet Labs SkySat constellation of the Tanana River in central Alaska. Surface flow velocities were estimated to within 8.65% of radar gauging measurements and were further assessed using asynchronously acquired acoustic Doppler current profiler (aDcp) velocity data.

We apply and test the use of satellite video-based velocities for estimating discharge. We couple freely available, high-resolution topographic data with velocity estimates derived from satellite video Large-Scale Image Velocimetry (LSPIV) (Lewis et al., 2018; Muste et al., 2008b) and some critical assumptions regarding channel hydraulics to estimate flood discharge following monsoonal rainfall in Darling River at Tilpa, Australia. The accuracy of satellite video-derived velocity estimates was assessed via comparison to hydraulic model simulations; and discharge estimates were compared with in-situ gauging station observations.

6.2 Study Area

The River Darling at Tilpa is located within the Murray-Darling basin, with a 502,500 km^2 drainage area (Matheson and Thoms, 2018; Murray-Darling Basin Authority, 2010) (Figure 6.1). The river basin has a strongly episodic climate, with large floods followed by lengthy dry spells due to the influence of the El-Niño-Southern Oscillation (Grimaldi *et al*., 2019). Prolonged rainfall across south-eastern Australia from late February to early April 2022 led to a flood event with a 5-year return period (Q = 722 m^3 s^{-1}). This location is ideally suited to testing our ability to measure river discharge using non-contact, image-based velocity calculation techniques due to the availability of: (i) cloud-free satellite video sensor overpass; (ii) high-resolution LiDAR digital elevation model (DEM) that was acquired when the river bed was dry and; (iii) gauged in-situ discharge observations at Tilpa (Station number 425900; Water New South Wales, https://realtimedata.waternsw.com.au/, last access: 6 March 2023).

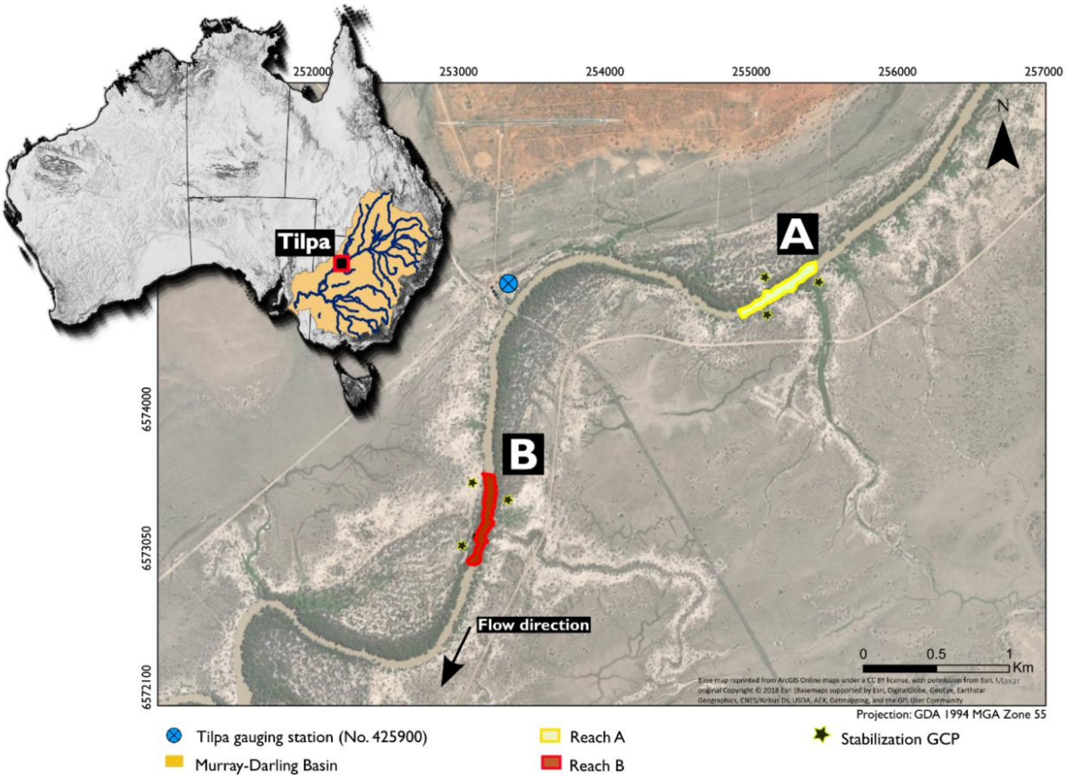

Figure 6.1 Study area indicating investigated reaches A and B.

6.3 Data and Methods

6.3.1 Satellite Video

Satellite video was acquired over our study area on 5 February 2022 at 23:12 UTC by a Jilin-1 GF-03 sensor, part of the constellation by the Chang Guang Satellite Technology Company. Video had a 1.22 m spatial resolution and native frame rate of 5 Hz for 28 seconds. To counter sensor platform movement and scene ‘morphing’ due to the changing view angle of the satellite overpass, we stabilized the video using FIJI’s TrakEM2 plugin (Cardona *et al.*, 2012; FIJI-ImageJ, 2020; Schindelin *et al.*, 2012). FIJI is an open-source image processing toolkit. TrakEM2 relies on a Scale Invariant Feature Transform (SIFT) algorithm to align image stacks based on common features. To avoid geometric distortions, and because all video frames had a similar resolution, we utilized an affine transform to register our image stacks.

Temporal displacement errors related to image stabilization can significantly influence the accuracy of LSPIV velocities. We quantified the temporal distribution of frame-by-frame residual motion, by evaluating the cumulative frame-by-frame displacement (*d*) of six manually selected ground control points (GCPs; Figure 1) in every frame of the stabilized frame sequence. The movement of these GCPs post-stabilization provided a clear picture of the residual motion. To analyze this residual motion, we employed the differential Root Mean Square Difference metric (*d*(RMSD)) (Ljubičić *et al.*, 2021). The *d*(RMSD) metric quantified the magnitude of the residual displacement of static features, based on a pixel intensity RMSD. This RMSD metric operates by directly comparing several subregions within subsequent images. In each subregion, it calculates the differences in pixel intensities at corresponding locations between two images. These differences are then squared, summed over all pixels in the subregions, and averaged. The square root of this average provides the *d*(RMSD) value. This value quantified residual motion magnitude and aided in understanding the temporal distribution of residual displacements in the video.

6.3.2 Large-scale Particle Image Velocimetry

LSPIV, based on Eulerian principles of motion (Euler, 2008), was originally introduced by Fujita *et al.*, (1998), enabling the estimation of instantaneous flow velocities from a series of consecutive images. Here, LSPIV velocities were computed using PIVlab (Thielicke and Sonntag, 2021; Thielicke and Stamhuis, 2014).

Computation of surface flow velocities in PIVlab is attained by cross-correlation algorithms applied to orthorectified images recorded at a known time interval. We evaluate the accuracy of both Fast Fourier Transform window deformation (direct FFT correlation with multiple passes and deforming windows) and Ensemble correlation (Figure 2). Interrogation areas (IA), which are small windows of defined size (in pixels), are used to track the displacement of image patterns within a chosen larger search area (SA) in subsequent images. The multi-pass FFT window deformation approach allows for the spatial resolution of velocity measurements to be improved through multiple reductions in the size of the interrogation areas over which correlations are calculated. Ensemble correlation is better suited for sparsely seeded images as it relies on averaging correlation matrices followed by detecting a correlation peak with the resultant benefit of lower bias and displacement errors (Thielicke and Sonntag, 2021). Given the relatively coarse spatial resolution of satellite video frames for PIV, where inter-frame movement of features are small, often less than the width of a single pixel (e.g. Legleiter and Kinzel, 2021), PIVlab's sub-pixel motion estimation functions allow for more accurate and reliable sub-pixel peak determination. PIVlab implements both 2.3-point and 9-point Gaussian functions to resolve sub-pixel displacements (see Thielicke, 2014 for detail) making sub-pixel motion estimation possible.

We focused on two cloud-free and straight river reaches A and B (Figure 1) to reduce computational cost. Image pre-processing was performed to amplify the visibility of surface tracers with respect to the background (riverbanks/static ground), applying a Contrast-limited adaptive histogram equalization (CLAHE) filter (with a window size of 8 pixels, matching our smallest IA size, see section 3.2.1) to enhance image contrast (Li and Yan, 2022; Masafu *et al*., 2022). Pre-processing of images for LSPIV has a significant impact on the quality of flow velocity estimates. Although image enhancement techniques such as high pass filters and intensity capping (amongst a multitude of others) exist, CLAHE offered a balanced approach to image enhancement due to its ability to enhance local contrast and visibility of tracer particles without excessively amplifying noise.

Distinct features on the water surface were difficult to discern in the raw images, which would be expected in natural rivers observed from the height of the optical sensor. However, CLAHE contrast enhancement enabled the tracking of seeding surrogates in the image sequences, which occur when specular reflection formed by incident light interacts with free-surface deformations on the river. Image intensity variations associated with these surface deformations were visible in post-processed images.

6.3.2.1 Sensitivity to Image Frame Rate and PIV algorithm

The primary free parameters in LSPIV are the sampling frequency (frame extraction rate), interrogation (IA) and search (SA) areas; optimal configurations vary significantly (Kim *et al.*, 2008; Legleiter and Kinzel, 2020; Sharif, 2022). IA should be small enough to eliminate spurious velocities whilst being large enough to accommodate an adequate window for surface pattern tracking (Tauro *et al.*, 2018; Zhu and Lipeme Kouyi, 2019). Sampling frequency (frame extraction rate) and the IA are closely coupled and must be considered in tandem, with frame-to-frame displacement influencing the accuracy of pattern/particle detection on images.

FFT window deformation and Ensemble correlation algorithms were utilized with the maximum allowable number of PIV algorithm passes within PIVlab (four) for our sensitivity analysis (see Zhu and Lipeme Kouyi, 2019). We processed images using an IA of 64×64 pixels, with successive passes of 32×32, 16×16 and 8×8 pixels, all with 50% overlaps, corresponding to a minimum spatial distance of 9.8 m. SA sizes for our analyses were 128, 64, 32 and 16 pixels. For the ~70 m wide river, this was sufficient to allow the detection of displaced surface features. Whilst smaller IAs would allow for higher-resolution vector maps, this would also significantly increase noise and thus the number of erroneous correlations.

We processed two configurations based on FFT window deformation and ensemble correlation algorithms at three sampling rates (1, 0.5 and 0.25 Hz), resulting in 6 different LSPIV runs for each scenario. These sampling frequencies resulted in image sequences consisting of 28, 14 and 7 frames which enabled us to experiment with varied frame extraction rates for image-based velocity analysis. Subsampling our original 5 Hz video to lower frame rates (similar to the approach taken by Legleiter and Kinzel, 2021) was beneficial for detecting velocities, especially for slower-moving phenomena. At a lower frame rate, features in our video had more time to move between frames, resulting in larger displacements that are easier to detect and measure, particularly when dealing with a nominal ground resolution of 1.2 m.

Following LSPIV cross-correlation, we post-processed the resultant velocity fields to filter out spurious velocities. Specifically, we utilized filters that removed velocity vectors that differed by 8 x (PIVLab's default threshold) the standard deviation from the mean velocity, and further applied a local median filter threshold of 3 x 3 pixels to remove outliers. Velocity vectors were georeferenced within PIVlab from an image coordinate system back into a projected coordinate reference system (GDA 1994 MGA Zone 55). We used GCP coordinates to assess the accuracy of our georeferencing against actual locations, using 1 m Maxar satellite imagery.

6.3.2.2 Validation of PIV velocity vectors

We use a calibrated 2D hydraulic model to evaluate the accuracy of LSPIV velocities. 2D models offer particular value as they can map velocities in diverse hydraulic conditions rather than at a few idealized sections, including locations where the range and resolution of traditional equipment (such as aDcps and current meters) is limited or where the deployment of velocity sensors can be complex, time-consuming, and hazardous, particularly during flood events when flow depths and velocities prevent field deployment.

6.3.2.2.1 HEC-RAS 2D Hydrodynamic Modelling

The hydrodynamic model HEC-RAS (6.4.1), developed by the U.S. Army Corps of Engineers (USACE) has been used in various catchments for one-dimensional (1D), two-dimensional (2D), and coupled (1D/2D) flood simulation studies (see, for example, Costabile *et al*., 2020; Dasallas *et al*., 2019; Patel *et al*., 2017). Here we perform unsteady flow modelling using HEC-RAS's full 2D Saint Venant equations (full momentum) as we aim to obtain detailed velocities and water surface elevations for a river in flood flow.

The input data requirements and parameters for 2D modelling were: a digital terrain model; a computational mesh; boundary conditions; computation simulation interval and Manning's roughness coefficient values. Topographical data was a 1 m resolution LiDAR-based bare-earth digital surface model acquired when the river channel was dry (Geoscience Australia, 2022). A hybrid 2D computational mesh was defined using a cell size of 30 x 30 m across the floodplain and 2 x 2 m between channel banks. Model upstream inflow boundary conditions were set using data from the gauge located at Tilpa (Figure 6.1), with 15-minute interval gauged streamflow being used. The model's downstream boundary condition was normal depth, which required a single energy slope to be computed (0.0028) which is then in turn used in a Manning's equation to compute the downstream stage for any flow occurring.

6.3.2.2.2 Model Calibration

Model calibration data were available in the form of stage height from the gauge at Tilpa (Figure 6.1). 2D model runs were calibrated by adjusting a spatially discretized manning's roughness coefficient *n* over a parameter space between 0.025 – 0.033 until model simulations closely matched observed stage height data. Modelled stage height accuracy was assessed using two commonly used metrics (Moriasi *et al.*, 2007), the percent bias (PBIAS) (Equation 6.1) and root-mean-square error (RMSE) (Equation 6.2).

$$PBIAS = \frac{\sum_{i=1}^{n}(Y_i^{obs} - Y_i^{sim})^2}{\sum_{i=0}^{n}(Y_i^{obs})} \tag{6.1}$$

$$RMSE = \sqrt{\sum_{i=0}^{n}\frac{(Y_i^{obs} - Y_i^{sim})^2}{n}} \tag{6.2}$$

where Y^{sim} is simulated values, Y^{obs} is observed values and *n* is the number of observations.

The 2D hydraulic model was calibrated to observed stage at the Tilpa gauging station by varying Manning's *n* roughness values in the range of 0.025 to 0.033, with 0.002 increments. *n* values of 0.031 minimized stage simulation error. In our investigation, the 2D model was considered to be adequately calibrated with RMSE (0.46 m) and PBIAS (0.77), comparable to ranges reported in other similar studies where HEC-RAS 2D flood flow simulations were calibrated against observed water levels (see, for example, Iroume *et al.*, 2022; Timbadiya *et al.*, 2011; Zeiger and Hubbart, 2021).

6.3.2.2.3 LSPIV velocity vector validation metrics

We verified the accuracy of our PIV derived vectors against derived velocity predictions from our calibrated HEC-RAS 2D model. We used a suite of validation metrics commonly used in literature including basic statistical measures such as mean absolute error (MAE) and RMSE-observations standard deviation ratio (RSR) (Equations 6.3 and 6.4 respectively). We also report regression analysis results including regression slope and intercept standard errors and R^2 values.

$$MAE = \frac{\sum_{i=1}^{n}\left|Y^{obs} - Y^{sim}\right|}{n} \tag{6.3}$$

$$RSR = \frac{RMSE}{STDEV_{obs}} = \frac{\sqrt{\sum_{i=0}^{n}(Y_i^{obs} - Y_i^{sim})^2}}{\sqrt{\sum_{i=0}^{n}(Y_i^{obs} - Y^{obs,mean})^2}} \tag{6.4}$$

where Y^{sim} is simulated values, Y^{obs} is observed values and *n* is the number of observations.

6.3.3 Discharge estimation using LSPIV velocities

The velocity-area method was used to calculate discharge (*Q*) (Turnipseed and Sauer, 2010). Channel depth and velocity are integrated from discrete locations along a channel's width. Discharges estimated at each vertical sections spanning the channel width are summed to total discharge (*Q*) (Cohn *et al*., 2013).

$$Q = \sum_{i=1}^{m} A_i v_i = \sum_{i=1}^{m} b_i d_i v_i$$

where *m* = number of verticals across channel; A_i = cross-sectional area of vertical *i?*; b_i = width of vertical $i = (x_{i+1} - x_{i-1})/2$ with *x* = horizontal distance of vertical from the edge of water; d_i = average depth of vertical *i*; and v_i = average downstream velocity in vertical *i*. We define a minimum of 25 vertical subsections at each cross-section, with sub-sectional area extending half the distance to the preceding and following measurements.

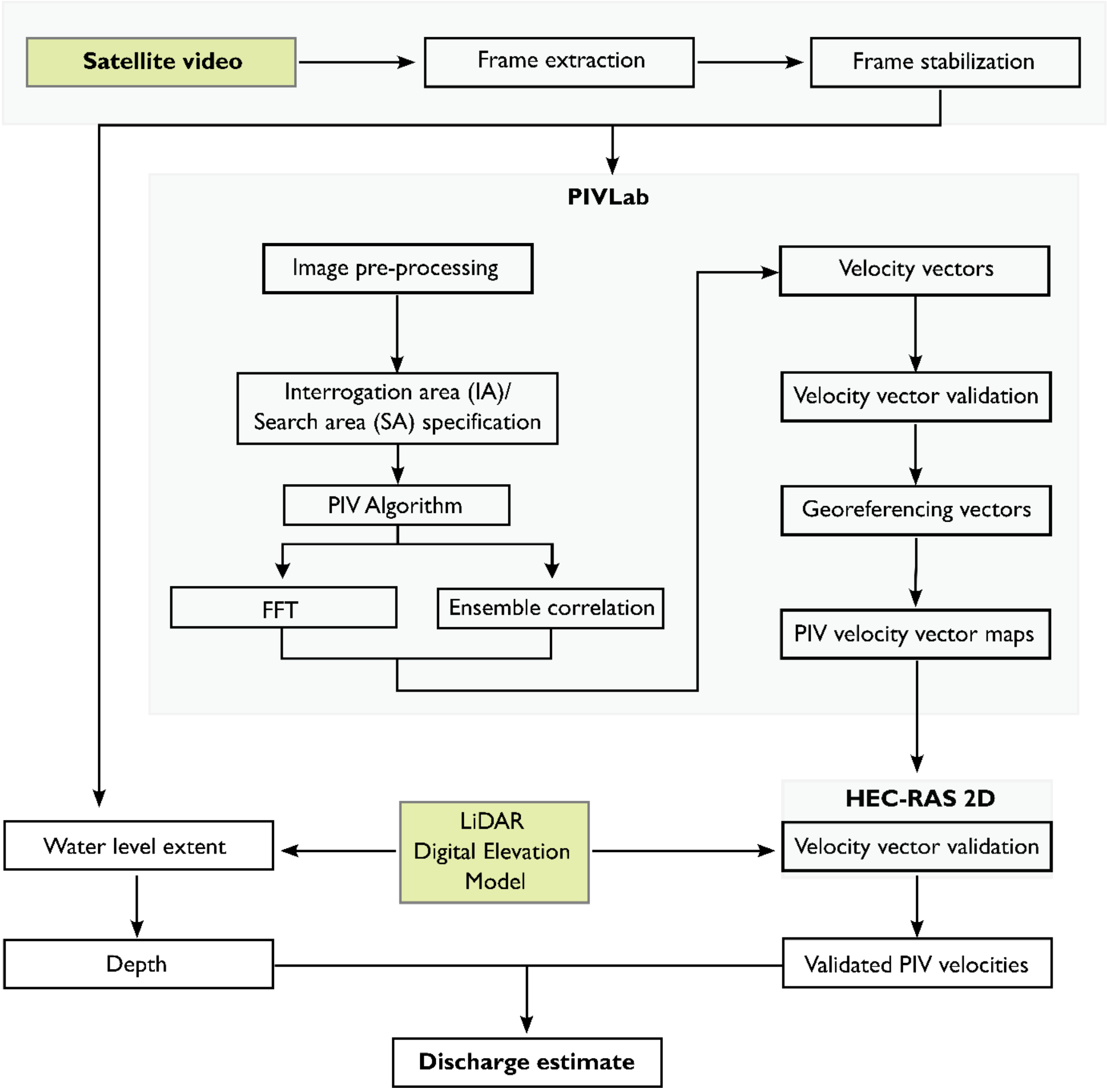

Figure 6.2 Discharge estimation workflow

Water depths were estimated by intersecting the flood extent limits in the satellite imagery with a DEM. Depths at each vertical are computed by subtracting the local bed elevation from the maximum water elevation along a cross-section (Figure 6.2) from a 1 m resolution LiDAR DEM with a vertical and horizontal accuracy of 0.3 m and 0.8 m respectively (Geoscience Australia, 2022). The DEM was acquired when the river channel was dry, effectively incorporating bathymetry. Since PIVLab provides discrete velocity measurements at specific vector locations, interpolation was necessary to obtain continuous velocity maps. Here we used inverse distance weighting, a spatial interpolation approach where sample points are weighted based on their distances from the unknown location being interpolated. LSPIV-derived surface velocities along cross-sections are converted to depth-averaged using a specified coefficient α. Hauet *et al.* (2018) and Le Coz *et al.* (2010) constrain α between 0.8 – 1 for deep natural channels experiencing flood discharges.

6.4 Results

6.4.1 LSPIV velocity accuracy

Stabilization and georectification of frames used in PIV are subject to errors that propagated uncertainty to computed velocity estimates. Maximum, minimum, and mean displacement errors associated with stabilization of extracted frame sequences were 0.42, 0.055, 0.237 and 0.442, 0.15, 0.261 pixels for reach A and B respectively, all less than a single pixel width. Total georectification root mean square error (RMSE) was 0.5 and 0.77 m at reach A and B, respectively. Since our smallest search area was 8 pixels, equivalent to a distance of 9.8 m, our residual georeferencing errors were 5.1% and 7.9% of the spacing between our PIV velocity vectors.

Results of the frame-by-frame analysis of residual motion showed that our GCP locations had a high R^2 of the *d*(RMSD) metric at both reach A and B (Figure 6.3 a, b). The displacement of our GCPs in the stabilized frame sequence further confirmed that all our residual motion at both reaches was within the subpixel range, with average displacements of 0.475 and 0.462 pixels at reach A and B respectively (Figure 6.3 c, d).

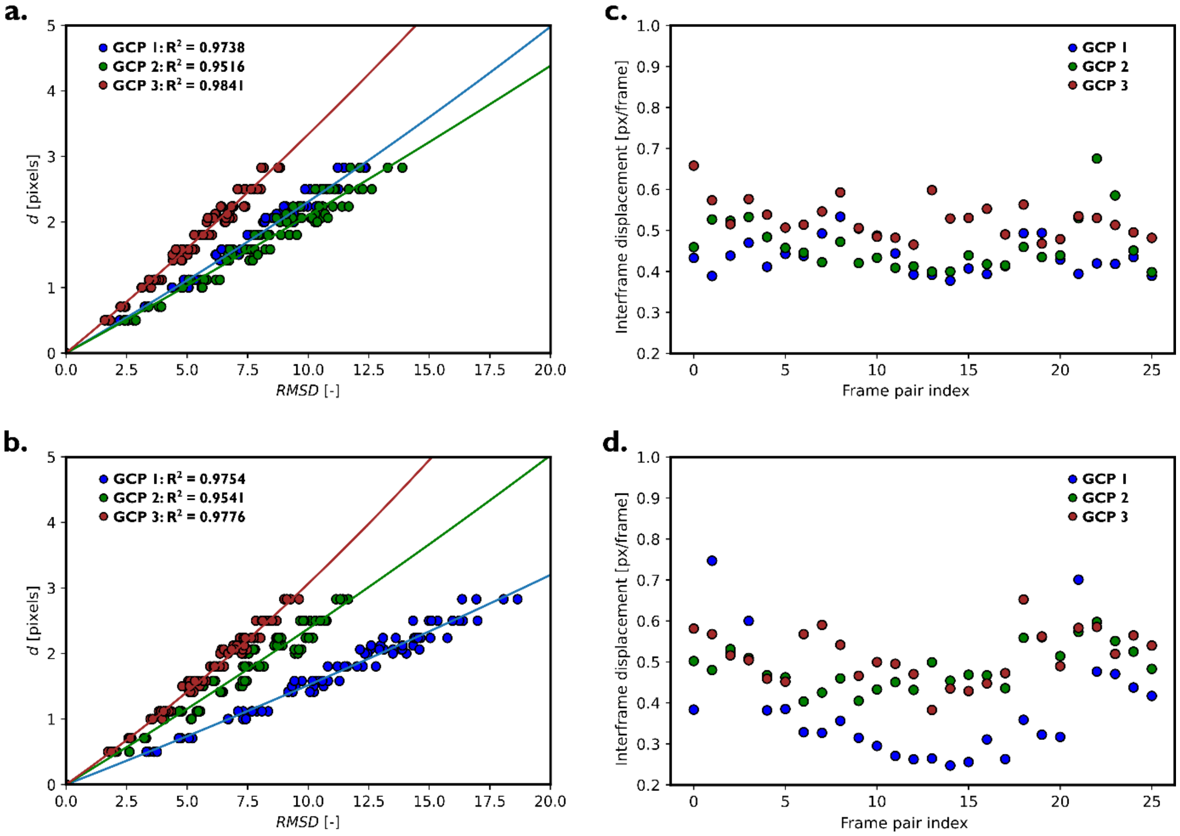

Figure 6.3 Displacement vs. RMSD for Ground Control Points in reach A (a) and B (b). Each color-coded scatter point corresponds to a different GCP, showing how the displacement within a predefined area around each point affects the RMSD. Stabilization

effectiveness across Ground Control Points (GCPs) in reach A (c) and B (d). These plots present the calculated RMSD values for each GCP across different frames, showing the stabilization performance. Each point represents the distance (distortion measure) at a GCP for a specific frame, offering insights into the temporal consistency of stabilization accuracy.

Figures 6.4 and 6.5 summarize the results of the quantitative velocity accuracy assessment of LSPIV (processed using both FFT and Ensemble correlation PIV algorithms at frame rates of 0.25, 0.5 and 1 Hz) against calibrated HEC-RAS 2D model predictions.

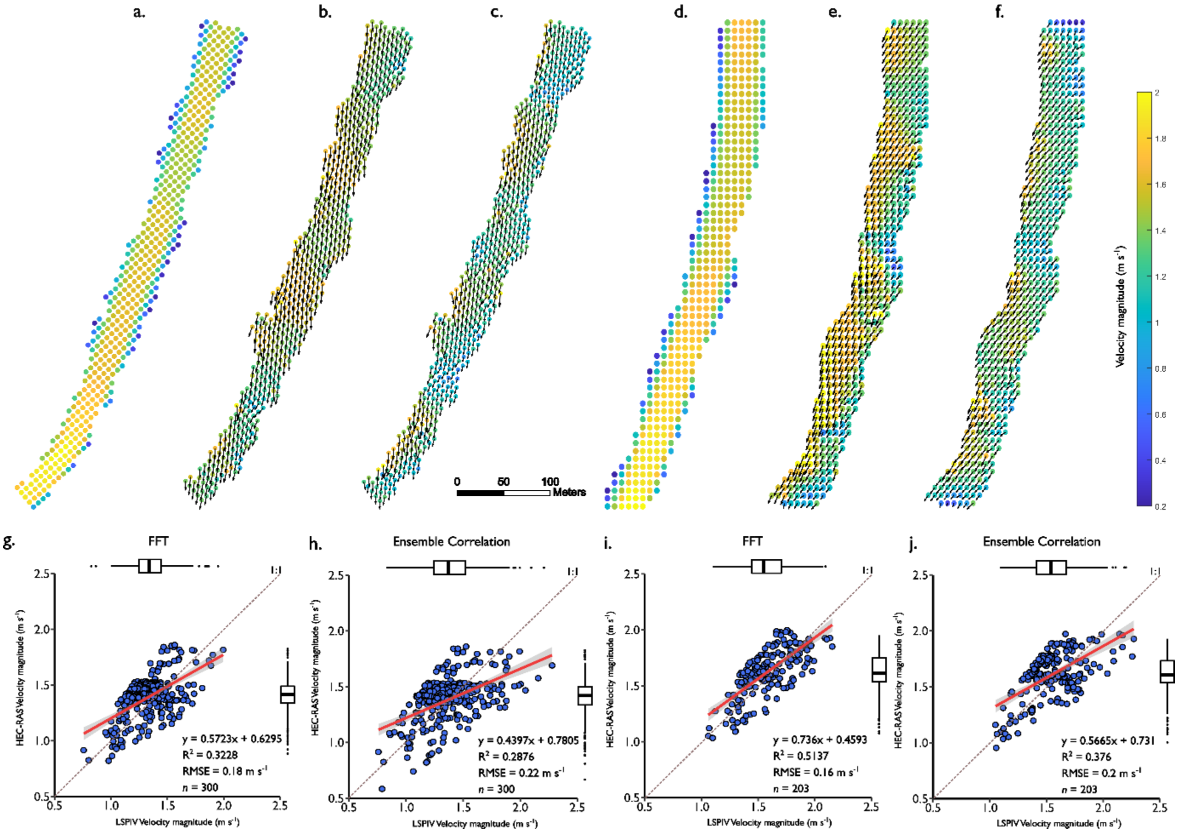

Note. R^2 = coefficient of determination; RMSE = root mean square error; *n* = number of observations

Figure 6.4 Comparative visualization of river flow velocities. (a) and (d): HEC-RAS 2D model-derived velocity fields at reaches A and B. (b), (c), (e) and (f): Surface velocity vectors derived from satellite-based LSPIV, computed using different algorithms. The LSPIV velocity vectors are positioned to correspond precisely with the locations used in the HEC-RAS 2D model. (g) to (h): scatter plots showing correlations between LSPIV velocities and HEC-RAS 2D model predictions.

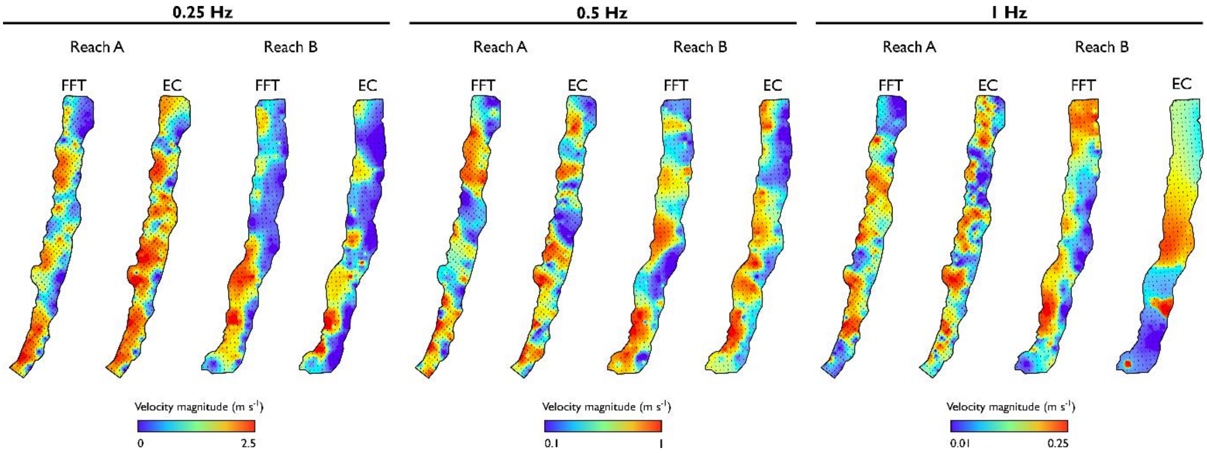

Figure 6.5 LSPIV surface velocity maps for reaches A and B computed using varied frame rates.

Regression analysis results in R^2 values of 0.32 – 0.51 ($p < 0.001$) between LSPIV estimates and HEC-RAS 2D model velocities. To contextualize these results, Legleiter and Kinzel (2021) attained R^2 values of between 0.34 – 0.39 when comparing aDcp versus satellite video-based PIV velocities across their study area. Root Mean Square Error (RMSE) values at the 0.25 Hz frame rate were 0.18 m s^{-1} for FFT and 0.22 m s^{-1} for EC in Reach A, and 0.16 m s^{-1} for FFT and 0.20 m s^{-1} for EC in Reach B. Our results indicated a tendency of the FFT algorithm to underestimate flow velocities in both study reaches. Specifically, for Reach A, the Mean Error observed was −0.071 m s^{-1} suggesting that the FFT algorithm, on average, estimated velocities lower than those predicted by the HEC-RAS model. Similarly, in Reach B, this underestimation persisted, albeit to a slightly lesser degree, with a Mean Error of −0.041 m s^{-1}.

Table 6.1 Error metrics for validation of PIV velocity magnitude vectors against HEC-RAS 2D model predictions at reach A and B using different combinations of PIV algorithms and frame rates.

Error metric	PIV Algorithm	Reach A			Reach B		
		Frame rate (Hz)			Frame rate (Hz)		
		0.25	0.5	1	0.25	0.5	1
R^2	FFT	0.32	0.002	0.03	0.51	0.06	0.04
	EC	0.29	0.02	0.05	0.38	0.19	0.08
RMSE, m s^{-1}	FFT	0.18	1.06	1.32	0.16	1.30	1.54
	EC	0.22	1.07	1.31	0.2	1.23	1.52
MAE, m s^{-1}	FFT	0.15	1.04	1.30	0.14	1.29	1.52
	EC	0.18	1.06	1.29	0.17	1.21	1.51
RSR	FFT	0.98	25.79	85.43	0.79	24.15	113.3
	EC	0.89	13.72	38.07	0.88	8.61	263.2
RS Standard Error	FFT	0.048	0.284	0.749	0.051	0.271	1.087
	EC	0.040	0.148	0.331	0.052	0.094	2.495
RI Standard Error	FFT	0.065	0.098	0.065	0.081	0.093	0.111
	EC	0.056	0.051	0.032	0.081	0.042	0.292
n		300	300	300	203	203	203

Note. R^2 = coefficient of determination; RMSE = root mean square error; MAE = Mean absolute error; RSR = ratio of the root mean square error to the standard deviation of observed data; RS Standard Error = regression slope standard error; RI Standard Error = regression intercept standard error; FFT = direct Fourier transform correlation with multiple passes and deforming windows; EC = Ensemble correlation; *n* = number of observations

6.4.2 Discharge accuracy

The measured discharge was 582.01 m3s-1 at the Tilpa gauge at 23:12 UTC on 5/2/2022. LSPIV-based discharge estimates were computed at three cross-sections located in each reach (Figure 6.1) and ranged from 429.7 m^3 s^{-1} to 710.1 m^3 s^{-1}, with median discharges of 536.2 m^3 s^{-1} (reach A) and 483.4 m^3 s^{-1} (reach B). Mean absolute percentage error for LSPIV-based discharge estimate was 10% (reach A) and 19.7% (reach B), with significant sensitivity to α. At both reaches, we experimented with *α* values between 0.7 – 1.0; previous studies have found that α values of between 0.8 – 1 are appropriate for computing depth-averaged velocities in natural rivers with a depth of greater than 2 m (Hauet *et al*., 2018; Vigoureux *et al*., 2022). At reach A, *α* values in the range 0.8 - 0.9 minimize the difference between PIV-derived discharge and gauged discharge to within 15%. At reach B a narrow band of α values in the range 0.94 - 0.97 minimize the error, and values in the range 0.9 - 1.0 result in MAE < 10%.

Table 6.2 LSPIV-based discharge estimates at reaches A and B

Cross-section	PIV Algorithm	Alpha (α)	Discharge ($m^3 s^{-1}$)	Mean Absolute Error ($m^3 s^{-1}$)	Mean Absolute Error (%)	PBIAS
XS-A1	**FFT**	0.7	497.7	84.31	14.49%	-0.14
		0.8	568.8	13.21	2.27%	-0.02
		0.9	639.9	57.89	9.95%	0.10
	Ensemble Correlation	0.7	389.1	192.91	33.15%	-0.33
		0.8	444.7	137.31	23.59%	-0.24
		0.9	500.3	81.71	14.04%	-0.14
XS-A2	**FFT**	0.7	454	128.01	21.99%	-0.22
		0.8	518.9	63.11	10.84%	-0.11
		0.9	583.8	1.79	0.31%	0.00
	Ensemble Correlation	0.7	404.9	177.11	30.43%	-0.30
		0.8	462.7	119.31	20.50%	-0.20
		0.9	520.6	61.41	10.55%	-0.11
XS-A3	**FFT**	0.7	469.2	112.81	19.38%	-0.19
		0.8	536.2	45.81	7.87%	-0.08
		0.9	603.3	21.29	3.66%	0.04
	Ensemble Correlation	0.7	425.7	156.31	26.86%	-0.27
		0.8	486.5	95.51	16.41%	-0.16
		0.9	547.3	34.71	5.96%	-0.06
XS-B1	**FFT**	0.7	423.4	158.61	27.25%	-0.27
		0.8	483.9	98.11	16.86%	-0.17
		0.9	544.4	37.61	6.46%	-0.06
	Ensemble Correlation	0.7	330.1	251.91	43.28%	-0.43
		0.8	377.3	204.71	35.17%	-0.35
		0.9	424.4	157.61	27.08%	-0.27
XS-B2	**FFT**	0.7	427.5	154.51	26.55%	-0.27
		0.8	488.6	93.41	16.05%	-0.16
		0.9	549.6	32.41	5.57%	-0.06
	Ensemble Correlation	0.7	489.3	92.71	15.93%	-0.16
		0.8	559.2	22.81	3.92%	-0.04
		0.9	629.1	47.09	8.09%	0.08
XS-B3	**FFT**	0.7	375.9	206.11	35.41%	-0.35
		0.8	429.7	152.31	26.17%	-0.26
		0.9	483.4	98.61	16.94%	-0.17
	Ensemble Correlation	0.7	385.6	196.41	33.75%	-0.34
		0.8	440.7	141.31	24.28%	-0.24
		0.9	495.8	86.21	14.81%	-0.15

Note. FFT = direct Fourier transform correlation with multiple passes and deforming windows; RMSE= Root Mean Square Error; PBIAS = percent bias

6.5 Discussion

6.5.1 LSPIV velocity estimation

We quantified video stabilization uncertainties using the *d*(RMSD) metric. Our mean values of displacement following stabilization were both within the subpixel range, with mean *d*(RMSD) being slightly higher than the mean displacement values we obtained following initial stabilization using SIFT (section 6.3.1). The presence of a lower mean displacement alongside higher *d*(RMSD) values highlighted the complex nature of surface flow dynamics and the challenges in capturing these using satellite based LSPIV. It underscored the importance of considering not just the average movement but also the distribution and variability of movement across the video frames. Given our discharge analysis was conducted using velocities derived from a 0.25 Hz sampling rate (i.e., displacements >1 pixel), stabilization errors did not significantly impact the accuracy of our computed velocities (at the 0.25 Hz sampling rate, which provided best correspondence to modelled velocities).

Our sensitivity analysis (section 6.3.2.1) highlighted the significance of frame sampling frequency when computing LSPIV velocities, similar to other investigations (e.g. Legleiter and Kinzel, 2021; Muste *et al*., 2008; Pearce *et al*., 2020). In lieu of reference field velocity measurements, we conducted a direct comparison to 2D model velocity predictions. Statistical analysis of LSPIV velocity deviations, using our best-case scenario of 0.25 Hz processed using the FFT algorithm, showed that LSPIV tended to underestimate velocities compared to 2D model predictions. Our analysis showed variability in the performance metrics (R^2, RMSE, ME) across different algorithms and settings, indicating the accuracy and reliability of satellite PIV can be context-dependent: R^2 values for both algorithms ranged from 0.29 to 0.51. Potential reasons for this variability include limitations due to satellite image resolution, atmospheric interference, and the inherent limitations of PIV in capturing the complex flow dynamics. Both algorithms generally performed better at Reach B than at Reach A, indicating that channel geometry and flow conditions could impact PIV accuracy. Additionally, some variability may be associated with 2D hydrodynamic model uncertainty (Dewals *et al*., 2023; Pasternack, 2011; Bates, 2022). Whilst calibrated 2D models are a viable means to assess PIV velocities for cases where flows exceed the safe operating ranges of conventional sensors, we recommend PIV velocity assessment with aDcp measurements.

6.5.2 Discharge accuracy assessment

LSPIV-based surface velocities, combined with preexisting, independent information on channel bathymetry, have been successfully used to obtain river discharge estimates in previous studies (e.g. Le Coz *et al*., 2010; Lewis *et al*., 2018). Using the velocity-area technique, we estimate discharge with a maximum mean absolute error of 35% which could be reduced to 0.3% and 3.78% at reaches A and B, respectively, by tuning α. The accuracy and precision of our reported discharge estimates compare favourably with Sun *et al*. (2010) and Lewis *et al*. (2018) who computed river discharges using LSPIV-based measurements to within -5 to 7% and < 20% respectively. The ephemeral nature of the River Darling at Tilpa is advantageous for acquiring high accuracy bathymetric topography, here using airborne LiDAR. In other ephemeral locations, lower resolution datasets with near-global coverage could be used for large rivers. In temperate and tropical locations, direct bathymetric surveys or bathymetry derived from multispectral satellite imagery, altimetry (e.g., Liu *et al*., 2020; Moramarco *et al*., 2019) or the inference of depths from PIV-derived velocities using a flow resistance equation-based framework (Legleiter and Kinzel, 2021b) would be required. Despite these additional data demands, our results demonstrate that satellite-based optical video sensors could be deployed for near real-time estimation of riverine velocity and discharge, within tolerable uncertainties common to traditional discharge estimation techniques.

6.5.3 Variability of surface coefficient values, *α*

Our satellite-video based LSPIV discharge estimation procedure yielded promising results, in terms of absolute flow magnitude, but the selection of the coefficient (α), used to convert surface to depth-averaged velocities, remains a source of uncertainty in discharge estimation. Fulton *et al*. (2020), Moramarco *et al*. (2017) and Welber *et al*. (2016) all observed local variability of α (0.52 – 0.78; 0.85 – 1.05 and 0.71 – 0.92 respectively) when estimating discharge using non-contact techniques, attributable to variations in stage (especially during higher flows due to changes in wetted channel perimeter), channel geometry, slope, and channel alignment. Significant shifts in the error of LSPIV-based discharges due to variations in α indicated that sufficient cross-section specificity in defining α is critical to our technique. Higher α values generally led to less error in our discharge estimates, particularly in areas where LSPIV velocities differed substantially from velocities in the hydraulic model sued for benchmarking. Hauet *et al*.,'s. (2018) recommendation of α values based on a river's hydraulic radius and depth, with a noted uncertainty of ± 15% at a 90% confidence level, are consistent with the optimal values reported here. However, without an empirically formulated, river-specific α based on in-situ measurements, the appropriate values of α remains largely unclear (Legleiter *et al.*, 2023).

When estimating flood flows in remote locations where remote sensing instruments are the sole source of depths (i.e., derived from a DEM), experimenting with values provided by Rantz, (1982) (α = 0.85 or 0.86), Turnipseed and Sauer (2010) (α = 0.84 – 0.90), and, in extreme cases, $\alpha > 1$ due to non-standard velocity distributions (see, for example, Moramarco *et al.*, 2017) is a sensible approach to improve the precision of flow measurements from surface velocimetry techniques. On average, in our study the α values that led to the closest approximations of observed discharge were all less than unity, indicating our velocity-depth distributions could be well approximated using logarithmic or power laws. The variability of our best fitting, cross-section averaged α at our reaches implies that the commonly used default value of 0.85 is not always appropriate in field conditions where spatial heterogeneities in channel beds have a significant impact on velocity profiles. Although we provide a method for assessing the variability of α, calibration of site-specific α values based on traditional contact measurements remains the preferred solution for accurate discharge estimation.

6.6 Conclusion

Satellite-based PIV presents a promising tool for estimating river discharges during cloud-free conditions. Key to constraining uncertainty and enhancing the accuracy and reliability of LSPIV-derived velocity estimates is the stabilization of satellite video frames and the independent assessment of residual error, particularly for sub-pixel displacements. Performance metrics from the comparison of PIV velocity magnitude vectors against 2D model predictions of surface velocity exhibited reasonable correspondence. The FFT algorithm at a frame rate of 0.25 Hz, revealed best correspondence, but differences between study reaches highlight how site-specific characteristics can influence LSPIV performance. The observed R^2 values (0.3 - 0.5) highlight the need for careful consideration in the application of PIV techniques, particularly for low-frame-rate satellite videos. LSPIV accuracy also depends on α. Using realistic α values (0.7 to 1.0) from literature, our resulting error and bias was -6.9 $m^3 s^{-1}$/-0.01 and -85.6 $m^3 s^{-1}$/-0.15 at our study reaches. Despite these uncertainties, when combined with high-resolution topographic data, the ability of satellite-based LSPIV to provide large-scale, non-intrusive river surface discharge measurements in inaccessible or dangerous areas remains a compelling advantage. The level of accuracy offers a promising foundation for enhancing LSPIV methodologies; uncertainties are comparable to traditional methods and avoid the need for extrapolation of rating curves during high flow conditions. While acknowledging the necessity for further ground truthing to assess uncertainty, there is considerable potential for satellite video to be used to estimate discharge.

Chapter 7 - Synthesis and discussion

This chapter discusses the substantive research contributions made in this thesis. For this, each of the research questions outlined in section 1.2 are addressed. A critical assessment of the methods is then made, followed by an identification of prospective future research directions building on the work presented herein.

7.1 Synthesis

2D hydraulic model predictions are typically delivered with a degree of uncertainty and yet the robust validation of the skill of these models has been sporadic, thanks to the paucity of observations. New methods were adopted to harness the temporal richness of imagery from UAV and satellite platforms to extract velocities for 2D model validation. This marked the first instance where such comprehensive validation has been undertaken, bridging the gap between new image velocimetry techniques and their tangible application in 2D hydraulic modelling. The choice of a depth averaging parameter when converting surface velocities into depth-averaged velocities was a common theme across all empirical chapters and is recognized as a significant source of uncertainty, even though efforts to address this were made through use of the probability concept. Another significant highlight was the application of satellite video, combined with high resolution topography to estimate river discharge. Although satellite video offers previously unattainable high temporal resolution data, the limitations of cloud cover, typical with optical sensors, were notable through a significant reduction of the portion of video available for analysis. Thus, while these new age datasets offer a venue for comprehensively validating 2D model predictions, their fidelity still warrants further assessment before they can attain widespread adoption.

7.2 Discussion

RQ1a. Can UAV-based video be used to comprehensively calibrate and validate hydraulic model predictions at the reach scale?

The first published example of the comprehensive calibration and validation of a hydraulic model using velocities derived from UAV video was presented in Chapter 4. Flood modelling plays a pivotal role in understanding and managing the complex dynamics of flood events. However, a persistent challenge has been the limited utilization of surface velocities in calibrating and validating these models. Traditionally, flood models have primarily relied on hydrological inputs and water level data for calibration, with surface velocities often overlooked due to the technical complexities associated with their measurement. Chapter 4 addressed the challenge of assessing spatial velocity distributions in hydraulic models and demonstrated how UAV-based LSPIV velocities can be utilized to calibrate and validate 2D hydraulic model predictions in a gravel bed river reach. Chapter 4 further delved into the uncertainty surrounding the accurate determination of the velocity coefficient α, which relates surface velocity to depth-averaged velocity, especially in non-contact velocity computation methods. Prior research (Dramais *et al*., 2011; Vigoureux *et al*., 2022) had highlighted the significant influence of α variability on error in LSPIV-based velocity estimation. Chapter 4 successfully employed Chiu's Probability Concept (PC), based on Shannon's Information Entropy, to compute α values for specific cross-sections, revealing considerable variation across them. Locally derived α values demonstrated improved accuracy in constraining velocity bias and resulted in substantial enhancements in velocity predictions. These findings are aligned with existing research (Fulton and Ostrowski, 2008; Fulton *et al*., 2020a) and suggest that probabilistically determined α values better accommodate the intricacies of field-based velocity distributions, emphasizing the significance of considering alternative velocity distribution approaches when depth-averaging LSPIV velocities.

RQ1b. Can satellite-video based image velocimetry and deep-learning-based image segmentation be used to validate hydraulic model predictions at the reach scale?

Chapter 5 presented results from investigations attempting to validate 2D model predictions using a combination of satellite based LSPIV measurements and flood extents drawn from individual RGB satellite video frames. When validating flood models using satellite-based LSPIV, despite achieving results comparable to existing scientific literature (Barker *et al*., 2018; Pasternack, 2011), the uncertainty tied to selecting a depth-averaging constant, α, which was identified in Chapter 4, persisted. The interplay of flow velocities, channel morphology, bed roughness, and transient river behaviours necessitate careful application of published depth-averaging constants in LSPIV workflows. 2D model predictions were further validated using flood extents segmented by a hybrid transformer-encoder CNN-decoder neural network, with the influence of Test-time augmentation (TTA) on segmentation performance examined. While TTA enhanced metrics like CSI, model bias, and F scores significantly, the flood capture rate decreased, indicating increased model overprediction as flood pixel classification decreased. Model validation highlighted the impact of uncertain discharge data on flood extent accuracy, emphasizing the significance of quantifying discharge data uncertainty for reliable inundation mapping. Crucially, areas with complex channels and localized spill showed sustained high scores in HR, CSI, and F, indicating satisfactory flood extent prediction accuracy by our hydraulic model.

RQ2a. Can image velocimetry techniques provide plausible riverine velocity estimates from space?

Chapter 6 presented the estimation of riverine velocities based on satellite-LSPIV. Sensitivity analysis emphasized the importance of frame sampling frequency in computing LSPIV velocities, as seen in previous satellite-video based LSPIV field studies (such that of Legleiter and Kinzel, 2021). In the absence of reference measurements, we directly compared LSPIV velocities to those from a 2D model (HEC-RAS) simulation. Statistical analysis revealed that LSPIV tended to underestimate velocities compared to the 2D model predictions. While acknowledging the limitations of 2D models, primarily due to simplifications of the complex three-dimensional flow of water, neglecting variations in vertical flow profiles that can occur in real-world scenarios, it was still demonstrated that calibrated 2D models can be used to assess LSPIV velocities, particularly for high flows where conventional sensors are limited.

RQ2b. How well do discharge estimates based on satellite-video compare with ground observations and hydraulic model predictions?

Quantification of river discharge remains integral to effective flood risk management, emergency response and policy making efforts. Chapter 6 furthered previous work on satellite based LSPIV velocity estimation by combining high resolution bathymetric data to derive discharge estimates. By employing the velocity-area technique, discharge estimates closely match gauged measurements to within a 0.3% average difference, when the depth averaging constant α was finetuned. Although the satellite-video based LSPIV discharge estimation procedure yielded promising results in terms of absolute flow magnitude the choice of the coefficient (α) for converting surface to depth-averaged velocities remained a significant source of uncertainty in discharge estimation. In remote locations, using empirically derived values or experimenting with different values of α can enhance flow measurement precision. It was found that site-specific α calibration based on traditional measurements is the preferred approach for accurate discharge estimation.

Riverine velocities derived from satellite video, computed LSPIV, showed promising alignment with predictions from a hydraulic model. Notably, the hydraulic model used was of high resolution and was driven by observed discharges. While there existed some inherent uncertainties in comparing the satellite-derived velocities with the hydraulic model's predictions, the methodology demonstrated significant value. Particularly in regions where direct observations of velocities are scarce or unavailable, leveraging satellite video data processed via LSPIV offers an innovative and efficient approach to estimate flow velocities. This advancement in remote sensing and hydraulic modelling convergence suggests potential for broader applications, especially in areas where traditional data collection is challenging or hazardous. Such methods can greatly enhance our understanding of flow dynamics and offer more comprehensive flood risk assessments.

7.3 Critical assessment of methodology

Throughout this thesis, various limitations have been identified in both the research presented here, as well as in the underlying research upon which some of this work is based.

7.3.1 Limitations of LSPIV in riverine hydrometry

Whilst LSPIV holds promise as a remote sensing technique for river surface velocity estimation, velocity data generated from LSPIV workflows are far from perfect. Even though this thesis has shown that these imperfect data can be useful in fine-tuning hydraulic models, the explicit quantification of errors related to this data is imperative. Indeed, the limitations discussed here are common across LSPIV studies and have been adequately characterized in the empirical chapters. Reporting these limitations is key in order to enhance reproducibility of investigations and allow for credible inter-study comparison.

LSPIV assumes that riverine flow is two-dimensional and that the surface patterns detected accurately represent the velocity distribution throughout the water column. This assumption might not hold in cases of complex three-dimensional flow patterns. During river floods, three-dimensional flow patterns can indeed become more prominent due to the increased complexity of the flow dynamics (Bates, 2022). Whilst the dominance of these flow patterns can vary based on factors such as the river's morphology, discharge magnitude, channel geometry and the presence of obstacles, research into how these impact LSPIV measurements is necessary.

The variability of depth-averaging coefficients for converting LSPIV surface velocity estimates into depth-averaged values has been a common theme throughout this thesis. In Chapters 4 and 7, it was found that the choice of the coefficient (α) has a significant influence on the accuracy of LSPIV surface velocity estimates. Indeed, when comparing LSPIV-derived velocities to those computed by 2D hydraulic models, the choice of α is an additional parameter that needs to be calibrated, introducing uncertainty into the comparison process. Furthermore, turbulence and secondary flow patterns (e.g., eddies) can significantly affect velocity profiles across the water column. A single depth-averaging coefficient cannot fully account for these complex flow dynamics, potentially leading to mismatches between estimated depth-averaged velocities and those computed by 2D models. The work in Chapter

4 begins to explore this issue highlighting the challenges of accurately representing the complex and variable flow dynamics in rivers.

It was further observed that when comparing LSPIV to 2D model velocities, there was an increase in scatter with increasing flow velocities (< 2 m s^{-1}). The observed scatter could be a result of the combined influence of uncertainties in both the 2D model and LSPIV measurements. Interactions between inaccuracies in model predictions and the depth-averaging limitations of LSPIV could amplify discrepancies, especially as flow velocities increase. Additional field measurements and model validation in high-velocity scenarios to cross-verify results and identify specific areas of discrepancy seem to be means to further understand this phenomenon.

In windy conditions, particles used for velocity tracking may experience advection and drift, leading to difficulties in accurately following their trajectories. This can result in errors in LSPIV surface velocity measurements. Additionally, high winds can create turbulence and waves on the water surface, making it challenging for LSPIV to accurately track and measure surface velocities. This turbulence may affect the movement of tracer particles, leading to inaccuracies in velocity calculations. This calls for careful site selection when conducting these measurements.

The Large-Scale Particle Image Velocimetry (LSPIV) technique involves various parameters that need to be carefully selected to ensure accurate and reliable velocity measurements, as was shown in Chapters 4, 5 and 6. The uncertainty related to the choice of LSPIV parameters can stem from a multitude of factors such as frame rate and image resolution, georeferencing, parametrization of the PIV algorithm (choice of interrogation area sizes), image enhancement techniques and image resolution amongst other sources such as those discussed in Jolley *et al.* (2021), Kim (2006) and Perks *et al.* (2016). Resolving these uncertainties requires a combination of careful experimental design, advanced image processing techniques, and validation procedures. In fact, to account for the conflating effects of all these uncertainties, a multivariate sensitivity analysis is necessary in order to attain insight into the cooperative effects of all sources of error in LSPIV measurements. A systematic and iterative approach, along with a thorough understanding of the flow conditions seem to be an appropriate means for parameter selection which will improve the accuracy of velocity measurements obtained using LSPIV.

7.3.2 Limitations of Satellite video datasets

This thesis evidences the utility of satellite video datasets in assessing reach scale 2D hydraulic model simulations. It is envisaged that in time, the proliferation of nanosatellite constellations will lead to the ready availability of satellite video for similar studies. However, satellite video datasets come with limitations that can affect their applicability and accuracy in analysing river dynamics. While video datasets capture dynamic changes over time, their spatial resolution is still limited compared to dedicated high-resolution still imagery. Further, the limited spectral bands in satellite video means that some information relevant to river dynamics is not available, unlike when using standard still satellite imagery. Similar to other commercial satellite data, satellite video is not yet open access and requires tasking for image acquisition. Further, the current satellite video imaging catalogue is still rather limited as compared to other publicly available satellite data. In Chapter 5, it was demonstrated that the processing and interpretation of satellite video is a complex endeavour that requires advanced image processing techniques. Finally, ensuring the accurate validation of satellite video-derived river dynamics can be challenging due to the limited availability of ground truth data. The difficulty of acquiring accurate field measurements in order to validate satellite video remote sensing observations can hinder the assessment of accuracy. Challenges including limited accessibility of some remote or politically sensitive locations as well as constraints linked to geographic, environmental, and logistical constraints make it hard to collect ground truth data. However, it is envisaged that availability of more satellite video data will allow for more locations to be analysed and improve confidence in the quality of space-based video.

7.3.3 Limitations of 2D hydraulic modelling

All numerical models are required to make some form of numerical approximations in order to simulate flow. Assumptions touching on various factors such as channel geometry and boundary conditions can introduce uncertainties in model results. Furthermore, the selection of appropriate parameters for the calibration of 2D models can be affected by the problem of model equifinality (Beven, 2006) where multiple different model parameter combinations can produce equally satisfactory fits to observed data. Addressing the issue of model equifinality can require approaches such as extensive sensitivity and uncertainty analysis or assimilation of additional data (such as remotely sensed data) in order to help constrain model outputs. In 2D hydraulic models, vertical variations in flow are generally not well accounted for, leading to potential inaccuracies especially in regions with steep topography and intricate geometries. In such cases, 3D models are better suited to offer accurate representation of complex flow phenomena, although this comes with significant computational, data and expertise requirements. Despite these limitations, 2D models remain valuable tools for characterizing flood dynamics with the choice between 1D, 2D or 3D models depending on the objectives of the modelling exercise, available data, computational resources and the desired level of accuracy.

7.4 Contributions to wider research

Improving the accuracy of 2D hydraulic models is pivotal in the endeavour to reduce flood risk. The rigorous calibration and validation of these models will ensure that predictions of flood depths, velocities, and inundation extents closely mirror reality, which is crucial for decision making. This thesis has applied extensive hydraulic modelling, acquisition, and analysis of field data, complemented with new-age satellite data, in order to advance flood science. The research in this thesis has contributed to flood risk modelling in a number of ways.

(i) Chapter 4 demonstrated, for the first time, that 2D hydraulic models can be effectively calibrated and validated using velocities obtained through Large-Scale Particle Image Velocimetry (LSPIV) techniques. This approach yielded accuracies comparable to traditional observations conducted with Acoustic Doppler Current Profilers (aDcps). It was further shown that the use standard depth-averaging coefficients (α) in LSPIV workflows can introduce significant uncertainty to velocity estimates, as opposed to using channel-specific choice of the coefficients (α). Although the aDcp has been the gold standard for acquiring velocity data in hydrology, LSPIV velocities can serve as a reliable substitute. The successful integration of LSPIV data into flood modelling techniques represents a methodological advancement, particularly in regions where data collection infrastructure is limited. This insight is transformative as it introduces a cost-effective alternative to calibrating and validating flood models without the need for expensive and complex instrumentation.

(ii) Chapter 5 was also the first study to show the integration of satellite video and deep learning into 2D hydraulic modelling workflows to provide more accurate and dynamic insights into flood events. By successfully using satellite video imagery to validate 2D model simulations, the operational utility of satellite video for hydrological applications was demonstrated. Although satellite video imposes significant pre-processing and computational costs, results obtained in this chapter showed their utility in improving hydraulic modelling predictions.

This research validates the use of emerging technologies, such as deep learning and image velocimetry, in hydrological applications bridging the gap between remote sensing, deep learning, and hydrology. The integration of image velocimetry to estimate surface river velocities from satellite video imagery opens avenues for addressing the challenge of obtaining real-time flow velocity information during flood events. Additionally, the use of a hybrid deep neural network for precise mapping of flood extents from satellite video imagery offers a departure from traditional methods such as thresholding and rule-based approaches. Deep learning methods for flood imagery segmentation offer contextual understanding and excel at capturing spatial context and relationships within images automatically, leading to more objective results as compared to traditional methods which often rely on user-defined thresholds or rules. Advancements offered by deep-neural networks in delineating food extents will have far-reaching implications for flood monitoring systems.

(iii) Chapter 6 offered a significant leap forward in satellite remote-sensing based discharge estimation via a pioneering approach of integrating satellite video-derived velocities and high-resolution topography. This marked a significant departure from conventional methods such as those based on satellite altimetry, which measure water level changes as a proxy for discharge, or other indirect methods relying solely on hydraulic equations. The advance here stemmed from the ability to observe and incorporate real-time river behaviour, made possible by utilization of satellite video velocities. The findings in Chapter 6 guide future applications of these techniques and highlights where targeted improvements may yield the best accuracy gains when computing discharge via satellite remote sensing for wide rivers (>50 m).

7.5 Perspectives on future research

The findings in this thesis suggest several directions for future research which are discussed below.

7.5.1 Harnessing LSPIV Velocity Data for Improved Hydraulic Modelling

Chapter 4 provides a strong foundation for future research into means of using LSPIV velocities for real-time flood forecasting and management. The development of techniques to assimilate LSPIV data in real-time into 2D hydraulic models could further enhance their predictive capability during ongoing flood events. Leveraging on data assimilation techniques, such as those previously applied by Barthélémy *et al*. (2018) and Neal *et al*.

(2009), LSPIV velocity data can be integrated into hydraulic models, optimizing model parameters in real-time and thus enhancing the accuracy of model simulations. Further research could also explore the integration of data from multiple sensors, including both LSPIV and aDcp, which could provide a more robust dataset for model calibration and validation. Multi-sensor integration could potentially mitigate limitations and uncertainties associated with individual methods. Given that the studies here were mostly focused on rural catchments, an interesting direction to extend this research would encompass modelling and acquiring LSPIV-velocities in complex river terrain and urban environments. Hydraulic models struggle to accurately predict flow behaviour in areas such as river confluences or urban environments. Concurrently, it would be interesting to investigate how LSPIV-derived velocities perform in challenging urban settings with intricate flow dynamics and artificial structures. Insights gained from urban catchments could help refine model parameters that are less influenced in rural catchments, making these parameter adjustments more applicable across various scenarios.

7.5.2 Spatial and Temporal Trends in α Variability through LSPIV-Hydraulic Model Integration

The spatial and temporal variability of the depth-averaging coefficient, α, could further be investigated by integrating LSPIV velocity data with hydraulic model predictions. Analysing LSPIV data over time intervals and comparing resulting depth-averaged velocities with model outputs could indicate how α values change in response to varying flow regimes. The spatial variability of α could also be investigated through integrating LSPIV data into hydraulic models, which can provide insights into patterns and trends in alpha value changes as relates to variations in channel geometry, bed roughness and flow conditions.

7.5.3 AI-Driven Advancements in 2D Hydraulic Modelling

Recent advances in AI and computing power have the potential to significantly enhance 2D hydraulic modelling, as was demonstrated in Chapter 5. In fact, responsibility now lies on hydraulic and flood modellers to adapt current physical flood models to take full advantage of AI-driven techniques, particularly deep learning, which can assist in calibrating and validating 2D hydraulic models more efficiently. AI-powered hydraulic modelling can bridge the gap between hydrology, geospatial analysis, and computer science and offer a transformative leap in 2D hydraulic modelling of floods. As and when satellite video datasets become more available, future research could investigate how generative AI models, such as such as Generative Adversarial Networks (GANs) or Variational Autoencoders (VAEs), can generate high-resolution synthetic images that closely resemble real-world satellite video frames. These synthetic images can augment the limited observational data available, allowing for higher-quality inputs to the 2D hydraulic models. Generative AI could also be explored for inferring river channel bathymetric information by analysing satellite video frames and estimating water depths, with the potential to integrate this information into 2D hydraulic models, further improving the representation of terrain and flow interactions. This could advance the application of the techniques trialled in Chapter 6 where globally available topographic datasets, such as SRTM DEMs, can be explored, rather than the LiDAR topography used in this thesis, which is not always available globally.

Chapter 8 - Conclusion

In an effort to contribute to the refinement of outputs from 2D hydraulic models, this thesis integrated satellite and UAV video, LSPIV techniques and AI-driven analysis, offering a multi-faceted approach into providing an understanding of flood dynamics at reach scale. In particular, the field of satellite remote sensing is witnessing an explosive growth in datasets encompassing various spatial, spectral, and temporal resolutions, thanks to advancements in satellite technology and sensor capabilities. In parallel, there has been a significant growth in computing power, driven by advances in hardware, cloud computing, and parallel processing technologies. The convergence of explosive growth in remote sensing datasets and computing power holds transformative potential for flood sciences. The work in this thesis has showcased how 2D physics-based hydraulic models can leverage on contemporary datasets and methods. This should open up diverse research pathways that will ultimately lead to improved flood prediction capabilities.

There is still a sore need for more rigorous validation of 2D hydraulic models. In this thesis, it was shown how the adoption of advanced remote sensing techniques will help overcome some of the legacy technical, logistical, and methodological challenges associated with traditional data for model validation. The use of video from the rapidly ubiquitous airborne platforms was shown to enhance the accuracy and reliability of model predictions by addressing the limitations of traditional calibration/validation methods. Surface river velocities derived from high resolution aerial imagery offer unprecedented spatial coverage that allowed for assessing the accuracy of 2D model predictions across different flow regimes and eco-hydraulic conditions where traditional measurement methods struggle to capture accurate flow velocities especially during extreme flow conditions such as high floods or low-flow periods. It is speculated that the use of these non-intrusive techniques, which eliminate the need for personnel to operate within hazardous flood conditions and also ensure no disruption to the natural flow conditions unlike invasive physical sensors, will be able to offer the opportunity to validate specific hydraulic processes such as flow separation and eddy formation with even better accuracies.

The estimation of velocities and discharge using satellite video can offer a transformative solution to the problem of inadequate river discharge data globally, especially in the wake of declining numbers of gauging stations globally. Although concomitant topographical data is required for application of space-based discharge estimation techniques demonstrated in this thesis, the resolution of globally available DEMs is rapidly improving, therefore a crucial parameter is velocity. Satellite video can offer near-real time to real-time discharge information which can further serve as independent validation to traditional discharge measurement techniques. Although satellite video data will be particularly beneficial for the comprehensive understanding of river flow dynamics, particularly for transboundary rivers and basins, more work on validation of these measurements remains.

Overall, the findings in this thesis underscored how through rigorous validation of 2D hydraulic models, it is possible to quantify and minimize the uncertainties associated with a multitude of input parameters, including topographic data, boundary conditions and roughness coefficients, enhancing confidence in 2D models' predictive capabilities. Evolving environmental conditions such as land-use changes and changes in channel morphology can significantly alter the dynamics of flood events. To accurately account for these changes, 2D hydraulic models must be validated against recent and relevant data, which will ensure that the full complexity of hydraulic phenomena is captured, resulting in more reliable flood predictions and improved management of flood risk.

References

Abd Elaziz, M., Oliva, D., Ewees, A.A., Xiong, S., 2019. Multi-level thresholding-based grey scale image segmentation using multi-objective multi-verse optimizer. Expert Systems with Applications 125, 112–129.

ABS, 2019. Water use on Australian farms, 2017–18. Cat no. 4618.0.

Adrian, R.J., 1991. Particle-Imaging Techniques for Experimental Fluid Mechanics. Annual Review of Fluid Mechanics 23, 261–304. https://doi.org/10.1146/annurev.fl.23.010191.001401

AghaKouchak, A., Nasrollahi, N., Habib, E., 2009. Accounting for Uncertainties of the TRMM Satellite Estimates. Remote Sensing 1, 606–619. https://doi.org/10.3390/rs1030606

Alcantarilla, P.F., Bartoli, A., Davison, A.J., 2012. KAZE Features, in: Fitzgibbon, A., Lazebnik, S., Perona, P., Sato, Y., Schmid, C. (Eds.), Computer Vision – ECCV 2012, Lecture Notes in Computer Science. Springer, Berlin, Heidelberg, pp. 214–227. https://doi.org/10.1007/978-3-642-33783-3_16

Alfieri, L., Burek, P., Feyen, L., Forzieri, G., 2015. Global warming increases the frequency of river floods in Europe. Hydrology and Earth System Sciences 19, 2247–2260. https://doi.org/10.5194/hess-19-2247-2015

Alifu, H., Hirabayashi, Y., Imada, Y., Shiogama, H., 2022. Enhancement of river flooding due to global warming. Sci Rep 12, 20687. https://doi.org/10.1038/s41598-022-25182-6

Al-mamari, M., Kantoush, S., Kobayashi, S., Sumi, T., Saber, M., 2019. Real-Time Measurement of Flash-Flood in a Wadi Area by LSPIV and STIV. Hydrology 6, 27. https://doi.org/10.3390/hydrology6010027

Alvarez, L.V., Schmeeckle, M.W., Grams, P.E., 2017. A detached eddy simulation model for the study of lateral separation zones along a large canyon-bound river. Journal of Geophysical Research: Earth Surface 122, 25–49. https://doi.org/10.1002/2016JF003895

Alvarez-Vanhard, E., Corpetti, T., Houet, T., 2021. UAV & satellite synergies for optical remote sensing applications: A literature review. Science of Remote Sensing 3, 100019. https://doi.org/10.1016/j.srs.2021.100019

Annis, A., Nardi, F., Petroselli, A., Apollonio, C., Arcangeletti, E., Tauro, F., Belli, C., Bianconi, R., Grimaldi, S., 2020. UAV-DEMs for Small-Scale Flood Hazard Mapping. Water 12, 1717. https://doi.org/10.3390/w12061717

Aragon, B., Ziliani, M.G., Houborg, R., Franz, T.E., McCabe, M.F., 2021. CubeSats deliver new insights into agricultural water use at daily and 3 m resolutions. Sci Rep 11, 12131. https://doi.org/10.1038/s41598-021-91646-w

Archer, L., Neal, J.C., Bates, P.D., House, J.I., 2018. Comparing TanDEM-X Data With Frequently Used DEMs for Flood Inundation Modeling. Water Resources Research 54, 10,205-10,222. https://doi.org/10.1029/2018WR023688

Aronica, G., Bates, P.D., Horritt, M.S., 2002. Assessing the uncertainty in distributed model predictions using observed binary pattern information within GLUE. Hydrol. Process. 16, 2001–2016. https://doi.org/10.1002/hyp.398

Astarita, T., 2008. Analysis of velocity interpolation schemes for image deformation methods in PIV. Experiments in Fluids 45, 257–266.

Attari, M., Hosseini, S.M., 2019. A simple innovative method for calibration of Manning's roughness coefficient in rivers using a similarity concept. Journal of Hydrology 575, 810–823. https://doi.org/10.1016/j.jhydrol.2019.05.083

Auliagisni, W., Wilkinson, S., Elkharboutly, M., 2022. Using community-based flood maps to explain flood hazards in Northland, New Zealand. Progress in Disaster Science 14, 100229. https://doi.org/10.1016/j.pdisas.2022.100229

Authority, M.-D.B., 2017. Basin Plan Evaluation 2017. Murray-Darling Basin Authority.

Bales, J.D., Wagner, C.R., 2009. Sources of uncertainty in flood inundation maps. Journal of Flood Risk Management 2, 139–147. https://doi.org/10.1111/j.1753-318X.2009.01029.x

Ballard, E., Gard, M., Pelle, B., 2010. Flow–habitat relationships for spring and fall-run Chinook Salmon and steelhead/Rainbow Trout spawning in the Yuba River. US Fish and Wildlife Service, Sacramento Fish and Wildlife Office, Sacramento, California.

Bandini, F., Kooij, L., Mortensen, B.K., Caspersen, M.B., Thomsen, L.G., Olesen, D., Bauer-Gottwein, P., 2023. Mapping inland water bathymetry with Ground Penetrating Radar (GPR) on board Unmanned Aerial Systems (UASs). Journal of Hydrology 616, 128789. https://doi.org/10.1016/j.jhydrol.2022.128789

Barker, J.R., Pasternack, G.B., Bratovich, P.M., Massa, D.A., Wyrick, J.R., Johnson, T.R., 2018. Kayak drifter surface velocity observation for 2D hydraulic model validation. River Research and Applications 34, 124–134. https://doi.org/10.1002/rra.3238

Barthélémy, S., Ricci, S., Morel, T., Goutal, N., Le Pape, E., Zaoui, F., 2018. On operational flood forecasting system involving 1D/2D coupled hydraulic model and data assimilation. Journal of Hydrology 562, 623–634. https://doi.org/10.1016/j.jhydrol.2018.05.007

Basnyat, B., Roy, N., Gangopadhyay, A., 2021. Flood Detection using Semantic Segmentation and Multimodal Data Fusion, in: 2021 IEEE International Conference on Pervasive Computing and Communications Workshops and Other Affiliated Events (PerCom Workshops). Presented at the 2021 IEEE International Conference on Pervasive Computing and Communications Workshops and other Affiliated Events (PerCom Workshops), pp. 135–140. https://doi.org/10.1109/PerComWorkshops51409.2021.9430985

Bates, P.D., 2022. Flood Inundation Prediction. Annu. Rev. Fluid Mech. 54, 287–315. https://doi.org/10.1146/annurev-fluid-030121-113138

Bates, P.D., 2012. Integrating remote sensing data with flood inundation models: how far have we got?: INVITED COMMENTARY. Hydrol. Process. 26, 2515–2521. https://doi.org/10.1002/hyp.9374

Bates, P.D., 2004. Remote sensing and flood inundation modelling. Hydrological Processes 18, 2593–2597. https://doi.org/10.1002/hyp.5649

Bates, P.D., De Roo, A.P.J., 2000. A simple raster-based model for flood inundation simulation. Journal of Hydrology 236, 54–77. https://doi.org/10.1016/S0022-1694(00)00278-X

Bates, P.D., Horritt, M.S., Hunter, N.M., Mason, D., Cobby, D., 2005. Numerical Modelling of Floodplain Flow, in: Bates, Paul D., Lane, S.N., Ferguson, R.I. (Eds.), Computational Fluid Dynamics. John Wiley & Sons, Ltd, Chichester, UK, pp. 271–304. https://doi.org/10.1002/0470015195.ch11

Bates, P.D., Neal, J.C., Alsdorf, D., Schumann, G.J.-P., 2014a. Observing Global Surface Water Flood Dynamics. Surv Geophys 35, 839–852. https://doi.org/10.1007/s10712-013-9269-4

Bates, P.D., Pappenberger, F., Romanowicz, R.J., 2014b. Uncertainty in Flood Inundation Modelling, in: Applied Uncertainty Analysis for Flood Risk Management. IMPERIAL COLLEGE PRESS, pp. 232–269. https://doi.org/10.1142/9781848162716_0010

Bates, P.D., Quinn, N., Sampson, C., Smith, A., Wing, O., Sosa, J., Savage, J., Olcese, G., Neal, J., Schumann, G., Giustarini, L., Coxon, G., Porter, J.R., Amodeo, M.F., Chu, Z., Lewis-Gruss, S., Freeman, N.B., Houser, T., Delgado, M., Hamidi, A., Bolliger, I., McCusker, K., Emanuel, K., Ferreira, C.M., Khalid, A., Haigh, I.D., Couasnon, A., Kopp, R., Hsiang, S., Krajewski, W.F., 2021. Combined Modeling of US Fluvial, Pluvial, and Coastal Flood Hazard Under Current and Future Climates. Water Res. 57. https://doi.org/10.1029/2020WR028673

Bauer-Marschallinger, B., Cao, S., Tupas, M.E., Roth, F., Navacchi, C., Melzer, T., Freeman, V., Wagner, W., 2022. Satellite-Based Flood Mapping through Bayesian Inference from a Sentinel-1 SAR Datacube. Remote Sensing 14, 3673. https://doi.org/10.3390/rs14153673

Bay, H., Ess, A., Tuytelaars, T., Van Gool, L., 2008. Speeded-Up Robust Features (SURF). Computer Vision and Image Understanding, Similarity Matching in Computer Vision and Multimedia 110, 346–359. https://doi.org/10.1016/j.cviu.2007.09.014

Bebis, G., Boyle, R., Parvin, B., Koracin, D., Porikli, F., Skaff, S., Entezari, A., Min, J., Iwai, D., Sadagic, A., Scheidegger, C., Isenberg, T. (Eds.), 2016. Advances in Visual Computing: 12th International Symposium, ISVC 2016, Las Vegas, NV, USA, December 12-14, 2016, Proceedings, Part I, Lecture Notes in Computer Science. Springer International Publishing, Cham. https://doi.org/10.1007/978-3-319-50835-1

Bernhofen, M.V., Whyman, C., Trigg, M.A., Sleigh, P.A., Smith, A.M., Sampson, C.C., Yamazaki, D., Ward, P.J., Rudari, R., Pappenberger, F., Dottori, F., Salamon, P., Winsemius, H.C., 2018. A first collective validation of global fluvial flood models for major floods in Nigeria and Mozambique. Environ. Res. Lett. 13, 104007. https://doi.org/10.1088/1748-9326/aae014

Beven, K., 2006. A manifesto for the equifinality thesis. Journal of Hydrology 320, 18–36. https://doi.org/10.1016/j.jhydrol.2005.07.007

Beven, K., Binley, A., 2014. GLUE: 20 years on: GLUE: 20 YEARS ON. Hydrol. Process. 28, 5897–5918. https://doi.org/10.1002/hyp.10082

Beven, K., Freer, J., 2001. Equifinality, data assimilation, and uncertainty estimation in mechanistic modelling of complex environmental systems using the GLUE methodology. Journal of hydrology 249, 11–29.

Beven, K., Lamb, R., Leedal, D., Hunter, N., 2015. Communicating uncertainty in flood inundation mapping: a case study. International Journal of River Basin Management 13, 285–295. https://doi.org/10.1080/15715124.2014.917318

Bharti, V., Singh, C., Ettema, J., Turkington, T., 2016. Spatiotemporal characteristics of extreme rainfall events over the Northwest Himalaya using satellite data. International Journal of Climatology 36, 3949–3962.

Bhushan, S., Shean, D., Alexandrov, O., Henderson, S., 2021. Automated digital elevation model (DEM) generation from very-high-resolution Planet SkySat triplet stereo and video imagery. ISPRS Journal of Photogrammetry and Remote Sensing 173, 151–165. https://doi.org/10.1016/j.isprsjprs.2020.12.012

Biggs, H., Smart, G., Doyle, M., Holwerda, H., McDonald, M., Ede, M., 2021. River discharge from surface velocity measurements–A field guide for selecting alpha. Envirolink Advice Report. Christchurch, New Zealand.

Bleau, A., Leon, L.J., 2000. Watershed-based segmentation and region merging. Computer Vision and Image Understanding 77, 317–370.

Bommasani, R., Hudson, D.A., Adeli, E., Altman, R., Arora, S., von Arx, S., Bernstein, M.S., Bohg, J., Bosselut, A., Brunskill, E., 2021. On the opportunities and risks of foundation models. arXiv preprint arXiv:2108.07258.

Bonafilia, D., Tellman, B., Anderson, T., Issenberg, E., 2020. Sen1Floods11: A georeferenced dataset to train and test deep learning flood algorithms for sentinel-1. Presented at the Proceedings of the IEEE/CVF Conference on Computer Vision and Pattern Recognition Workshops, pp. 210–211.

Bravo, J.M., Allasia, D., Paz, A.R., Collischonn, W., Tucci, C.E.M., 2012. Coupled Hydrologic-Hydraulic Modeling of the Upper Paraguay River Basin. J. Hydrol. Eng. 17, 635–646. https://doi.org/10.1061/(ASCE)HE.1943-5584.0000494

Brierley, G., Fryirs, K., Outhet, D., Massey, C., 2002. Application of the River Styles framework as a basis for river management in New South Wales, Australia. Applied Geography 22, 91–122. https://doi.org/10.1016/S0143-6228(01)00016-9

Brooks, S., 2017. Classification of aquatic ecosystems in the Murray-Darling Basin: 2017 update. Canberra, ACT: Murray-Darling Basin Authority and Commonwealth Environmental Water Office.

Brunner, G.W., Piper, S.S., Jensen, M.R., Chacon, B., 2015. Combined 1D and 2D Hydraulic Modeling within HEC-RAS, in: World Environmental and Water Resources Congress 2015. Presented at the World Environmental and Water Resources Congress 2015, American Society of Civil Engineers, Austin, TX, pp. 1432–1443. https://doi.org/10.1061/9780784479162.141

Brunner, G.W., United States., Army., Corps of Engineers., Institute for Water Resources (U.S.), Hydrologic Engineering Center (U.S.), 2020. HEC-RAS river analysis system : hydraulic reference manual. US Army Corps of Engineers, Institute for Water Resources, Hydrologic Engineering Center, Davis, CA.

Bureau of Meteorology, 2022. Special Climate Statement 76 – Extreme rainfall and flooding in south-eastern Queensland and eastern New South Wales.

Buslaev, A., Iglovikov, V.I., Khvedchenya, E., Parinov, A., Druzhinin, M., Kalinin, A.A., 2020. Albumentations: Fast and Flexible Image Augmentations. Information 11, 125. https://doi.org/10.3390/info11020125

Camilus, K.S., Govindan, V., 2012. A review on graph based segmentation. International Journal of Image, Graphics and Signal Processing 4, 1.

Cao, Y., Wu, Y., Yao, Q., Yu, J., Hou, D., Wu, Z., Wang, Z., 2022. River Surface Velocity Estimation Using Optical Flow Velocimetry Improved With Attention Mechanism and Position Encoding. IEEE Sensors Journal 22, 16533–16544.

Cardona, A., Saalfeld, S., Schindelin, J., Arganda-Carreras, I., Preibisch, S., Longair, M., Tomancak, P., Hartenstein, V., Douglas, R.J., 2012. TrakEM2 software for neural circuit reconstruction. PloS one 7, e38011.

Carreño Conde, F., De Mata Muñoz, M., 2019. Flood monitoring based on the study of Sentinel-1 SAR images: The Ebro River case study. Water 11, 2454.

Carrivick, J.L., Smith, M.W., 2019. Fluvial and aquatic applications of Structure from Motion photogrammetry and unmanned aerial vehicle/drone technology. WIREs Water 6, e1328. https://doi.org/10.1002/wat2.1328

Carrivick, J.L., Smith, M.W., Quincey, D.J., 2016. Structure from Motion in the Geosciences. John Wiley & Sons.

Casulli, V., 2009. A high-resolution wetting and drying algorithm for free-surface hydrodynamics. International Journal for Numerical Methods in Fluids 60, 391–408.

Chen, C., Liang, D., Wang, X., Li, Z., 2021. Application of UAV-based PIV to Rivers, in: 2021 7th International Conference on Hydraulic and Civil Engineering & Smart Water Conservancy and Intelligent Disaster Reduction Forum (ICHCE & SWIDR). Presented at the 2021 7th International Conference on Hydraulic and Civil Engineering & Smart Water Conservancy and Intelligent Disaster Reduction Forum (ICHCE & SWIDR), pp. 1707–1712. https://doi.org/10.1109/ICHCESWIDR54323.2021.9656476

Chen, C.P., Zhang, C.-Y., 2014. Data-intensive applications, challenges, techniques and technologies: A survey on Big Data. Information sciences 275, 314–347.

Chen, J., Lu, Y., Yu, Q., Luo, X., Adeli, E., Wang, Y., Lu, L., Yuille, A.L., Zhou, Y., 2021. Transunet: Transformers make strong encoders for medical image segmentation. arXiv preprint arXiv:2102.04306.

Chen, L.-C., Papandreou, G., Kokkinos, I., Murphy, K., Yuille, A.L., 2017. DeepLab: Semantic Image Segmentation with Deep Convolutional Nets, Atrous Convolution, and Fully Connected CRFs.

Chow, V.T., 1959. Open Channel Hydraulics. Caldwell.

Clement, M.A., Kilsby, C.G., Moore, P., 2018. Multi-temporal synthetic aperture radar flood mapping using change detection: Multi-temporal SAR flood mapping using change detection. J Flood Risk Management 11, 152–168. https://doi.org/10.1111/jfr3.12303

Cohn, T.A., Kiang, J.E., Mason, R.R., 2013. Estimating Discharge Measurement Uncertainty Using the Interpolated Variance Estimator. Journal of Hydraulic Engineering 139, 502–510. https://doi.org/10.1061/(ASCE)HY.1943-7900.0000695

Cordts, M., Omran, M., Ramos, S., Scharwächter, T., Enzweiler, M., Benenson, R., Franke, U., Roth, S., Schiele, B., 2015. The cityscapes dataset. Presented at the CVPR Workshop on the Future of Datasets in Vision, sn.

Costabile, P., Costanzo, C., Ferraro, D., Macchione, F., Petaccia, G., 2020. Performances of the new HEC-RAS version 5 for 2-D hydrodynamic-based rainfall-runoff simulations at basin scale: Comparison with a state-of-the art model. Water 12, 2326.

Coveney, S., Roberts, K., 2017. Lightweight UAV digital elevation models and orthoimagery for environmental applications: data accuracy evaluation and potential for river flood risk modelling. International Journal of Remote Sensing 38, 3159–3180. https://doi.org/10.1080/01431161.2017.1292074

Creutin, J.D., Muste, M., Bradley, A.A., Kim, S.C., Kruger, A., 2003. River gauging using PIV techniques: a proof of concept experiment on the Iowa River. Journal of Hydrology 277, 182–194. https://doi.org/10.1016/S0022-1694(03)00081-7

d'Angelo, P., Kuschk, G., Reinartz, P., 2014. Evaluation of Skybox Video and Still Image products. Int. Arch. Photogramm. Remote Sens. Spatial Inf. Sci. XL–1, 95–99. https://doi.org/10.5194/isprsarchives-XL-1-95-2014

d'Angelo, P., Máttyus, G., Reinartz, P., 2016. Skybox image and video product evaluation. International Journal of Image and Data Fusion 7, 3–18. https://doi.org/10.1080/19479832.2015.1109565

Dal Sasso, S.F., Pizarro, A., Manfreda, S., 2021. Recent Advancements and Perspectives in UAS-Based Image Velocimetry. Drones 5, 81. https://doi.org/10.3390/drones5030081

Dallow, G., 2020. Quantifying Transient Storage in Realigned and Non-realigned River Reaches.

Dasallas, L., Kim, Y., An, H., 2019. Case study of HEC-RAS 1D–2D coupling simulation: 2002 Baeksan flood event in Korea. Water 11, 2048.

Dasgupta, A., Grimaldi, S., Ramsankaran, R.A.A.J., Pauwels, V.R.N., Walker, J.P., 2018. Towards operational SAR-based flood mapping using neuro-fuzzy texture-based approaches. Remote Sensing of Environment 215, 313–329. https://doi.org/10.1016/j.rse.2018.06.019

Dasgupta, A., Thakur, P.K., Gupta, P.K., 2020. Potential of SAR-Derived Flood Maps for Hydrodynamic Model Calibration in Data Scarce Regions. J. Hydrol. Eng. 25, 05020028. https://doi.org/10.1061/(ASCE)HE.1943-5584.0001988

Davoli, F., Kourogiorgas, C., Marchese, M., Panagopoulos, A., Patrone, F., 2019. Small satellites and CubeSats: Survey of structures, architectures, and protocols. Int J Satell Commun Network 37, 343–359. https://doi.org/10.1002/sat.1277

DeBell, L., Anderson, K., Brazier, R.E., King, N., Jones, L., 2016. Water resource management at catchment scales using lightweight UAVs: current capabilities and future perspectives 4, 24.

Dechesne, C., Lassalle, P., Lefèvre, S., 2021. Bayesian u-net: Estimating uncertainty in semantic segmentation of earth observation images. Remote Sensing 13, 3836.

DeTone, D., Malisiewicz, T., Rabinovich, A., 2018. SuperPoint: Self-Supervised Interest Point Detection and Description, in: 2018 IEEE/CVF Conference on Computer Vision and Pattern Recognition Workshops (CVPRW). Presented at the 2018 IEEE/CVF Conference on Computer Vision and Pattern Recognition Workshops (CVPRW), pp. 337–33712. https://doi.org/10.1109/CVPRW.2018.00060

Dewals, B., Kitsikoudis, V., Angel Mejía-Morales, M., Archambeau, P., Mignot, E., Proust, S., Erpicum, S., Pirotton, M., Paquier, A., 2023. Can the 2D shallow water equations model flow intrusion into buildings during urban floods? Journal of Hydrology 619, 129231. https://doi.org/10.1016/j.jhydrol.2023.129231

Di Baldassarre, G., Schumann, G., Bates, P.D., 2009. A technique for the calibration of hydraulic models using uncertain satellite observations of flood extent. Journal of Hydrology 367, 276–282.

Di Baldassarre, G., Uhlenbrook, S., 2012. Is the current flood of data enough? A treatise on research needs for the improvement of flood modelling. Hydrological Processes 26, 153–158. https://doi.org/10.1002/hyp.8226

Dietrich, J.T., 2017. Bathymetric structure-from-motion: Extracting shallow stream bathymetry from multi-view stereo photogrammetry. Earth Surface Processes and Landforms 42, 355–364.

Dixon, S.J., Sear, D.A., Odoni, N.A., Sykes, T., Lane, S.N., 2016. The effects of river restoration on catchment scale flood risk and flood hydrology. Earth Surface Processes and Landforms 41, 997–1008. https://doi.org/10.1002/esp.3919

Domeneghetti, A., Schumann, G.J.-P., Tarpanelli, A., 2019. Preface: Remote Sensing for Flood Mapping and Monitoring of Flood Dynamics. Remote Sensing 11, 943. https://doi.org/10.3390/rs11080943

Domeneghetti, A., Tarpanelli, A., Brocca, L., Barbetta, S., Moramarco, T., Castellarin, A., Brath, A., 2014. The use of remote sensing-derived water surface data for hydraulic model calibration. Remote Sensing of Environment 149, 130–141. https://doi.org/10.1016/j.rse.2014.04.007

Dong, C., Loy, C.C., He, K., Tang, X., 2014. Learning a deep convolutional network for image super-resolution. Presented at the Computer Vision–ECCV 2014: 13th European Conference, Zurich, Switzerland, September 6-12, 2014, Proceedings, Part IV 13, Springer, pp. 184–199.

Dosovitskiy, A., Beyer, L., Kolesnikov, A., Weissenborn, D., Zhai, X., Unterthiner, T., Dehghani, M., Minderer, M., Heigold, G., Gelly, S., Uszkoreit, J., Houlsby, N., 2021. An Image is Worth 16x16 Words: Transformers for Image Recognition at Scale. https://doi.org/10.48550/arXiv.2010.11929

Dottori, F., Todini, E., 2013. Testing a simple 2D hydraulic model in an urban flood experiment. Hydrological Processes 27, 1301–1320.

Dramais, G., Le Coz, J., Camenen, B., Hauet, A., 2011. Advantages of a mobile LSPIV method for measuring flood discharges and improving stage–discharge curves. Journal of Hydro-environment Research 5, 301–312. https://doi.org/10.1016/j.jher.2010.12.005

Durand, M., Neal, J., Rodríguez, E., Andreadis, K.M., Smith, L.C., Yoon, Y., 2014. Estimating reach-averaged discharge for the River Severn from measurements of river water surface elevation and slope. Journal of Hydrology 511, 92–104. https://doi.org/10.1016/j.jhydrol.2013.12.050

Eilander, D., Couasnon, A., Leijnse, T., Ikeuchi, H., Yamazaki, D., Muis, S., Dullaart, J., Haag, A., Winsemius, H.C., Ward, P.J., 2023. A globally applicable framework for compound flood hazard modeling. Natural Hazards and Earth System Sciences 23, 823–846. https://doi.org/10.5194/nhess-23-823-2023

Elkhrachy, I., 2022. Flash flood water depth estimation using SAR images, digital elevation models, and machine learning algorithms. Remote Sensing 14, 440.

Eltner, A., Bertalan, L., Grundmann, J., Perks, M.T., Lotsari, E., 2021. Hydro-morphological mapping of river reaches using videos captured with UAS. Earth Surface Processes and Landforms 46, 2773–2787. https://doi.org/10.1002/esp.5205

Eltner, A., Kaiser, A., Castillo, C., Rock, G., Neugirg, F., Abellán, A., 2016. Image-based surface reconstruction in geomorphometry – merits, limits and developments. Earth Surf. Dynam. 4, 359–389. https://doi.org/10.5194/esurf-4-359-2016

Eltner, A., Sardemann, H., Grundmann, J., 2019. Flow velocity and discharge measurement in rivers using terrestrial and UAV imagery. Hydrol. Earth Syst. Sci. Discuss. 1–29. https://doi.org/10.5194/hess-2019-289

Environment Agency, 2009. Eden Catchment Flood Management Plan Summary Report December 2009.

Euler, L., 2008. Principles of the motion of fluids. Physica D: Nonlinear Phenomena, Euler Equations: 250 Years On 237, 1840–1854. https://doi.org/10.1016/j.physd.2008.04.019

European Space Agency, 2022. Technical Note on Quality Assessment for Jilin-1 SP and GF03C Video Missions.

Farag, A.A., Mohamed, R.M., El-Baz, A., 2005. A unified framework for map estimation in remote sensing image segmentation. IEEE Transactions on Geoscience and Remote Sensing 43, 1617–1634.

Fekete, B.M., Vörösmarty, C.J., 2007. The current status of global river discharge monitoring and potential new technologies complementing traditional discharge measurements. IAHS publ 309, 129–136.

Fewtrell, T.J., 2008. Development of simple numerical methods for improving two-dimensional hydraulic models of urban flooding.

Fewtrell, T.J., Duncan, A., Sampson, C.C., Neal, J.C., Bates, P.D., 2011. Benchmarking urban flood models of varying complexity and scale using high resolution terrestrial LiDAR data. Physics and Chemistry of the Earth, Parts A/B/C, Recent Advances in Mapping and Modelling Flood Processes in Lowland Areas 36, 281–291. https://doi.org/10.1016/j.pce.2010.12.011

Feyisa, G.L., Meilby, H., Fensholt, R., Proud, S.R., 2014. Automated Water Extraction Index: A new technique for surface water mapping using Landsat imagery. Remote Sensing of Environment 140, 23–35. https://doi.org/10.1016/j.rse.2013.08.029

FIJI-ImageJ, 2020. FIJI-ImageJ. Available online at: https://imagej.net/Fiji (accessed August 6, 2023).

Fischer, J.L., Bennion, D., Roseman, E.F., Manny, B.A., 2015. Validation of a spatial model used to locate fish spawning reef construction sites in the St. Clair–Detroit River system. Journal of Great Lakes Research 41, 1178–1184. https://doi.org/10.1016/j.jglr.2015.09.019

Fischler, M.A., Bolles, R.C., 1981. Random sample consensus: a paradigm for model fitting with applications to image analysis and automated cartography. Commun. ACM 24, 381–395. https://doi.org/10.1145/358669.358692

Fisher, A., Flood, N., Danaher, T., 2016. Comparing Landsat water index methods for automated water classification in eastern Australia. Remote Sensing of Environment 175, 167–182. https://doi.org/10.1016/j.rse.2015.12.055

FluViSat - Hydrological Flow Measurements from Satellite Video, n.d. URL https://www.ceh.ac.uk/our-science/projects/Fluvisat (accessed 10.7.22).

Fujita, I., Muste, M., Kruger, A., 1998. Large-scale particle image velocimetry for flow analysis in hydraulic engineering applications. Journal of Hydraulic Research 36, 397–414. https://doi.org/10.1080/00221689809498626

Fukushima, K., 1980. Neocognitron: A self-organizing neural network model for a mechanism of pattern recognition unaffected by shift in position. Biol. Cybernetics 36, 193–202. https://doi.org/10.1007/BF00344251

Fulton, J., Ostrowski, J., 2008. Measuring real-time streamflow using emerging technologies: Radar, hydroacoustics, and the probability concept. Journal of Hydrology 357, 1–10. https://doi.org/10.1016/j.jhydrol.2008.03.028

Fulton, J.W., Anderson, I.E., Chiu, C.-L., Sommer, W., Adams, J.D., Moramarco, T., Bjerklie, D.M., Fulford, J.M., Sloan, J.L., Best, H.R., Conaway, J.S., Kang, M.J., Kohn, M.S., Nicotra, M.J., Pulli, J.J., 2020a. QCam: sUAS-Based Doppler Radar for Measuring River Discharge. Remote Sensing 12, 3317. https://doi.org/10.3390/rs12203317

Fulton, J.W., Mason, C.A., Eggleston, J.R., Nicotra, M.J., Chiu, C.-L., Henneberg, M.F., Best, H.R., Cederberg, J.R., Holnbeck, S.R., Lotspeich, R.R., Laveau, C.D., Moramarco, T., Jones, M.E., Gourley, J.J., Wasielewski, D., 2020b. Near-Field Remote Sensing of Surface Velocity and River Discharge Using Radars and the Probability Concept at 10 U.S. Geological Survey Streamgages. Remote Sensing 12, 1296. https://doi.org/10.3390/rs12081296

Gard, M., 2008. Flow-habitat relationships for juvenile spring/fall-run chinook salmon and steelhead/rainbow trout rearing in the Yuba River. Draft report prepared by the Energy Planning and Instream Flow Branch of the USFWS, Sacramento, California.

Garg, R., Kumar, A., Bansal, N., Prateek, M., Kumar, S., 2021. Semantic segmentation of PolSAR image data using advanced deep learning model. Scientific Reports 11, 1–18.

Gebrehiwot, A., Hashemi-Beni, L., Thompson, G., Kordjamshidi, P., Langan, T.E., 2019. Deep Convolutional Neural Network for Flood Extent Mapping Using Unmanned Aerial Vehicles Data. Sensors 19, 1486. https://doi.org/10.3390/s19071486

Geoscience Australia, 2022. Elvis - Elevation and Depth - Foundation Spatial Data.

Ghamisi, P., Rasti, B., Yokoya, N., Wang, Q., Hofle, B., Bruzzone, L., Bovolo, F., Chi, M., Anders, K., Gloaguen, R., Atkinson, P.M., Benediktsson, J.A., 2018. Multisource and Multitemporal Data Fusion in Remote Sensing. arXiv:1812.08287 [cs, eess, stat].

Girisha, S., M.M., M.P., Verma, U., Pai, R.M., 2019. Semantic Segmentation of UAV Aerial Videos using Convolutional Neural Networks, in: 2019 IEEE Second International Conference on Artificial Intelligence and Knowledge Engineering (AIKE). Presented at the 2019 IEEE Second International Conference on Artificial Intelligence and Knowledge Engineering (AIKE), IEEE, Sardinia, Italy, pp. 21–27. https://doi.org/10.1109/AIKE.2019.00012

Giustarini, L., Chini, M., Hostache, R., Pappenberger, F., Matgen, P., 2015. Flood Hazard Mapping Combining Hydrodynamic Modeling and Multi Annual Remote Sensing data. Remote Sensing 7, 14200–14226. https://doi.org/10.3390/rs71014200

Gleason, C.J., Durand, M.T., 2020. Remote Sensing of River Discharge: A Review and a Framing for the Discipline. Remote Sensing 12, 1107. https://doi.org/10.3390/rs12071107

Gonçalves, D.N., Junior, J.M., Carrilho, A.C., Acosta, P.R., Ramos, A.P.M., Gomes, F.D.G., Osco, L.P., da Rosa Oliveira, M., Martins, J.A.C., Júnior, G.A.D., 2023. Transformers for mapping burned areas in Brazilian Pantanal and Amazon with PlanetScope imagery. International Journal of Applied Earth Observation and Geoinformation 116, 103151.

Gonzalo-Martín, C., García-Pedrero, A., Lillo-Saavedra, M., 2021. Improving deep learning sorghum head detection through test time augmentation. Computers and Electronics in Agriculture 186, 106179. https://doi.org/10.1016/j.compag.2021.106179

Govedarica, M., Jakovljević, G., Álvarez-Taboada, F., 2018. Flood risk assessment based on LiDAR and UAV points clouds and DEM. Presented at the Remote Sensing for Agriculture, Ecosystems, and Hydrology XX, SPIE, pp. 66–76.

Grimaldi, ., Schumann, G.J.-P., Shokri, A., Walker, J.P., Pauwels, V.R.N., 2019. Challenges, Opportunities, and Pitfalls for Global Coupled Hydrologic-Hydraulic Modeling of Floods. Water Resources Research 55, 5277–5300. https://doi.org/10.1029/2018WR024289

Grimaldi, S., Li, Y., Pauwels, V.R.N., Walker, J.P., 2016a. Remote Sensing-Derived Water Extent and Level to Constrain Hydraulic Flood Forecasting Models: Opportunities and Challenges. Surv Geophys 37, 977–1034. https://doi.org/10.1007/s10712-016-9378-y

Grimaldi, S., Li, Y., Pauwels, V.R.N., Walker, J.P., 2016b. Remote Sensing-Derived Water Extent and Level to Constrain Hydraulic Flood Forecasting Models: Opportunities and Challenges. Surv Geophys 37, 977–1034. https://doi.org/10.1007/s10712-016-9378-y

Grimaldi, S., Xu, J., Li, Y., Pauwels, V.R.N., Walker, J.P., 2020. Flood mapping under vegetation using single SAR acquisitions. Remote Sensing of Environment 237, 111582. https://doi.org/10.1016/j.rse.2019.111582

Grimes, D.R., Rogers, D.P., Schumann, A., Day, B.F., 2022. Charting a Course for Sustainable Hydrological and Meteorological Observation Networks in Developing Countries.

Group, T.A.H., Vörösmarty, C., Askew, A., Grabs, W., Barry, R.G., Birkett, C., Döll, P., Goodison, B., Hall, A., Jenne, R., Kitaev, L., Landwehr, J., Keeler, M., Leavesley, G., Schaake, J., Strzepek, K., Sundarvel, S.S., Takeuchi, K., Webster, F., 2001. Global water data: A newly endangered species. Eos, Transactions American Geophysical Union 82, 54–58. https://doi.org/10.1029/01EO00031

Gu, X., Li, S., Ren, S., Zheng, H., Fan, C., Xu, H., 2022. Adaptive enhanced swin transformer with U-net for remote sensing image segmentation. Computers and Electrical Engineering 102, 108223. https://doi.org/10.1016/j.compeleceng.2022.108223

Haile, A.T., Asfaw, W., Rientjes, T., Worako, A.W., 2022. Deterioration of streamflow monitoring in Omo-Gibe basin in Ethiopia. Hydrological Sciences Journal 67, 1040–1053. https://doi.org/10.1080/02626667.2022.2060110

Han, K., Wang, Y., Chen, H., Chen, X., Guo, J., Liu, Z., Tang, Y., Xiao, A., Xu, C., Xu, Y., 2022. A survey on vision transformer. IEEE transactions on pattern analysis and machine intelligence 45, 87–110.

Hao, W., Yizhou, W., Yaqin, L., Zhili, S., 2020. The role of activation function in CNN. Presented at the 2020 2nd International Conference on Information Technology and Computer Application (ITCA), IEEE, pp. 429–432.

Hart, B.T., Bond, N.R., Byron, N., Pollino, C.A., Stewardson, M.J., 2021. Chapter 1 - Introduction to the Murray–Darling Basin system, Australia, in: Hart, B.T., Bond, N.R., Byron, N., Pollino, C.A., Stewardson, M.J. (Eds.), Murray-Darling Basin, Australia, Ecohydrology from Catchment to Coast. Elsevier, pp. 1–17. https://doi.org/10.1016/B978-0-12-818152-2.00001-2

Hasan, H.H., Mohd Razali, S.F., Ahmad Zaki, A.Z.I., Mohamad Hamzah, F., 2019. Integrated hydrological-hydraulic model for flood simulation in tropical urban catchment. Sustainability 11, 6700.

Hashemi-Beni, L., Gebrehiwot, A., 2020. Deep learning for remote sensing image classification for agriculture applications. The International Archives of Photogrammetry, Remote Sensing and Spatial Information Sciences 51–54.

Hashemi-Beni, L., Gebrehiwot, A.A., 2021. Flood Extent Mapping: An Integrated Method Using Deep Learning and Region Growing Using UAV Optical Data. IEEE Journal of Selected Topics in Applied Earth Observations and Remote Sensing 14, 2127–2135. https://doi.org/10.1109/JSTARS.2021.3051873

Hashemi-Beni, L., Jones, J., Thompson, G., Johnson, C., Gebrehiwot, A., 2018. Challenges and opportunities for UAV-based digital elevation model generation for flood-risk management: a case of Princeville, North Carolina. Sensors 18, 3843.

Hauet, A., Morlot, T., Daubagnan, L., 2018. Velocity profile and depth-averaged to surface velocity in natural streams: A review over alarge sample of rivers. E3S Web Conf. 40, 06015. https://doi.org/10.1051/e3sconf/20184006015

Hawker, L., Bates, P., Neal, J., Rougier, J., 2018. Perspectives on Digital Elevation Model (DEM) Simulation for Flood Modeling in the Absence of a High-Accuracy Open Access Global DEM. Front. Earth Sci. 6, 233. https://doi.org/10.3389/feart.2018.00233

He, A., Wang, K., Li, T., Du, C., Xia, S., Fu, H., 2023. H2Former: An Efficient Hierarchical Hybrid Transformer for Medical Image Segmentation. IEEE Transactions on Medical Imaging 1–1. https://doi.org/10.1109/TMI.2023.3264513

He, Q., Yang, Q., Xie, M., 2023. HCTNet: A hybrid CNN-transformer network for breast ultrasound image segmentation. Computers in Biology and Medicine 155, 106629. https://doi.org/10.1016/j.compbiomed.2023.106629

Heimhuber, V., Tulbure, M.G., Broich, M., 2016. Modeling 25 years of spatio-temporal surface water and inundation dynamics on large river basin scale using time series of Earth observation data. Hydrol. Earth Syst. Sci. 20, 2227–2250. https://doi.org/10.5194/hess-20-2227-2016

Heller, N., Dean, J., Papanikolopoulos, N., 2018. Imperfect Segmentation Labels: How Much Do They Matter?, in: Stoyanov, D., Taylor, Z., Balocco, S., Sznitman, R., Martel, A., Maier-Hein, L., Duong, L., Zahnd, G., Demirci, S., Albarqouni, S., Lee, S.-L., Moriconi, S., Cheplygina, V., Mateus, D., Trucco, E., Granger, E., Jannin, P. (Eds.), Intravascular Imaging and Computer Assisted Stenting and Large-Scale Annotation of Biomedical Data and Expert Label Synthesis. Springer International Publishing, Cham, pp. 112–120. https://doi.org/10.1007/978-3-030-01364-6_13

Hesselink, A.W., Stelling, G.S., Kwadijk, J.C.J., Middelkoop, H., 2003. Inundation of a Dutch river polder, sensitivity analysis of a physically based inundation model using historic data: SENSITIVITY ANALYSIS OF AN INUNDATION MODEL. Water Resour. Res. 39. https://doi.org/10.1029/2002WR001334

Hoch, J.M., Trigg, M.A., 2019. Advancing global flood hazard simulations by improving comparability, benchmarking, and integration of global flood models. Environ. Res. Lett. 14, 034001. https://doi.org/10.1088/1748-9326/aaf3d3

Hong, S., Bonkhoff, A.K., Hoopes, A., Bretzner, M., Schirmer, M.D., Giese, A.-K., Dalca, A.V., Golland, P., Rost, N.S., 2021. Hypernet-Ensemble Learning of Segmentation Probability for Medical Image Segmentation with Ambiguous Labels.

Horner, I., Renard, B., Le Coz, J., Branger, F., McMillan, H.K., Pierrefeu, G., 2018. Impact of Stage Measurement Errors on Streamflow Uncertainty. Water Resour. Res. 54, 1952–1976. https://doi.org/10.1002/2017WR022039

Horritt, M., Bates, P., 2002. Evaluation of 1D and 2D numerical models for predicting river flood inundation. Journal of hydrology 268, 87–99.

Horritt, M.S., 2006. A methodology for the validation of uncertain flood inundation models. Journal of Hydrology 326, 153–165. https://doi.org/10.1016/j.jhydrol.2005.10.027

Horritt, M.S., Bates, P.D., Fewtrell, T.J., Mason, D.C., Wilson, M.D., 2010. Modelling the hydraulics of the Carlisle 2005 flood event. Proceedings of the Institution of Civil Engineers - Water Management 163, 273–281. https://doi.org/10.1680/wama.2010.163.6.273

Hosseiny, H., 2021. A deep learning model for predicting river flood depth and extent. Environmental Modelling & Software 145, 105186. https://doi.org/10.1016/j.envsoft.2021.105186

Houghton-Carr, H., Fry, M., Wallingford, U., 2006. The decline of hydrological data collection for development of integrated water resource management tools in Southern Africa. IAHS publication 308, 51.

Hu, J., Li, L., Lin, Y., Wu, F., Zhao, J., 2019. A Comparison and Strategy of Semantic Segmentation on Remote Sensing Images. https://doi.org/10.48550/ARXIV.1905.10231

Hu, P., Caba, F., Wang, O., Lin, Z., Sclaroff, S., Perazzi, F., 2020. Temporally distributed networks for fast video semantic segmentation. Presented at the Proceedings of the IEEE/CVF Conference on Computer Vision and Pattern Recognition, pp. 8818–8827.

Huang, B., Li, Y., Han, X., Cui, Y., Li, W., Li, R., 2015. Cloud Removal From Optical Satellite Imagery With SAR Imagery Using Sparse Representation. IEEE Geosci. Remote Sensing Lett. 12, 1046–1050. https://doi.org/10.1109/LGRS.2014.2377476

Huang, W.-C., Young, C.-C., Liu, W.-C., 2018. Application of an automated discharge imaging system and LSPIV during typhoon events in Taiwan. Water 10, 280.

Huh, M., Agrawal, P., Efros, A.A., 2016. What makes ImageNet good for transfer learning?

Hunter, N.M., Bates, P.D., Neelz, S., Pender, G., Villanueva, I., Wright, N.G., Liang, D., Falconer, R.A., Lin, B., Waller, S., Crossley, A.J., Mason, D.C., 2008. Benchmarking 2D hydraulic models for urban flooding. Proceedings of the Institution of Civil Engineers - Water Management 161, 13–30. https://doi.org/10.1680/wama.2008.161.1.13

Iroume, J.Y.-A., Onguéné, R., Djanna Koffi, F., Colmet-Daage, A., Stieglitz, T., Essoh Sone, W., Bogning, S., Olinga Olinga, J.M., Ntchantcho, R., Ntonga, J.-C., Braun, J.-J., Briquet, J.-P., Etame, J., 2022. The 21st August 2020 Flood in Douala (Cameroon): A Major Urban Flood Investigated with 2D HEC-RAS Modeling. Water 14, 1768. https://doi.org/10.3390/w14111768

Ivliev, N., Evdokimova, V., Podlipnov, V., Petrov, M., Ganchevskaya, S., Tkachenko, I., Abrameshin, D., Yuzifovich, Y., Nikonorov, A., Skidanov, R., Kazanskiy, N., Soifer, V., 2022. First Earth-Imaging CubeSat with Harmonic Diffractive Lens. Remote Sensing 14, 2230. https://doi.org/10.3390/rs14092230

Jadon, S., 2020. A survey of loss functions for semantic segmentation, in: 2020 IEEE Conference on Computational Intelligence in Bioinformatics and Computational Biology (CIBCB). Presented at the 2020 IEEE Conference on Computational Intelligence in Bioinformatics and Computational Biology (CIBCB), IEEE, Via del Mar, Chile, pp. 1–7. https://doi.org/10.1109/CIBCB48159.2020.9277638

James, M.R., Chandler, J.H., Eltner, A., Fraser, C., Miller, P.E., Mills, J.P., Noble, T., Robson, S., Lane, S.N., 2019. Guidelines on the use of structure-from-motion photogrammetry in geomorphic research. Earth Surface Processes and Landforms 44, 2081–2084. https://doi.org/10.1002/esp.4637

Javadnejad, F., Slocum, R.K., Gillins, D.T., Olsen, M.J., Parrish, C.E., 2021. Dense Point Cloud Quality Factor as Proxy for Accuracy Assessment of Image-Based 3D Reconstruction. J. Surv. Eng. 147, 04020021. https://doi.org/10.1061/(ASCE)SU.1943-5428.0000333

Javernick, L., Brasington, J., Caruso, B., 2014. Modeling the topography of shallow braided rivers using Structure-from-Motion photogrammetry. Geomorphology 213, 166–182. https://doi.org/10.1016/j.geomorph.2014.01.006

Jiang, L., Madsen, H., Bauer-Gottwein, P., 2019. Simultaneous calibration of multiple hydrodynamic model parameters using satellite altimetry observations of water surface elevation in the Songhua River. Remote Sensing of Environment 225, 229–247. https://doi.org/10.1016/j.rse.2019.03.014

Jiménez-Jiménez, S.I., Ojeda-Bustamante, W., Marcial-Pablo, M. de J., Enciso, J., 2021. Digital Terrain Models Generated with Low-Cost UAV Photogrammetry: Methodology and Accuracy. ISPRS International Journal of Geo-Information 10, 285. https://doi.org/10.3390/ijgi10050285

Jolley, M.J., Russell, A.J., Quinn, P.F., Perks, M.T., 2021. Considerations When Applying Large-Scale PIV and PTV for Determining River Flow Velocity. Front. Water 3, 709269. https://doi.org/10.3389/frwa.2021.709269

Jowett, I.G., Duncan, M.J., 2012. Effectiveness of 1D and 2D hydraulic models for instream habitat analysis in a braided river. Ecological Engineering, Ecohydraulic Approaches for Restoring Habitat Connectivity and Suitability 48, 92–100. https://doi.org/10.1016/j.ecoleng.2011.06.036

Jung, Y., Merwade, V., 2012. Uncertainty Quantification in Flood Inundation Mapping Using Generalized Likelihood Uncertainty Estimate and Sensitivity Analysis. Journal of Hydrologic Engineering 17, 507–520. https://doi.org/10.1061/(ASCE)HE.1943-5584.0000476

Kääb, A., Altena, B., Mascaro, J., 2019. River-ice and water velocities using the Planet optical cubesat constellation. Hydrol. Earth Syst. Sci. 23, 4233–4247. https://doi.org/10.5194/hess-23-4233-2019

Karimi, D., Vasylechko, S.D., Gholipour, A., 2021. Convolution-free medical image segmentation using transformers. Presented at the Medical Image Computing and Computer Assisted Intervention–MICCAI 2021: 24th International Conference, Strasbourg, France, September 27–October 1, 2021, Proceedings, Part I 24, Springer, pp. 78–88.

Kasvi, E., Salmela, J., Lotsari, E., Kumpula, T., Lane, S., 2019. Comparison of remote sensing based approaches for mapping bathymetry of shallow, clear water rivers. Geomorphology 333, 180–197.

Kato, Z., Zerubia, J., 2012. Markov random fields in image segmentation. Foundations and Trends® in Signal Processing 5, 1–155.

Khalid, H.W., Khalil, R.M.Z., Qureshi, M.A., 2021. Evaluating spectral indices for water bodies extraction in western Tibetan Plateau. The Egyptian Journal of Remote Sensing and Space Science 24, 619–634. https://doi.org/10.1016/j.ejrs.2021.09.003

Khan, S., Naseer, M., Hayat, M., Zamir, S.W., Khan, F.S., Shah, M., 2022. Transformers in Vision: A Survey. ACM Comput. Surv. 54, 1–41. https://doi.org/10.1145/3505244

Kiang, J.E., Gazoorian, C., McMillan, H., Coxon, G., Le Coz, J., Westerberg, I.K., Belleville, A., Sevrez, D., Sikorska, A.E., Petersen-Øverleir, A., Reitan, T., Freer, J., Renard, B., Mansanarez, V., Mason, R., 2018. A Comparison of Methods for Streamflow Uncertainty Estimation. Water Resour. Res. 54, 7149–7176. https://doi.org/10.1029/2018WR022708

Kim, Y., 2006. Uncertainty analysis for non-intrusive measurement of river discharge using image velocimetry (Ph.D.). The University of Iowa, United States -- Iowa.

Kim, Y., Muste, M., Hauet, A., Krajewski, W.F., Kruger, A., Bradley, A., 2008. Stream discharge using mobile large-scale particle image velocimetry: A proof of concept. Water Resources Research 44. https://doi.org/10.1029/2006WR005441

King, A.D., Pitman, A.J., Henley, B.J., Ukkola, A.M., Brown, J.R., 2020. The role of climate variability in Australian drought. Nature Climate Change 10, 177–179.

King, T.V., Neilson, B.T., Rasmussen, M.T., 2018. Estimating Discharge in Low-Order Rivers With High-Resolution Aerial Imagery. Water Resour. Res. 54, 863–878. https://doi.org/10.1002/2017WR021868

Kirillov, A., Mintun, E., Ravi, N., Mao, H., Rolland, C., Gustafson, L., Xiao, T., Whitehead, S., Berg, A.C., Lo, W.-Y., 2023. Segment anything. arXiv preprint arXiv:2304.02643.

Komi, K., Neal, J., Trigg, M.A., Diekkrüger, B., 2017. Modelling of flood hazard extent in data sparse areas: a case study of the Oti River basin, West Africa. Journal of Hydrology: Regional Studies 10, 122–132.

Koutalakis, P., Tzoraki, O., Zaimes, G., 2019. UAVs for Hydrologic Scopes: Application of a Low-Cost UAV to Estimate Surface Water Velocity by Using Three Different Image-Based Methods. Drones 3, 14. https://doi.org/10.3390/drones3010014

Koutalakis, P., Zaimes, G.N., 2022. River Flow Measurements Utilizing UAV-Based Surface Velocimetry and Bathymetry Coupled with Sonar. Hydrology 9, 148.

Krieger, G., Moreira, A., Fiedler, H., Hajnsek, I., Werner, M., Younis, M., Zink, M., 2007. TanDEM-X: A satellite formation for high-resolution SAR interferometry. IEEE Transactions on Geoscience and Remote Sensing 45, 3317–3341.

Krizhevsky, A., Sutskever, I., Hinton, G.E., 2017. Imagenet classification with deep convolutional neural networks. Communications of the ACM 60, 84–90.

Kugelman, J., Allman, J., Read, S.A., Vincent, S.J., Tong, J., Kalloniatis, M., Chen, F.K., Collins, M.J., Alonso-Caneiro, D., 2022. A comparison of deep learning U-Net architectures for posterior segment OCT retinal layer segmentation. Sci Rep 12, 14888. https://doi.org/10.1038/s41598-022-18646-2

Kulkarni, S.C., Rege, P.P., 2020. Pixel level fusion techniques for SAR and optical images: A review. Information Fusion 59, 13–29.

Kumar, N., Lal, D., Sherring, A., Issac, R.K., 2017. Applicability of HEC-RAS & GFMS tool for 1D water surface elevation/flood modeling of the river: a Case Study of River Yamuna at Allahabad (Sangam), India. Model. Earth Syst. Environ. 3, 1463–1475. https://doi.org/10.1007/s40808-017-0390-0

Lane, S.N., Bradbrook, K.F., Richards, K.S., Biron, P.A., Roy, A.G., 1999. The application of computational fluid dynamics to natural river channels: three-dimensional versus two-dimensional approaches. Geomorphology 29, 1–20. https://doi.org/10.1016/S0169-555X(99)00003-3

Le Boursicaud, R., Pénard, L., Hauet, A., Thollet, F., Le Coz, J., 2016. Gauging extreme floods on YouTube: Application of LSPIV to home movies for the post-event determination of stream discharges. Hydrological Processes 30, 90–105.

Le Coz, J., Hauet, A., Pierrefeu, G., Dramais, G., Camenen, B., 2010a. Performance of image-based velocimetry (LSPIV) applied to flash-flood discharge measurements in

Mediterranean rivers. Journal of Hydrology 394, 42–52. https://doi.org/10.1016/j.jhydrol.2010.05.049

Le Coz, J., Hauet, A., Pierrefeu, G., Dramais, G., Camenen, B., 2010b. Performance of image-based velocimetry (LSPIV) applied to flash-flood discharge measurements in Mediterranean rivers. Journal of Hydrology 394, 42–52. https://doi.org/10.1016/j.jhydrol.2010.05.049

Le Coz, Jérôme, Jodeau, M., Hauet, A., Marchand, B., Le Boursicaud, R., 2014. Image-based velocity and discharge measurements in field and laboratory river engineering studies using the free FUDAA-LSPIV software. Presented at the Proceedings of the international conference on fluvial hydraulics, River Flow, pp. 2014–05.

Le Coz, J., Renard, B., Bonnifait, L., Branger, F., Le Boursicaud, R., 2014. Combining hydraulic knowledge and uncertain gaugings in the estimation of hydrometric rating curves: A Bayesian approach. Journal of Hydrology 509, 573–587. https://doi.org/10.1016/j.jhydrol.2013.11.016

Leach, N.R., Popien, P., Goodman, M.C., Tellman, B., 2022. Leveraging convolutional neural networks for semantic segmentation of global floods with PlanetScope imagery. Presented at the IGARSS 2022-2022 IEEE International Geoscience and Remote Sensing Symposium, IEEE, pp. 314–317.

Lecun, Y., Bengio, Y., 1995. Convolutional networks for images, speech, and time-series, in: Arbib, M.A. (Ed.), The Handbook of Brain Theory and Neural Networks. MIT Press.

Lee, H., Kwon, H., 2017. Going deeper with contextual CNN for hyperspectral image classification. IEEE Transactions on Image Processing 26, 4843–4855.

Lee, Sunmin, Kim, J.-C., Jung, H.-S., Lee, M.J., Lee, Saro, 2017. Spatial prediction of flood susceptibility using random-forest and boosted-tree models in Seoul metropolitan city, Korea. Geomatics, Natural Hazards and Risk 8, 1185–1203. https://doi.org/10.1080/19475705.2017.1308971

Leedal, D., Weerts, A., Smith, P., Beven, K.J., 2013. Application of data-based mechanistic modelling for flood forecasting at multiple locations in the Eden catchment in the

National Flood Forecasting System (England and Wales). Hydrology and Earth System Sciences 17, 177–185.

Legleiter, C.J., Kinzel, P.J., 2021a. Surface Flow Velocities From Space: Particle Image Velocimetry of Satellite Video of a Large, Sediment-Laden River. Front. Water 3, 652213. https://doi.org/10.3389/frwa.2021.652213

Legleiter, C.J., Kinzel, P.J., 2021b. Depths Inferred from Velocities Estimated by Remote Sensing: A Flow Resistance Equation-Based Approach to Mapping Multiple River Attributes at the Reach Scale. Remote Sensing 13, 4566. https://doi.org/10.3390/rs13224566

Legleiter, C.J., Kinzel, P.J., 2020. Inferring surface flow velocities in sediment-laden Alaskan rivers from optical image sequences acquired from a helicopter. Remote Sensing 12, 1282.

Legleiter, C.J., Kinzel, P.J., Laker, M., Conaway, J.S., 2023. Moving Aircraft River Velocimetry (MARV): Framework and proof-of-concept on the Tanana River. Water Resources Research. https://doi.org/10.1029/2022WR033822

Leitão, J.P., Peña-Haro, S., Lüthi, B., Scheidegger, A., de Vitry, M.M., 2018. Urban overland runoff velocity measurement with consumer-grade surveillance cameras and surface structure image velocimetry. Journal of Hydrology 565, 791–804.

Lenc, K., Vedaldi, A., 2016. Learning Covariant Feature Detectors, in: Hua, G., Jégou, H. (Eds.), Computer Vision – ECCV 2016 Workshops, Lecture Notes in Computer Science. Springer International Publishing, Cham, pp. 100–117. https://doi.org/10.1007/978-3-319-49409-8_11

Leutenegger, S., Chli, M., Siegwart, R.Y., 2011. BRISK: Binary Robust invariant scalable keypoints, in: 2011 International Conference on Computer Vision. Presented at the 2011 International Conference on Computer Vision, pp. 2548–2555. https://doi.org/10.1109/ICCV.2011.6126542

Lewis, Q.W., Lindroth, E.M., Rhoads, B.L., 2018. Integrating unmanned aerial systems and LSPIV for rapid, cost-effective stream gauging. Journal of Hydrology 560, 230–246. https://doi.org/10.1016/j.jhydrol.2018.03.008

Li, G., Liu, J., Shao, W., 2022. Flood Risk Assessment Using TELEMAC-2D Models Integrated with Multi-Index Analysis in Shenzhen River Basin, China. Water 14, 2513. https://doi.org/10.3390/w14162513

Li, L., Yan, H., 2022. A robust filtering algorithm based on the estimation of tracer visibility and stability for large scale particle image velocimetry. Flow Measurement and Instrumentation 87, 102204. https://doi.org/10.1016/j.flowmeasinst.2022.102204

Li, Y., Shi, J., Lin, D., 2018. Low-latency video semantic segmentation. Presented at the Proceedings of the IEEE Conference on Computer Vision and Pattern Recognition, pp. 5997–6005.

Li, Z., Shen, H., Cheng, Q., Li, W., Zhang, L., 2019. Thick Cloud Removal in High-Resolution Satellite Images Using Stepwise Radiometric Adjustment and Residual Correction. Remote Sensing 11, 1925. https://doi.org/10.3390/rs11161925

Liddle, J.D., Holt, A.P., Jason, S.J., O’Donnell, K.A., Stevens, E.J., 2020. Space science with CubeSats and nanosatellites. Nat Astron 4, 1026–1030. https://doi.org/10.1038/s41550-020-01247-2

Lins, H.F., 2008. Challenges to hydrological observations. WMO Bulletin 57, 55–58.

Liu, H., Ruan, Z., Zhao, P., Dong, C., Shang, F., Liu, Y., Yang, L., Timofte, R., 2022. Video super-resolution based on deep learning: a comprehensive survey. Artificial Intelligence Review 55, 5981–6035.

Liu, J., Liu, G., Zhao, Y., 2022. Improve Semantic Segmentation of High-Resolution Remote Sensing Imagery with RS-TTA. Presented at the 2022 5th International Conference on Pattern Recognition and Artificial Intelligence (PRAI), IEEE, pp. 817–825.

Liu, J., Shao, W., Xiang, C., Mei, C., Li, Z., 2020. Uncertainties of urban flood modeling: Influence of parameters for different underlying surfaces. Environmental Research 182, 108929. https://doi.org/10.1016/j.envres.2019.108929

Liu, K., Song, C., Wang, J., Ke, L., Zhu, Y., Zhu, J., Ma, R., Luo, Z., 2020. Remote Sensing-Based Modeling of the Bathymetry and Water Storage for Channel-Type Reservoirs Worldwide. Water Resources Research 56, e2020WR027147. https://doi.org/10.1029/2020WR027147

Liu, W.-C., Lu, C.-H., Huang, W.-C., 2021. Large-Scale Particle Image Velocimetry to Measure Streamflow from Videos Recorded from Unmanned Aerial Vehicle and Fixed Imaging System. Remote Sensing 13, 2661. https://doi.org/10.3390/rs13142661

Liu, Y., Han, T., Ma, S., Zhang, J., Yang, Y., Tian, J., He, H., Li, A., He, M., Liu, Z., 2023. Summary of chatgpt/gpt-4 research and perspective towards the future of large language models. arXiv preprint arXiv:2304.01852.

Liu, Z., Lin, Y., Cao, Y., Hu, H., Wei, Y., Zhang, Z., Lin, S., Guo, B., 2021. Swin Transformer: Hierarchical Vision Transformer using Shifted Windows. https://doi.org/10.48550/arXiv.2103.14030

Ljubičić, R., Strelnikova, D., Perks, M.T., Eltner, A., Peña-Haro, S., Pizarro, A., Dal Sasso, S.F., Scherling, U., Vuono, P., Manfreda, S., 2021. A comparison of tools and techniques for stabilising unmanned aerial system (UAS) imagery for surface flow observations. Hydrology and Earth System Sciences 25, 5105–5132. https://doi.org/10.5194/hess-25-5105-2021

Lo Conti, F., Hsu, K.-L., Noto, L.V., Sorooshian, S., 2014. Evaluation and comparison of satellite precipitation estimates with reference to a local area in the Mediterranean Sea. Atmospheric Research 138, 189–204. https://doi.org/10.1016/j.atmosres.2013.11.011

Lomaka, I.A., Elisov, N.A., Boltov, E.A., Shafran, S.V., 2022. A novel design of CubeSat deployment system for transformable structures. Acta Astronautica 197, 179–190. https://doi.org/10.1016/j.actaastro.2022.05.027

Longuet-Higgins, H.C., 1981. A computer algorithm for reconstructing a scene from two projections. Nature 293, 133–135. https://doi.org/10.1038/293133a0

Lou, L., Liu, Y., Sheng, M., Han, J., Doonan, J.H., 2014. A Cost-Effective Automatic 3D Reconstruction Pipeline for Plants Using Multi-view Images, in: Mistry, M., Leonardis, A., Witkowski, M., Melhuish, C. (Eds.), Advances in Autonomous Robotics Systems, Lecture Notes in Computer Science. Springer International Publishing, Cham, pp. 221–230. https://doi.org/10.1007/978-3-319-10401-0_20

Lowe, D.G., 2004. Distinctive Image Features from Scale-Invariant Keypoints. International Journal of Computer Vision 60, 91–110. https://doi.org/10.1023/B:VISI.0000029664.99615.94

Ma, D., Wu, R., Xiao, D., Sui, B., 2023. Cloud Removal from Satellite Images Using a Deep Learning Model with the Cloud-Matting Method. Remote Sensing 15, 904.

Ma, W., Wen, Z., Wu, Y., Jiao, L., Gong, M., Zheng, Y., Liu, L., 2016. Remote sensing image registration with modified SIFT and enhanced feature matching. IEEE Geoscience and Remote Sensing Letters 14, 3–7.

Ma, Y., Wu, H., Wang, L., Huang, B., Ranjan, R., Zomaya, A., Jie, W., 2015. Remote sensing big data computing: Challenges and opportunities. Future Generation Computer Systems, Special Section: A Note on New Trends in Data-Aware Scheduling and Resource Provisioning in Modern HPC Systems 51, 47–60. https://doi.org/10.1016/j.future.2014.10.029

Ma, Y., Xu, N., Liu, Z., Yang, B., Yang, F., Wang, X.H., Li, S., 2020. Satellite-derived bathymetry using the ICESat-2 lidar and Sentinel-2 imagery datasets. Remote Sensing of Environment 250, 112047. https://doi.org/10.1016/j.rse.2020.112047

Marinan, A., Nicholas, A., Cahoy, K., 2013. Ad hoc CubeSat constellations: Secondary launch coverage and distribution, in: 2013 IEEE Aerospace Conference. Presented at the 2013 IEEE Aerospace Conference, IEEE, Big Sky, MT, pp. 1–15. https://doi.org/10.1109/AERO.2013.6497174

Masafu, C., Williams, R., Shi, X., Yuan, Q., Trigg, M., 2022. Unpiloted Aerial Vehicle (UAV) image velocimetry for validation of two-dimensional hydraulic model simulations. Journal of Hydrology 612, 128217. https://doi.org/10.1016/j.jhydrol.2022.128217

Mason, D.C., Bates, P.D., Dall’ Amico, J.T., 2009. Calibration of uncertain flood inundation models using remotely sensed water levels. Journal of Hydrology 368, 224–236. https://doi.org/10.1016/j.jhydrol.2009.02.034

Mateo-Garcia, G., Veitch-Michaelis, J., Smith, L., Oprea, S.V., Schumann, G., Gal, Y., Baydin, A.G., Backes, D., 2021. Towards global flood mapping onboard low cost satellites with machine learning. Sci Rep 11, 7249. https://doi.org/10.1038/s41598-021-86650-z

Matgen, P., Montanari, M., Hostache, R., Pfister, L., Hoffmann, L., Plaza, D., Pauwels, V.R.N., De Lannoy, G.J.M., De Keyser, R., Savenije, H.H.G., 2010. Towards the sequential assimilation of SAR-derived water stages into hydraulic models using the Particle Filter: proof of concept. Hydrology and Earth System Sciences 14, 1773–1785. https://doi.org/10.5194/hess-14-1773-2010

Matheson, A., Thoms, M.C., 2018. The spatial pattern of large wood in a large low gradient river: the Barwon–Darling River. International Journal of River Basin Management 16, 21–33. https://doi.org/10.1080/15715124.2017.1387123

Mayes, W. m., Walsh, C. l., Bathurst, J. c., Kilsby, C. g., Quinn, P. f., Wilkinson, M. e., Daugherty, A. j., O'Connell, P. e., 2006. Monitoring a flood event in a densely instrumented catchment, the Upper Eden, Cumbria, UK. Water and Environment Journal 20, 217–226. https://doi.org/10.1111/j.1747-6593.2005.00006.x

McCabe, M.F., Rodell, M., Alsdorf, D.E., Miralles, D.G., Uijlenhoet, R., Wagner, W., Lucieer, A., Houborg, R., Verhoest, N.E.C., Franz, T.E., Shi, J., Gao, H., Wood, E.F., 2017a. The future of Earth observation in hydrology. Hydrol. Earth Syst. Sci. 21, 3879–3914. https://doi.org/10.5194/hess-21-3879-2017

McCabe, M.F., Rodell, M., Alsdorf, D.E., Miralles, D.G., Uijlenhoet, R., Wagner, W., Lucieer, A., Houborg, R., Verhoest, N.E.C., Franz, T.E., Shi, J., Gao, H., Wood, E.F., 2017b. The future of Earth observation in hydrology. Hydrol. Earth Syst. Sci. 21, 3879–3914. https://doi.org/10.5194/hess-21-3879-2017

McFeeters, S.K., 1996. The use of the Normalized Difference Water Index (NDWI) in the delineation of open water features. International Journal of Remote Sensing 17, 1425–1432. https://doi.org/10.1080/01431169608948714

McIlvenny, J., Williamson, B., Fairley, I., Lewis, M., Neill, S., Masters, I., Reeve, D.E., 2022. Comparison of dense optical flow and PIV techniques for mapping surface current flow in tidal stream energy sites. International Journal of Energy and Environmental Engineering 1–13.

McMillan, H., Krueger, T., Freer, J., 2012. Benchmarking observational uncertainties for hydrology: rainfall, river discharge and water quality: BENCHMARKING OBSERVATIONAL UNCERTAINTIES FOR HYDROLOGY. Hydrol. Process. 26, 4078–4111. https://doi.org/10.1002/hyp.9384

MDBA, 2010. Guide to the proposed Basin Plan: overview.

Meraner, A., Ebel, P., Zhu, X.X., Schmitt, M., 2020. Cloud removal in Sentinel-2 imagery using a deep residual neural network and SAR-optical data fusion. ISPRS Journal of Photogrammetry and Remote Sensing 166, 333–346.

Mester, B., Willner, S.N., Frieler, K., Schewe, J., 2021. Evaluation of river flood extent simulated with multiple global hydrological models and climate forcings. Environ. Res. Lett. 16, 094010. https://doi.org/10.1088/1748-9326/ac188d

Minaee, S., Boykov, Y., Porikli, F., Plaza, A., Kehtarnavaz, N., Terzopoulos, D., 2020. Image Segmentation Using Deep Learning: A Survey. arXiv:2001.05566 [cs].

Mishra, A.K., Coulibaly, P., 2009. Developments in hydrometric network design: A review. Reviews of Geophysics 47. https://doi.org/10.1029/2007RG000243

Mishra, B.K., Rafiei Emam, A., Masago, Y., Kumar, P., Regmi, R.K., Fukushi, K., 2018. Assessment of future flood inundations under climate and land use change scenarios in the Ciliwung River Basin, Jakarta. Journal of Flood Risk Management 11, S1105–S1115.

Moazami, S., Golian, S., Kavianpour, M.R., Hong, Y., 2014. Uncertainty analysis of bias from satellite rainfall estimates using copula method. Atmospheric Research 137, 145–166.

Mobley, W., Sebastian, A., Blessing, R., Highfield, W.E., Stearns, L., Brody, S.D., 2021. Quantification of continuous flood hazard using random forest classification and flood insurance claims at large spatial scales: a pilot study in southeast Texas. Nat. Hazards Earth Syst. Sci. 21, 807–822. https://doi.org/10.5194/nhess-21-807-2021

Mokhtar, E.S., Pradhan, B., Ghazali, A.H., Shafri, H.Z.M., 2018. Assessing flood inundation mapping through estimated discharge using GIS and HEC-RAS model. Arab J Geosci 11, 682. https://doi.org/10.1007/s12517-018-4040-2

Molinari, D., De Bruijn, K.M., Castillo-Rodríguez, J.T., Aronica, G.T., Bouwer, L.M., 2019. Validation of flood risk models: Current practice and possible improvements. International Journal of Disaster Risk Reduction 33, 441–448. https://doi.org/10.1016/j.ijdrr.2018.10.022

Moliner, E., Romero, L.S., Vilaplana, V., 2020. Weakly supervised semantic segmentation for remote sensing hyperspectral imaging. Presented at the ICASSP 2020-2020 IEEE International Conference on Acoustics, Speech and Signal Processing (ICASSP), IEEE, pp. 2273–2277.

Mondal, S., Patel, P.P., 2018. Examining the utility of river restoration approaches for flood mitigation and channel stability enhancement: a recent review. Environ Earth Sci 77, 195. https://doi.org/10.1007/s12665-018-7381-y

Montanari, M., Hostache, R., Matgen, P., Schumann, G., Pfister, L., Hoffmann, L., 2009. Calibration and sequential updating of a coupled hydrologic-hydraulic model using remote sensing-derived water stages. Hydrology and Earth System Sciences 13, 367–380. https://doi.org/10.5194/hess-13-367-2009

Moradkhani, H., Hsu, K., Hong, Y., Sorooshian, S., 2006. Investigating the impact of remotely sensed precipitation and hydrologic model uncertainties on the ensemble streamflow forecasting. Geophysical Research Letters 33. https://doi.org/10.1029/2006GL026855

Moraitis, G., Baltas, E., 2020. Dealing with LSPIV questions on the field: An approach for autonomous flood gauging using UAVs. European Water 71, 27–40.

Moramarco, T., Barbetta, S., Bjerklie, D.M., Fulton, J.W., Tarpanelli, A., 2019. River Bathymetry Estimate and Discharge Assessment from Remote Sensing. Water Resources Research 55, 6692–6711. https://doi.org/10.1029/2018WR024220

Moramarco, T., Barbetta, S., Tarpanelli, A., 2017. From Surface Flow Velocity Measurements to Discharge Assessment by the Entropy Theory. Water 9, 120. https://doi.org/10.3390/w9020120

Moshkov, N., Mathe, B., Kertesz-Farkas, A., Hollandi, R., Horvath, P., 2020. Test-time augmentation for deep learning-based cell segmentation on microscopy images. Sci Rep 10, 5068. https://doi.org/10.1038/s41598-020-61808-3

Mueller, D.S., 2003. Field evaluation of boat-mounted acoustic Doppler instruments used to measure streamflow. Presented at the Proceedings of the IEEE/OES Seventh Working Conference on Current Measurement Technology, 2003., IEEE, pp. 30–34.

Mueller, D.S., Wagner, C.R., Rehmel, M.S., Oberg, K.A., Rainville, F., 2013. Measuring discharge with acoustic Doppler current profilers from a moving boat (USGS Numbered Series No. 3-A22), Measuring discharge with acoustic Doppler current profilers from a moving boat, Techniques and Methods. U.S. Geological Survey, Reston, VA. https://doi.org/10.3133/tm3A22

Muja, M., Lowe, D.G., 2009. Fast approximate nearest neighbors with automatic algorithm configuration. VISAPP (1) 2, 2.

Mukul, Manas, Srivastava, V., Jade, S., Mukul, Malay, 2017. Uncertainties in the Shuttle Radar Topography Mission (SRTM) Heights: Insights from the Indian Himalaya and Peninsula. Sci Rep 7, 41672. https://doi.org/10.1038/srep41672

Munawar, H.S., Hammad, A.W., Waller, S.T., 2022. Remote sensing methods for flood prediction: A review. Sensors 22, 960.

Murray-Darling Basin Authority, 2010. Guide to the proposed Basin Plan: Technical background (MDBA publication no. 61/10).

Muste, M., Fujita, I., Hauet, A., 2008a. Large-scale particle image velocimetry for measurements in riverine environments. Water Resources Research 44. https://doi.org/10.1029/2008WR006950

Muste, M., Fujita, I., Hauet, A., 2008b. Large-scale particle image velocimetry for measurements in riverine environments: LARGE-SCALE PARTICLE VELOCIMETRY. Water Resour. Res. 44. https://doi.org/10.1029/2008WR006950

Nandi, I., Srivastava, P.K., Shah, K., 2017. Floodplain Mapping through Support Vector Machine and Optical/Infrared Images from Landsat 8 OLI/TIRS Sensors: Case Study from Varanasi. Water Resour Manage 31, 1157–1171. https://doi.org/10.1007/s11269-017-1568-y

Navarro-Hernández, M.I., Valdes-Abellan, J., Tomás, R., Tessitore, S., Ezquerro, P., Herrera, G., 2023. Analysing the Impact of Land Subsidence on the Flooding Risk:

Evaluation Through InSAR and Modelling. Water Resour Manage. https://doi.org/10.1007/s11269-023-03561-6

Neal, J., Schumann, G., Bates, P., Buytaert, W., Matgen, P., Pappenberger, F., 2009. A data assimilation approach to discharge estimation from space. Hydrological Processes 23, 3641–3649. https://doi.org/10.1002/hyp.7518

Néelz, S., Pender, G., 2013. Benchmarking the latest generation of 2D hydraulic modelling packages. Environment Agency: Bristol, UK.

Nguyen, H.M., Wünsche, B., Delmas, P., Lutteroth, C., 2012. 3D models from the black box: investigating the current state of image-based modeling. Proceedings of the 20th International Conference on Computer Graphics, Visualisation and Computer Vision (WSCG), 2012 249–258.

Nguyen, T.H., Ricci, S., Fatras, C., Piacentini, A., Delmotte, A., Lavergne, E., Kettig, P., 2022. Improvement of flood extent representation with remote sensing data and data assimilation. IEEE Transactions on Geoscience and Remote Sensing 60, 1–22.

Niethammer, U., Rothmund, S., Schwaderer, U., Zeman, J., Joswig, M., 2012. OPEN SOURCE IMAGE-PROCESSING TOOLS FOR LOW-COST UAV-BASED LANDSLIDE INVESTIGATIONS. Int. Arch. Photogramm. Remote Sens. Spatial Inf. Sci. XXXVIII-1/C22, 161–166. https://doi.org/10.5194/isprsarchives-XXXVIII-1-C22-161-2011

Nkwunonwo, U., Whitworth, M., Baily, B., 2020. A review of the current status of flood modelling for urban flood risk management in the developing countries. Scientific African 7, e00269.

Ocio, D., Le Vine, N., Westerberg, I., Pappenberger, F., Buytaert, W., 2017. The role of rating curve uncertainty in real-time flood forecasting: THE ROLE OF RCU IN FLOOD FORECASTING. Water Resour. Res. 53, 4197–4213. https://doi.org/10.1002/2016WR020225

O'Connell, P., Quinn, P., Bathurst, J., Parkin, G., Kilsby, C., Beven, K., Burt, T., Kirkby, M., Pickering, A., Robinson, M., 2007. Catchment Hydrology and Sustainable Management (CHASM): an integrating methodological framework for prediction. IAHS Publication 309, 53–62.

Ongdas, N., Akiyanova, F., Karakulov, Y., Muratbayeva, A., Zinabdin, N., 2020. Application of HEC-RAS (2D) for Flood Hazard Maps Generation for Yesil (Ishim) River in Kazakhstan. Water 12, 2672. https://doi.org/10.3390/w12102672

Oubanas, H., Gejadze, I., Malaterre, P.-O., Mercier, F., 2018. River discharge estimation from synthetic SWOT-type observations using variational data assimilation and the full Saint-Venant hydraulic model. Journal of Hydrology 559, 638–647. https://doi.org/10.1016/j.jhydrol.2018.02.004

Özcan, Orkan, Özcan, Okan, 2021. Multi-temporal UAV based repeat monitoring of rivers sensitive to flood. Journal of Maps 17, 163–170.

Padmapriya, B., Kesavamurthi, T., Ferose, H.W., 2012. Edge based image segmentation technique for detection and estimation of the bladder wall thickness. Procedia engineering 30, 828–835.

Palharini, R.S.A., Vila, D.A., Rodrigues, D.T., Quispe, D.P., Palharini, R.C., de Siqueira, R.A., de Sousa Afonso, J.M., 2020. Assessment of the Extreme Precipitation by Satellite Estimates over South America. Remote Sensing 12, 2085. https://doi.org/10.3390/rs12132085

Pally, R., Samadi, S., 2022. Application of image processing and convolutional neural networks for flood image classification and semantic segmentation. Environmental Modelling & Software 148, 105285.

Pare, S., Kumar, A., Singh, G.K., Bajaj, V., 2020. Image segmentation using multilevel thresholding: a research review. Iranian Journal of Science and Technology, Transactions of Electrical Engineering 44, 1–29.

Parkes, B.L., Cloke, H.L., Pappenberger, F., Neal, J., Demeritt, D., 2013. Reducing Inconsistencies in Point Observations of Maximum Flood Inundation Level. Earth Interactions 17, 1–27. https://doi.org/10.1175/2012EI000475.1

Pasternack, G.B., 2011. 2D Modeling and Ecohydraulic Analysis.

Patel, D.P., Ramirez, J.A., Srivastava, P.K., Bray, M., Han, D., 2017. Assessment of flood inundation mapping of Surat city by coupled 1D/2D hydrodynamic modeling: a case application of the new HEC-RAS 5. Nat Hazards 89, 93–130. https://doi.org/10.1007/s11069-017-2956-6

Pearce, S., Ljubičić, R., Peña-Haro, S., Perks, M., Tauro, F., Pizarro, A., Dal Sasso, S., Strelnikova, D., Grimaldi, S., Maddock, I., Paulus, G., Plavšić, J., Prodanović, D., Manfreda, S., 2020a. An Evaluation of Image Velocimetry Techniques under Low Flow Conditions and High Seeding Densities Using Unmanned Aerial Systems. Remote Sensing 12, 232. https://doi.org/10.3390/rs12020232

Pearce, S., Ljubičić, R., Peña-Haro, S., Perks, M., Tauro, F., Pizarro, A., Dal Sasso, S., Strelnikova, D., Grimaldi, S., Maddock, I., Paulus, G., Plavšić, J., Prodanović, D., Manfreda, S., 2020b. An Evaluation of Image Velocimetry Techniques under Low Flow Conditions and High Seeding Densities Using Unmanned Aerial Systems. Remote Sensing 12, 232. https://doi.org/10.3390/rs12020232

Peña, F., Nardi, F., 2018. Floodplain Terrain Analysis for Coarse Resolution 2D Flood Modeling. Hydrology 5, 52. https://doi.org/10.3390/hydrology5040052

Pender, G., Faulkner, H., 2011. Flood risk science and management. Wiley Online Library.

Perks, M.T., 2020. KLT-IV v1. 0: Image velocimetry software for use with fixed and mobile platforms. Geoscientific Model Development 13, 6111–6130.

Perks, M.T., Dal Sasso, S.F., Hauet, A., Le Coz, J., Pearce, S., Peña-Haro, S., Tauro, F., Grimaldi, S., Hortobágyi, B., Jodeau, M., Maddock, I., Pénard, L., Manfreda, S., 2019. Towards harmonization of image velocimetry techniques for riversurface velocity observations (preprint). Hydrology and Soil Science – Hydrology. https://doi.org/10.5194/essd-2019-133

Perks, M.T., Russell, A.J., Large, A.R.G., 2016. Technical Note: Advances in flash flood monitoring using unmanned aerial vehicles (UAVs). Hydrology and Earth System Sciences 20, 4005–4015. https://doi.org/10.5194/hess-20-4005-2016

Perks, M.T., Sasso, S.F.D., Hauet, A., Jamieson, E., Coz, J.L., Pearce, S., Peña-Haro, S., Pizarro, A., Strelnikova, D., Tauro, F., Bomhof, J., Grimaldi, S., Goulet, A., Hortobágyi, B., Jodeau, M., Käfer, S., Ljubicˇic, R., Maddock, I., Mayr, P., Paulus, G., Pénard, L., Sinclair, L., Manfreda, S., 2020. Towards harmonisation of image velocimetry techniques for river surface velocity observations 15.

Perrou, T., Garioud, A., Parcharidis, I., 2018. Use of Sentinel-1 imagery for flood management in a reservoir-regulated river basin. Frontiers of Earth Science 12, 506–520.

Pinos, J., Timbe, L., 2019. Performance assessment of two-dimensional hydraulic models for generation of flood inundation maps in mountain river basins. Water science and engineering 12, 11–18.

Pizer, S.M., 1990. Contrast-limited adaptive histogram equalization: Speed and effectiveness stephen m. pizer, r. eugene johnston, james p. ericksen, bonnie c. yankaskas, keith e. muller medical image display research group. Presented at the Proceedings of the first conference on visualization in biomedical computing, Atlanta, Georgia, p. 2.

Pradhan, D., Sahu, R.T., Verma, M.K., 2022. Flood Inundation Mapping Using GIS and Hydraulic Model (HEC-RAS): A Case Study of the Burhi Gandak River, Bihar, India, in: Kumar, R., Ahn, C.W., Sharma, T.K., Verma, O.P., Agarwal, A. (Eds.), Soft Computing: Theories and Applications, Lecture Notes in Networks and Systems. Springer Nature Singapore, Singapore, pp. 135–145. https://doi.org/10.1007/978-981-19-0707-4_14

Preetha, M.M.S.J., Suresh, L.P., Bosco, M.J., 2012. Image segmentation using seeded region growing. Presented at the 2012 International Conference on Computing, Electronics and Electrical Technologies (ICCEET), IEEE, pp. 576–583.

Qi, X., Li, K., Liu, P., Zhou, X., Sun, M., 2020. Deep attention and multi-scale networks for accurate remote sensing image segmentation. IEEE Access 8, 146627–146639.

Raffel, M., Willert, C.E., Kompenhans, J., 1998. Particle image velocimetry: a practical guide. Springer.

Rahnemoonfar, M., Chowdhury, T., Sarkar, A., Varshney, D., Yari, M., Murphy, R.R., 2021. FloodNet: A High Resolution Aerial Imagery Dataset for Post Flood Scene Understanding. IEEE Access 9, 89644–89654. https://doi.org/10.1109/ACCESS.2021.3090981

Rambour, C., Audebert, N., Koeniguer, E., Le Saux, B., Crucianu, M., Datcu, M., 2020. Sen12-flood: a sar and multispectral dataset for flood detection. IEEE: Piscataway, NJ, USA.

Rantz, S.E., 1982a. Measurement and Computation of Streamflow. U.S. Department of the Interior, Geological Survey.

Rantz, S.E., 1982b. Measurement and computation of streamflow (USGS Numbered Series No. 2175), Measurement and computation of streamflow, Water Supply Paper. U.S. G.P.O. https://doi.org/10.3133/wsp2175

Rauniyar, S.P., Protat, A., Kanamori, H., 2017. Uncertainties in TRMM-Era multisatellite-based tropical rainfall estimates over the Maritime Continent. Earth and Space Science 4, 275–302. https://doi.org/10.1002/2017EA000279

Rees, W.G., 2013. Physical principles of remote sensing. Cambridge university press.

Rentschler, J., Salhab, M., 2020. People in Harm’s Way: Flood Exposure and Poverty in 189 Countries, Policy Research Working Papers. The World Bank. https://doi.org/10.1596/1813-9450-9447

Revel, M., Zhou, X., Yamazaki, D., Kanae, S., 2023. Assimilation of transformed water surface elevation to improve river discharge estimation in a continental-scale river. Hydrology and Earth System Sciences 27, 647–671. https://doi.org/10.5194/hess-27-647-2023

Reynolds, J., Halldin, S., Seibert, J., Xu, C.-Y., Grabs, T., 2020. Robustness of flood-model calibration using single and multiple events. Hydrological Sciences Journal 65, 842–853.

Ridnik, T., Ben-Baruch, E., Noy, A., Zelnik-Manor, L., 2021. ImageNet-21K Pretraining for the Masses.

Riggs, R.M., Allen, G.H., David, C.H., Lin, P., Pan, M., Yang, X., Gleason, C., 2022. RODEO: An algorithm and Google Earth Engine application for river discharge retrieval from Landsat. Environmental Modelling & Software 148, 105254. https://doi.org/10.1016/j.envsoft.2021.105254

Rollason, E., Bracken, L.J., Hardy, R.J., Large, A.R.G., 2018. The importance of volunteered geographic information for the validation of flood inundation models. Journal of Hydrology 562, 267–280. https://doi.org/10.1016/j.jhydrol.2018.05.002

Ronneberger, O., Fischer, P., Brox, T., 2015. U-Net: Convolutional Networks for Biomedical Image Segmentation.

Rosten, E., Drummond, T., 2005. Fusing points and lines for high performance tracking, in: Tenth IEEE International Conference on Computer Vision (ICCV’05) Volume 1. Presented at the Tenth IEEE International Conference on Computer Vision (ICCV’05) Volume 1, pp. 1508-1515 Vol. 2. https://doi.org/10.1109/ICCV.2005.104

Rublee, E., Rabaud, V., Konolige, K., Bradski, G., 2011. ORB: An efficient alternative to SIFT or SURF, in: 2011 International Conference on Computer Vision. Presented at the 2011 International Conference on Computer Vision, pp. 2564–2571. https://doi.org/10.1109/ICCV.2011.6126544

Sarkar, S., Das, S., 2013. Multilevel image thresholding based on 2D histogram and maximum Tsallis entropy—a differential evolution approach. IEEE Transactions on Image Processing 22, 4788–4797.

Satarzadeh, E., Sarraf, A., Hajikandi, H., Sadeghian, M.S., 2022. Flood hazard mapping in western Iran: assessment of deep learning vis-à-vis machine learning models. Natural Hazards 1–19.

Schindelin, J., Arganda-Carreras, I., Frise, E., Kaynig, V., Longair, M., Pietzsch, T., Preibisch, S., Rueden, C., Saalfeld, S., Schmid, B., Tinevez, J.-Y., White, D.J., Hartenstein, V., Eliceiri, K., Tomancak, P., Cardona, A., 2012. Fiji: an open-source platform for biological-image analysis. Nat Methods 9, 676–682. https://doi.org/10.1038/nmeth.2019

Schumann, G., Bates, P.D., Horritt, M.S., Matgen, P., Pappenberger, F., 2009. Progress in integration of remote sensing–derived flood extent and stage data and hydraulic models. Reviews of Geophysics 47. https://doi.org/10.1029/2008RG000274

Schumann, G.J.-P., 2017. Remote Sensing of Floods, in: Oxford Research Encyclopedia of Natural Hazard Science. Oxford University Press. https://doi.org/10.1093/acrefore/9780199389407.013.265

Schumann, G.J.-P., Bates, P.D., Neal, J.C., Andreadis, K.M., 2015. Chapter 2 - Measuring and Mapping Flood Processes, in: Shroder, J.F., Paron, P., Baldassarre, G.D. (Eds.), Hydro-Meteorological Hazards, Risks and Disasters. Elsevier, Boston, pp. 35–64. https://doi.org/10.1016/B978-0-12-394846-5.00002-3

Schumann, G.J.-P., Moller, D.K., 2015. Microwave remote sensing of flood inundation. Physics and Chemistry of the Earth, Parts A/B/C 83–84, 84–95. https://doi.org/10.1016/j.pce.2015.05.002

Schumann, Muhlhausen, Andreadis, 2019. Rapid Mapping of Small-Scale River-Floodplain Environments Using UAV SfM Supports Classical Theory. Remote Sensing 11, 982. https://doi.org/10.3390/rs11080982

Scotti, V., Giannini, M., Cioffi, F., 2020. Enhanced flood mapping using synthetic aperture radar (SAR) images, hydraulic modelling, and social media: A case study of Hurricane Harvey (Houston, TX). J Flood Risk Management 13. https://doi.org/10.1111/jfr3.12647

Seitz, S.M., Curless, B., Diebel, J., Scharstein, D., Szeliski, R., 2006. A Comparison and Evaluation of Multi-View Stereo Reconstruction Algorithms, in: 2006 IEEE Computer Society Conference on Computer Vision and Pattern Recognition (CVPR'06). Presented at the 2006 IEEE Computer Society Conference on Computer Vision and Pattern Recognition (CVPR'06), pp. 519–528. https://doi.org/10.1109/CVPR.2006.19

Selva, D., Krejci, D., 2012. A survey and assessment of the capabilities of Cubesats for Earth observation. Acta Astronautica 74, 50–68. https://doi.org/10.1016/j.actaastro.2011.12.014

Sevak, J.S., Kapadia, A.D., Chavda, J.B., Shah, A., Rahevar, M., 2017. Survey on semantic image segmentation techniques. Presented at the 2017 International Conference on Intelligent Sustainable Systems (ICISS), IEEE, pp. 306–313.

Sharif, O., 2022. Measuring surface water flow velocities by a drone and large-scale particle image velocimetry (LSPIV) [WWW Document]. URL http://essay.utwente.nl/93022/ (accessed 1.5.23).

Shastry, A., Carter, E., Coltin, B., Sleeter, R., McMichael, S., Eggleston, J., 2023. Mapping floods from remote sensing data and quantifying the effects of surface obstruction by clouds and vegetation. Remote Sensing of Environment 291, 113556. https://doi.org/10.1016/j.rse.2023.113556

Shen, C., 2018. A Transdisciplinary Review of Deep Learning Research and Its Relevance for Water Resources Scientists. Water Resour. Res. 54, 8558–8593. https://doi.org/10.1029/2018WR022643

Shen, D., Wang, J., Cheng, X., Rui, Y., Ye, S., 2015. Integration of 2-D hydraulic model and high-resolution lidar-derived DEM for floodplain flow modeling. Hydrology and Earth System Sciences 19, 3605–3616.

Shen, S., 2013. Accurate Multiple View 3D Reconstruction Using Patch-Based Stereo for Large-Scale Scenes. IEEE Transactions on Image Processing 22, 1901–1914. https://doi.org/10.1109/TIP.2013.2237921

Shen, X., Wang, D., Mao, K., Anagnostou, E., Hong, Y., 2019. Inundation Extent Mapping by Synthetic Aperture Radar: A Review. Remote Sensing 11, 879. https://doi.org/10.3390/rs11070879

Shiklomanov, A.I., Lammers, R.B., Vörösmarty, C.J., 2002. Widespread decline in hydrological monitoring threatens Pan-Arctic Research. Eos, Transactions American Geophysical Union 83, 13–17. https://doi.org/10.1029/2002EO000007

Shrestha, A., Mascaro, G., Garcia, M., 2022. Effects of stormwater infrastructure data completeness and model resolution on urban flood modeling. Journal of Hydrology 607, 127498.

Shu, M., Zhong, Y., Lv, P., 2021. Small moving vehicle detection via local enhancement fusion for satellite video. International Journal of Remote Sensing 42, 7189–7214. https://doi.org/10.1080/01431161.2021.1944694

Shustikova, I., Domeneghetti, A., Neal, J.C., Bates, P., Castellarin, A., 2019. Comparing 2D capabilities of HEC-RAS and LISFLOOD-FP on complex topography. Hydrological Sciences Journal 64, 1769–1782. https://doi.org/10.1080/02626667.2019.1671982

Simonyan, K., Zisserman, A., 2015. Very Deep Convolutional Networks for Large-Scale Image Recognition.

Singh, S., Kansal, M.L., 2022. Chamoli flash-flood mapping and evaluation with a supervised classifier and NDWI thresholding using Sentinel-2 optical data in Google earth engine. Earth Sci Inform 15, 1073–1086. https://doi.org/10.1007/s12145-022-00786-8

Sit, M., Demiray, B.Z., Xiang, Z., Ewing, G.J., Sermet, Y., Demir, I., 2020. A Comprehensive Review of Deep Learning Applications in Hydrology and Water Resources. https://doi.org/10.48550/ARXIV.2007.12269

Smith, A., 2010. Image segmentation scale parameter optimization and land cover classification using the Random Forest algorithm. Journal of Spatial Science 55, 69–79.

Smith, M.W., Carrivick, J.L., Quincey, D.J., 2016. Structure from motion photogrammetry in physical geography. Progress in physical geography 40, 247–275.

Smith, M.W., Vericat, D., 2015. From experimental plots to experimental landscapes: topography, erosion and deposition in sub-humid badlands from Structure-from-Motion photogrammetry. Earth Surface Processes and Landforms 40, 1656–1671. https://doi.org/10.1002/esp.3747

Smith, R.A.E., Bates, P.D., Hayes, C., 2012. Evaluation of a coastal flood inundation model using hard and soft data. Environmental Modelling & Software 30, 35–46. https://doi.org/10.1016/j.envsoft.2011.11.008

Snavely, N., 2011. Scene reconstruction and visualization from internet photo collections: A survey. IPSJ Transactions on Computer Vision and Applications 3, 44–66.

Song, M., Civco, D., 2004. Road extraction using SVM and image segmentation. Photogrammetric Engineering & Remote Sensing 70, 1365–1371.

Stewardson, M.J., Walker, G., Coleman, M., 2021. Hydrology of the Murray–Darling Basin, in: Murray-Darling Basin, Australia. Elsevier, pp. 47–73. https://doi.org/10.1016/B978-0-12-818152-2.00003-6

Stott, E., Williams, R.D., Hoey, T.B., 2020. Ground Control Point Distribution for Accurate Kilometre-Scale Topographic Mapping Using an RTK-GNSS Unmanned Aerial Vehicle and SfM Photogrammetry. Drones 4, 55. https://doi.org/10.3390/drones4030055

Strelnikova, D., Perks, M.T., Dal Sasso, S.F., Pizarro, A., 2023. River flow monitoring with unmanned aerial system, in: Unmanned Aerial Systems for Monitoring Soil, Vegetation, and Riverine Environments. Elsevier, pp. 231–269.

Strudel, R., Garcia, R., Laptev, I., Schmid, C., 2021. Segmenter: Transformer for semantic segmentation. Presented at the Proceedings of the IEEE/CVF international conference on computer vision, pp. 7262–7272.

Su, T., Liu, T., Zhang, S., Qu, Z., Li, R., 2020. Machine learning-assisted region merging for remote sensing image segmentation. ISPRS Journal of Photogrammetry and Remote Sensing 168, 89–123.

Su, Y., Cheng, J., Wang, W., Bai, H., Liu, H., 2022. Semantic segmentation for high-resolution remote-sensing images via dynamic graph context reasoning. IEEE Geoscience and Remote Sensing Letters 19, 1–5.

Sultana, F., Sufian, A., Dutta, P., 2018. Advancements in image classification using convolutional neural network. Presented at the 2018 Fourth International Conference on Research in Computational Intelligence and Communication Networks (ICRCICN), IEEE, pp. 122–129.

Sun, G., Liu, Y., Ding, H., Probst, T., Van Gool, L., 2022. Coarse-to-fine feature mining for video semantic segmentation. Presented at the Proceedings of the IEEE/CVF Conference on Computer Vision and Pattern Recognition, pp. 3126–3137.

Sun, X., Shiono, K., Chandler, J.H., Rameshwaran, P., Sellin, R.H.J., Fujita, I., 2010. Discharge estimation in small irregular river using LSPIV. Proceedings of the Institution of Civil Engineers - Water Management 163, 247–254. https://doi.org/10.1680/wama.2010.163.5.247

Sun, Y., Bi, F., Gao, Y., Chen, L., Feng, S., 2022. A Multi-Attention UNet for Semantic Segmentation in Remote Sensing Images. Symmetry 14, 906. https://doi.org/10.3390/sym14050906

Sun, Z., Sandoval, L., Crystal-Ornelas, R., Mousavi, S.M., Wang, Jinbo, Lin, C., Cristea, N., Tong, D., Carande, W.H., Ma, X., Rao, Y., Bednar, J.A., Tan, A., Wang, Jianwu, Purushotham, S., Gill, T.E., Chastang, J., Howard, D., Holt, B., Gangodagamage, C., Zhao, P., Rivas, P., Chester, Z., Orduz, J., John, A., 2022. A review of Earth Artificial

Intelligence. Computers & Geosciences 159, 105034. https://doi.org/10.1016/j.cageo.2022.105034

Swain, D., Wing, O.E., Bates, P.D., Done, J., Johnson, K., Cameron, D., 2020. Increased flood exposure due to climate change and population growth in the United States. Earth’s Future 8, e2020EF001778.

Szegedy, C., Liu, W., Jia, Y., Sermanet, P., Reed, S., Anguelov, D., Erhan, D., Vanhoucke, V., Rabinovich, A., 2015. Going deeper with convolutions. Presented at the Proceedings of the IEEE conference on computer vision and pattern recognition, pp. 1–9.

Tabari, H., 2020. Climate change impact on flood and extreme precipitation increases with water availability. Scientific reports 10, 1–10.

Tachikawa, T., Hato, M., Kaku, M., Iwasaki, A., 2011. Characteristics of ASTER GDEM version 2. Presented at the 2011 IEEE international geoscience and remote sensing symposium, IEEE, pp. 3657–3660.

Tadono, T., Takaku, J., Tsutsui, K., Oda, F., Nagai, H., 2015. Status of “ALOS World 3D (AW3D)” global DSM generation, in: 2015 IEEE International Geoscience and Remote Sensing Symposium (IGARSS). Presented at the 2015 IEEE International Geoscience and Remote Sensing Symposium (IGARSS), pp. 3822–3825. https://doi.org/10.1109/IGARSS.2015.7326657

Tai, Y., Yang, J., Liu, X., 2017. Image super-resolution via deep recursive residual network. Presented at the Proceedings of the IEEE conference on computer vision and pattern recognition, pp. 3147–3155.

Tan, C., Sun, F., Kong, T., Zhang, W., Yang, C., Liu, C., 2018. A Survey on Deep Transfer Learning, in: Kůrková, V., Manolopoulos, Y., Hammer, B., Iliadis, L., Maglogiannis, I. (Eds.), Artificial Neural Networks and Machine Learning – ICANN 2018, Lecture Notes in Computer Science. Springer International Publishing, Cham, pp. 270–279. https://doi.org/10.1007/978-3-030-01424-7_27

Tanim, A.H., McRae, C.B., Tavakol-Davani, H., Goharian, E., 2022. Flood Detection in Urban Areas Using Satellite Imagery and Machine Learning. Water 14, 1140. https://doi.org/10.3390/w14071140

Tarpanelli, Angelica, Barbetta, S., Brocca, L., Moramarco, T., 2013. River Discharge Estimation by Using Altimetry Data and Simplified Flood Routing Modeling. Remote Sensing 5, 4145–4162. https://doi.org/10.3390/rs5094145

Tarpanelli, A., Brocca, L., Melone, F., Moramarco, T., 2013. Hydraulic modelling calibration in small rivers by using coarse resolution synthetic aperture radar imagery. Hydrological Processes 27, 1321–1330. https://doi.org/10.1002/hyp.9550

Tauro, F., Petroselli, A., Grimaldi, S., 2018. Optical sensing for stream flow observations: A review. Journal of Agricultural Engineering 49, 199–206. https://doi.org/10.4081/jae.2018.836

Tauro, F., Piscopia, R., Grimaldi, S., 2017. Streamflow Observations From Cameras: Large-Scale Particle Image Velocimetry or Particle Tracking Velocimetry? Water Resources Research 53, 10374–10394. https://doi.org/10.1002/2017WR020848

Tauro, F., Porfiri, M., Grimaldi, S., 2014. Orienting the camera and firing lasers to enhance large scale particle image velocimetry for streamflow monitoring. Water Resources Research 50, 7470–7483. https://doi.org/10.1002/2014WR015952

Tellman, B., Sullivan, J.A., Kuhn, C., Kettner, A.J., Doyle, C.S., Brakenridge, G.R., Erickson, T.A., Slayback, D.A., 2021. Satellite imaging reveals increased proportion of population exposed to floods. Nature 596, 80–86. https://doi.org/10.1038/s41586-021-03695-w

Teodoro, A.C., 2016. Optical satellite remote sensing of the coastal zone environment—An overview. Environment Applications of Remote Sensing. London, UK, InTechOpen 165–196.

Thielicke, W., 2014. The flapping flight of birds. Diss. University of Groningen.

Thielicke, W., Sonntag, R., 2021. Particle Image Velocimetry for MATLAB: Accuracy and enhanced algorithms in PIVlab. Journal of Open Research Software 9.

Thielicke, W., Stamhuis, E., 2014. PIVlab – Towards User-friendly, Affordable and Accurate Digital Particle Image Velocimetry in MATLAB. Journal of Open Research Software 2, e30. https://doi.org/10.5334/jors.bl

Tiampo, K.F., Huang, L., Simmons, C., Woods, C., Glasscoe, M.T., 2022. Detection of Flood Extent Using Sentinel-1A/B Synthetic Aperture Radar: An Application for Hurricane Harvey, Houston, TX. Remote Sensing 14, 2261. https://doi.org/10.3390/rs14092261

Tian, C., Yuan, Y., Zhang, S., Lin, C.-W., Zuo, W., Zhang, D., 2022. Image super-resolution with an enhanced group convolutional neural network. Neural Networks 153, 373–385.

Timbadiya, P.V., Patel, P.L., Porey, P.D., 2011. Calibration of HEC-RAS Model on Prediction of Flood for Lower Tapi River, India. Journal of Water Resource and Protection 3, 805–811. https://doi.org/10.4236/jwarp.2011.311090

Tong, X., Luo, X., Liu, Shuguang, Xie, H., Chao, W., Liu, Shuang, Liu, Shijie, Makhinov, A., Makhinova, A., Jiang, Y., 2018. An approach for flood monitoring by the combined use of Landsat 8 optical imagery and COSMO-SkyMed radar imagery. ISPRS journal of photogrammetry and remote sensing 136, 144–153.

Tong, X.-Y., Xia, G.-S., Lu, Q., Shen, H., Li, S., You, S., Zhang, L., 2020. Land-cover classification with high-resolution remote sensing images using transferable deep models. Remote Sensing of Environment 237, 111322.

Triggs, B., McLauchlan, P.F., Hartley, R.I., Fitzgibbon, A.W., 2000. Bundle adjustment—a modern synthesis. Presented at the Vision Algorithms: Theory and Practice: International Workshop on Vision Algorithms Corfu, Greece, September 21–22, 1999 Proceedings, Springer, pp. 298–372.

Tsakiris, G., 2014. Flood risk assessment: concepts, modelling, applications. Natural Hazards and Earth System Sciences 14, 1361–1369.

Tunstall, L., Von Werra, L., Wolf, T., 2022. Natural language processing with transformers. O’Reilly Media, Inc.

Turnipseed, D.P., Sauer, V.B., 2010. Discharge measurements at gaging stations (USGS Numbered Series No. 3-A8), Discharge measurements at gaging stations, Techniques and Methods. U.S. Geological Survey, Reston, VA. https://doi.org/10.3133/tm3A8

Uddin, K., Matin, M.A., Meyer, F.J., 2019. Operational flood mapping using multi-temporal Sentinel-1 SAR images: A case study from Bangladesh. Remote Sensing 11, 1581.

Ullman, S., 1979. The interpretation of structure from motion. Proceedings of the Royal Society of London. Series B. Biological Sciences 203, 405–426.

Upadhyay, P., Chhabra, J.K., 2021. Multilevel thresholding based image segmentation using new multistage hybrid optimization algorithm. Journal of Ambient Intelligence and Humanized Computing 12, 1081–1098.

Verdie, Y., Yi, K.M., Fua, P., Lepetit, V., 2015. TILDE: A Temporally Invariant Learned DEtector, in: 2015 IEEE Conference on Computer Vision and Pattern Recognition (CVPR). Presented at the 2015 IEEE Conference on Computer Vision and Pattern Recognition (CVPR), pp. 5279–5288. https://doi.org/10.1109/CVPR.2015.7299165

Vigoureux, S., Liebard, L.-L., Chonoski, A., Robert, E., Torchet, L., Poveda, V., Leclerc, F., Billant, J., Dumasdelage, R., Rousseau, G., Delestre, O., Brigode, P., 2022. Comparison of Streamflow Estimated by Image Analysis (LSPIV) and by Hydrologic and Hydraulic Modelling on the French Riviera During November 2019 Flood, in: Gourbesville, P., Caignaert, G. (Eds.), Advances in Hydroinformatics, Springer Water. Springer Nature, Singapore, pp. 255–273. https://doi.org/10.1007/978-981-19-1600-7_16

Walker, D., Forsythe, N., Parkin, G., Gowing, J., 2016. Filling the observational void: Scientific value and quantitative validation of hydrometeorological data from a community-based monitoring programme. Journal of Hydrology 538, 713–725. https://doi.org/10.1016/j.jhydrol.2016.04.062

Wang, J., Wang, S., Wang, F., Zhou, Y., Wang, Z., Ji, J., Xiong, Y., Zhao, Q., 2022. FWENet: a deep convolutional neural network for flood water body extraction based on SAR images. International Journal of Digital Earth 15, 345–361. https://doi.org/10.1080/17538947.2021.1995513

Wang, L., Li, R., Zhang, C., Fang, S., Duan, C., Meng, X., Atkinson, P.M., 2022. UNetFormer: A UNet-like transformer for efficient semantic segmentation of remote sensing urban scene imagery. ISPRS Journal of Photogrammetry and Remote Sensing 190, 196–214.

Wang, T., Lan, J., Han, Z., Hu, Z., Huang, Y., Deng, Y., Zhang, H., Wang, J., Chen, M., Jiang, H., 2022. O-Net: a novel framework with deep fusion of CNN and transformer for simultaneous segmentation and classification. Frontiers in neuroscience 16, 876065.

WaterNSW, 2023. Water New South Wales. https://realtimedata.waternsw.com.au/. https://realtimedata.waternsw.com.au/

Welber, M., Le Coz, J., Laronne, J.B., Zolezzi, G., Zamler, D., Dramais, G., Hauet, A., Salvaro, M., 2016. Field assessment of noncontact stream gauging using portable surface velocity radars (SVR): FIELD ASSESSMENT OF PORTABLE SURFACE VELOCITY RADARS. Water Resour. Res. 52, 1108–1126. https://doi.org/10.1002/2015WR017906

Westerweel, J., Scarano, F., 2005. Universal outlier detection for PIV data. Experiments in fluids 39, 1096–1100.

Wieland, M., Martinis, S., Kiefl, R., Gstaiger, V., 2023. Semantic segmentation of water bodies in very high-resolution satellite and aerial images. Remote Sensing of Environment 287, 113452.

Williams, R.D., Brasington, J., Hicks, M., Measures, R., Rennie, C.D., Vericat, D., 2013. Hydraulic validation of two-dimensional simulations of braided river flow with spatially continuous aDcp data. Water Resources Research 49, 5183–5205. https://doi.org/10.1002/wrcr.20391

Wilson, M., Bates, P., Alsdorf, D., Forsberg, B., Horritt, M., Melack, J., Frappart, F., Famiglietti, J., 2007. Modeling large-scale inundation of Amazonian seasonally flooded wetlands. Geophysical Research Letters 34. https://doi.org/10.1029/2007GL030156

Wing, O.E.J., 2019. Understanding Flood Risk at Large Spatial Scales: Testing, Development and Application of a Continental Flood Hazard Model.

Wing, O.E.J., Bates, P.D., Sampson, C.C., Smith, A.M., Johnson, K.A., Erickson, T.A., 2017. Validation of a 30 m resolution flood hazard model of the conterminous United States: 30 m RESOLUTION FLOOD MODEL OF CONUS. Water Resour. Res. 53, 7968–7986. https://doi.org/10.1002/2017WR020917

Wing, O.E.J., Smith, A.M., Marston, M.L., Porter, J.R., Amodeo, M.F., Sampson, C.C., Bates, P.D., 2021. Simulating historical flood events at the continental scale:

observational validation of a large-scale hydrodynamic model. Nat. Hazards Earth Syst. Sci. 21, 559–575. https://doi.org/10.5194/nhess-21-559-2021

Wolf, T., Debut, L., Sanh, V., Chaumond, J., Delangue, C., Moi, A., Cistac, P., Rault, T., Louf, R., Funtowicz, M., 2020. Transformers: State-of-the-art natural language processing. Presented at the Proceedings of the 2020 conference on empirical methods in natural language processing: system demonstrations, pp. 38–45.

Woodget, A.S., Carbonneau, P.E., Visser, F., Maddock, I.P., 2015. Quantifying submerged fluvial topography using hyperspatial resolution UAS imagery and structure from motion photogrammetry: SUBMERGED FLUVIAL TOPOGRAPHY FROM UAS IMAGERY AND SfM. Earth Surf. Process. Landforms 40, 47–64. https://doi.org/10.1002/esp.3613

World Bank, 2019. Weathering the Change: How to Improve Hydromet Services in Developing Countries?

Xiao, A., Wang, Z., Wang, L., Ren, Y., 2018. Super-Resolution for “Jilin-1” Satellite Video Imagery via a Convolutional Network. Sensors 18, 1194. https://doi.org/10.3390/s18041194

Xiao, Y., Su, X., Yuan, Q., Liu, D., Shen, H., Zhang, L., 2021. Satellite video super-resolution via multiscale deformable convolution alignment and temporal grouping projection. IEEE Transactions on Geoscience and Remote Sensing 60, 1–19.

Xie, E., Wang, W., Yu, Z., Anandkumar, A., Alvarez, J.M., Luo, P., 2021. SegFormer: Simple and efficient design for semantic segmentation with transformers. Advances in Neural Information Processing Systems 34, 12077–12090.

Xiong, D., He, C., Liu, X., Liao, M., 2020. An end-to-end Bayesian segmentation network based on a generative adversarial network for remote sensing images. Remote Sensing 12, 216.

Xu, H., 2006. Modification of normalised difference water index (NDWI) to enhance open water features in remotely sensed imagery. International Journal of Remote Sensing 27, 3025–3033. https://doi.org/10.1080/01431160600589179

Xu, X., Li, J., Tolson, B.A., 2014. Progress in integrating remote sensing data and hydrologic modeling. Progress in Physical Geography 38, 464–498.

Xu, Z., Zhang, W., Zhang, T., Yang, Z., Li, J., 2021. Efficient Transformer for Remote Sensing Image Segmentation. Remote Sensing 13, 3585. https://doi.org/10.3390/rs13183585

Yadav, G., Maheshwari, S., Agarwal, A., 2014. Contrast limited adaptive histogram equalization based enhancement for real time video system. Presented at the 2014 international conference on advances in computing, communications and informatics (ICACCI), IEEE, pp. 2392–2397.

Yalcin, E., 2020. Assessing the impact of topography and land cover data resolutions on two-dimensional HEC-RAS hydrodynamic model simulations for urban flood hazard analysis. Nat Hazards 101, 995–1017. https://doi.org/10.1007/s11069-020-03906-z

Yalcin, E., 2019. Two-dimensional hydrodynamic modelling for urban flood risk assessment using unmanned aerial vehicle imagery: A case study of Kirsehir, Turkey. Journal of Flood Risk Management 12, e12499. https://doi.org/10.1111/jfr3.12499

Yamashita, R., Nishio, M., Do, R.K.G., Togashi, K., 2018. Convolutional neural networks: an overview and application in radiology. Insights Imaging 9, 611–629. https://doi.org/10.1007/s13244-018-0639-9

Yamazaki, D., Ikeshima, D., Neal, J.C., O'Loughlin, F., Sampson, C.C., Kanae, S., Bates, P.D., 2017. MERIT DEM: A new high-accuracy global digital elevation model and its merit to global hydrodynamic modeling. Presented at the AGU fall meeting abstracts, pp. H12C-04.

Yamazaki, D., Ikeshima, D., Sosa, J., Bates, P.D., Allen, G.H., Pavelsky, T.M., 2019. MERIT Hydro: a high-resolution global hydrography map based on latest topography dataset. Water Resources Research 55, 5053–5073.

Yan, K., Di Baldassarre, G., Solomatine, D.P., Schumann, G.J., 2015. A review of low-cost space-borne data for flood modelling: topography, flood extent and water level. Hydrological processes 29, 3368–3387.

Yang, Z., Wang, J., Tang, Y., Chen, K., Zhao, H., Torr, P.H., 2022. Lavt: Language-aware vision transformer for referring image segmentation. Presented at the Proceedings of the IEEE/CVF Conference on Computer Vision and Pattern Recognition, pp. 18155–18165.

Yi, K.M., Trulls, E., Lepetit, V., Fua, P., 2016. Lift: Learned invariant feature transform. Presented at the Computer Vision–ECCV 2016: 14th European Conference, Amsterdam, The Netherlands, October 11-14, 2016, Proceedings, Part VI 14, Springer, pp. 467–483.

Yuan, F., Zhang, L., Xia, X., Huang, Q., Li, X., 2021. A Gated Recurrent Network With Dual Classification Assistance for Smoke Semantic Segmentation. IEEE Transactions on Image Processing 30, 4409–4422. https://doi.org/10.1109/TIP.2021.3069318

Yuan, F., Zhang, Z., Fang, Z., 2023. An effective CNN and Transformer complementary network for medical image segmentation. Pattern Recognition 136, 109228. https://doi.org/10.1016/j.patcog.2022.109228

Yurtkulu, S.C., Şahin, Y.H., Unal, G., 2019. Semantic segmentation with extended DeepLabv3 architecture. Presented at the 2019 27th Signal Processing and Communications Applications Conference (SIU), IEEE, pp. 1–4.

Zakharova, E., Nielsen, K., Kamenev, G., Kouraev, A., 2020. River discharge estimation from radar altimetry: Assessment of satellite performance, river scales and methods. Journal of Hydrology 583, 124561. https://doi.org/10.1016/j.jhydrol.2020.124561

Zeiger, S.J., Hubbart, J.A., 2021. Measuring and modeling event-based environmental flows: An assessment of HEC-RAS 2D rain-on-grid simulations. Journal of Environmental Management 285, 112125. https://doi.org/10.1016/j.jenvman.2021.112125

Zhang, C., Jiang, W., Zhang, Y., Wang, W., Zhao, Q., Wang, C., 2022. Transformer and CNN hybrid deep neural network for semantic segmentation of very-high-resolution remote sensing imagery. IEEE Transactions on Geoscience and Remote Sensing 60, 1–20.

Zhang, R., Yi, X., Li, H., Liu, L., Lu, G., Chen, Y., Guo, X., 2022. Multiresolution Patch-Based Dense Reconstruction Integrating Multiview Images and Laser Point Cloud, in: The International Archives of Photogrammetry, Remote Sensing and Spatial Information Sciences. Copernicus GmbH, Gottingen, Germany, pp. 153–159. https://doi.org/10.5194/isprs-archives-XLIII-B2-2022-153-2022

Zhao, H., Shi, J., Qi, X., Wang, X., Jia, J., 2017. Pyramid Scene Parsing Network.

Zheng, C., Wang, L., 2014. Semantic segmentation of remote sensing imagery using object-based Markov random field model with regional penalties. IEEE Journal of Selected Topics in Applied Earth Observations and Remote Sensing 8, 1924–1935.

Zhou, B., Zhao, H., Puig, X., Fidler, S., Barriuso, A., Torralba, A., 2017. Scene parsing through ade20k dataset. Presented at the Proceedings of the IEEE conference on computer vision and pattern recognition, pp. 633–641.

Zhou, Z., Zhang, J., Gong, C., 2023. Hybrid semantic segmentation for tunnel lining cracks based on Swin Transformer and convolutional neural network. Computer-Aided Civil and Infrastructure Engineering.

Zhu, X., Lipeme Kouyi, G., 2019. An Analysis of LSPIV-Based Surface Velocity Measurement Techniques for Stormwater Detention Basin Management. Water Resour. Res. 55, 888–903. https://doi.org/10.1029/2018WR023813